

Shelf-specific processes in the ocean carbon cycle: an investigation of tides

Dissertation

zur Erlangung des Doktorgrades

an der Fakultät für Mathematik, Informatik und Naturwissenschaften

Fachbereich Erdsystemwissenschaften

der Universität Hamburg

vorgelegt von

Jan Felix Gottlieb Kossack

Hamburg, 2024

Fachbereich Erdsystemwissenschaften

Datum der Disputation:

09.12.2024

Gutachter:innen der Dissertation:

Prof. Dr. Corinna Schrum

Dr. Moritz Mathis

Zusammensetzung der Prüfungskommission:

Prof. Dr. Corinna Schrum

Dr. Moritz Mathis

Prof. Dr. Helmuth Thomas

PD Dr. Thomas Pohlmann

Prof. Dr. Dirk Notz

Vorsitzender des Fach-Promotionsausschusses

Erdsystemwissenschaften:

Prof. Dr. Hermann Held

Dekan der Fakultät MIN:

Prof. Dr. Ing. Nobert Ritter

ABSTRACT

Continental shelves function as a highly dynamic transition zone that connects the carbon reservoirs of the terrestrial biosphere and the ocean, and disproportionately contribute to the global ocean sink for atmospheric CO₂. Despite their relevance for the global carbon cycle and hence the Earth's climate, major knowledge gaps on the control of oceanic CO₂ uptake on continental shelves and the relative contributions of processes specific to the shelf environment remain. This dissertation contributes to a better mechanistic understanding of carbon cycling on continental shelves by investigating the role of tides on the Northwest European Shelf (NWES), one of the largest temperate shelf seas in the global ocean.

Tides are one of the dominant physical forcing mechanisms on the NWES. Multifaceted tidal processes affect the shelf carbon cycle across varying spatial scales and modulate the biological cycling of carbon and nutrients. The compound impact of tides on the shelf carbon cycle is poorly understood, but it is relevant for global modelling approaches that often neglect tidal forcing, such as those utilized in climate change assessment reports.

In this dissertation, the novel three-dimensional coupled physical-biogeochemical numerical model framework SCHISM-ECOSMO-CO₂ is presented and applied for the first time. The model framework, which is based on an unstructured grid approach, is established as a flexible and adaptable platform for research on the NWES carbon cycle and applied to comprehensively investigate how tidal processes influence carbon transport, transformation and air-sea gas exchange at regional and shelf-wide scales.

The dissertation is divided into three individual studies following the development trajectory of the model framework. As a first step, I explore the capabilities of the cross-scale physical model component and present two new unstructured horizontal grid configurations developed for research on the NWES carbon cycle: a coarse resolution configuration optimized for the computationally efficient application of complex biogeochemical models and a high-resolution configuration applying local grid refinement to realize kilometrical-scale resolution to improve physical process representation. Both configurations encompass the same model domain, which covers the entire NWES, the Baltic Sea, and a portion of the eastern North Atlantic to enable a consistent investigation of regional-scale impacts, including ocean-shelf exchange. The validation of both model configurations against observations demonstrates adequate model performance regarding the general hydrography on the NWES, with the high-resolution configuration resolving small-scale internal tides and showing better process representation in numerically challenging regions like the Norwegian Trench and the Baltic Sea. The overall high consistency between the results of the two grid configurations underlines the flexibility and configurability of the model framework. The successful implementation of the cross-scale physical model component thus lays the foundation for research on the NWES carbon cycle along two connected avenues, namely the improved representations of physical and biogeochemical shelf-specific processes.

Subsequently, I validate and apply the coupled physical-biogeochemical model framework for a hindcast simulation over the period 2011-2014 and a sensitivity experiment to obtain a quantification of the impact of tidal forcing on shelf primary production. Tidally enhanced vertical mixing of nutrients is found responsible for about 1/6 of the total annual primary production on the NWES. However, the tidal impact on primary production is largely restricted

to shallow inner-shelf regions. The application of the cross-scale model framework for the first time provides an estimate of the compound impact of internal-tide-driven mixing on NWES primary production and reveals that the kilometrical-scale internal tide field only marginally contributes to biological carbon fixation on the shelf.

In a final step, I extend the model framework by additionally coupling and validating a carbonate system model which is subsequently applied for a hindcast simulation over the period 2001-2005 to investigate tidal impacts on air-sea CO₂ exchange and carbon cycling on the NWES. Tidal forcing is found to weaken the NWES CO₂ sink, with a sensitivity experiment neglecting tides resulting in a 13% stronger shelf CO₂ sink. This impact is dominated by physical tidal processes such as tidal mixing in inner-shelf regions and tide-induced shelf circulation. The previously identified enhanced biological carbon fixation, in contrast, has a minor effect on net CO₂ uptake. The impact of internal tides on air-sea CO₂ exchange on the NWES is found to be negligible. In terms of the shelf carbon budget, tides are shown to mainly affect carbon reservoirs on the NWES. Tides primarily modulate the dissolved inorganic carbon stock in the water column, while tidal impacts on off-shelf carbon export and long-term carbon burial in the sediments are small.

This dissertation provides new insights on the role of tides in the NWES carbon cycle and thereby informs on the consequences of neglecting tides in modelling approaches. The presented results, however, preclude an extrapolation to global continental shelves because of the heterogeneity in the main forcing mechanisms of coastal carbon dynamics in different shelf seas. The gained process understanding and the extensive validation of the SCHISM-ECOSMO-CO₂ model framework performed in the course of the dissertation further highlight several promising avenues for active model development that show potential to improve simulations of the shelf carbon cycle and may help address key uncertainties and capacitate critical future research.

ZUSAMMENFASSUNG

Kontinentalschelfs fungieren als eine hochdynamische Übergangszone, die die Kohlenstoffreservoirs der terrestrischen Biosphäre und des Ozeans verbindet und überproportional zur Aufnahme von atmosphärischem CO₂ durch den globalen Ozean beiträgt. Trotz ihrer Relevanz für den globalen Kohlenstoffkreislauf und damit für das Klimasystem der Erde bestehen erhebliche Wissenslücken bezüglich der Kontrolle der ozeanischen CO₂-Aufnahme auf Kontinentalschelfs und der relativen Beiträge schelfspezifischer Prozesse. Diese Dissertation trägt zu einem besseren mechanistischen Verständnis des Kohlenstoffkreislaufs auf Kontinentalschelfs bei, indem sie die Rolle der Gezeiten auf dem Nordwest-Europäischen Schelf (NWES) untersucht, einem der größten Schelfmeere im globalen Ozean in gemäßigten Breiten.

Gezeiten sind einer der dominierenden physikalischen Prozesse auf dem NWES. Vielschichtige Gezeitenprozesse beeinflussen den Kohlenstoffkreislauf auf dem Schelf über verschiedene räumliche Skalen hinweg und modulieren den biologischen Kreislauf von Kohlenstoff und Nährstoffen. Die komplexen Auswirkungen der Gezeiten auf den Kohlenstoffkreislauf auf dem Schelf sind bisher nicht umfassend untersucht, obwohl sie relevant für globale Modellierungsansätze sind, wie sie in Weltklimaberichten verwendet werden, da diese häufig Gezeiten vernachlässigen.

Das neue drei-dimensionale gekoppelte physikalisch-biogeochemische numerische Modellsystem SCHISM-ECOSMO-CO₂ wird in dieser Dissertation vorgestellt und erstmals angewendet. Das Modellsystem, welches auf einem unstrukturierten Gitteransatz basiert, wird als flexible und anpassbare Plattform für Forschung zum Kohlenstoffkreislauf auf dem NWES etabliert und angewendet, um umfassend zu untersuchen, wie Gezeitenprozesse den Transport von Kohlenstoff, seine Umwandlung sowie den Austausch von Kohlenstoff zwischen Ozean und Atmosphäre auf regionaler und schelfweiter Skala beeinflussen.

Die Dissertation ist in drei einzelne Studien unterteilt, die auf den Entwicklungsschritten des Modellsystems beruhen. Im ersten Schritt erschließe ich die Potenziale der flexiblen physikalischen Modellkomponente und präsentiere zwei neue unstrukturierte horizontale Gitterkonfigurationen, die für die Forschung zum Kohlenstoffkreislauf auf dem NWES entwickelt wurden: eine grob aufgelöste Konfiguration, die für die rechnereffiziente Anwendung komplexer biogeochemischer Modelle optimiert ist, und eine hochauflösende Konfiguration, die lokale Gitterverfeinerung anwendet, um eine Auflösung im Kilometermaßstab zu realisieren und dadurch die Darstellung physikalischer Prozesse zu verbessern. Beide Konfigurationen umfassen dasselbe Modellgebiet, das den gesamten NWES, die Ostsee und einen Teil des östlichen Nordatlantiks abdeckt, um eine konsistente Untersuchung regionaler Auswirkungen, einschließlich des Austauschs zwischen Ozean und Schelf, zu ermöglichen. Die Validierung beider Modellkonfigurationen anhand von Beobachtungen zeigt eine angemessene Modellleistung hinsichtlich der allgemeinen Hydrographie auf dem NWES, wobei die hochauflösende Konfiguration kleinskalige interne Gezeiten auflöst und bessere Modellergebnisse in numerisch herausfordernden Regionen wie dem Norwegischen Rinne oder der Ostsee aufweist. Die insgesamt hohe Konsistenz der Ergebnisse der beiden Gitterkonfigurationen unterstreicht die Flexibilität und Konfigurierbarkeit des Modellsystems. Die erfolgreiche Implementierung der physikalischen Modellkomponente bildet somit die Grundlage für die Forschung zum Kohlenstoffkreislauf auf

dem NWES entlang zweier miteinander verbundener Wege, nämlich der verbesserten Darstellung physikalischer und biogeochemischer schelfspezifischer Prozesse.

Anschließend validiere ich das gekoppelte physikalisch-biogeochemische Modellsystem und generiere damit eine Hindcast-Simulation über den Zeitraum 2011-2014 und ein Sensitivitätsexperiment, welche die Quantifizierung des Einflusses von Gezeiten auf die Primärproduktion auf dem NWES ermöglichen. Es wird festgestellt, dass durch Gezeiten verstärkte vertikale Vermischung von Nährstoffen für etwa 1/6 der gesamten jährlichen Primärproduktion auf dem NWES verantwortlich ist. Der Einfluss der Gezeiten auf die Primärproduktion beschränkt sich jedoch weitgehend auf flache innere Schelfregionen. Die Anwendung des hochaufgelösten Modellsystems liefert erstmals eine Abschätzung des Einflusses von internen Gezeiten auf die Primärproduktion auf dem NWES und zeigt, dass das interne Gezeitenfeld nur marginal zur biologischen Kohlenstoffbindung auf dem Schelf beiträgt.

Im letzten Schritt erweitere ich das Modellsystem durch die zusätzliche Kopplung und Validierung eines Karbonatsystem-Modells, das anschließend für eine Hindcast-Simulation über den Zeitraum 2001-2005 und ein Sensitivitätsexperiment verwendet wird, um Gezeiteinflüsse auf den CO₂-Austausch zwischen Ozean und Atmosphäre und den Kohlenstoffkreislauf auf dem NWES zu untersuchen. Es wird festgestellt, dass Gezeiten die CO₂-Senke auf dem NWES schwächen, wobei ein Sensitivitätsexperiment ohne Gezeiten zu einer um 13 % stärkeren CO₂-Senke führt. Dieser Einfluss wird von physikalischen Prozessen wie der Vermischung durch Gezeiten in inneren Schelfregionen und der durch Gezeiten induzierten Schelfzirkulation dominiert. Die zuvor identifizierte verstärkte biologische Kohlenstoffbindung hat im Gegensatz dazu nur eine geringe Auswirkung auf die Netto-CO₂-Aufnahme. Schließlich wird festgestellt, dass der Einfluss interner Gezeiten auf den CO₂-Austausch zwischen Ozean und Atmosphäre auf dem NWES vernachlässigbar ist. In Bezug auf den Kohlenstoffhaushalt des NWES wirken Gezeiten hauptsächlich auf die Kohlenstoffreservoirs auf dem Schelf selbst. Gezeiten modulieren hauptsächlich den Bestand an gelöstem anorganischem Kohlenstoff in der Wassersäule, während die Auswirkungen der Gezeiten auf den Kohlenstoffexport vom Schelf und die langfristige Kohlenstoffsequestration in den Sedimenten gering sind.

Diese Dissertation liefert neue Erkenntnisse über die Rolle der Gezeiten für den Kohlenstoffkreislauf auf dem NWES und informiert damit über die Konsequenzen der Vernachlässigung von Gezeiten in Modellierungsansätzen. Die präsentierten Ergebnisse lassen jedoch keine Extrapolation auf weitere Kontinentalschelfs im globalen Ozean zu, da die Hauptantriebsmechanismen der Kohlenstoffdynamik in verschiedenen Schelfmeeren unterschiedlich sind. Das gewonnene Prozessverständnis und die umfangreiche Validierung des SCHISM-ECOSMO-CO₂-Modellsystems, die im Verlauf der Dissertation durchgeführt wurde, zeigen zudem mehrere vielversprechende Wege für die aktive Modellentwicklung auf, die Potenzial zur Verbesserung der Simulationen des Schelfkohlenstoffkreislaufs haben und dazu beitragen können, zentrale Unsicherheiten zu adressieren. Diese Dissertation eröffnet somit die Möglichkeit für wichtige Forschung in der Zukunft.

LIST OF PUBLICATIONS

Publications related to this dissertation:

Appendix A

Kossack, J., Mathis, M., Daewel, U., Zhang, Y. J., Schrum, C. (2024). A cross-scale hydrodynamic model framework for the Northwest European Shelf and Baltic Sea based on unstructured grids. (*to be submitted*)

Appendix B

Kossack, J., Mathis, M., Daewel, U., Zhang, Y. J., Schrum, C. (2023). Barotropic and baroclinic tides increase primary production on the Northwest European Shelf. *Frontiers in Marine Science* 10:1206062. <https://doi.org/10.3389/fmars.2023.1206062>

Appendix C

Kossack, J., Mathis, M., Daewel, U., Liu, F., Demir, K. T., Thomas, H., Schrum, C. (2024). Tidal impacts on air-sea CO₂ exchange on the Northwest European Shelf. *Frontiers in Marine Science* (*under review*)

Contents

ABSTRACT	I
ZUSAMMENFASSUNG	III
LIST OF PUBLICATIONS	V
1. Introduction	1
1.1. The Northwest European Shelf (NWES)	3
1.2. Tides on the NWES	5
1.3. The marine carbon cycle on the NWES	6
1.4. Research gap	7
1.5. Approach and Outline	9
2. On unstructured grid modelling of the NWES	11
3. On the role of tide-induced biological carbon fixation for the NWES carbon cycle	12
4. On the role of internal tides for the NWES carbon cycle	15
5. On tidal impacts on carbon cycling and air-sea CO ₂ exchange on the NWES	17
6. Outlook	20
Appendices	25
Appendix A – A cross-scale hydrodynamic model framework for the Northwest European Shelf and Baltic Sea based on unstructured grids	27
Appendix B - Barotropic and baroclinic tides increase primary production on the Northwest European Shelf	55
Appendix C – Tidal impacts on air-sea CO ₂ exchange on the Northwest European Shelf ..	89
Bibliography	139

1. Introduction

Continental shelves only make up a small part of the global ocean surface area (<10%), but function as a highly dynamic transition zone that connects the carbon reservoirs of the terrestrial biosphere and the ocean. Continental shelves, particularly those at high latitudes, disproportionately contribute to the global ocean sink for atmospheric CO₂ (Roobaert et al., 2019; Dai et al., 2022; Resplandy et al., 2024), which is estimated to have taken up ~26% of the combined CO₂ emissions from fossil fuel burning and land use changes between 1850 and 2022 (Friedlingstein et al., 2023). Despite the important role of continental shelves, major knowledge gaps on the control of oceanic CO₂ uptake on continental shelves and the relative contributions of shelf-specific processes remain. Continental shelves thus persist as a key source of uncertainty in the oceanic carbon cycle (Laruelle et al., 2014; Hauck et al., 2020; Dai et al., 2022; Resplandy et al., 2024).

Carbon is present in inorganic and organic form in the ocean and is constantly being exchanged between the different reservoirs of the global ocean. A biological and a physical carbon pump mechanism mediate the majority of oceanic uptake of atmospheric CO₂ by transporting carbon into the deep ocean, where it is isolated from exchange with the atmosphere on timescales of several hundreds of years (Sarmiento et al., 2007). The vertical gradient of carbon in the ocean resulting from the pump mechanisms, with higher concentrations at depths, controls the effective CO₂ exchange with the atmosphere. The physical pump (or also solubility pump) relies on the inverse relationship between sea-water temperature and CO₂ solubility (solubility of CO₂ increases with decreasing temperature) and the (large-scale) ocean circulation. When the large-scale meridional overturning circulation (Broecker, 1991) transports cool and carbon-enriched surface waters to depth, primarily at high latitudes, the carbon is removed from contact with the atmosphere for the time scales of the circulation. In the biological carbon pump, phytoplankton assimilates dissolved inorganic carbon (DIC) into organic carbon, of which a fraction sinks to deeper layers as particulate organic carbon (POC) or is transported into the deep ocean with the overturning circulation (Ducklow et al., 2001; Sarmiento et al., 2007). The organic matter is either transformed back into dissolved inorganic carbon in the deep ocean or deposited in the sediment. The latter only constitutes a small part of the ocean carbon cycle but is crucial for the earth system, as the deposition of organic matter in the sediment allows CO₂ to be removed from the carbon cycle for millions of years.

The coastal ocean (a term used as an equivalent to continental shelves in the present study) constitutes a specific environment that connects the continental land masses and the deep oceans. At the shelf break, the steep continental slope forms the boundary between the shallow continental shelves (global median water depth ~160m; Paris et al., 2016) and the deep open ocean. Several physical and biogeochemical processes specific to continental shelves contribute to the constant exchange of carbon between different reservoirs and make the coastal ocean a complex and highly dynamic component of the global carbon cycle. Energetic shelf-specific physical processes like strong internal mixing, the relevant interaction between the water column and the sediment or high riverine inputs of nutrients are for example characteristic for the coastal ocean (see schematic illustration in Fig. 1). Continental shelves further exhibit large regional heterogeneity and strong spatial gradients and feature disproportionately high biological productivity (up to 30% of global primary production) and diverse ecosystems (Gattuso et al., 1998; Borges et al., 2005).

The various shelf-specific physical and biogeochemical processes modulate and transform carbon inputs from land and the open ocean and ultimately determine air-sea CO₂ exchange on continental shelves and carbon export to the open ocean or sediments. In contrast to the deep open ocean, a larger fraction of sinking POC can reach the sea floor on continental shelves before being remineralized. Sedimentation on continental shelves is accordingly estimated to contribute about ~80% to global organic carbon burial in the sediment (Gattuso et al., 1998). The shallow water depths however also implies that winter convection can ventilate the entire water column on continental shelves. This allows a direct interaction between the atmosphere and the bottom of the water column and the sediments on continental shelves. This means that removing carbon from contact with the atmosphere on continental shelves often requires lateral transport into the subsurface layers of the open ocean.

A specific combination of physical and biogeochemical shelf-specific processes, referred to as the continental shelf pump, provides a crucial pathway for lateral carbon export from continental shelves to the open ocean. Originally proposed for the East China Sea by Tsunogai et al. (1999), the continental shelf pump describes a mechanism through which dense and carbon-enriched water from the subsurface layer of the shelf is transported into the deep open ocean. The physical component of the continental shelf pump relies on stronger winter cooling on mid- and high-latitude continental shelves due to the limitation of deep convection by shallow bathymetry. The colder water temperatures on the shelf enable high uptake of atmospheric CO₂. Seasonal stratification in spring then isolates the cold and carbon-enriched water from the atmosphere, and horizontal advection or (isopycnal) mixing can subsequently transport it to the deep open ocean. In the biological component of the continental shelf pump, the biological pump mechanism is responsible for the accumulation of carbon in the subsurface layer on the shelf (Thomas et al., 2004).

The effects of the developing climate crisis, such as the increase in ocean temperatures, sea level rise, ocean acidification or changes in the large-scale ocean circulation, significantly affect the dynamic and complex continental shelf regime (e.g. Cooley et al., 2009; Holt et al., 2012; Gröger et al., 2013; Schrum et al., 2016). Global continental shelves further provide key resources and opportunities for society and consequently face high additional anthropogenic pressures, for example from pollution, extensive fishing or the expansion of offshore wind energy infrastructure. Continental shelves are moreover in the focus of carbon storage management or more deliberate climate mitigation efforts such as the enhancement of carbon storage as “negative emissions” (Minx et al., 2018), which might alleviate or exacerbate future pressures on the shelf system. Potential changes in shelf-specific physical or biological processes may affect oceanic CO₂ uptake and the future role of continental shelves in the marine carbon cycle. A comprehensive scientific understanding of continental shelf seas, particularly of processes relevant to the marine carbon cycle, is therefore essential for the development of sustainable mitigation and adaption strategies to climate change and other future challenges.

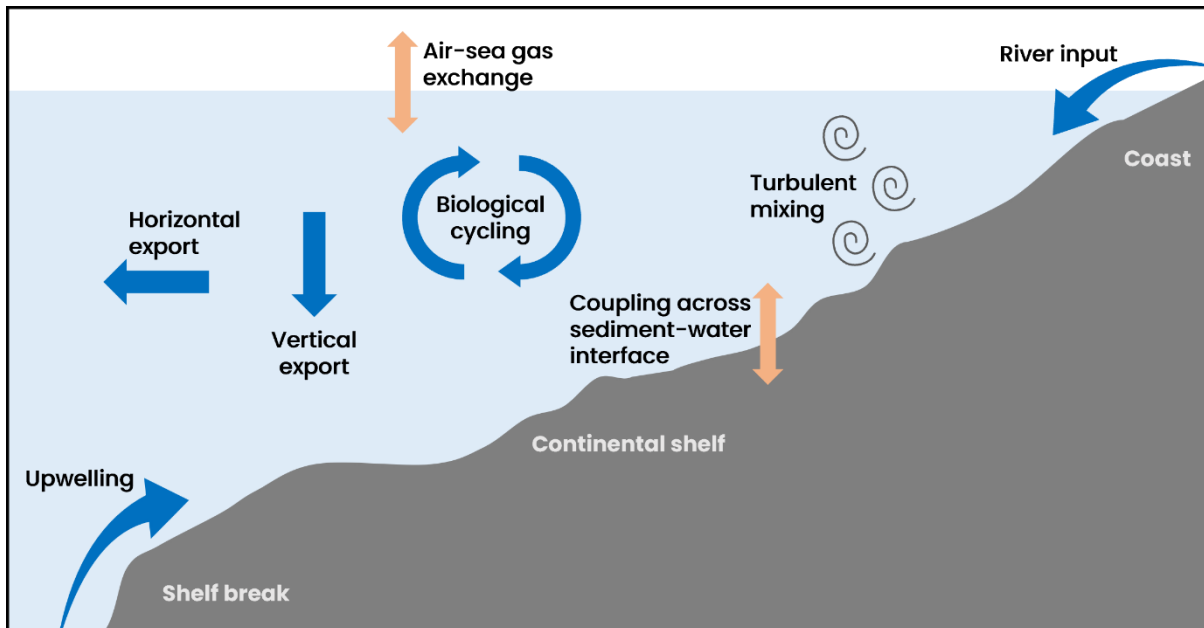


Figure 1: Schematic of key processes relevant for carbon cycling on continental shelves. Adapted from Mathis et al. (2022).

1.1. The Northwest European Shelf (NWES)

This study focuses on the dynamics of the Northwest European shelf (NWES), as being one of the largest temperate shelf seas in the global coastal ocean. The NWES is located on the northeastern margin of the North Atlantic to the northwest of Europe and extends from the Bay of Biscay in the south to the coast of Norway in the north (see Fig. 2). The NWES comprises several distinct shelf seas, for example the broad North Sea and Celtic Sea, and narrower shelf regions along the shelf break like the West-Irish Shelf or the Malin and Hebrides Shelves. The semi-enclosed Baltic Sea in the east is connected to the North Sea via the shallow Danish straits in the Kattegat region. The NWES is exposed to strong seasonality in the atmospheric conditions, where thermal forcing, winds and tides structure the shelf into permanently mixed and deeper seasonally stratified regions separated by dynamic tidal frontal zones (Simpson and Hunter, 1974). Large freshwater input from river discharge further impacts stratification and circulation in coastal areas of the NWES.

Regional hydrodynamic conditions and biogeochemistry on the NWES are influenced by the adjacent Northeast Atlantic, which in turn is predominantly influenced by the warm North Atlantic current (Mann, 1967; Häkkinen et al., 2011). The European Slope current, an eastern boundary current driven by density gradients and wind (Huthnance, 1984) transports warm and salty subtropical water poleward along the shelf break of the NWES. The slope current is weaker or can even exhibit seasonal equatorward flow along the southern shelf break section along the Celtic Sea and Armorican Shelf (Pingree et al., 1999). The mean circulation in the North Sea (see Fig. 2) is cyclonic, with southward flow along the eastern UK coast, east to northeastward flow along the continental European coast and northward flow along the Norwegian coast (Otto et al., 1990). Atlantic water enters the North Sea through the Fair-Isle Channel, the Shetland shelf and along the western slope of the Norwegian Trench. North

Atlantic water advected through the English Channel further enters the southern North Sea through the Calais-Dover strait. The inflow of

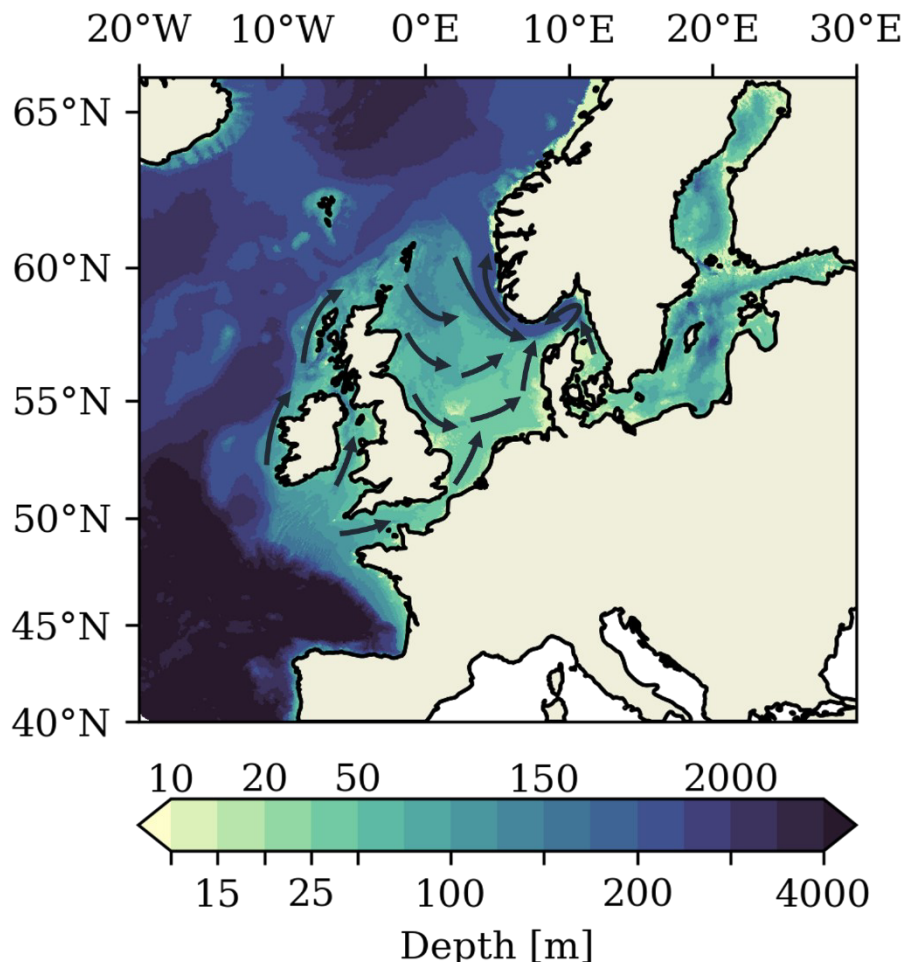


Figure 2: Bathymetry in model domain of the NWES and Baltic Sea applied in this work. Arrows schematically show the general circulation on the NWES (adapted from Ricker and Stanev, 2020).

Atlantic water along the western edge of the Norwegian Trench, additionally fed by the Dooley current system in the North Sea, retroflects in the Skagerrak and joins the low-salinity Baltic waters and the flow from the southern North Sea which leave the NWES in the northward flowing Norwegian Coastal Current. Mean residual circulation in the Celtic Sea is generally weaker and shows a relevant baroclinic contribution (Brown et al., 2003). Water from the Celtic Sea is also transported northward through the Irish Sea and joins a general northward flow on the Malin and Hebrides Shelves, which then merges with the inflow of Atlantic water into the North Sea (Brown and Gmitrowicz, 1995; Marsh et al., 2017).

Dynamic processes on the NWES are spatially and temporally highly variable and largely determined by the shallow shelf bathymetry. Circulation on the NWES is dominantly driven by wind and tides, but density-driven circulation is also relevant (Hill et al., 2008; Sündermann and Pohlmann, 2011). Turbulence and mixing are especially important on the shallow shelf, with a significant contribution by tides. The shallow water depths on continental shelves means that the horizontal length scales of dominant physical processes are smaller than in the deep ocean (the 1st internal Rossby Radius on the NWES for example is $\sim 4\text{km}$; Holt and Proctor,

2008). The dynamics of the shelf system therefore strongly depend on small-scale processes, such as internal tides, frontal jets and tidally rectified transport (Holt et al., 2017). The topographic length scale of local topography can also be relevant on continental shelves, as variations in topography can be large compared to the water depths and for example induce topographic steering of currents (e.g. Svendsen et al., 1991).

The steep continental slope that connects the NWES and the open ocean, constitutes a distinct dynamic regime in which the topographically steered eastern boundary current on the continental slope effectively limits exchange between the open ocean and the shelf (Huthnance et al., 2022). The NWES features a downwelling circulation, with net on-shelf flow at the surface and off-shelf flow at depth, that is driven by regional wind fields and Ekman drain generated by the slope current (Holt et al., 2009; Huthnance et al., 2022). Multiple processes, e.g. internal waves, eddies, tidal and wind-driven transports, directly contribute to cross-shelf exchange and typically have small spatial scales and high frequency (Huthnance et al., 2022). The complex dynamics in the shelf break regime control the exchange of carbon, nutrients and water between the shelf and open ocean and are therefore highly relevant for the role of the shelf in the marine carbon cycle.

1.2. Tides on the NWES

The NWES is one of the most tidally energetic regions in the world and dissipates about 200 GW of tidal energy, which amounts to 5-6% of contemporary global tidal dissipation (Egbert and Ray, 2001). Tidal energy, in form of Atlantic Kelvin waves, enters the NWES across the Celtic Sea shelf break in the south and progresses to the north and east (Coughlan and Stips; Pugh, 1996). A part of the tidal energy propagates into the Irish Sea and the Bristol Channel, or into the English Channel and further into the southern North Sea. The northward propagating Atlantic tidal waves are partly diffracted around the north of Scotland and turn into the North Sea, where the Kelvin waves cyclonically propagate along the UK and continental coasts. The resulting tides on the NWES are dominated by semi-diurnal tidal constituents and are particularly energetic in the Celtic Sea, the English Channel and the Irish Sea.

The regular tidal forcing constitutes a dominant physical forcing mechanism on the NWES. Resuspension of sediments by strong tidal currents significantly affects the coupling between the water column and the sediment. Tidal mixing, generated by the dissipation of tidal energy by frictional stresses acting at the seabed, vertically mixes the water column and partitions the NWES into permanently mixed regions, tidal frontal zones and seasonally stratified regions (Bowers and Simpson, 1987). In addition to bottom-driven tidal mixing, tides can also generate vertical mixing within the stratified water column on the shelf. Such tide-related internal mixing can be caused by breaking internal tides (Rippeth, 2005), the interaction of wind-induced inertial oscillations with internal tides (van Haren et al., 1999; Hopkins et al., 2014), or the barotropic tide itself (Becherer et al., 2022). Internal tides are generated by a conversion of energy from the barotropic tide to the baroclinic tide through interaction of stratified flow with extreme topography like the shelf break (Baines, 1982). The NWES is a hotspot of internal tide generation, and particularly high tidal energy conversion has been reported for the steep Celtic Sea shelf break (Baines, 1982; Vlasenko et al., 2014). Tides also induce residual mean flow at small-scale bathymetric features (Polton, 2015) and contribute to the large-scale residual

circulation on the NWES, for example by generating baroclinic residual currents (Hill et al., 2008) or by directly affecting the barotropic residual circulation on the NWES (Tinker et al., 2022).

1.3. The marine carbon cycle on the NWES

The recent extensive carbon budget for the NWES (not including the Baltic Sea) presented in Legge et al. (2020) finds the NWES to be a net CO₂ sink that is estimated to take up between 1.3 – 3.3 $Tmol\ C\ yr^{-1}$ of CO₂ from the atmosphere. Rivers additionally discharge 2.3 – 5 $Tmol\ C\ yr^{-1}$ of terrestrial carbon into the NWES. Carbon inputs to the NWES are mainly balanced by net off-shelf transport into the North Atlantic of 3.5 – 8.2 $Tmol\ C\ yr^{-1}$. Burial of carbon in the sediments on the NWES exhibits especially large uncertainty and estimates are poorly constrained ($-2.2 - 6\ Tmol\ C\ yr^{-1}$).

High biological productivity on the NWES is crucial for oceanic uptake of atmospheric CO₂ on the NWES (Wakelin et al., 2012). Primary production and associated carbon drawdown are especially high during the short spring phytoplankton bloom, after which primary production in the surface mixed layer of the seasonally stratified shelf areas of the NWES is largely nutrient limited (Simpson and Sharples, 2012). During the period of summer stratification, diapycnal nutrient fluxes, for example induced by tides, sustain relevant subsurface production at the base of the surface mixed layer (Richardson, 2000; Sharples et al., 2001). Observational estimates suggest subsurface production on the NWES during summer may amount to half of the biological carbon fixation during the spring bloom (Hickman et al., 2012) or even be equivalent to the spring bloom (Richardson, 2000; Fernand et al., 2013). Diapycnal mixing at the base of the surface mixed layer is thus an important control for shelf-sea biological processes and carbon cycling on the NWES. Nutrient depletion in the surface layer through convective mixing in autumn additionally triggers an autumn bloom, which has recently been suggested to also relevantly contribute to the seasonal drawdown of carbon on the NWES (Wihsgott et al., 2019). Permanently mixed inner-shelf regions commonly show high biological productivity throughout the productive period, as primary production in the well-mixed near-coast regime is rather limited by light and not by nutrients (Cadée and Hegeman, 2002).

The continental shelf pump operating on the NWES depends on the vigorous biological carbon pump and the downwelling circulation on the shelf (Thomas et al., 2004; Holt et al., 2009; Wakelin et al., 2012). The efficient export of carbon-enriched subsurface waters to the North Atlantic via the continental shelf pump facilitates disproportionately high oceanic CO₂ uptake on the NWES (Thomas et al., 2004; Kitidis et al., 2019). The observation-based carbon budget of the North Sea presented by Thomas et al. (2005) found off-shelf export to be the dominant export flux for the North Sea and estimated that 90% of the CO₂ taken up from the atmosphere is exported to the North Atlantic. Holt et al. (2009) further demonstrated in an idealized modelling study that the downwelling circulation of the NWES is capable of removing ~40% of carbon sequestered by one growing season before the onset of the next, of which about half is exported into the subsurface layer of the North Atlantic and thus isolated from the atmosphere on time scales of hundreds of years.

Sediment carbon is estimated to be the largest carbon reservoir on the NWES (Legge et al., 2020). Deposition of particulate organic carbon, and to a far lesser extent particulate inorganic

carbon, in the sediment removes carbon from the water column on the NWES. The sedimented carbon can be remineralized and subsequently diffusively released back into the water column or buried long-term in the sediment. Current scientific literature only finds a small contribution of sediment burial to the overall carbon fluxes on the NWES (Thomas et al., 2005; Wakelin et al., 2012; Kitidis et al., 2019). Estimates of sediment carbon stocks and fluxes are however constrained by a severe lack of observational data and exhibit especially large uncertainty (Legge et al., 2020).

The carbonate system on the NWES shows high spatial and temporal heterogeneity (Hartman et al., 2019) that is caused by the dynamic interactions between biological and chemical processes and shelf physics. River inputs and complex ecosystem dynamics in estuaries and other coastal ecosystems (e.g. tidal flats like the Wadden Sea in the North Sea) affect biological productivity and carbon fluxes in the near-coast regime (e.g. Middelburg and Herman, 2007; Thomas et al., 2009; Gypens et al., 2011). Tidal mixing and tidal frontal systems locally affect primary production by resupplying nutrients to the otherwise nutrient depleted surface layer (Sharples et al., 2001; Sharples, 2007; Zhao et al., 2019) or by modulating the light regime (Porter et al., 2010; Zhao et al., 2019). Tidal forcing and bathymetry further partition the NWES into distinct physical regimes that exhibit distinct biogeochemical dynamics relevant for carbon cycling (Thomas et al., 2004; van Leeuwen et al., 2015). The vertical separation of the water column in seasonally stratified shelf regions allows strong drawdown of CO₂ from the atmosphere via the biological pump mechanism. In the permanently mixed water column, constant mixing by wind and tides keeps the water masses in contact with the atmosphere, so that the carbonate system in the entire water column can constantly equilibrate with the atmosphere. The continental shelf pump consequently only operates in seasonally stratified regions of the NWES, which accordingly generally act as a net sink for atmospheric CO₂, while permanently mixed regions rather exhibit weak oceanic CO₂ uptake or act as a net source of CO₂ to the atmosphere.

1.4. Research gap

The dynamic and highly heterogeneous shelf regime presents significant challenges for the quantification of oceanic CO₂ uptake and the identification of processes relevant for the carbon cycle on continental shelves like the NWES. Limited spatial and temporal observational coverage particularly impedes a detailed assessment of spatio-temporal variability and trends in air-sea CO₂ exchange on continental shelves, and the relative contributions of shelf-specific processes mediating carbon fluxes between the various reservoirs of the coastal ocean remain elusive. The contribution of shelf and coastal seas accordingly remains one of the major sources of uncertainty in current estimates of the global oceanic carbon budget (Laruelle et al., 2014; Hauck et al., 2020; Dai et al., 2022; Resplandy et al., 2024).

In this context, coupled ocean-biogeochemical models are an invaluable tool to expand our understanding of the shelf carbon cycle, quantify carbon fluxes and assess potential future changes in the shelf system. Current state-of-the-art global ocean-biogeochemical models however substantially overestimate oceanic CO₂ uptake in the global coastal ocean (by ~60%) compared to observation-based approaches (Resplandy et al., 2024). The difference in CO₂ uptake between model- and observation-based approaches can in part be attributed to the

presence of systematic biases in the global models due to their inability to resolve small-scale coastal dynamics and shelf-specific biogeochemical processes. The horizontal grid resolution in the global ocean-biogeochemical models investigated in (Resplandy et al., 2024) for example was about $1/4^\circ$ or coarser, and thus too coarse to resolve coastal ocean dynamics ($1/16^\circ$ or higher; Hallberg, 2013; Holt et al., 2017). So far only regional modeling approaches allow for the high resolution necessary to resolve the horizontal length scales of dominant physical processes on the shelf, although recent advances in global ocean modeling made significant progress in this regard (Mathis et al., 2022). Even regional models however often only represent shelf-specific processes in an over-simplified manner.

In their review of prospects for the improvement of coastal and shelf seas in ocean models, Holt et al. (2017) suggest that kilometrical-scale horizontal model resolution ($\sim 1.5\text{km}$) is necessary to fully resolve dominant physical processes on the shelf. Realizing kilometrical-scale horizontal model resolution in large-scale regional model frameworks that include dynamic exchange with the open ocean is challenging in terms of computational resources and model stability and has only recently been implemented in a new generation of physical ocean models for the NWES. Kilometrical-scale model resolution however remains at the threshold of current feasibility for coupled physical-biogeochemical regional models of the NWES (Tonani et al., 2019), especially considering the multitude of shelf-specific biogeochemical processes constitutive for the high spatio-temporal variability on the shelf. The benefit of kilometrical-scale horizontal resolution in modelling the carbon cycle on the NWES has consequently not been assessed to date. A careful evaluation of the benefit of high resolution in models applied to simulate the shelf carbon cycle is important, as modelling the shelf carbon cycle does not only face methodological uncertainty stemming from the inadequate resolution of shelf physics but also from knowledge gaps regarding shelf-specific biogeochemical processes. The benefit of applying computationally costly high resolution in a modelling framework for the shelf carbon cycle accordingly needs to be weighed against the benefit of the, also computationally costly, increase in biogeochemical model complexity.

The implementation of kilometrical-scale horizontal resolution in an operational forecasting model system for the NWES has for example lead to a moderate improvement in the simulation of temperature and salinity on the shelf, along with an improved reproduction of the pattern and variability of surface currents (Tonani et al., 2019). Graham et al. (2018b) demonstrated that kilometrical-scale horizontal model resolution significantly affects cross-shelf fluxes on the NWES, with potential implications for the continental shelf pump mechanism. Guihou et al. (2018) further demonstrated that only kilometrical-scale horizontal model resolution realistically reproduces the internal tide field on the NWES. Internal tides are a key shelf-specific process suggested to be an important source for pycnocline mixing in seasonally stratified shelf areas (Rippeth, 2005), which supplies nutrients for subsurface primary production and is crucial for the exchange of carbon between the bottom mixed layer and the surface layer in contact with the atmosphere (Rippeth et al., 2014). Significant internal-tide-driven diapycnal nutrient fluxes have been observed along the shelf break of the NWES (Sharples et al., 2007) and at small-scale bathymetric features on the shelf (Tweddle et al., 2013). The high spatial variability and episodic nature of mixing by internal tides however impede a comprehensive observation-based analysis of the role of internal tides for biological carbon fixation and associated oceanic CO_2 uptake on the shelf. A model-based investigation of internal tides is in turn impeded by the high computational demand resulting from the

kilometrical-scale horizontal resolution necessary to resolve the internal tide field on the NWES.

The recently realized representation of the internal tide field in kilometrical-scale physical models of the NWES has been suggested to improve sea surface temperature along the shelf break of the NWES by enhancing vertical mixing (Graham et al., 2018a). The impact of the kilometrical-scale internal tide field on simulated vertical mixing of nutrients and associated biological productivity or oceanic CO₂ uptake on the NWES has so far not been assessed, primarily because of the substantially higher computational demand of coupled physical-biogeochemical models. Improving simulated vertical mixing in the seasonally stratified shelf regime by resolving the internal tide field in ocean models holds potential to affect air-sea CO₂ exchange on the NWES, for example by alleviating the common underestimation of subsurface production in coupled ocean-biogeochemical models attributed to challenges in reproducing adequate levels of internal mixing (van Leeuwen et al., 2013).

The evaluation of key physical and biogeochemical processes controlling the shelf carbon cycle and air-sea CO₂ exchange on the shelf is important for the assessment of how future changes in the shelf system affect the NWES CO₂ sink and is thus at the core of model development. In a model, the representation of the diverse and complex physical and biogeochemical processes that characterize the shelf environment necessarily requires a measure of simplification and prioritization. This is particularly the case in view of constraints on computational resources necessary for high resolution or global modeling approaches. Given this context, this study aims to expand current knowledge on shelf-specific physical and biogeochemical processes and their relevance for carbon cycling on the NWES by focusing on tidal processes. Tides affect a wide range of physical and biogeochemical processes on continental shelves that are relevant for the marine carbon cycle (see previous sections 1.2 and 1.3) but are commonly not explicitly included in global ocean models. The role of the multifaceted tidal processes in the NWES carbon cycle and air-sea CO₂ exchange has so far not been assessed.

A detailed understanding of tide-related shelf-specific processes would provide valuable insights on the role of key shelf-specific processes in the ocean carbon cycle and help inform on the systematic bias introduced by unresolved tides in model-based assessments of the shelf CO₂ sink. This dissertation therefore addresses the following overarching research question:

How do tides, as one of the dominant physical forcing mechanisms on continental shelves, affect air-sea CO₂ exchange on the NWES?

The following sub-questions are addressed to answer the overarching research question:

- **How do tides impact biological carbon fixation on the NWES?**
- **What is the influence of internal tides on the carbon cycle on the NWES?**
- **Which tidal processes are most relevant for air-sea CO₂ exchange on the NWES?**

1.5. Approach and Outline

The study aims to expand current knowledge on the role of shelf-specific processes by addressing the role of tidal forcing for carbon cycling in a temperate continental shelf system. The research is focused on the Northwest European Shelf, for which a novel coupled physical-

biogeochemical regional model framework was developed and implemented in the course of this work. The model framework, referred to as SCHISM-ECOSMO-CO₂, integrates the three-dimensional cross-scale physical model SCHISM (Zhang et al., 2016), the lower-trophic-level ecosystem model ECOSMO II (Daewel and Schrum, 2013) and a carbonate system model introduced by Blackford and Gilbert (2007). The model domain spans the entire NWES as well as the Baltic Sea and a part of the eastern North Atlantic to permit a realistic investigation of regional-scale impacts. The model domain is illustrated in Fig. 2. The technical coupling and overhead necessary for the integration of the three different models was substantially extended, tested, validated and optimized for modeling the marine carbon cycle.

The physical model component SCHISM is based on an unstructured triangular horizontal model grid. Such new generation physical ocean models offer the possibility for flexible localized grid refinement in areas of interest and therefore hold potential to circumvent the problem of high computational demand faced with standard structured grid approaches when realizing high resolution. The implementation of ocean models based on unstructured grids however brings its own set of methodological challenges, particularly in model domains that include the deep open ocean (Zhang et al., 2016).

Given current numerical constraints, model-based research on the role of shelf-specific processes in the marine carbon cycle needs to balance the high model resolution necessary for a realistic representation of shelf physics with the representation of the diverse ecosystems and complex biogeochemical processes that affect carbon cycling in the shelf environment. The application of an unstructured grid model in research on the NWES carbon cycle consequently calls for an evaluation of the performance of the physical model across different model adaptations tailored to meet the differing research requirements resulting from prioritizing the improved representation of either physical or biogeochemical shelf-specific processes. This dissertation consequently addresses a preceding methodological research question:

Can the cross-scale capability of unstructured-grid ocean models be leveraged to establish an adaptable physical-biogeochemical modelling framework for the NWES that enables kilometrical-scale horizontal resolution?

Three research articles associated with the dissertation are presented as appendices to this dissertation. The dissertation and the associated articles follow the course of model development and document the comprehensive validation and application of the model configuration. The first study presents two horizontal grid configurations for the physical model component SCHISM: a coarse resolution configuration optimized for the application with more complex biogeochemical models and a cross-scale high-resolution configuration realizing kilometrical-scale horizontal resolution to resolve the internal tide field in the Celtic Sea and shelf regions adjacent to the shelf break of the NWES. The first study investigates the model performance of the two model adaptations and addresses the preceding methodological research question on the applied unstructured modelling approach. In the second study, the results of the physical model SCHISM and the lower-trophic-level model ECOSMO II are validated against observations. We apply the model framework to assess the impact of tidal forcing on primary production on the NWES and investigate the impact of the resolved kilometrical-scale internal tide field. The third study introduces and validates the carbonate system model component and investigates tidal impacts on air-sea CO₂ exchange on the NWES, with the goal of determining dominant tidal processes affecting the shelf carbon cycle.

The following chapters of the dissertation highlight and discuss the main results of the research articles in relation to the outlined research questions. The final chapter provides an outlook on future research needs and specifically addresses avenues for active model development for the modelling approach used in this dissertation.

2. On unstructured grid modelling of the NWES

The implementation of a new coupled physical-biogeochemical model framework based on the unstructured grid model SCHISM establishes a flexible and adaptable platform for research on the NWES carbon cycle. Two horizontal grid configurations have been developed to meet computational efficiency requirements or resolve small-scale physical processes such as internal tides. The coarse-resolution NWES-LR configuration and the high-resolution NWES-IT configuration are presented and validated in *Study I*. Differences in the physical model results derived with the two configurations are further assessed to demonstrate the consistency of the adaptable modelling framework and guide future applications.

The coarse-resolution NWES-LR configuration is optimized for a computationally efficient and fast simulation of the NWES and Baltic Sea areas and thus facilitates application with more complex biogeochemical model components. In the NWES-IT configuration, SCHISM's cross-scale capabilities are utilized to realize kilometrical-scale horizontal resolution in the Celtic Sea and in shelf regions adjacent to the shelf break of the NWES, where small-scale processes such as internal tides are understood to be particularly relevant. Both grid configurations extend into the deep Northeast Atlantic to resolve cross-shelf exchange necessary for a realistic simulation of the shelf system (see Fig. 2). Both grid configurations further include the Baltic Sea, here again utilizing SCHISM's cross-scale capabilities to realistically resolve inter-basin exchange across the narrow Danish straits connecting the North Sea and the Baltic Sea.

Study I confirms the presence of internal tides on the NWES in the high resolution NWES-IT configuration. Internal tides excited by the regionally dominant M2 tide have wavelengths in the range of 12-25km on the NWES and are thus not resolved by the coarse NWES-LR configuration with a horizontal grid resolution of ~10km in the respective shelf areas. The simulated internal tide activity in the NWES-IT configuration is validated against available observations in *Study II*. The NWES-IT configuration is found to reproduce an internal tide field comparable to a kilometrical-scale structured grid model presented in Guihou et al. (2018). The applied strategy of local grid refinement in the NWES-IT configuration shows high efficiency in computational cost and storage requirements, as the number of grid nodes is reduced by a factor of ~6 compared with a uniform high resolution configuration (see *Study II*).

The validation of both model configurations in *Study I* demonstrates adequate and largely consistent model performance regarding the general hydrography on the NWES. Comprehensive analysis and comparison revealed that model biases in both configurations could further be reduced by improving the vertical discretization, the general model performance in the Baltic Sea and the representation of inter-basin exchange between the North Sea and Baltic Sea. Differences between the model configurations are found to primarily relate to differences in horizontal grid resolution and thus the simulation of shelf physics. In the Norwegian Trench, validation of sea surface salinity indicates a better representation of locally

relevant mesoscale processes and associated lateral mixing (Ikeda et al., 1989) in the high resolution NWES-IT configuration. The simulation of sea surface temperature on the numerically challenging steep continental slope shows high sensitivity to the applied local grid resolution, with lower model performance in the coarse resolution NWES-LR configuration.

The comparison of the two model configurations however also highlights deficiencies in the NWES-LR configuration that should be addressed in future applications. The model performance regarding sea surface salinity in the Baltic Sea is notably lower in the NWES-LR configuration compared to the NWES-IT configuration, potentially due to limitations in the representation of locally relevant mesoscale activity and its impact on vertical mixing (Reissmann et al., 2009). A particularly concerning difference in the model results further occurs in the Norwegian Trench, where the NWES-LR configuration reproduces low inflow from the North Atlantic and thus substantially underestimates volume transports compared to observations and the NWES-IT configuration. An investigation of the causes for the difference in volume transports in the Norwegian Trench was however beyond the scope of *Study I*. As the Norwegian Trench functions as the largest pathway for carbon export from the NWES (Thomas et al., 2005), the consequences of this limitation in model performance for simulations of the shelf carbon cycle should be addressed in future studies.

The overall large consistency between the results of the two model grid configurations presented in *Study I* underlines the high flexibility and configurability of the model framework. *Study I* lastly also shows, that, despite its comparatively coarse resolution, the NWES-LR configuration achieves adequate model performance for a wide range of research applications. The identified differences between the model configurations highlight the need for individual validation procedures for adaptations of the modelling framework as well as the difficulty in directly comparing model results across different grid configurations. The validation performed in *Studies I-III* contributed to establishing two baseline model configurations that lay the groundwork for research on the NWES carbon cycle along two connected avenues, namely the improved representations of physical and biogeochemical shelf-specific processes.

3. On the role of tide-induced biological carbon fixation for the NWES carbon cycle

Study II elucidates hydrodynamic control on shelf primary production and explores how tides, as one of the dominant shelf-specific processes on the NWES, contribute to elevated primary production observed on continental shelves. *Study II* applies the unstructured grid model SCHISM with the NWES-IT horizontal grid configuration that realizes kilometrical-scale horizontal resolution on the NWES. SCHISM is coupled to the state-of-the-art lower trophic level ecosystem model ECOSMO II (Daewel and Schrum, 2013) based on a nutrient–phytoplankton–zooplankton–detritus conceptual model approach well suited to resolve the competing major bottom-up tidal processes controlling primary production, i.e. the reduction of light availability by resuspension and mixing of organic matter and the supply of nutrients by tidal mixing (Zhao et al., 2019). The novel coupled physical–biogeochemical regional model framework SCHISM-ECOSMO is extensively validated in *Study II* and applied for the first

time to obtain a comprehensive quantification of tidal impacts on primary production on the entire NWES, explicitly including the impact of internal tides.

The major finding of *Study II* suggests that tidally enhanced vertical mixing of nutrients is responsible for about 1/6 of the total annual primary production on the NWES. However, the tidal impact on primary production is largely restricted to shallow inner-shelf regions characterized by tidal frontal systems and a weak separation of the bottom and surface mixed layers (see Fig. 3). The deep outer-shelf area in the southwestern Celtic Sea was found to be an

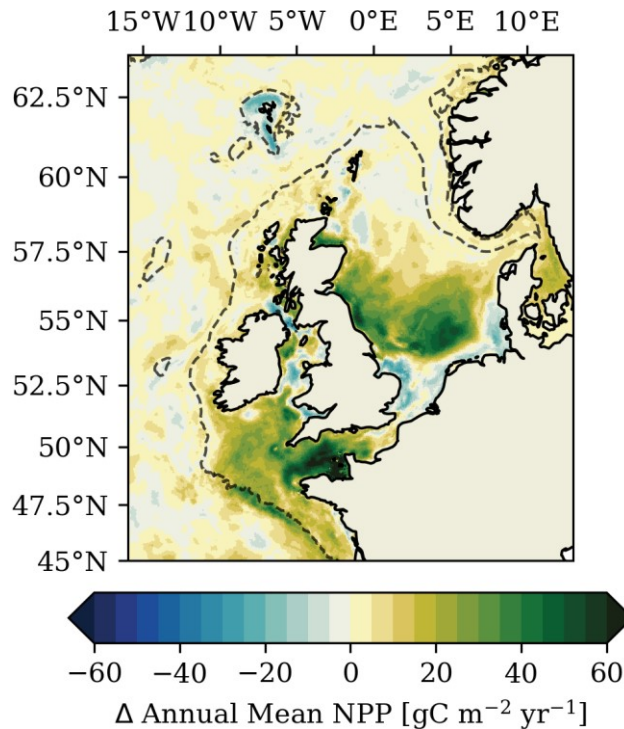


Figure 3: Tidal impact on annual primary production illustrated by calculating the difference of a simulation with tides and a sensitivity experiment without tides. The figure is taken from Kossack et al. (2023) documented in Appendix B.

exception in this regard, as it also showed a substantial tide-induced increase in primary production. The dynamic tidal frontal systems in the southern North Sea, northeastern Celtic Sea and western English Channel were found to particularly invigorate local primary production. In permanently mixed regions of the NWES, tidal resuspension of particulate organic matter (POM) and mixing degrades light conditions and thus locally constrains phytoplankton growth. Previous studies further show that tides affect the dominance and succession patterns of phytoplankton species (van Leeuwen et al., 2015) and spring bloom phenology (Zhao et al., 2019) on the NWES.

Study III complements the investigation of tidal impacts on primary production by directly evaluating tidal impacts on air-sea CO₂ exchange and exploring underlying physical and biogeochemical processes. A key result of *Study III* is that the tidally enhanced primary production on the NWES does not translate into enhanced oceanic CO₂ uptake. *Study III* comprehensively assesses tide-induced biological impacts on the shelf carbon cycle by evaluating net community production, i.e. the balance of biological carbon fixation and heterotrophic remineralization back into dissolved inorganic carbon, which ultimately determines the biological impact on the carbonate system. The investigation of tidal impacts on

net community production reveals an increase in net heterotrophy (i.e. the net remineralization of biologically fixed carbon) with tidal forcing, which actually reduces the shelf's uptake capacity for atmospheric CO₂.

Tide-induced resuspension of organic matter from the sediment back into the water column is shown to be highly relevant for the tidal impact on net community production. Tidal resuspension, however, mainly affects the balance of heterotrophic remineralization occurring in the water column or the sediments and thus primarily modulates the lateral distribution and timing of heterotrophic remineralization on the shelf rather than its magnitude. *Study III* shows that the tidal impacts on net community production do not relevantly influence annual oceanic CO₂ uptake on the NWES. This result indicates that physical tidal processes are the prevailing factors for tidal impacts on air-sea CO₂ flux on the NWES. These processes are further addressed in Chapter 5.

The restriction of tidal impacts on primary production to inner-shelf regions demonstrated in *Study II* strongly limits the potential of tidal impacts on the biological pump and thus the continental shelf pump mechanism. Comparison to the stratification regimes derived for the North Sea by van Leeuwen et al. (2015) suggests that a relevant part of tidally enhanced primary production, however, still occurs in transitional (high interannual variability in number of stratified days), intermittently stratified (<40 days stratified) and also seasonally stratified (>120 days stratified) parts of the North Sea. The results of *Study II* and *Study III* therefore indicate that the effective decoupling of the magnitude of local primary production and oceanic CO₂ uptake, and thus also the well described spatial distinction between the strong oceanic CO₂ sink in the seasonally stratified northern North Sea and the weak CO₂ source/ near-neutrality in air-sea CO₂ exchange in the southern North Sea (Thomas et al., 2004; Prowe et al., 2009), is maintained not only by the divide between stratified and mixed regimes but also by the overall hydrodynamic conditions in the inner shelf.

The general circulation in inner-shelf regions of the NWES results in long residence times, which will significantly contribute to the insensitivity of oceanic CO₂ uptake to tide-induced primary production. A water parcel entering the North Sea via the Fair-Isle Passage and passing through the southern North Sea is for example estimated to have a residence time of 3-4 years on the shelf, with a residence time of 1-2 years in the southern North Sea alone (Mathis et al., 2013). For the Irish Sea, a tracer released in summer is estimated to have an average residence time in the Irish Sea of 386 days (Dabrowski et al., 2012). Due to the generally weak circulation, the transit time of a water parcel from the Celtic Sea shelf break to the central Irish Sea is even estimated to be 6 years (Hydes et al., 2004). Given these long residence times, carbon that is biologically fixed and transported to the subsurface layer in inner-shelf regions of the NWES would likely at least once face re-exposure to the atmosphere by winter mixing before potential export from the NWES. The enhanced biological productivity in tidal frontal areas or elevated subsurface primary production maintained by pycnocline mixing induced by the barotropic tide in shallow stratified inner-shelf settings, as for example theoretically demonstrated by Becherer et al. (2022) for the German Bight, can thus only marginally contribute to net oceanic CO₂ uptake on the shelf.

A potential constraint in the applied ecosystem modelling approach is the neglect of macrobenthos and associated bioturbation, which dynamically affect the interaction between the water column and the sediments and particularly sediment retention in the tidal system (Zhang et al., 2019). The lack of semi-labile and recalcitrant fractions of dissolved organic

carbon (DOM) with turnover times in the order of the residence times on the shelf also potentially affects tidal impacts on air-sea CO₂ exchange mediated by biological carbon fixation. Production of long-lived DOM in the course of tide-induced primary production would isolate carbon from exchange with the atmosphere and thus potentially affect the impact of tide-induced primary production on shelf CO₂ uptake. The inclusion of long-lived DOM is however not expected to significantly change the sensitivity of shelf CO₂ uptake to tidal forcing established in this work, as net DOM fluxes on the NWES derived from observations are small compared to DIC fluxes (Thomas et al., 2005).

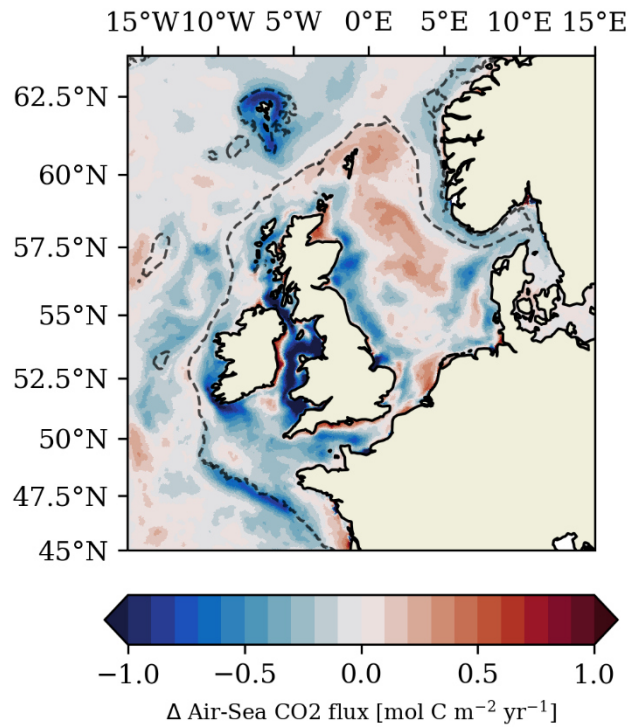


Figure 4: Tidal impact on air-sea CO₂ exchange illustrated by calculating the difference of a simulation with tides and a sensitivity experiment without tides. The figure is taken from Kossack et al. (2023) documented in Appendix B.

4. On the role of internal tides for the NWES carbon cycle

The kilometrical-scale horizontal resolution realized in the high resolution NWES-IT model configuration for the first time enabled a regional-scale assessment of the impact of internal tides on the NWES carbon cycle. *Study I* and *II* confirm the presence of internal-tide related vertical pycnocline displacements far onto the shelf, consistent with the results of the kilometrical-scale modelling study by Guihou et al. (2018). *Study II* finds internal tides to primarily contribute to biological carbon fixation in the southwestern Celtic Sea region along the Celtic Sea shelf break, which is known to be hotspot of global internal tide generation due to its extreme and complex topography (Baines, 1982).

Study II however suggests that significant diapycnal mixing attributable to internal tides only occurs within tens of kilometres from their generation sites, in line with observation-based estimates of Inall et al. (2011) and Green et al. (2008), and therefore does not relevantly increase

diapycnal mixing in stratified inner-shelf regions. The spatial limitation of diapycnal mixing constrains the overall impact of the kilometrical-scale internal tide field on the shelf carbon cycle. Internal-tide-driven vertical mixing of nutrients is consequently found to only explain one-fifth of the substantial tidal response in primary production found in the southwestern Celtic Sea (see Fig. 3). *Study III* further finds concurrent diapycnal mixing of DIC to further reduce the impact of internal-tide-driven biological carbon fixation on air-sea CO₂ exchange. Such mutual compensation was previously proposed by Rippeth et al. (2014) based on analytical model estimates at individual sites on the NWES. *Study III* for the first time assessed the compound impact of internal-tide-driven mixing in a 3D regional-scale model, and ultimately finds only a marginal contribution of the kilometrical-scale internal tide field for simulated air-sea CO₂ exchange on the NWES (<1% of annual oceanic CO₂ uptake in the southwestern Celtic Sea).

The tidal response of primary production along the northern sections of the NWES shelf break (i.e. along the Malin, Hebrides and northern North Sea shelves) is found to be negligible, which further constrains the impact of internal tides on biological carbon fixation on the NWES. The results of *Study II* therefore suggest that tide-induced mixing does not explain the strong shelf-slope gradient in chlorophyll-a (as a proxy for primary production) regularly documented in remote sensing products. The gradient in primary production may instead be attributed to seasonal iron limitation in the North Atlantic, which was observed to extend to the northern shelf break sections of the NWES (Birchill et al., 2019). In this case, elevated primary production on the NWES margins is suggested to be caused by the more effective (re-)supply of iron to the water column from continental shelf sediments. The iron cycle is however not resolved in the applied biogeochemical ECOSMO II model configuration.

Although not explicitly assessed, the results of *Study II* further imply that resolving internal tides with kilometrical-scale horizontal model resolution does not substantially increase subsurface primary production that critically depends on simulated diapycnal mixing in the seasonally stratified shelf regime. This suggests that kilometrical-scale resolution alone will not significantly improve the underestimation of subsurface primary production often found in coupled hydrodynamic-biogeochemical models applied on continental shelves (e.g. van Leeuwen et al., 2013).

Beyond the tide-related impacts investigated here, kilometrical-scale processes are estimated to relevantly contribute to cross-shelf exchange across the shelf break of the NWES (Huthnance et al., 2022). A kilometrical-scale modelling study by Graham et al. (2018b) demonstrated significant contributions of kilometrical-scale processes, suggested to likely be resolved internal tides and small-scale topography, to cross-shelf volume transport on the NWES. An evaluation of the impact of internal-tide-driven cross-shelf transport on the shelf carbon cycle was however beyond the scope of this dissertation but is clearly warranted given the importance of cross-shelf exchange for the continental shelf pump mechanism.

The applied modelling approach for the first time enabled an incorporation of internal tide effects in simulated shelf carbon dynamics. Nevertheless, several methodological challenges related to traditional ocean modelling still remain. Nonlinear steepening of the on-shelf propagating internal tide excites non-hydrostatic internal solitary waves that significantly mediate energy dissipation and associated mixing (Pingree and Mardell, 1985; Xie et al., 2015). In the Celtic Sea, internal solitary waves with amplitudes of up to 105m have been observed (Vlasenko et al., 2014). Hydrostatic ocean models like SCHISM, used because of their superior

computational efficiency compared to non-hydrostatic models, are not able to resolve the full non-hydrostatic internal wave field and therefore systematically underestimate associated vertical mixing. The results of this work thus have to be considered as a lower bound for the impact of internal tides on vertical mixing on the NWES.

Moreover, despite significant progress in the development of turbulence closure models suitable for the shelf environment, it needs to be emphasized that state-of-the-art turbulence closures are still incomplete with respect to physical process representation and that the sensitivity of model results to different closure schemes is as large as the sensitivity to horizontal resolution on the NWES (Luneva et al., 2019). The GLS k-kl turbulence (Umlauf and Burchard, 2003) closure applied in this study does not explicitly parameterize internal wave breaking, so vertical mixing introduced by resolved internal tide activity only results from the production of vertical shear. As resolving internal tides with kilometrical-scale horizontal model resolution increasingly becomes feasible for regional-scale ocean model configurations, a more comprehensive evaluation of the performance of turbulence closures regarding internal tides should be a priority. The representation of non-linear interactions of inertial oscillations and internal tides, as for example reported by Hopkins et al. (2014), would be another interesting aspect in kilometrical-scale modelling. A realistic representation of such complex process interaction would potentially improve the simulation of episodic mixing events suggested to be particularly important for diapycnal mixing on the NWES (Williams et al., 2013).

5. On tidal impacts on carbon cycling and air-sea CO₂ exchange on the NWES

Study III expands the investigation of tidal impacts on biological carbon fixation on the NWES and explores how multifaceted tidal processes modulate air-sea CO₂ exchange on the shelf. To this end, the physical-biogeochemical SCHISM-ECOSMO framework is coupled to a carbonate system model introduced by Blackford and Gilbert (2007). The carbonate system model simulates carbonate chemistry in seawater using dissolved inorganic carbon and total alkalinity as prognostic variables. The extended model framework is extensively validated against observations in *Study III* and applied to gain quantitative process understanding of the impact of tides on oceanic CO₂ uptake on the NWES by comparing a hindcast simulation over the period 2001-2005 and a sensitivity experiment without tidal forcing, both of which were performed with the high-resolution NWES-IT model configuration.

Study III shows that tidal forcing weakens the NWES CO₂ sink, which was an unexpected result given the marked tide-induced increase in primary production found in *Study II*. The spatial heterogeneity of tidal impacts on air-sea CO₂ exchange on the NWES is documented in Fig. 4. The simulations at kilometrical-scale horizontal resolution evaluated in *Study III* suggest physical tidal impacts are most relevant for oceanic CO₂ uptake on the NWES, with the effects of tidal mixing in inner-shelf regions and tidal impacts on shelf circulation dominating tidal impacts on air-sea CO₂ exchange on the NWES (see schematic illustration in Fig. 5). Neglecting tides results in a 13% stronger shelf CO₂ sink (0.15 Tmol C yr⁻¹). For reference, the tidal impact on NWES CO₂ uptake amounts to ~1% of annual greenhouse gas emissions (in CO₂ equivalents) of the transport sector in Germany alone (~12 Tmol C yr⁻¹; Umweltbundesamt,

2024). The annual CO₂ uptake on the entire NWES obtained in *Study III* (1.16 Tmol C yr⁻¹) amounts to ~10% of annual German transport sector emissions.

The largest tide-related impact on air-sea CO₂ exchange on the NWES is caused by tidal mixing in the inner-shelf (approx. 40% of the tidal response in annual oceanic CO₂ uptake). Observations have long established a key role of the mixing-stratification status for air-sea CO₂ exchange in the North Sea (Thomas et al., 2004; Omar et al., 2010) and this is further set into context for the entire tide-dominated NWES system by *Study III*. Shelf regions in which tides permanently mix the water column do not exhibit the seasonal biological drawdown of surface DIC in spring and summer that counteracts the effect of seasonal warming on the partial pressure of CO₂ (pCO₂) in the surface layer, and consequently on air-sea CO₂ exchange. Our results here show that the suppression of this biological effect on surface pCO₂ by tides dominates over the concurrent impact of tides on surface temperatures.

A surprising result in *Study III* was the large impact of tide-induced baroclinic circulation on water mass composition in the Celtic Sea and the associated impact on CO₂ uptake in the region, which accounts for approximately 34% of the tidal reduction of oceanic CO₂ uptake on the entire NWES. Scientific literature generally assumes weak residual flow in the Celtic Sea, particularly in the outer-shelf area (Simpson, 1998). The relevance of baroclinic transports associated with cold and dense bottom pools in the Celtic Sea has previously been emphasized (Brown et al., 2003; Hill et al., 2008), but research has primarily addressed the northward transport via the seasonal jet-like circulation associated with the tidal frontal systems in the English Channel, along the UK coast and in the St. George Channel. Pingree and Le Cann (1989) observed a southeastward flow on the outer Celtic shelf, but could not identify a forcing mechanism and suggested it was a counter-current to northward transport in the inner Celtic Sea. The model results presented in *Study III* indicate that the southeastward flow is tide-driven and significantly affects water mass composition and associated surface DIC concentrations in the Celtic Sea. It is also to be noted that the hypothesis put forward in *Study II*, according to which differences in nitrate concentrations on the outer Celtic Shelf underlying the local tidal increase in primary production were likely linked to tidal impacts on large-scale on-shelf transport of Atlantic water masses, is at odds with the results of *Study III*. Instead, the local tide-induced residual circulation is also proposed to relevantly contribute to the tidal impacts on annual primary production in the southwestern Celtic Sea demonstrated in *Study II*.

Observations of the dynamic Celtic Sea circulation remain sparse and establishing dominant circulation patterns in the Celtic Sea is particularly challenged by the small-scale structure and high temporal variability of relevant hydrodynamic features. In addition to tide-induced baroclinic circulation, the numerous small-scale canyons and ridges in the Celtic Sea can additionally generate relevant tidal residual flow that potentially affects large-scale circulation (Polton, 2015). The impact of tide-induced circulation on primary production and oceanic CO₂ uptake demonstrated in *Study II* and *Study III* clearly motivates further investigation and the careful representation of respective phenomena in ocean models.

Another interesting result in *Study III* was the marginal influence of tidal resuspension on annual oceanic CO₂ uptake on the shelf. Neglecting tides increases organic carbon deposition in the shelf system and increases long-term carbon burial in the shelf sediment by a factor of ~10. The annual net carbon flux to the shelf sediment resulting from the neglect of tides on the NWES still remains small compared to other fluxes in the shelf carbon cycle (e.g. <1% of annual shelf CO₂ uptake from the atmosphere). This is because remineralization in the

sediments returns the bulk of the deposited carbon back into the water column. *Study III* further indicates that tidal resuspension also facilitates efficient lateral export of organic carbon in some regions, for example in the central and northern North Sea, which locally enhances the net uptake of atmospheric CO₂ (see Fig. 4). The results of *Study III* thus suggest that while tidal forcing affects the spatial distribution of long-term carbon burial in the shelf sediments, it does not have a significant impact on the role of sedimentation for air-sea CO₂ exchange. However, this result strongly depends on the remineralization and burial rates used in the applied ecosystem model, which are subject to large uncertainty (Legge et al., 2020). The minor tidal impact on the net carbon flux to the sediment implies that the increase in the net remineralization of organic carbon on the NWES, which contributes the remaining ~26% of the tidal reduction of oceanic CO₂ uptake, mainly stems from higher organic carbon import onto the shelf.

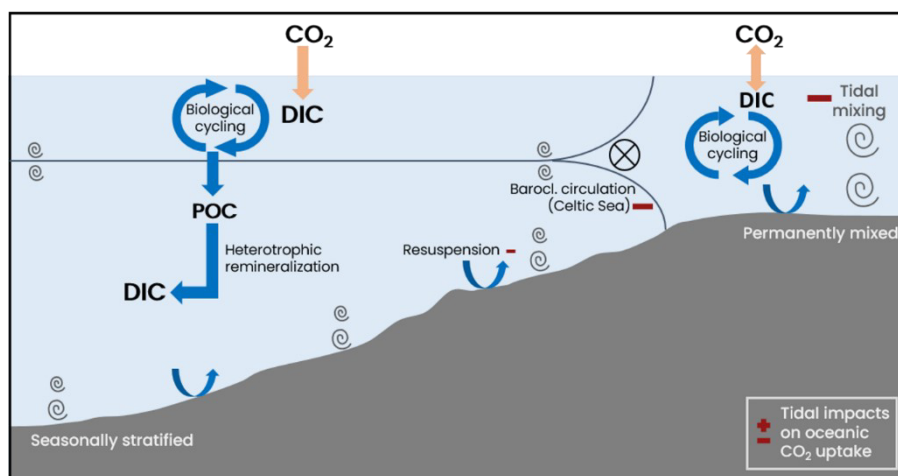


Figure 5: Schematic illustration of tidal impacts on air-sea CO₂ exchange on the NWES taken from Kossack et al. (submitted) documented in Appendix C.

A final evaluation of the shelf carbon budget demonstrates that the tidal impacts constrain the annual increase of the dissolved inorganic carbon stock in the water column due to the rising atmospheric CO₂ concentration. The assessed tidal impact on the increase rate of the dissolved inorganic carbon stock on the shelf also reveals that only about ~20% of the enhanced shelf CO₂ uptake obtained when neglecting tides on the NWES is ultimately exported off-shelf. Tides are thus concluded to predominantly affect carbon reservoirs on the shelf.

The validation performed in *Study III* generally establishes reasonable model performance in reproducing the spatial and temporal variability of the carbonate system on the NWES. Quantitative validation demonstrates that dissolved inorganic carbon is generally well represented in the model. Total alkalinity and particularly pCO₂ show lower quantitative model performance and imply limitations in the simulation of the full spatial heterogeneity and temporal variability of the shelf carbonate system. The main cause for an underestimation of simulated shelf CO₂ uptake compared to observations is assumed to be the underestimation of biological carbon fixation in the ecosystem model component ECOSMO II. However, as the tidal response is rather determined by the tidal impact on the balance between net primary production and heterotrophic remineralization, the good agreement between simulated net community production and observations gives confidence that the underestimated primary production is unlikely to significantly affect the results of *Study III*. Other key priorities for

further model development that show potential to improve simulations of the shelf carbon cycle are summarized in the Outlook Chapter 6.

6. Outlook

A novel coupled physical-biogeochemical model framework for the NWES based on unstructured grids is presented and applied in this dissertation to elucidate the role of tide-related shelf-specific physical and biogeochemical processes in the marine carbon cycle. The model framework enables a comprehensive investigation of tidal impacts on the marine carbon cycle at shelf-wide scale and, for the first time, allows the investigation of the impact of kilometrical-scale internal tides on primary production and air-sea CO₂ exchange. Tidal forcing is found to weaken oceanic CO₂ uptake on the NWES, with physical tidal processes dominating the tidal impact on shelf CO₂ uptake. Tidally enhanced biological carbon fixation, in contrast, is found to only marginally affect oceanic CO₂ uptake.

The process understanding gained in the course of this dissertation informs on the consequences of neglecting tides in modelling approaches currently applied in climate research. The direct extrapolation of the results from the NWES to other continental shelves is however difficult due to the large heterogeneity among shelf regions and the differences in the mechanisms driving air-sea CO₂ exchange. Future studies with global ocean models that explicitly resolve tides and other shelf-specific processes, such as the ICON-Coast model presented in Mathis et al. (2022), will therefore have to assess the global impact of tides on air-sea CO₂ exchange.

Apart from the NWES, several other mid-latitude shelves that relevantly contribute to oceanic CO₂ uptake exhibit tidal frontal systems and well-mixed inner-shelf regions (Belkin et al., 2009). The pattern of neutral air-sea CO₂ exchange or net outgassing in permanently mixed shelf regions and net oceanic CO₂ uptake on the stratified side of tidal mixing fronts has also been reported for the Patagonian shelf (Bianchi et al., 2005; Bianchi et al., 2009), another temperate continental shelf that significantly contributes to oceanic CO₂ uptake. The findings of this dissertation thus suggest that resolving tidal mixing in global modeling approaches could lead to a decrease in oceanic CO₂ uptake on global continental shelves. This may help to close the gap between model-based and observation-based estimates of the global shelf CO₂ sink emphasized in Resplandy et al. (2024).

The process understanding gained in the course of this dissertation further enables the identification of priorities for model-based research on the shelf carbon cycle and active model development. On a technical level, this dissertation demonstrates the utility of using unstructured grid models to realize kilometrical-scale horizontal resolution in coupled physical-biogeochemical modelling studies. The benefit of high model resolution depends on the research scope and needs to be carefully weighed against other constraints required to maintain computational feasibility. Shelf carbon cycle modelling primarily requires a balance against the computational demand introduced by the further sophistication of applied ecosystem models. Kilometrical-scale horizontal resolution is expected to generally improve simulations of the shelf carbon cycle by improving physical model performance, but the impacts on the shelf carbon cycle are yet to be fully assessed. The limited impact of the kilometrical-scale internal tide field on the NWES carbon cycle demonstrated in this study does not support prioritizing

the realization of kilometrical-scale resolution in carbon cycle modelling at shelf-wide scale in the near-term. This result of the dissertation supports the conclusion that available computational resources are better placed for the extension of biogeochemical process representations that hold potential for improvements in shelf carbon cycle modelling.

Although the NWES is one of the most intensively studied shelf regions of the world, the understanding of the NWES carbon cycle remains restricted due to several key knowledge gaps and a persistent lack of data. Legge et al. (2020) accordingly suggest, based on their synthesis on the NWES carbon budget, that there is no large-scale biogeochemical basis to support a conclusion on the future fate of the NWES carbon sink. The extensive validation of the SCHISM-ECOSMO-CO₂ model framework performed during this work here highlights several promising avenues for active model development that show potential in model-based research on the shelf carbon cycle and may help address key uncertainties.

A central limitation in ECOSMO II is that all organic matter reservoirs are constrained to elemental Redfield ratios. There is a growing understanding of the significant variability in the stoichiometry of marine organic matter in scientific literature (Martiny et al., 2013; Moreno and Martiny, 2018; Liang et al., 2023). Several recent studies have investigated organic matter stoichiometry on the NWES and shown POM and DOM pools to be carbon-rich relative to Redfield stoichiometry (Painter et al., 2017; Chaichana et al., 2019; Davis et al., 2019). The mechanism of “carbon overconsumption” by phytoplankton under situations of nutrient limitation (Toggweiler, 1993) has previously also been proposed to explain high summer DIC drawdown observed in the central and northern North Sea (Prowe et al., 2009). Allowing for variable organic matter stoichiometry in ECOSMO II may account for the underestimated surface DIC drawdown in seasonally stratified shelf regions identified in *Study III*. Fixed stoichiometry models are also suggested to underestimate ocean carbon uptake (Prowe et al., 2009; Kwiatkowski et al., 2018). For considering the effects of variable stoichiometry on ecosystem dynamics and carbon cycling, it is essential to first identify the main drivers of variability and how these affect organic matter production and respiration.

The significant interaction of the sediment and water column constitutive for the shelf regime further motivates a sophistication of sediment processes in the applied ECOSMO II configuration. Sediment processes remain poorly represented in state-of-the-art ecosystem models, largely because of limited observational data and constraints on computational resources (Lessin et al., 2018). On the NWES, the assumption of low net POC burial in the tidally energetic shelf environment (Thomas et al., 2005; Kitidis et al., 2019) supports a simplified representation of sediment biogeochemistry in shelf carbon cycle modelling. Recent research has however demonstrated high variability in processes affecting carbon fluxes across the sediment-water interface on the NWES (Queirós et al., 2019; Zhang et al., 2019), which complicates a quantitative syntheses of carbon fluxes to the sediment. A promising next step in the development of the SCHISM-ECOSMO-CO₂ model framework would be the introduction of macrobenthos following Daewel et al. (2019), including the integration of associated bioturbation as a dynamic process as presented in Zhang et al. (2019). Such a process-based sophistication of the coupling between the sediment and the water column would contribute to resolving spatial and temporal variability in the interaction across the sediment-water interface and is also expected to enhance model accuracy in air-sea CO₂ exchange. In light of the high sensitivity of shelf carbon cycle seasonality to (tide-induced) changes of sediment-water interactions demonstrated in *Study III*, the inclusion of macrobenthos and bioturbation is particularly expected to improve the representation of seasonal variability in surface pCO₂.

Another priority for model development is the prognostic calculation of total alkalinity implemented in SCHISM-ECOSMO-CO₂. The prognostic treatment of total alkalinity enables the simultaneous simulation of the NWES and the Baltic Sea but is challenging due to the complexity of processes that affect total alkalinity in the shelf regime. Validation against observations in *Study III* consequently shows limitations in model performance for total alkalinity. Given the limited knowledge on calcification, the current model configuration neglects the impact of calcium carbonate production and dissolution on total alkalinity and dissolved inorganic carbon. An inclusion of currently neglected borate alkalinity would likely increase accuracy in the calculation of total alkalinity, but would have to account for an anomaly in the boron-salinity ratio observed in the Baltic Sea (Kuliński et al., 2018). Growing evidence for a contribution of organic alkalinity to total alkalinity (Middelburg et al., 2020), particularly in the Baltic Sea (Hammer et al., 2017) and other coastal regimes (Song et al., 2020; Song et al., 2023), also motivates consideration in the parameterization of total alkalinity. Current scientific understanding lastly highlights the importance of total alkalinity input from the Wadden Sea for the carbonate system in the southern North Sea (Thomas et al., 2009; Voynova et al., 2019; Schwichtenberg et al., 2020), making the inclusion of additional coastal total alkalinity sources a priority in model development.

There further is a growing recognition of the contribution of dissolved organic matter export from continental shelves to the global ocean carbon budget in recent research (Hopkinson and Vallino, 2005; Barrón and Duarte, 2015). Chaichana et al. (2019) demonstrated annual variations in dissolved organic carbon (DOC) concentrations in the North Sea that suggest a DOC contribution to lateral off-shelf export by episodic flushing events. Humphreys et al. (2019) found a relevant fraction of primary production in the Celtic Sea is transformed into long-lasting dissolved organic matter and also inferred episodic exchange with the open ocean from their observations. Carbon export via DOM crucially depends on the distinct lifecycles of highly heterogeneous DOM (i.e. the lability/ bioavailability of DOM). The export efficiency is further linked to the stoichiometry in organic matter, with observations showing C-rich DOM on the NWES relative to Redfield stoichiometry (Painter et al., 2017; Davis et al., 2019). Especially long-lived recalcitrant DOM is assumed to be more carbon-rich relative to Redfield stoichiometry (Jiao et al., 2010).

The ECOSMO II configuration implemented in this study only incorporates a labile DOM fraction and does not include more long-lived or recalcitrant DOM pools required to maintain relevant carbon export via off-shelf transport of DOM. The parameterization of the marine DOM cycle is impeded by persistent knowledge gaps on the diverse sources and sinks of recalcitrant DOM fractions in the marine environment (Hansell, 2013). Terrigenous sources of DOM affect ecosystem dynamics and the carbon budget on the NWES and consequently need to be accounted for when simulating the shelf carbon cycle (Powley et al., 2024). One potential approach is the explicit representation of DOM fractions of different lability in ECOSMO II. This approach would however require estimates for carbon flows into respective DOM fractions, which are difficult to obtain and therefore remain poorly understood. Another option is the inclusion of an additional bacterial functional group and the explicit parameterization of the microbial loop (Azam et al., 1983), including the “microbial carbon pump” mechanism proposed by Jiao et al. (2010) that transforms labile DOM into recalcitrant DOM. The second approach however comes with a significant increase in model complexity. The inclusion of a more sophisticated DOM functional group would facilitate model-based investigations of the role of shelf-derived DOM for the ocean carbon cycle. The developed cross-scale model

configuration, which resolves cross-shelf exchange with the North Atlantic and the dynamical coupling of the Baltic and North Sea systems, may particularly benefit the investigation of terrestrial DOM export from the river-dominated Baltic Sea (see Seidel et al., 2017).

In conclusion, this dissertation proves the developed SCHISM-ECOSMO-CO₂ model framework based on unstructured horizontal grids as an innovative and adaptable tool that offers a flexible platform for future research on the NWES carbon cycle. The model framework holds potential for future research that extends biogeochemical model complexity as well as physical process representation. The model framework has so far been successfully applied in research on the impact of bottom trawling on sedimentary organic carbon (Porz et al., 2024). Ongoing applications include research on the impact of variable stoichiometry on biological carbon fixation and oceanic CO₂ uptake (Demir et al., in prep.), the impact of bottom trawling on primary production and air-sea CO₂ exchange (Tiwari et al., in prep.) and a model-based evaluation of anthropogenic ocean alkalization as a carbon drawdown mechanism (Liu et al., in prep.). In this perspective, this dissertation contributed to a better mechanistic understanding of the NWES carbon cycle by evaluating the role of tidal processes and is set to capacitate critical future research on the shelf carbon cycle.

Appendices

Appendix A – A cross-scale hydrodynamic model framework for the Northwest European Shelf and Baltic Sea based on unstructured grids

This appendix contains the first paper, which has not yet been published:

Kossack, J., Mathis, M., Daewel, U., Zhang, Y. J., Schrum, C. (2024). A cross-scale hydrodynamic model framework for the Northwest European Shelf and Baltic Sea based on unstructured grids.

The contribution of Jan Felix Gottlieb Kossack (JK) and others to this paper is as follows:

JK initiated the study, set up the numerical model, generated the data sets, performed the data analysis and wrote the manuscript. MM, UD, YZ and CS provided essential background knowledge. CS and MM advised the study.

Cross-scale hydrodynamic model framework for the Northwest European Shelf and Baltic Sea based on unstructured grids

Kossack, J.^{1*}, Mathis, M.¹, Daewel, U.¹, Zhang, Y. J.², Schrum, C.³

¹ Institute of Coastal Systems, Helmholtz-Zentrum Hereon, Geesthacht, Germany

² Center for Coastal Resource Management, Virginia Institute of Marine Science, College of William & Mary, Gloucester Point, VA, United States

³ Institute of Oceanography, University of Hamburg, Hamburg, Germany

* Corresponding author: jan.kossack@hereon.de

Abstract

Regional-scale coupled physical-biogeochemical models applied on continental shelves like the North-Western European Shelf (NWES) must balance computational demands imposed by the high model resolution necessary to adequately resolve shelf dynamics and biogeochemical model complexity. In this context, the cross-scale capability of a new generation of ocean models based on unstructured grids raises new options for model-based research on the shelf carbon cycle. Local grid refinement possible with unstructured grid models facilitates the realization of high resolution at reasonable computational cost. Unstructured grids additionally allow flexible grid adaptations that can be tailored to meet differing research requirements, for example resulting from the prioritization of the representation of physical or biogeochemical processes in the shelf regime. The high configurability and specific set of numerical challenges associated with the unstructured grid approach however requires a thorough evaluation of potential impacts of unstructured grid topology on shelf physics. This study introduces a novel hydrodynamic modelling framework based on the unstructured grid model SCHISM and presents two new model grid configurations for the NWES and the Baltic Sea. A high resolution configuration applies local grid refinement to realize small-scale processes relevant for cross-shelf exchange and vertical mixing in the Celtic Sea and shelf regions adjacent to the shelf break of the NWES, while a coarse resolution configuration is optimized for the computationally efficient application of complex biogeochemical models. A validation of hindcast simulations from 2001-2005 demonstrates good and largely consistent model performance regarding the general hydrography on the NWES in both model configurations. Differences between the model configurations are found to primarily relate to differences in horizontal grid resolution and thus the representation of shelf physics. The most significant difference occurs in the Norwegian Trench, where the NWES-LR configuration is found to likely underestimate inflow from the North Atlantic, and the Baltic Sea, where the NWES-LR configuration shows a markedly lower model performance for sea surface salinity. The overall large consistency of the results of the two model grid configurations nevertheless underlines the high flexibility and configurability of the model framework and motivates its application in model-based research on physical and biogeochemical shelf-specific processes. The presented study here provides a baseline model validation that aims to capacitate future applications of the presented model framework.

1. Introduction

A new generation of ocean models based on unstructured grids offers relevant advantages in regional modelling of continental shelves. Unstructured grids permit flexible local grid refinement in areas of specific interest and therefore facilitate cross-scale modelling with enhanced numerical accuracy. Unstructured grid models further allow a faithful representation of coastal geometry and complex bathymetry (Chen et al., 2007) and are an effective tool to achieve the seamless transition between ocean basins connected by narrow straits (Zhang et al., 2016a). The realistic simulation of the Northwest European shelf (NWES) requires a large model domain that resolves dynamic cross-shelf exchange with the North Atlantic, as well as the dynamic coupling of the tide-dominated North Sea and the semi-enclosed Baltic Sea via the narrow Danish straits. The advantages of the unstructured grid approach therefore motivate an application on the NWES.

The cross-scale capability of unstructured grid models allows the local realization of telescoping kilometrical-scale horizontal model resolution necessary to for example resolve the 1st internal Rossby radius in areas of interest, and thus facilitates resolving small-scale physical processes relevant on continental shelves at reasonable computational costs (Holt et al., 2017). The effective cross-scale realization of high horizontal model resolution particularly benefits computationally demanding coupled physical-biogeochemical models and offers high potential in advancing process-oriented understanding of the shelf carbon cycle. Simulations of the shelf carbon cycle however do not only face methodological uncertainty stemming from inadequate resolution of shelf hydrodynamics but are also constrained by inadequate simplification of shelf-specific biogeochemical processes. Applying high model resolution ensues an increase in computational cost, which in the context of modelling the shelf carbon cycle needs to be carefully weighed against, also computationally costly, biogeochemical model complexity.

The unstructured grid approach delivers a hydrodynamic modelling framework that is highly adaptable and can be tailored to meet specific research needs. Unstructured grid models however face specific issues that need to be addressed in numerically challenging cross-scale model configurations. The essentially unlimited configurability of unstructured grids requires thorough validation against observations (and potentially pre-existing grid configurations) to assess sensitivity of the numerical solution to unstructured grid topology. Differences introduced through local grid refinement can for example affect the large-scale ocean circulation. Possible issues with unstructured grid quality in individual grid realizations may additionally impair the respective numerical solution. Controlling spurious numerical modes further is a delicate procedure in unstructured grid models (Danilov, 2013). Spurious modes are particularly severe at steep slopes and in the deep ocean and have thus for a long time impeded the extension of unstructured grid approaches to the deep eddying ocean (Zhang et al., 2016b). The flexibility and cross-scale capability of unstructured grid models lastly also come at a price, as the complex numerical methods and grid discretization are less efficient compared to structured grid approaches, which generally increases model integration time (Danilov, 2013).

In this study, we introduce a novel hydrodynamic modelling framework for the NWES and the Baltic Sea based on the unstructured grid model SCHISM (Zhang et al., 2016b), a numerically efficient and robust modelling system designed for the effective 3D baroclinic cross-scale simulation from creek to ocean. To our knowledge this is the first unstructured grid model of the NWES that includes the Baltic Sea and also extends into the deep North Atlantic to enable dynamic cross-shelf exchange.

Two separate SCHISM model grid configurations are presented. The coarse resolution NWES-LR configuration is optimized for a numerically efficient and fast simulation of the NWES and the Baltic Sea and thus facilitates application with more complex biogeochemical models. The NWES-IT configuration in contrast leverages SCHISM’s cross-scale capability to locally realize kilometrical-scale horizontal resolution in the Celtic Sea and shelf regions adjacent to the shelf break of the NWES, where kilometrical-scale processes are understood to be relevant for cross-shelf exchange and vertical mixing (Polton, 2015; Graham et al., 2018; Guihou et al., 2018; Huthnance et al., 2022).

The SCHISM model is extensively described in section 2. We further detail the grid generation of the NWES-IT and NWES-LR model configurations in section 2 and outline the applied approach for model forcing and initialization. Section 3 presents results from the validation of key hydrodynamic features on the NWES against observations and compares the results obtained with the two model configurations. Differences in the results of both model configurations are qualitatively assessed with the aim of establishing reference configurations for future model applications. Section 4 then summarizes the findings and provides an outlook on key aspects for active model development.

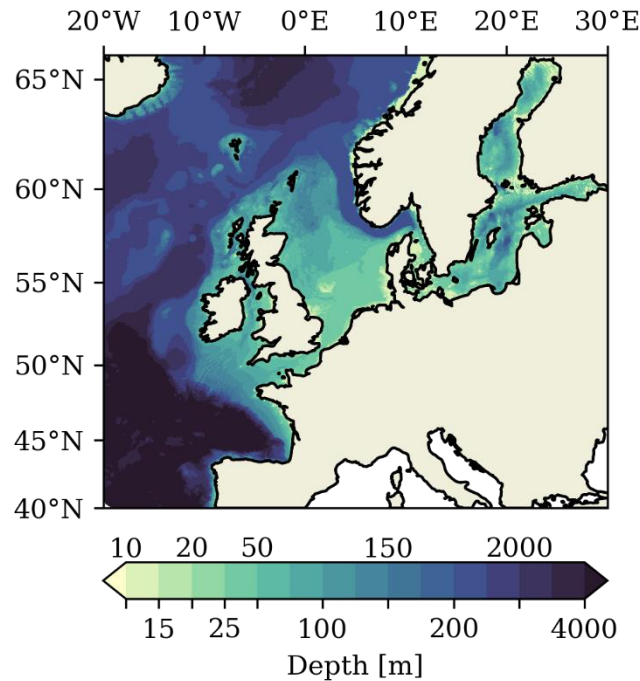


Figure 1: Model domain and bathymetry.

2. Methods

2.1. SCHISM

The 3D hydrodynamic Semi-implicit Cross-scale Hydroscience Integrated System Model (Zhang et al., 2016b) is a derivative product built from the original SELFE (Zhang and Baptista, 2008) and is distributed with an open-source Apache v2 license. SCHISM is based on a triangular unstructured horizontal grid that offers high cross-scale flexibility in local grid refinement. In the vertical dimension, SCHISM employs Localized Sigma Coordinates with

Shaved Cells (LSC²; Zhang et al., 2015), which effectively reduce spurious diapycnal mixing and pressure gradient errors.

SCHISM solves the Reynolds-averaged Navier–Stokes equations in hydrostatic- and Boussinesq- approximated form with a semi-implicit finite-element/finite-volume method and an Eulerian–Lagrangian method (ELM) for momentum advection. The 3D transport equation is solved with a third-order Weighted Essentially Non-Oscillatory (WENO) solver in the horizontal and an implicit Total Variation Diminishing (TVD) scheme in the vertical dimension. The semi-implicit formulation of the 3D transport equation and the hybridization of the finite volume horizontal transport scheme with the ELM method avoids limitation by the CFL-criteria ($CFL = (|u| + \sqrt{gH})\Delta t/\Delta x < 1$), which commonly restricts horizontal discretization in explicit (mode-splitting) models (Zhang et al., 2016b; Ye et al., 2019). In this configuration, SCHISM has an operational time step range in baroclinic applications of 100-200s (https://ccrm.vims.edu/schismweb/schism_manual.html; last accessed 05/2024). Density is calculated with the non-linear International Equation of State for Seawater (Fofonoff and Millard, 1983). The bulk aerodynamic model by (Zeng et al., 1998) is used to compute exchange with the atmosphere. Bottom drag is parameterized with the log law drag formula by Blumberg and Mellor (1987).

Several upgrades enable the accurate application of SCHISM in the large-scale eddying regime (i.e. the open ocean), which requires a particularly careful control of numerical dissipation and spurious modes maintained by the grid discretization. The third-order WENO solver for the horizontal transport equation achieves a good balance of accuracy, efficiency and monotonicity and has demonstrated superior behaviour in the eddying regime compared to lower-order schemes (Ye et al., 2019). In shallow waters (in this study water depths < 10m), the 3rd-order WENO scheme is replaced by a 1st-order but more efficient upwind scheme. SCHISM further applies bi-harmonic viscosity to the horizontal momentum equation to control spurious inertial modes. Laplacian viscosity in form of a spatially variable Shapiro filter is additionally added at steep bathymetry to control spurious modes excited by pressure gradient errors (Zhang et al., 2016b; Ye et al., 2020).

SCHISM computes turbulence in form of eddy viscosities and eddy diffusivities with the Generic Length-Scale formulation (GLS) introduced by Umlauf and Burchard (2003). The GLS turbulence closure is parameterized according to the k – kl model with KC94 stability functions (Kantha and Clayson, 1994), as previously done in a SCHISM model developed for the North Sea and Baltic Sea by Zhang et al. (2016a). The background diffusivity and maximum cut-off eddy diffusivity are set to $10^{-6} \text{ m}^2\text{s}^{-1}$ and $1 \text{ m}^2\text{s}^{-1}$, respectively.

2.2. Model configuration

2.2.1. Horizontal model grid generation

We use the grid generation software SMS (<https://www.aquaveo.com/software/sms-surface-water-modeling-system-introduction>; last accessed 05/2024) to construct a base grid design with geographic information at 5km resolution from the GSHHS shoreline database (Wessel and Smith, 1996) and bathymetry data from the EMODnet Digital Bathymetry Digital Terrain Model (version 2018; <http://www.emodnet-bathymetry.eu>; accessed 04/2020). A minimum water depth of 10m is prescribed to reduce computational demand, and because no wetting/

drying scheme is implemented. The robustness and stability of SCHISM allow the accurate replication of complex coastline geometry and bathymetry in the development of the model grids without having to observe too strict conditions on mesh quality. We use the base grid design to create two separate horizontal grids of the NWES that extend beyond the shelf break into the North Atlantic and also encompass the Baltic Sea (Fig. 1). The NWES-IT configuration is optimized for the high-resolution modelling of kilometrical-scale processes along the shelf break and in the Celtic Sea, while the NWES-LR configuration offers faster model integration through the implementation of lower horizontal grid resolution and a larger timestep.

Although SCHISM does not need to observe the CFL-criteria, horizontal grid design needs to adhere to a somewhat opposite inverse CFL-criteria ($CFL > 0.4$) to control numerical diffusion. We accordingly design the horizontal discretization in the low-resolution NWES-LR configuration by defining a size function in the SMS software based on the maximum model time step of 200s and local water depths. The SMS size function is further smoothed using a maximum area change limit of 0.75 to ensure smooth transition from high to coarse resolution, which ensures high model accuracy and aims to minimize the distortion of eddying processes (Danilov and Wang, 2015). In specific areas in the Baltic Sea that feature wind-driven upwelling, the grid resolution is kept quasi-uniform (B. Jacob, in pers. comm.). The resulting horizontal grid has a resolution (in shelf areas other than the Kattegat) that smoothly varies from approx. 4.8 km in the shallow coastal regions to a maximum of about 10km in the deep areas in the Baltic Sea and the NWES. At the shelf break, defined as the 200m-isobath, the horizontal grid size smoothly increases to approx. 15km in the deep North Atlantic. The resulting NWES-LR grid has approx. 74k grid nodes and 140k triangular grid elements. The NWES-LR model grid is documented in Fig. 2.

The horizontal discretization for the high-resolution model grid for the NWES-IT configuration is derived based on a higher model time step of 100s necessary to ensure high accuracy at the shelf break and in the open ocean. This yields a horizontal resolution that smoothly varies from a minimum of ~ 2.5 km in the shallow coastal zones to a maximum resolution of ~ 10 km in the deepest parts of the shelf. We additionally realize a telescoping high horizontal resolution of 1.5km throughout the Celtic Sea and Armorican Shelves and along the shelf break in a 75-km-wide band delimited in off-shelf direction by the 200-m isobath. At the shelf break, defined as the 200-m isobath, horizontal grid size transitions from 1.5 km to a quasi-uniform horizontal resolution of 10 km in the open ocean. We explicitly avoided over-refining the transitional regime at the shelf break to not violate the hydrostatic assumption (horizontal scale \gg vertical scale). The change in grid element size from the shelf break to the deep ocean is also restricted to a maximum of 0.2 to ensure a very smooth transition of the horizontal resolution, which contributes to controlling the distortion of eddies in the area. The resulting NWES-IT horizontal grid comprises a total number of ~ 386 k grid nodes and ~ 758 k triangular grid elements and is also documented in Fig. 2.

The horizontal resolution in the narrow channels of the Danish straits has a large effect on inter-basin exchange (Stanev et al., 2018), and thus on deep-water ventilation and upwelling in the Baltic Sea. We therefore employ SCHISM's cross-scale capabilities in the Danish Straits in both horizontal grid configurations and resolve the Danish straits region with a maximum of 1.5km horizontal resolution and a minimum grid size length of 500m in the Great Belt and the Sound. The Little Belt requires even higher horizontal resolution, it has a width of only ~ 1 km, and is therefore neglected in the applied meshing approach.

The bathymetry is linearly interpolated onto the two horizontal grids from the EMODnet Digital Bathymetry Digital Terrain Model (version 2018) dataset. The EMODnet DTMs have a horizontal resolution of $1/16 \times 1/16$ arc minutes (approx. 115m). As outlined above, the minimum water depth in the domain was set to 10 m. The bathymetry was only modified at deep fjords along the Norwegian coast to simplify the horizontal and vertical gridding processes in this region with extreme bathymetry gradients and small horizontal scales. No other bathymetry smoothing was applied, so that distinct features like the shelf break, submarine canyons and straits are faithfully resolved.

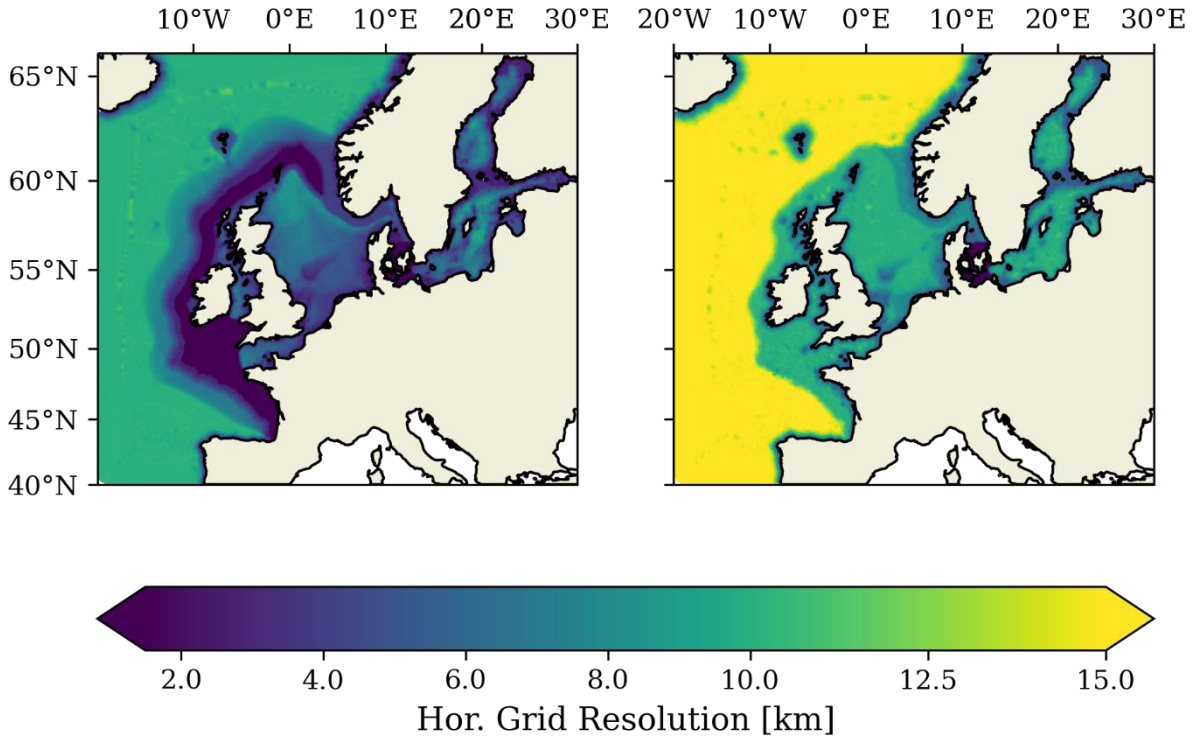


Figure 2: Horizontal model resolution of the unstructured triangular grid of the NWES-IT configuration (left) and NWES-LR configuration (right).

2.2.2. Vertical model grid generation

We use a hybrid terrain-following-like Localized Sigma Coordinate with shaved cells (LSC²; Zhang et al., 2015) as the vertical model coordinate in this study. The LSC² grid allows a variable number of vertical layers at each horizontal location and thus economizes the use of vertical layers in shallow parts of the model domain. The application of the Vanishing Quasi Sigma formalism (VQS; Dukhovskoy et al., 2009) ensures smoothness among neighbouring nodes, while the shaved cell technique avoids staircases, restricts diapycnal mixing and reduces pressure gradient errors by maintaining a milder coordinate slope compared to terrain-following coordinates. Zhang et al. (2016a) previously demonstrated that the LSC² coordinate contributes to the simulation of realistic stratification in the Baltic Sea not realizable with an S-grid, which further motivates the application of the LSC² coordinate in this study.

The design of the vertical grid was found to strongly affect numerical diffusion and spurious diapycnal mixing during model development, particularly at the steep shelf break of the NWES (not shown). The LSC² master grid used to generate the vertical grids for the both the NWES-

LR and NWES-IT model configurations was optimized for the NWES with the help of several tuning experiments. The key aspect in vertical grid design was the minimization of the sigma-coordinate slopes at the shelf break by a careful positioning of the reference grid depths used by the VQS formalism. The vertical coordinate was additionally skewed towards the surface and refined at mid-depth (20-60m) for an improved representation of the seasonal thermocline. The resulting vertical grids have a maximum number of 53 vertical layers. The average number of vertical layers is 25.5 in the NWES-IT configuration and 22.1 in the NWES-LR configuration.

2.3. Forcing, initialization and parameters

Atmospheric forcing is provided with an hourly timestep from a hindcast simulation with the regional atmospheric model COSMO-CLM version 5 with 0.11° horizontal resolution (Geyer, 2017). We implement a domain-wide bias correction of +15% to the COSMO-CLM shortwave radiation to correct for a sea surface temperature bias identified in tuning simulations (not shown). Surface albedo is set to a domain-wide constant value of 0.06. Light attenuation in the water column is parameterized according to the Jerlov type IA water type.

Open boundary forcing for temperature and salinity are provided from WOA2018 climatological data (Boyer et al., 2018). Daily-averaged subtidal SSH and horizontal velocities are prescribed from a HYCOM–ECOSMO hindcast simulation of the North Atlantic (Samuelson et al., 2022). The tidal component of the open boundary forcing is added to both SSH and the horizontal velocities from the FES2014 product (Lyard et al., 2021) for 15 tidal constituents (Q1, O1, P1, S1, K1, 2N2, MU2, N2, NU2, M2, L2, T2, S2, K2, M4). River forcing is provided in form of point sources at the respective river mouths for the 172 largest rivers in the model domain. River discharge represents a mean annual cycle calculated for the period 2000–2015 from a regional river dataset compiled and used by Daewel and Schrum (2013) and further updated as described by Zhao et al. (2019). We assume ambient temperatures for river discharge.

The temperature and salinity field for the NWES-LR configuration is initialized from WOA2018 climatological data. The NWES-LR configuration is spun up for 6 years from 1995 to 2000, and the simulation period from 2001 to 2005 is then evaluated for this study. A comparable spin up simulation is not possible for the NWES-IT configuration because of limitations in computational resources. The NWES-IT configuration is therefore initialized in January 2000 from an initial field interpolated from the NWES-LR simulation. The first year of simulation is treated as a secondary spin up, and model results from 2001-2005 are subsequently used for evaluation in this study.

We use a domain-wide constant bottom roughness of 0.5 mm in the bottom drag parameterization in this study. Additional Laplacian viscosity in form of the Shapiro filter is applied to control spurious modes excited by the pressure gradient error at steep slopes, especially along the shelf break of the NWES. The local strength of the Shapiro filter is calculated as a function of the local bathymetric slope α given by $\gamma = 0.5 \tanh\left(\frac{2\alpha}{\alpha_0}\right)$ with a reference slope of $\alpha_0 = 0.5$. The applied Shapiro filter strength is illustrated in Fig. 3. Sea ice

is neglected in this study. This particularly restricts accurate model performance the Baltic Sea, which commonly shows seasonal sea ice development.

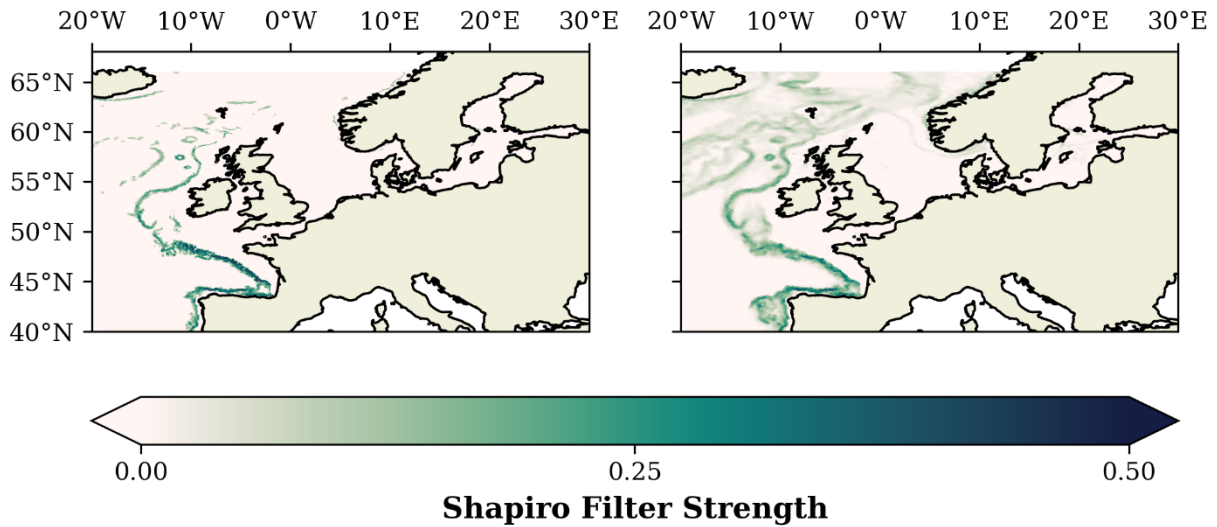


Figure 3: Shapiro filter strength in the model domain for the NWES-IT configuration (left) and the NWES-LR configuration (right).

3. Model comparison and validation

3.1. Resolving internal tides in NWES-IT

The NWES-IT configuration realizes kilometrical-scale horizontal resolution in the Celtic Sea and along the shelf break of the NWES, which is a prerequisite for the simulation of the internal tide field excited by the regionally dominant M2 tide. We assess vertical pycnocline displacement and vertical velocity during seasonal stratification at a station in the central Celtic Sea to assess simulated internal tides in the NWES-IT configuration in Fig. 4. The respective station data from the coarse resolution NWES-LR configuration is additionally presented for comparison.

The NWES-IT configuration shows high-frequency oscillatory vertical displacements of the pycnocline in the order of 5-10m and associated fluctuations in vertical velocity within the pycnocline not present in the NWES-LR configuration (Fig. 4). Frequency analysis of the vertical pycnocline displacements shows a local maximum at the frequency of the regionally dominant M2 tide (not shown). The documented vertical pycnocline displacements demonstrate the ability of the NWES-IT configuration to resolve internal tide generation at the shelf break or small-scale bathymetric features on the shelf and internal tide propagation in grid areas with locally refined kilometrical-scale horizontal resolution. The coarse resolution NWES-LR configuration does not resolve comparable internal tides. The presence of internal tides in the simulated pycnocline invokes shear production in the GLS turbulence closure model implemented in SCHISM (Umlauf and Burchard, 2003), which is suggested to increase simulated vertical mixing in the NWES-IT configuration.

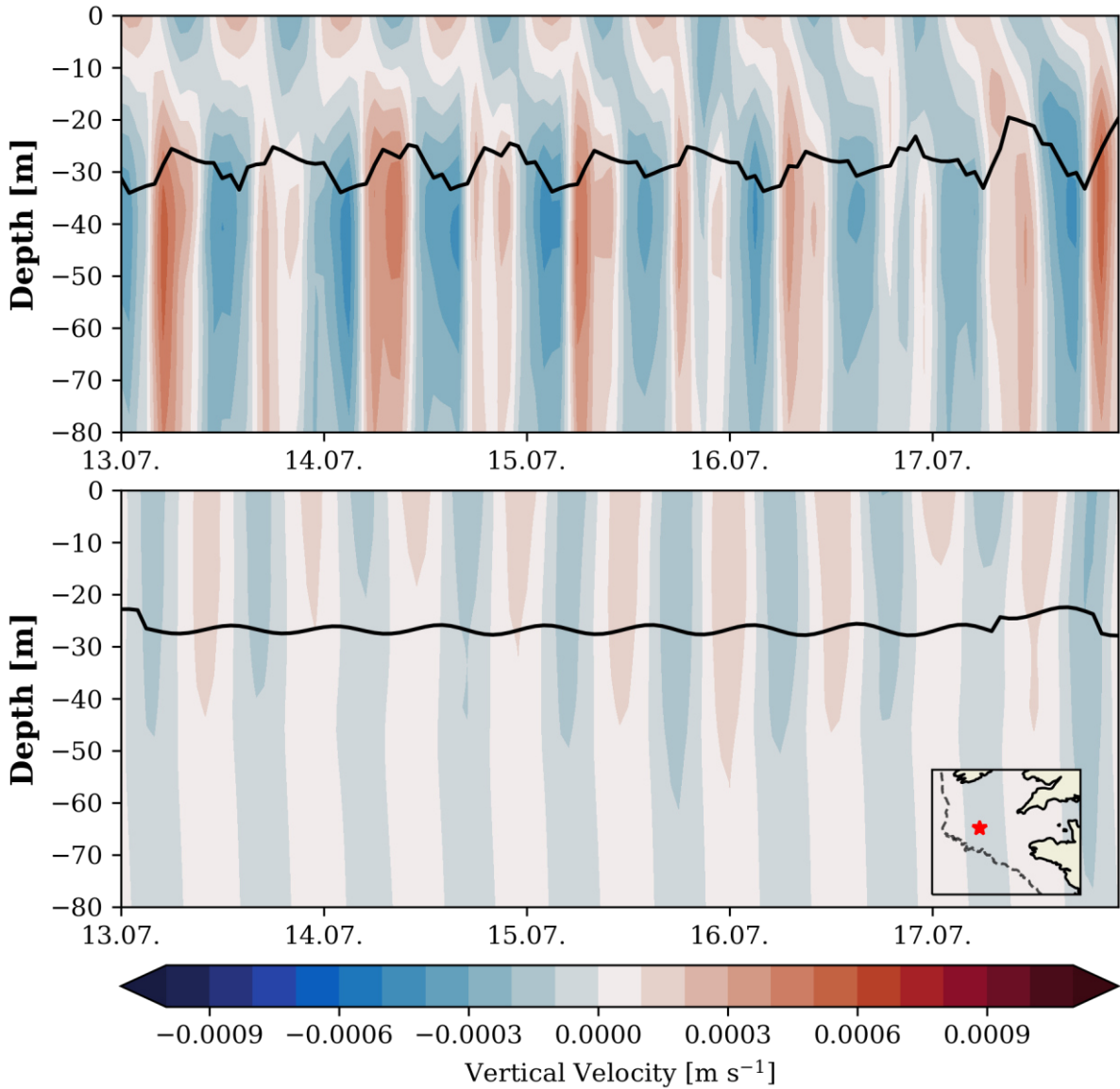


Figure 4: Vertical velocity in July 2004 at a station in the central Celtic Sea for the NWES-IT configuration (top) and the NWES-LR configuration (bottom). The black line shows the pycnocline. Inset figure in bottom panel shows position of the station in the Celtic Sea.

3.2. Tides

The model framework's ability to simulate barotropic tides and tidal currents on the NWES is evaluated against observational data from tide gauges and tidal current meters by means of harmonic analysis. The Baltic Sea is neglected as it does not feature relevant tides. Tide gauge data are compiled from CMEMS In Situ TAC (<http://www.marineinsitu.eu>; last accessed 08/2022), UHSLC tide gauge data (Caldwell et al., 2015), and the UK Tide Gauge Network provided by the British Oceanographic Data Centre (https://www.bodc.ac.uk/data/hosted_data_systems/sea_level/uk_tide_gauge_network; last accessed 08/2022). Simulated tidal currents are compared against observational data from the British Oceanographic Data Centre (made available by Karen Guihou under a CECILL license at https://github.com/Karen-Guihou/tidal_analysis; last accessed 08/2022). Harmonic analysis

of the tidal signal is performed with the Python implementation of the Utide tidal analysis and prediction package (<https://github.com/wesleybowman/UTide>; last accessed 05/2021) originally developed in MATLAB by Codiga (2011). Hourly model output from July and August 2014 from both the NWES-IT and NWES-LR configurations is used for the harmonic analysis of the tidal signal.

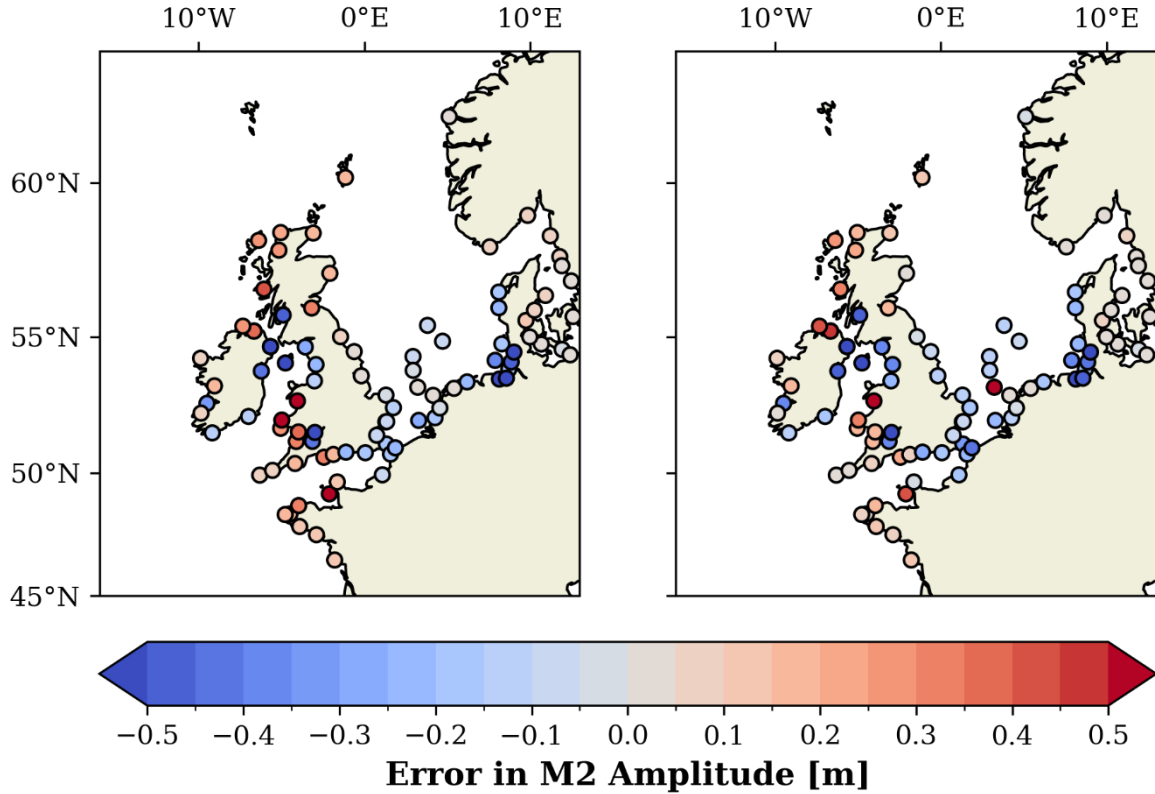


Figure 5: Spatial distribution of the error (model-observations) in M2 tidal amplitude against tide gauge data for the NWES-IT configuration (left) and NWES-LR configuration (right).

Fig. 5 shows the spatial distribution of the mean differences computed for the simulated regionally dominant M2 tide in the NWES-IT configuration and observational data from tide gauges. Agreement between the simulated sea level in the NWES-IT configuration and observations is generally high, with a mean bias of -3.5 cm and a root mean square error of 33.3 cm for the M2 constituent. The model underestimates tidal amplitudes at most tide gauges in the Irish Sea and in the German Bight, and to a lesser extent in the eastern English Channel and the along the continental coast in the North Sea. Tidal elevation is distinctly overestimated at tide gauges in the Bristol Channel and the south-eastern coast of the Irish Sea, and to a lesser extent along the coast of Scotland and in the western English Channel. The comparison of the simulated tidal current strength in NWES-IT by means of the M2 semi-major axis shown in Fig. 6 confirms the generally high agreement between the model and observations. Fig. 6 shows a minor overestimation of tidal current velocities in the north-eastern Celtic Sea and the Irish Sea and a minor underestimation of tidal currents in the south-eastern North Sea. The RMSE for the maximum M2 tidal current velocity is 14.7 cm/s, with a mean error of 4.6 cm/s.

The spatially constant bottom drag implemented in this study is likely the main factor contributing to the differences between modelled and observed tidal elevation and currents.

Model performance regarding tides would likely benefit from by the introduction of a spatially varying bottom roughness and further tuning simulations. The comparison to tide gauge data also is likely impaired by insufficient representation of local geographic and bathymetric settings in the model, particularly in light of the 10-m minimum water depth imposed in this study.

Model performance regarding the M2 tidal constituent in the coarser NWES-LR configuration (Fig. 5 and Fig. 6) shows negligible systematic differences to the high-resolution NWES-IT configuration. Minor differences between the model configurations particularly occur in the south-east of the NWES, where the NWES-LR configuration shows reduced overestimation of both the M2 tidal elevation and M2 tidal current velocities in the north-eastern Celtic Sea, Bristol Channel and in the Western English Channel. The NWES-LR configuration accordingly shows a more pronounced underestimation of the M2 tidal amplitude with a mean error of -5.7 cm, but exhibits a slightly lower RSME of 32 cm. The RMSE (13.6 cm/s) and mean error (3.5 cm/s) for the maximum M2 tidal current velocity in the NWES-LR are also both slightly lower than in the NWES-IT configuration.

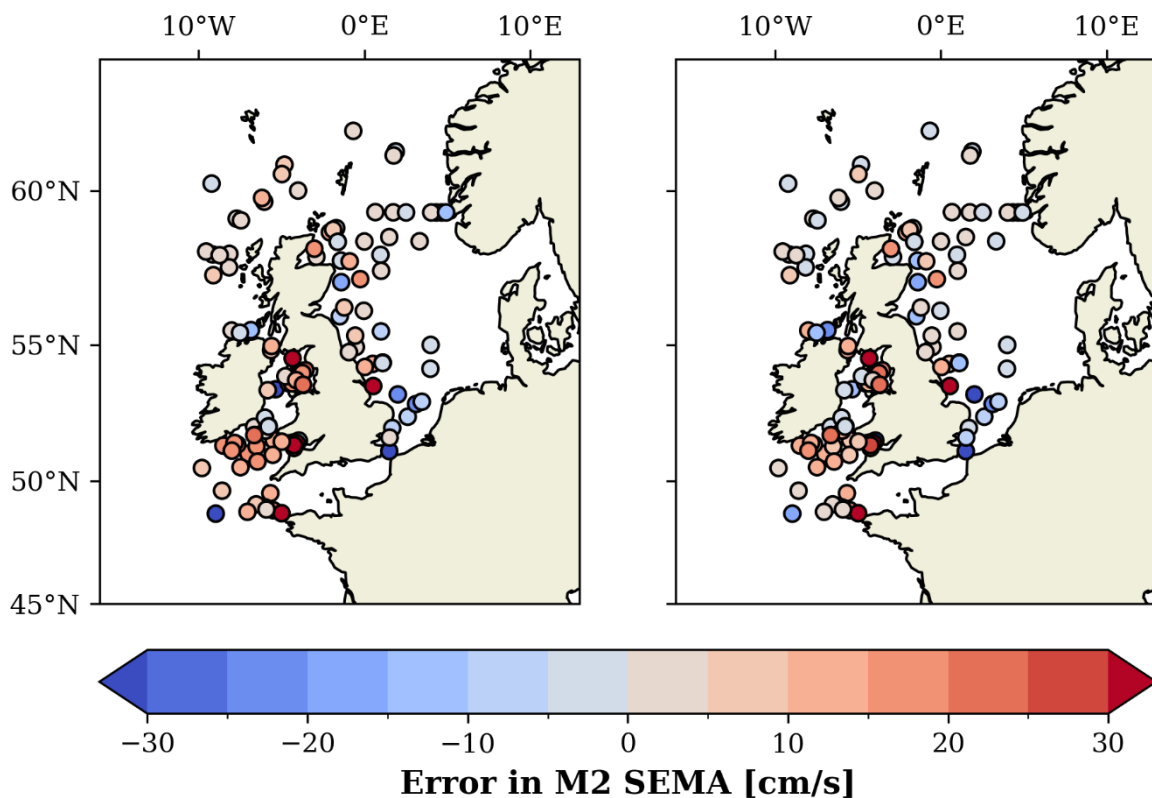


Figure 6: Spatial distribution of the error (model-observations) of the M2 semi-major axis against current meter data for NWES-IT configuration (left) and NWES-LR configuration (right).

3.3. Sea surface temperature

We compare simulated sea surface temperature against satellite observations obtained from the European Space Agency SST Climate Change Initiative (ESA SST CCI) reprocessed sea surface temperature analysis (<https://doi.org/10.48670/moi-00169>; downloaded 03/2024). The

ESA SST CCI product provides daily average SST at 20cm depth based on the OSTIA system (Good et al., 2020) and is gridded with a horizontal resolution of $0.05^\circ \times 0.05^\circ$ ($\sim 5\text{km}$). We interpolate seasonal mean model data for the period 2001-2005 onto the ESA SST CCI grid for the comparison. Fig. 7 shows observed seasonal SST and the respective model SST bias against satellite observations for the NWES. The Baltic Sea SST is separately addressed in Fig. 8.

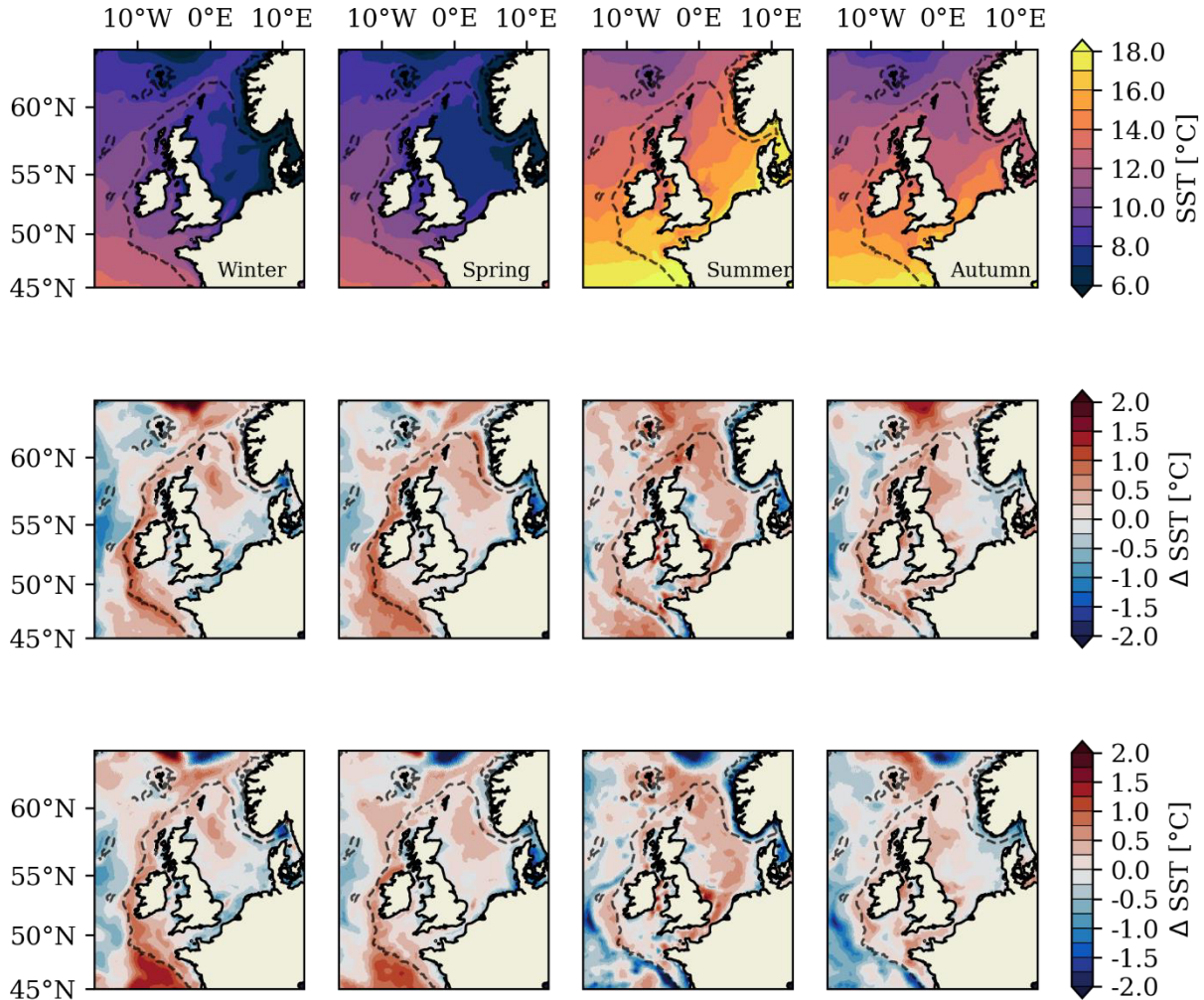


Figure 7: Seasonal mean sea surface temperature from satellite observations on the NWES (top panel) and respective temperature bias (model-observations) in the NWES-IT configuration (middle panel) and NWES-LR configuration (bottom panel).

We again first assess the NWES-IT configuration. Fig. 7 shows a warm bias in the North Atlantic north-east of the Faroe Islands throughout the year in the NWES-IT configuration, which originates from the northern open boundary of the model domain. Fig. 7 further shows a warm bias in the Bay of Biscay throughout the year, which is slightly more pronounced in spring and summer. This SST bias in the southern part of the model domain suggests a misrepresentation of the circulation in the Bay of Biscay, which potentially originates from the southern open model boundary. In summer, the NWES-IT configuration reproduces observed cooler summer SST on the continental slope along the Celtic Sea and Armorican shelf associated with enhanced vertical mixing at the shelf break (Pingree et al., 1982; New and Pingree, 1990). Simulated summer SST along on the continental slope of the Armorican Shelf in the south is slightly too low, which suggests local overmixing. The NWES-IT configuration

further exhibits a moderate warm bias of $0.75\text{-}1.25^{\circ}\text{C}$ along the NWES continental slope in winter and spring, which is most pronounced on the continental slope of the Armorican shelf and Celtic Sea. The steep bathymetry of the continental slope along the Armorican shelf and Celtic Sea is particularly challenging for the numerical schemes employed in ocean models and excites spurious numerical modes (Wise et al., 2022). Tuning simulations demonstrated a high sensitivity of the warm bias on this section of the continental slope to the design of the LSC² vertical grid (not shown). Further careful grid optimization will likely enable additional improvement of model performance in the region.

The mean SST bias on the NWES for the investigated period is 0.02°C and the RMSE is 0.4°C in the NWES-IT configuration and thus demonstrate generally good model performance. The outer shelf regions along the Celtic Sea shelf break show a warm bias, which suggests that the model system likely underestimates on-shelf pycnocline mixing driven by internal tides generated at the shelf break. There is a low-to-moderate warm bias on the North Western Approaches and in the (northern) North Sea throughout the year. This warm bias might be related to the warm bias along the Celtic Sea shelf break, as the European slope current advects the (winter) SST signal northwards. There is a distinct SST warm bias on the western side of the Norwegian Trench in spring and also to a lesser extent in winter. Near-coast summer SST along the Norwegian coast in the Norwegian Trench is underestimated in the model. The model further underestimates SST along the European continental coast in winter, spring and summer, especially in the German Bight. The near-coast SST bias in the German Bight is largest in spring (up to -2°C). Model performance in coastal regions influenced by freshwater discharge is likely constrained by the assumption of ambient temperatures for river discharge. Fig. 7 further shows a cold bias in the Skagerrak and Kattegat, especially in spring, which could be linked to errors in the simulation of the complex circulation in the region. The Kattegat further shows a marginal warm bias in autumn.

The lack of an ice model severely affects the simulation of the Baltic Sea and results in a large SST bias in the Bay of Bothnia and the Gulf of Finland (Fig. 8). The SST bias in the Baltic Proper is largely below $\pm 0.75^{\circ}\text{C}$ throughout the year in the NWES-IT configuration (Fig. 8). This is a promising result, as the horizontal grid in the Baltic Proper was optimized during grid generation (not shown) to avoid spurious upwelling that caused a large SST bias along the southern coast of Sweden present in a previous SCHISM model implementation by Zhang et al. (2016a). The remaining cold summer SST bias at the entrance to the Bay of Bothnia, along parts of the southern Baltic coast and in the Gulf of Finland, however, still indicates local overmixing and motivates further grid optimization in the region.

The SST bias for the NWES-LR configuration is shown for the NWES in Fig. 7 and for the Baltic Sea in Fig. 8. The mean SST bias in the low-resolution NWES-LR configuration is -0.03°C and the RMSE is 0.4°C . Simulated SST in NWES-LR therefore compares well against the results of the NWES-IT configuration. On the NWES, the NWES-LR configuration shows a similar pattern of a low warm bias in the North-Western Approaches and the North Sea, and a cold bias along the continental coast, especially in the German Bight. The SST bias in the Baltic Sea in the NWES-LR configuration (Fig. 8) shows high consistency with the results of the NWES-IT configuration. The largest differences between the NWES-IT and NWES-LR configurations occur in the Celtic Sea, the southern section of the shelf break along the Armorican shelf and in the Bay of Biscay. The low-resolution NWES-LR configuration exhibits a stronger warm bias in the Bay of Biscay in winter than the NWES-IT configuration, which

suggests differences in the simulation of regional circulation between the model configurations that are potentially caused by differences at the southern open model boundary. The NWES-LR configuration further reproduces a pronounced cold bias on the continental slope along the Armorican shelf, the Celtic Sea and along the Porcupine Seabank (south-west of Ireland) in summer and autumn, which suggests significant local overmixing on the steep slopes in the NWES-LR configuration. The outer-shelf areas in the Celtic Sea further show a lower warm bias in the NWES-LR configuration in spring, summer and autumn compared to the NWES-IT configuration, which likely results from lateral on-shelf mixing of the cold bias on the continental slope.

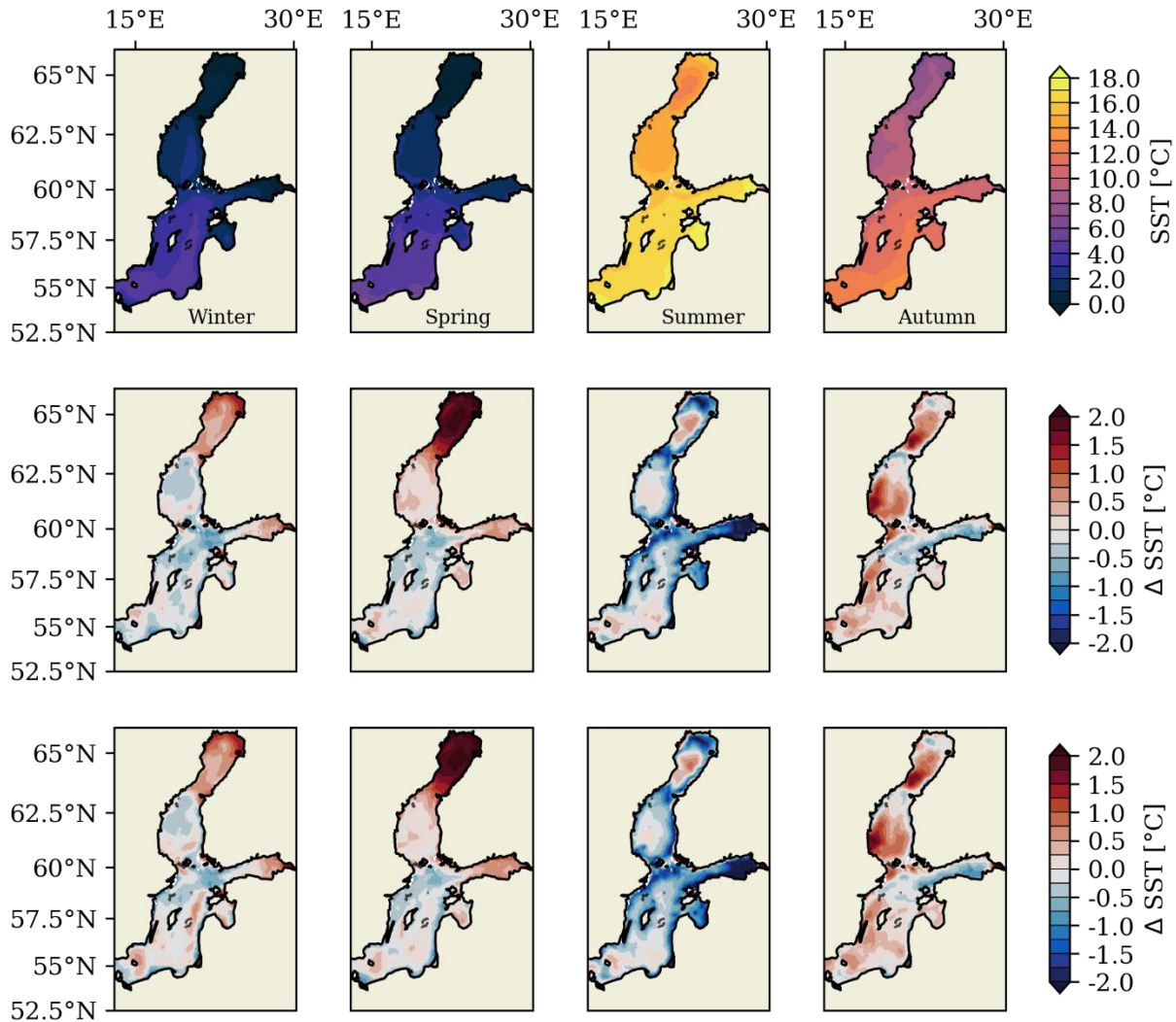


Figure 8: Seasonal mean sea surface temperature from satellite observations in the Baltic Sea (top panel) and respective temperature bias (model-observations) in the NWES-IT configuration (middle panel) and NWES-LR configuration (bottom panel).

3.4. Sea surface salinity

We compare simulated sea surface salinity (SSS) to surface salinity observations derived from observational EN4.2.2 profiles (Good et al., 2013) for the period 2001-2005. We seasonally aggregate the SSS observations and co-locate the model data in time and space for the four

seasons. The salinity bias calculated for the co-located observational and model data is shown for the NWES in Fig. 9 and for the Baltic Sea in Fig. 10.

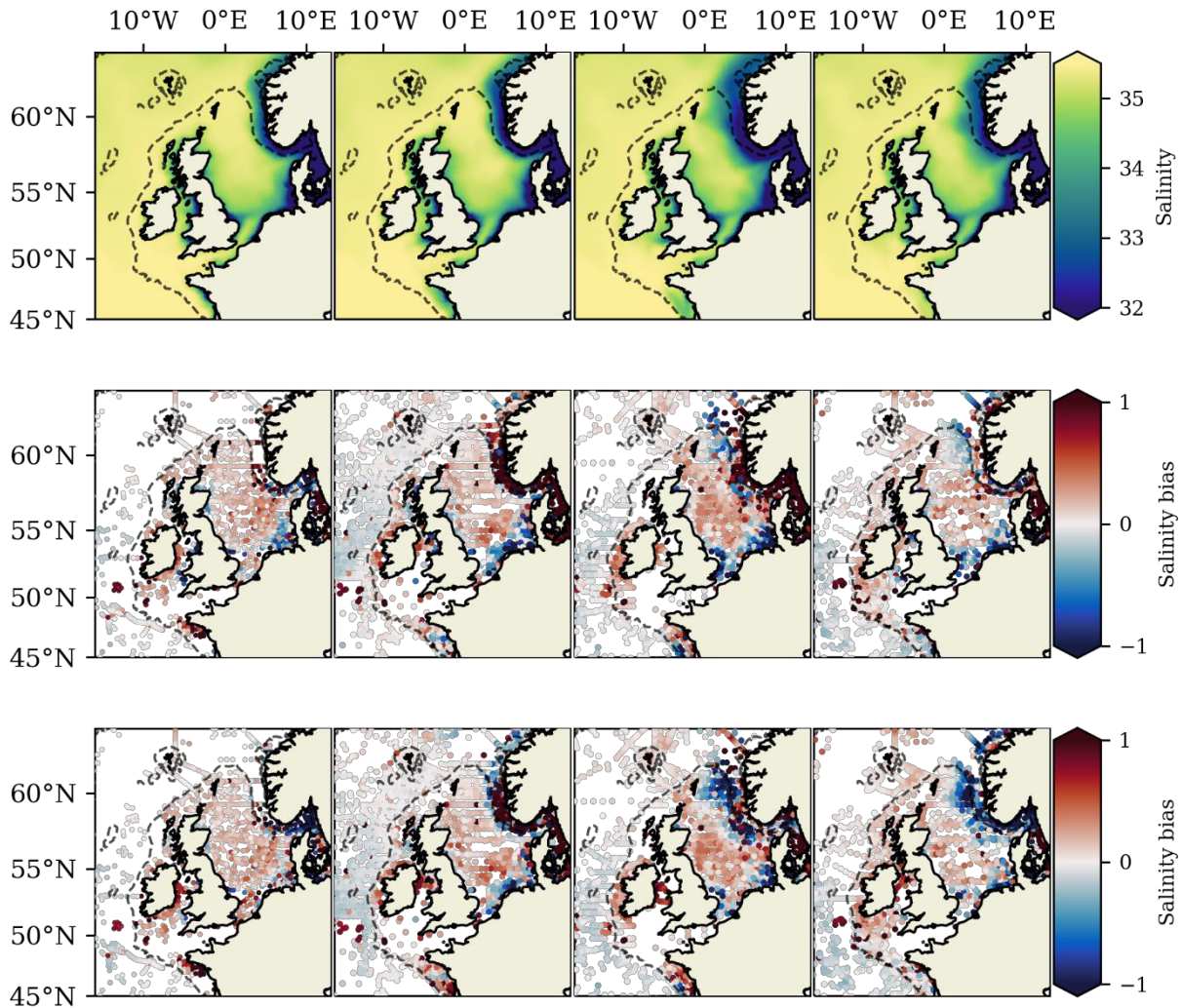


Figure 9: Simulated seasonal mean sea surface salinity on the NWES in the NWES-IT configuration (top panel) and salinity bias (model-observations) against observations from the EN4 dataset for the NWES-IT configuration (middle panel) and NWES-LR configuration (bottom panel).

The seasonal salinity bias in the NWES-IT configuration (Fig. 9 and Fig. 10) demonstrates generally reasonable model performance. The mean salinity bias on the NWES and in the Baltic Sea for the investigated period (2001-2005) is 0.3 and the RMSE is 1.9 in the NWES-IT configuration. The NWES-IT configuration slightly overestimates SSS in the central North Sea, particularly in summer (Fig. 9). The co-located salinities further show that the model underestimates salinity in near-coast areas on most of the NWES, particularly along the European continental coast and in the German Bight. The fresh bias along the coasts likely results from the model not fully capturing river plume dynamics, which require especially high horizontal resolution ($O(100\text{m})$; Briceno et al., 2014), and therefore underestimating lateral mixing in the coastal regime. The lack of interannual variability in the applied mean river forcing additionally limits model performance in the near-coast regime.

The Kattegat and Skagerrak regions show an especially high salinity bias, highlighting deficiencies in the challenging simulation of low-salinity Baltic outflow and the retroflection of North Atlantic inflow in the Skagerrak (Fig. 9). The simulation of the Baltic outflow would likely benefit from even higher horizontal grid resolution in the Danish straits, particularly in the under-resolved Little Belt (see Methods section 2.2.1; Stanev et al., 2018). The lack of interannual variability in the applied mean river forcing additionally limits the representation of the temporal variability of the Baltic outflow in the model. In the Norwegian Trench, SSS is overestimated along the Norwegian coast throughout the year. The overestimation of SSS along the Norwegian coast is particularly pronounced in spring and summer, which suggests overestimated lateral mixing and/ or a poor representation of large river discharge in the region after the ice melt in spring. The fresh bias in summer and autumn SSS on the western side of the Norwegian Trench and adjacent North Sea regions, particularly north of 57.5°N, is likely caused by an overestimation of lateral mixing that mixes too much low-salinity water from the Baltic outflow onto the shelf. The area is particularly dynamic, with instabilities and eddies facilitating mixing between the northward flowing low-saline outflow in the Norwegian Coastal current and the southward saline inflow from the North Atlantic along the western side of the Norwegian Trench (Ikeda et al., 1989). A distortion of eddies by inadequate or varying horizontal grid resolution in the region likely is the main cause for the overestimation of lateral mixing in the region.

The NWES-IT configuration reproduces the characteristic west-east salinity gradient in the Baltic Sea and shows only moderate-to-low seasonal surface salinity biases (Fig. 10). The model overestimates salinity in the Arkona Basin in the west of the Baltic Proper, and slightly underestimates SSS in central areas of the Baltic Proper. The distinct overestimation of SSS in the Gulf of Finland suggests local overmixing, which was also evident in the validation against satellite SST observations in Sect. 3.2. The local SSS bias may additionally indicate deficiencies in the representation of river discharge into the Gulf of Finland, especially from the Newa river in the east.

The comparison of the SSS biases in the NWES-IT configuration and the low-resolution NWES-LR in Fig. 9 demonstrates high consistency in model performance on the NWES, with exception of the Norwegian Trench and adjacent North Sea areas. Like the NWES-IT configuration, the NWES-LR configuration shows a tendency to overestimate spring SSS along the Norwegian coast. The NWES-LR configuration however shows a substantially stronger fresh bias on the western side of the Norwegian Trench in summer and autumn. The lower horizontal grid resolution in the Norwegian Trench in the NWES-LR configuration, and differences in the local horizontal grid size transition, likely contribute to the stronger fresh bias, as they further reduce model performance regarding locally relevant mesoscale processes.

The NWES-LR configuration further shows pronounced differences compared to the NWES-IT configuration in the Baltic Sea (Fig. 10). The NWES-LR configuration exhibits a fresh bias throughout most of the Baltic Sea over the entire annual cycle. The differences in model performance are potentially linked to a sensitivity of the haline stratification in the Baltic Sea to the coarser coastal horizontal model resolution in the NWES-LR configuration (the model resolution in central areas of the Baltic Sea is similar), as mesoscale processes relevantly contribute to lateral and vertical mixing in the region (Reissmann et al., 2009). The mean SSS bias on the NWES and in the Baltic Sea is 0.2 (RMSE = 1.7) and therefore lower than in the NWES-IT configuration. This likely doesn't suggest better model performance in the NWES-LR configuration, as it is assumed to be because of a higher penalization of spatial errors against

point data at higher model resolution (i.e. a minor shift in space in the higher resolution model will lead to a larger error) that complicates direct model comparison at different resolutions (as for example discussed in Sandvik et al., 2016).

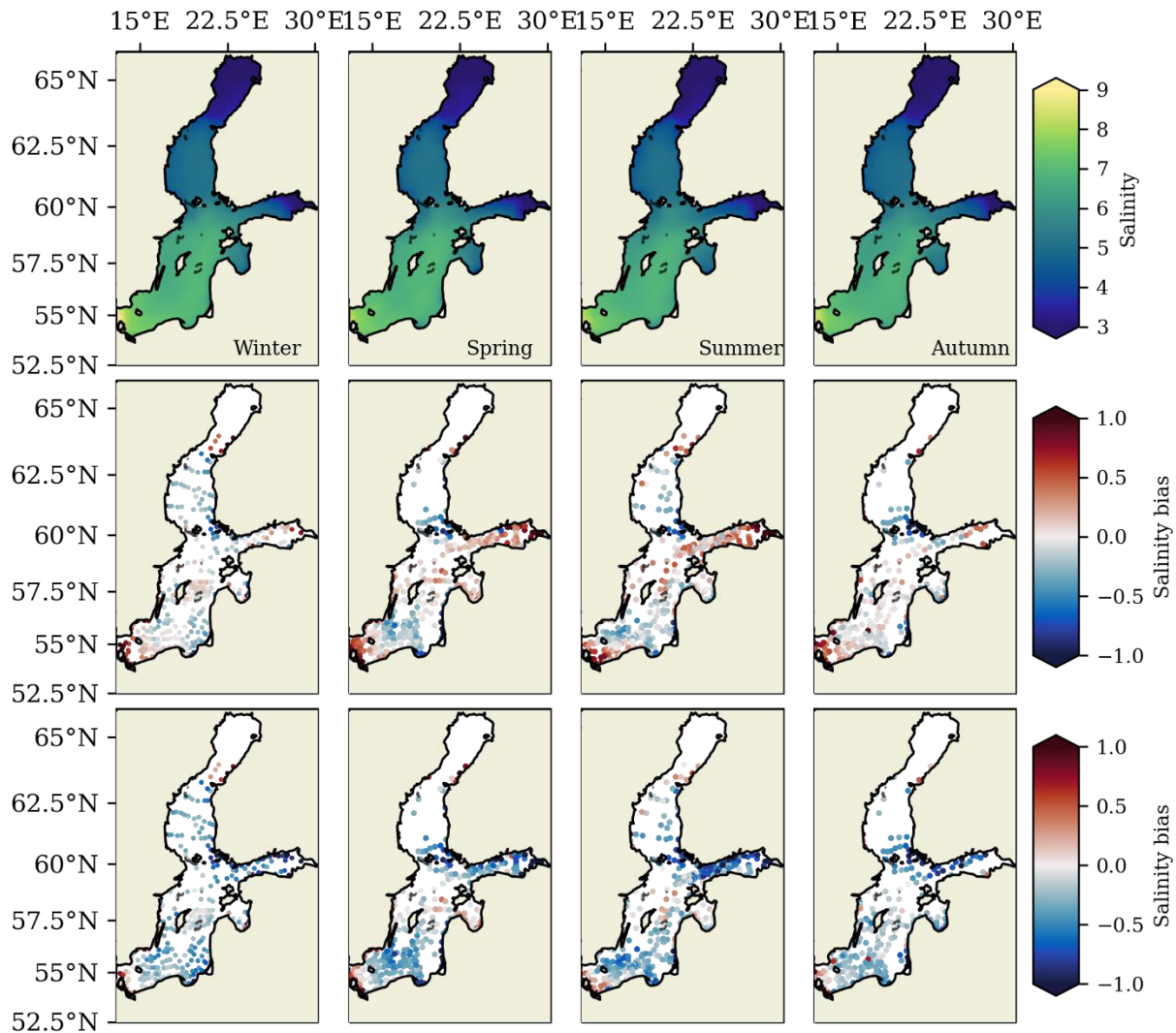


Figure 10: Simulated seasonal mean sea surface salinity in the Baltic Sea in the NWES-IT configuration (top panel) and salinity bias (model-observations) against observations from the EN4 dataset for the NWES-IT configuration (middle panel) and NWES-LR configuration (bottom panel).

3.5. Volume transports on the NWES

Fig. 11 shows the simulated time- and depth-averaged horizontal velocity field on the NWES in the NWES-IT configuration (2001-2005). The mean currents generally match the canonical circulation patterns on the NWES (Otto et al., 1990; Simpson, 1998; Holt and Proctor, 2008; Marsh et al., 2017). The model reproduces the pronounced northward flow in the European Slope current along the continental slope of the NWES north of $\sim 52.5^\circ\text{N}$. Northward flow on the Malin and Hebrides Shelves merges with the inflow of Atlantic water into the North Sea, where the model reproduces the cyclonic circulation and strong outflow through the Norwegian

Trench. Residual circulation in the Celtic Sea is weak and exhibits low spatial coherence. Mean currents in the Irish Sea also show low spatial coherence but transport is generally northwards.

We assess simulated mean transport in the NWES-IT and NWES-LR configurations by computing volume transports through key sections marked in Fig. 11. The computed transports are documented in Table 1. Table 1 also provides available observational estimates from scientific literature for the respective sections, which however are not exactly co-located in time or space and are based on sparse measurements. The simulated transports in Table 1 largely fit to the respective observational estimates and demonstrate a reasonable representation of the overall magnitude of the mean circulation in both model configurations. In combination with the identified model bias in sea surface salinity along the Norwegian Trench (Sect. 3.3), the marked deviation of simulated inflow of North Atlantic water into the North Sea in the Norwegian Trench from observations however further motivates a more thorough evaluation of model performance in this region.

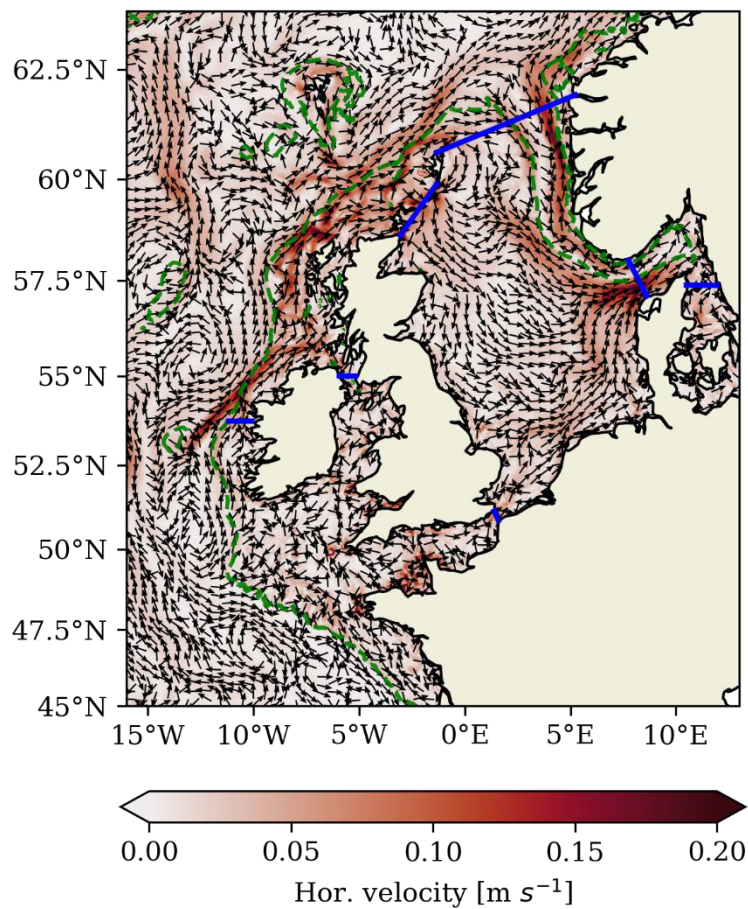


Figure 11: Annual mean depth-averaged horizontal velocity in the NWES-IT configuration for the period 2001-2005.

Table 1 additionally documents an overall low sensitivity of simulated transports to differences in horizontal resolution in the NWES-IT and NWES-LR configurations. The largest differences between the simulated transports occur in the Norwegian Trench and the Skagerrak. Simulated inflow from the North Atlantic via the Norwegian Trench is substantially lower in the NWES-LR configuration and thus shows an even larger difference compared to observations. Graham

et al. (2018) also found net transport in the Norwegian Trench to be sensitive to horizontal model resolution and similarly found higher net transport in a kilometrical-scale model configuration compared to a coarser configuration. The evaluation of the sensitivity of simulated transport in the Norwegian Trench to horizontal resolution is beyond the scope of this study but should be addressed in future work to improve model performance in the Norwegian Trench, as it constitutes the most significant pathway for carbon export on the NWES (Thomas et al., 2005).

Table 1: Mean transport across sections marked in Fig.11 for period 2001-2005.

	Mean Transport [Sv]		
	NWES-IT	NWES-LR	Literature *
1. Orkney-Shetland inflow	0.42	0.43	0.3 ¹
2. Shetland shelf inflow	0.53	0.47	0.6 ¹
3. Dover strait	0.06	0.07	0.1-0.17 ¹
4. Skagerrak (NET)	0.07	0.06	
IN	0.49	0.35	
OUT	-0.56	-0.41	-0.5 – -1.5 ¹
5. Kattegat	0.01	0.01	0.015 ¹
6. N. Trench (NET)	-1.28	-1.16	
IN	0.49	0.15	0.7 – 1.11 ¹
OUT	-1.77	-1.31	-1.8 ¹
7. North Channel	0.06	0.06	0.08 ²
8. Irish Shelf	0.29	0.27	0.24 ³

* Literature values summarized from following studies: ¹Winther and Johannessen (2006),²Knight and Howarth (1999), ³Fernand et al. (2006)

4. Conclusions and future work

This study presents a new highly configurable modelling framework for the NWES and Baltic Sea based on the unstructured grid model SCHISM. The modelling framework extends into the North Atlantic to dynamically resolve cross-shelf exchange and relevant shelf-specific processes along the shelf break. A first validation of the modelling system demonstrates the realistic simulation of key hydrodynamic features on the tidally-influenced NWES and in the semi-enclosed Baltic Sea. Differences in the results of two unstructured grid realizations are identified and overall consistent model behaviour is established across the two model configurations. The successful implementation of the unstructured grid model for the NWES

allows the application of the modelling framework in coupled physical-biogeochemical modelling of the shelf carbon cycle. The presented validation results can further serve as a reference case for future adaptations of the modelling framework.

One of the key areas for improvement in the presented physical modelling approach is the vertical discretization. The applied LSC² grid is an efficient tool in cross-scale modelling, but also requires time-consuming application-dependent optimization. The design of the LSC² grid applied in this study is particularly challenging, as it needs to accommodate for the specific requirements introduced by the shallow NWES, its steep continental slope as well as the deep Baltic Sea with its complex thermohaline vertical structure. We find reduced model performance at the steep continental slope of the NWES, particularly along the shelf break of the Armorican and Celtic Sea, that also differs between the two assessed model configurations. Pressure gradient errors excited at the steep continental slope likely contribute to the identified local reduction in model performance and are likely exacerbated by coarser horizontal model resolution. Pressure gradient errors at the extreme bathymetry of the shelf break of the NWES are common across modelling approaches and drive on-shelf inaccuracy in tracer fields and the tidal simulation on the shelf, but can potentially be effectively controlled by a further sophistication of vertical grid design (Wise et al., 2022).

A future application of the model framework in the Baltic Sea requires further optimization of the model configuration, especially of the horizontal grid in the Danish straits area. This study only provides an initial evaluation of the simulated surface fields in the Baltic Sea, and future work would need to address the accurate simulation of two-layer exchange across the Danish straits and the complex thermohaline structure in the Baltic Sea. It is however to be noted that previous SCHISM model implementations demonstrated good model performance in the Baltic Sea and were able to reproduce realistic inter-basin exchange (Zhang et al., 2016a; Stanev et al., 2018). Realistic simulations of the Baltic Sea further require the inclusion of sea ice. The coupling to a sea ice module has been technically implemented for the presented model framework, but still requires extensive validation and was therefore neglected in this study.

The results of the two model grid configurations presented in this study demonstrate reasonable consistency across large parts of the NWES, which underlines the high flexibility and configurability of the model framework. Differences between the model configurations particularly occur in numerically challenging regions like the steep continental slope, the Baltic Sea or the Norwegian Trench, where identified differences between the model configurations primarily relate to differences in horizontal grid resolution and thus the simulation of shelf physics. In the Norwegian Trench, validation of sea surface salinity indicates a better representation of locally relevant mesoscale processes and associated lateral mixing (Ikeda et al., 1989) in the high resolution NWES-IT configuration. Differences identified at the steep continental slope along the Celtic Sea and Armorican shelf in the south of the NWES may be related to differences in the discretization of the continental slope due to the differing horizontal resolutions and could thus potentially be alleviated by a configuration-dependent optimization of the vertical grid. Identified differences in the Baltic Sea and horizontal transport in the Norwegian Trench are however concerning. A resolution or time-step dependence in the model performance in these regions should be evaluated in future work. This study consequently demonstrates the necessity of an independent validation of unstructured model grid realizations, even for model configurations derived from equivalent baseline datasets, and highlights the challenges for the intercomparison of model results across grid configurations with differing resolution.

The successful development of the modelling framework ultimately enables pursuing two separate avenues in the model-based investigation of the role of shelf-specific physical and biogeochemical processes in the ocean carbon cycle. The effective local refinement of the horizontal grid applied in the NWES-IT configuration allows the realization of kilometrical-scale horizontal resolution in computationally demanding coupled physical-biogeochemical simulations of the NWES. The high horizontal resolution for the first time allows a model-based investigation of the role of kilometrical-scale shelf processes such as internal tides for the shelf carbon cycle. The numerically efficient design of the NWES-LR configuration in turn maintains the accurate representation of key hydrodynamic features on the NWES at reasonable computational cost. The cost-efficient NWES-LR configuration therefore facilitates a sophistication of applied ecosystem and carbonate system models. In combination, both research avenues provide a promising platform to deepen our understanding of the ocean carbon cycle.

Author Contributions

JK initiated the study, set up the numerical model, generated the data sets, performed the data analysis and wrote the manuscript. MM, UD, YZ and CS provided essential background knowledge. CS and MM advised the study.

Funding

The research was funded by the Deutsche Forschungsgemeinschaft (DFG, German Research Foundation) under Germany's Excellence Strategy – EXC 2037 ‘CLICCS - Climate, Climatic Change, and Society’ – Project Number: 390683824.

Acknowledgements

This study has been conducted using E.U. Copernicus Marine Service Information; <https://doi.org/10.48670/moi-00169>; <http://dx.doi.org/10.17183/REFMAR>. The manuscript contains data supplied by the Natural Environmental Research Council (NERC). The tidal validation and analysis in this manuscript used tools and open data sets made publicly available under a CECILL license at https://github.com/KarenGuihou/tidal_analysis. EN.4.2.2 data used in this study were obtained from <https://www.metoffice.gov.uk/hadobs/en4/> and are © British Crown Copyright, Met Office, 2013, provided under a Non-Commercial Government Licence <http://www.nationalarchives.gov.uk/doc/non-commercial-government-licence/version/2/>.

REFERENCES

- Blumberg, A. F., and Mellor, G. L. (1987). “A description of a three-dimensional coastal ocean circulation model,” in *Three-Dimensional Coastal Ocean Models*, ed. N. S. Heaps (Washington, D. C. American Geophysical Union), 1–16.
- Boyer, T. P., García, H. E., Locarnini, R. A., Zweng, M. M., Mishonov, A. V., Reagan, J. R., et al. (2018). World Ocean Atlas 2018. Dataset. Accessed July 29, 2022, <https://www.ncei.noaa.gov/archive/accession/NCEI-WOA18>
- Bricheno, L. M., Wolf, J. M., and Brown, J. M. (2014). Impacts of high resolution model downscaling in coastal regions. *Continental Shelf Research* 87, 7–16. doi: 10.1016/j.csr.2013.11.007
- Caldwell, P. C., Merrifield, M. A., and Thompson, P. R. (2015). Sea level measured by tide gauges from global oceans — the Joint Archive for Sea Level holdings (NCEI Accession 0019568): Version 5.5. Dataset. Accessed August 02, 2022. doi: 10.7289/V5V40S7W
- Chen, C., Huang, H., Beardsley, R. C., Liu, H., Xu, Q., and Cowles, G. (2007). A finite volume numerical approach for coastal ocean circulation studies: Comparisons with finite difference models. *J. Geophys. Res. Oceans* 112. doi: 10.1029/2006JC003485
- Codiga, D. (2011). *Unified Tidal Analysis and Prediction Using the UTide Matlab Functions: Technical Report 2011-01*. Accessed August 02, 2022, <ftp://www.po.gso.uri.edu/pub/downloads/codiga/pubs/2011Codiga-UTide-Report.pdf>
- Daewel, U., and Schrum, C. (2013). Simulating long-term dynamics of the coupled North Sea and Baltic Sea ecosystem with ECOSMO II: Model description and validation. *Journal of Marine Systems* 119-120, 30–49. doi: 10.1016/j.jmarsys.2013.03.008
- Danilov, S. (2013). Ocean modeling on unstructured meshes. *Ocean Modelling* 69, 195–210. doi: 10.1016/j.ocemod.2013.05.005
- Danilov, S., and Wang, Q. (2015). Resolving eddies by local mesh refinement. *Ocean Modelling* 93, 75–83. doi: 10.1016/j.ocemod.2015.07.006
- Dukhovskoy, D. S., Morey, S. L., Martin, P. J., O’Brien, J. J., and Cooper, C. (2009). Application of a vanishing, quasi-sigma, vertical coordinate for simulation of high-speed, deep currents over the Sigsbee Escarpment in the Gulf of Mexico. *Ocean Modelling* 28, 250–265. doi: 10.1016/j.ocemod.2009.02.009
- Fernand, L., Nolan, G. D., Raine, R., Chambers, C. E., Dye, S. R., White, M., et al. (2006). The Irish coastal current: A seasonal jet-like circulation. *Continental Shelf Research* 26, 1775–1793. doi: 10.1016/j.csr.2006.05.010
- Fofonoff, N. P., and Millard, R. C. (1983). *Algorithms for the computation of fundamental properties of seawater*. Unesco.
- Geyer, B. (2017). coastDat-3_COSMO-CLM_ERAi. World Data Center for Climate (WDCC) at DKRZ, http://cera-www.dkrz.de/WDCC/ui/Compact.jsp?acronym=coastDat-3_COSMO-CLM_ERAi
- Good, S., Fiedler, E., Mao, C., Martin, M. J., Maycock, A., Reid, R., et al. (2020). The Current Configuration of the OSTIA System for Operational Production of Foundation Sea Surface Temperature and Ice Concentration Analyses. *Remote Sensing* 12, 720. doi: 10.3390/rs12040720
- Good, S. A., Martin, M. J., and Rayner, N. A. (2013). EN4: Quality controlled ocean temperature and salinity profiles and monthly objective analyses with uncertainty estimates. *J. Geophys. Res. Oceans* 118, 6704–6716. doi: 10.1002/2013JC009067

- Graham, J. A., Rosser, J. P., O'Dea, E., and Hewitt, H. T. (2018). Resolving Shelf Break Exchange Around the European Northwest Shelf. *Geophys. Res. Lett.* 45. doi: 10.1029/2018GL079399
- Guihou, K., Polton, J., Harle, J., Wakelin, S., O'Dea, E., and Holt, J. (2018). Kilometric Scale Modeling of the North West European Shelf Seas: Exploring the Spatial and Temporal Variability of Internal Tides. *J. Geophys. Res. Oceans* 123, 688–707. doi: 10.1002/2017JC012960
- Holt, J., Hyder, P., Ashworth, M., Harle, J., Hewitt, H. T., Liu, H., et al. (2017). Prospects for improving the representation of coastal and shelf seas in global ocean models. *Geoscientific Model Development* 10, 499–523. doi: 10.5194/gmd-10-499-2017
- Holt, J., and Proctor, R. (2008). The seasonal circulation and volume transport on the northwest European continental shelf: A fine-resolution model study. *J. Geophys. Res. Oceans* 113. doi: 10.1029/2006JC004034
- Huthnance, J., Hopkins, J., Berx, B., Dale, A., Holt, J., Hosegood, P., et al. (2022). Ocean shelf exchange, NW European shelf seas: Measurements, estimates and comparisons. *Progress in Oceanography* 202, 102760. doi: 10.1016/j.pocean.2022.102760
- Ikeda, M., Johannessen, J. A., Lygre, K., and Sandven, S. (1989). A Process Study of Mesoscale Meanders and Eddies in the Norwegian Coastal Current. *J. Phys. Oceanogr.* 19, 20–35. doi: 10.1175/1520-0485(1989)019<0020:APSOMM>2.0.CO;2
- Kantha, L. H., and Clayson, C. A. (1994). An improved mixed layer model for geophysical applications. *J. Geophys. Res. Oceans* 99, 25235–25266. doi: 10.1029/94JC02257
- Knight, P. J., and Howarth, M. J. (1999). The flow through the north channel of the Irish Sea. *Continental Shelf Research* 19, 693–716. doi: 10.1016/S0278-4343(98)00110-1
- Lyard, F. H., Allain, D. J., Cancet, M., Carrère, L., and Picot, N. (2021). FES2014 global ocean tide atlas: design and performance. *Ocean Science* 17, 615–649. doi: 10.5194/os-17-615-2021
- Marsh, R., Haigh, I. D., Cunningham, S. A., Inall, M. E., Porter, M., and Moat, B. I. (2017). Large-scale forcing of the European Slope Current and associated inflows to the North Sea. *Ocean Science* 13, 315–335. doi: 10.5194/os-13-315-2017
- New, A. L., and Pingree, R. D. (1990). Evidence for internal tidal mixing near the shelf break in the Bay of Biscay. *Deep Sea Research Part A. Oceanographic Research Papers* 37, 1783–1803. doi: 10.1016/0198-0149(90)90078-A
- Otto, L., Zimmerman, J., Furnes, G. K., Mork, M., Saetre, R., and Becker, G. (1990). Review of the physical oceanography of the North Sea. *Netherlands Journal of Sea Research* 26, 161–238. doi: 10.1016/0077-7579(90)90091-T
- Pingree, R. D., Mardell, G. T., Holligan, P. M., Griffiths, D. K., and Smithers, J. (1982). Celtic Sea and Armorican current structure and the vertical distributions of temperature and chlorophyll. *Continental Shelf Research* 1, 99–116. doi: 10.1016/0278-4343(82)90033-4
- Polton, J. A. (2015). Tidally induced mean flow over bathymetric features: a contemporary challenge for high-resolution wide-area models. *Geophysical & Astrophysical Fluid Dynamics* 109, 207–215. doi: 10.1080/03091929.2014.952726
- Reissmann, J. H., Burchard, H., Feistel, R., Hagen, E., Lass, H. U., Mohrholz, V., et al. (2009). Vertical mixing in the Baltic Sea and consequences for eutrophication – A review. *Progress in Oceanography* 82, 47–80. doi: 10.1016/j.pocean.2007.10.004
- Samuelson, A., Schrum, C., Yumruktepe, V. Ç., Daewel, U., and Roberts, E. M. (2022). Environmental Change at Deep-Sea Sponge Habitats Over the Last Half Century: A Model

- Hindcast Study for the Age of Anthropogenic Climate Change. *Frontiers in Marine Science* 9. doi: 10.3389/fmars.2022.737164
- Sandvik, A. D., Skagseth, Ø., and Skogen, M. D. (2016). Model validation: Issues regarding comparisons of point measurements and high-resolution modeling results. *Ocean Modelling* 106, 68–73. doi: 10.1016/j.ocemod.2016.09.007
- Simpson, J. H. (1998). “The Celtic Seas coastal segment,” in *The Sea, Volume 11: The Global Coastal Ocean – Regional Studies and Syntheses* (New York: John Wiley & Sons Ltd), 659–695.
- Stanev, E. V., Pein, J., Grashorn, S., Zhang, Y., and Schrum, C. (2018). Dynamics of the Baltic Sea straits via numerical simulation of exchange flows. *Ocean Modelling* 131, 40–58. doi: 10.1016/j.ocemod.2018.08.009
- Thomas, H., Bozec, Y., Baar, H. J. W. de, Elkalay, K., Frankignoulle, M., Schiettecatte, L.-S., et al. (2005). The carbon budget of the North Sea. *Biogeosciences* 2, 87–96. doi: 10.5194/bg-2-87-2005
- Umlauf, L., and Burchard, H. (2003). A generic length-scale equation for geophysical turbulence models. *Journal of Marine Research* 61, 235–265. doi: 10.1357/002224003322005087
- Wessel, P., and Smith, W. H. F. (1996). A global, self-consistent, hierarchical, high-resolution shoreline database. *J. Geophys. Res.* 101, 8741–8743. doi: 10.1029/96JB00104
- Winther, N. G., and Johannessen, J. A. (2006). North Sea circulation: Atlantic inflow and its destination. *J. Geophys. Res.* 111. doi: 10.1029/2005JC003310
- Wise, A., Harle, J., Bruciaferri, D., O’Dea, E., and Polton, J. (2022). The effect of vertical coordinates on the accuracy of a shelf sea model. *Ocean Modelling* 170, 101935. doi: 10.1016/j.ocemod.2021.101935
- Ye, F., Zhang, Y. J., He, R., Wang, Z., Wang, H. V., and Du, J. (2019). Third-order WENO transport scheme for simulating the baroclinic eddying ocean on an unstructured grid. *Ocean Modelling* 143, 101466. doi: 10.1016/j.ocemod.2019.101466
- Ye, F., Zhang, Y. J., Yu, H., Sun, W., Moghimi, S., Myers, E., et al. (2020). Simulating storm surge and compound flooding events with a creek-to-ocean model: Importance of baroclinic effects. *Ocean Modelling* 145, 101526. doi: 10.1016/j.ocemod.2019.101526
- Zeng, X., Zhao, M., and Dickinson, R. E. (1998). Intercomparison of Bulk Aerodynamic Algorithms for the Computation of Sea Surface Fluxes Using TOGA COARE and TAO Data. *J. Climate* 11, 2628–2644. doi: 10.1175/1520-0442(1998)011%3C2628:IOBAAF%3E2.0.CO;2
- Zhang, Y., and Baptista, A. M. (2008). SELFE: A semi-implicit Eulerian–Lagrangian finite-element model for cross-scale ocean circulation. *Ocean Modelling* 21, 71–96. doi: 10.1016/j.ocemod.2007.11.005
- Zhang, Y. J., Ateljevich, E., Yu, H.-C., Wu, C. H., and Yu, J. C. (2015). A new vertical coordinate system for a 3D unstructured-grid model. *Ocean Modelling* 85, 16–31. doi: 10.1016/j.ocemod.2014.10.003
- Zhang, Y. J., Stanev, E. V., and Grashorn, S. (2016a). Unstructured-grid model for the North Sea and Baltic Sea: Validation against observations. *Ocean Modelling* 97, 91–108. doi: 10.1016/j.ocemod.2015.11.009
- Zhang, Y. J., Ye, F., Stanev, E. V., and Grashorn, S. (2016b). Seamless cross-scale modeling with SCHISM. *Ocean Modelling* 102, 64–81. doi: 10.1016/j.ocemod.2016.05.002
- Zhao, C., Daewel, U., and Schrum, C. (2019). Tidal impacts on primary production in the North Sea. *Earth System Dynamics* 10, 287–317. doi: 10.5194/esd-10-287-2019

Appendix B - Barotropic and baroclinic tides increase primary production on the Northwest European Shelf

This appendix contains a paper, which has been published in *Frontiers in Marine Science – Marine Biogeochemistry* as:

Kossack, J., Mathis, M., Daewel, U., Zhang, Y. J., Schrum, C. (2023). Barotropic and baroclinic tides increase primary production on the Northwest European Shelf. *Frontiers in Marine Science* 10:1206062. <https://doi.org/10.3389/fmars.2023.1206062>

The contribution of Jan Felix Gottlieb Kossack (JK) and others to this paper is as follows:

JK generated the data set, performed the data analysis, and wrote the manuscript. MM, YZ and CS provided essential background knowledge. CS and MM advised the study. CS initiated the idea of the study. All authors contributed to conception and design of the study and manuscript revision, and read and approved the submitted version.



OPEN ACCESS

EDITED BY

Koji Suzuki,
Hokkaido University, Japan

REVIEWED BY

Lei Lin,
Shandong University of Science and
Technology, China
Urmaz Lips,
Tallinn University of Technology, Estonia

*CORRESPONDENCE

Jan Kossack
✉ jan.kossack@hereon.de

RECEIVED 14 April 2023

ACCEPTED 19 June 2023

PUBLISHED 10 July 2023

CITATION

Kossack J, Mathis M, Daewel U, Zhang YJ
and Schrum C (2023) Barotropic and
baroclinic tides increase primary
production on the Northwest
European Shelf.
Front. Mar. Sci. 10:1206062.
doi: 10.3389/fmars.2023.1206062

COPYRIGHT

© 2023 Kossack, Mathis, Daewel, Zhang and
Schrum. This is an open-access article
distributed under the terms of the [Creative
Commons Attribution License \(CC BY\)](https://creativecommons.org/licenses/by/4.0/). The
use, distribution or reproduction in other
forums is permitted, provided the original
author(s) and the copyright owner(s) are
credited and that the original publication in
this journal is cited, in accordance with
accepted academic practice. No use,
distribution or reproduction is permitted
which does not comply with these terms.

Barotropic and baroclinic tides increase primary production on the Northwest European Shelf

Jan Kossack^{1*}, Moritz Mathis¹, Ute Daewel¹,
Yinglong Joseph Zhang² and Corinna Schrum³

¹Institute of Coastal Systems, Helmholtz-Zentrum Hereon, Geesthacht, Germany, ²Center for Coastal Resource Management, Virginia Institute of Marine Science, College of William & Mary, Gloucester Point, VA, United States, ³Institute of Oceanography, University of Hamburg, Hamburg, Germany

High biological productivity and the efficient export of carbon-enriched subsurface waters to the open ocean via the continental shelf pump mechanism make mid-latitude continental shelves like the northwest European shelf (NWES) significant sinks for atmospheric CO₂. Tidal forcing, as one of the regionally dominant physical forcing mechanisms, regulates the mixing-stratification status of the water column that acts as a major control for biological productivity on the NWES. Because of the complexity of the shelf system and the spatial heterogeneity of tidal impacts, there still are large knowledge gaps on the role of tides for the magnitude and variability of biological carbon fixation on the NWES. In our study, we utilize the flexible cross-scale modeling capabilities of the novel coupled hydrodynamic–biogeochemical modeling system SCHISM–ECOSMO to quantify the tidal impacts on primary production on the NWES. We assess the impact of both the barotropic tide and the kilometrical-scale internal tide field explicitly resolved in this study by comparing simulated hindcasts with and without tidal forcing. Our results suggest that tidal forcing increases biological productivity on the NWES and that around 16% (14.47 Mt C) of annual mean primary production on the shelf is related to tidal forcing. Vertical mixing of nutrients by the barotropic tide particularly invigorates primary production in tidal frontal regions, whereas resuspension and mixing of particulate organic matter by tides locally hinders primary production in shallow permanently mixed regions. The tidal impact on primary production is generally low in deep central and outer shelf areas except for the southwestern Celtic Sea, where tidal forcing substantially increases annual mean primary production by 25% (1.53 Mt C). Tide-generated vertical mixing of nutrients across the pycnocline, largely attributed to the internal tide field, explains one-fifth of the tidal response of summer NPP in the southwestern Celtic Sea. Our results therefore suggest that the tidal NPP response in the southwestern Celtic Sea is caused by a combination of processes likely including tide-induced lateral on-shelf transport of nutrients. The tidally enhanced turbulent mixing of nutrients fuels new production in the seasonally stratified parts of the NWES, which may impact the air–sea CO₂ exchange on the shelf.

KEYWORDS

NW Europe, tides, internal tides, vertical mixing, primary production, Celtic Sea, Malin-Hebrides shelf, 3D coupled hydrodynamic-biogeochemical modeling

1 Introduction

Continental shelves play an important role in the global carbon cycle. High biological productivity and the efficient export of carbon-enriched waters to the open ocean via the continental shelf pump mechanism (Tsunogai et al., 1999; Thomas et al., 2004) on middle- and high-latitude continental shelves are understood to contribute to globally significant oceanic uptake of atmospheric CO₂ (Frankignoulle and Borges, 2001; Laruelle et al., 2014; Legge et al., 2020). Both the physical and biological components of the continental shelf pump mechanism rely on seasonal stratification and processes specific to the respective shelf environments. Given the complexity of the dynamic shelf systems, there still are considerable knowledge gaps on the role of shelf-specific physical and biogeochemical processes for the magnitude and variability of carbon sequestration on continental shelves.

On the northwest European shelf (NWES; Figure 1A), the biological component of the continental shelf pump mechanism is suggested to be critical for observed carbon sequestration (Legge et al., 2020). Tidal forcing, as one of the regionally dominant physical forcing mechanisms, regulates the mixing-stratification status of the water column that acts as a major control for biological productivity in the shelf system. During seasonal stratification, tidal forcing structures the NWES into shallow permanently mixed regions, transitional regions with tidal fronts and weak stratification and deep stably stratified regions (Simpson and Hunter, 1974). Each of these tide-induced subsystems feature distinct primary production dynamics (van Leeuwen et al., 2015), in which tidal forcing impacts net primary production (NPP), both positively and negatively, by enhanced vertical mixing of nutrients, biomass, and suspended matter and by causing sediment resuspension (Zhao et al., 2019).

In tidally dominated shelf seas, tides produce turbulence due to friction of tidal currents with the sea bed (Simpson and Hunter, 1974; Rippeth, 2005). This tidally generated turbulence vertically mixes the bottom layer of a stratified shelf system, whereas wind

stress and breaking surface waves turbulently mix the surface layer. Bottom-driven tidal mixing is well reproduced by state-of-the-art numerical ocean models (Burchard et al., 2002). Its impact on water column stratification and vertical fluxes is strong in shallow shelf areas where the bottom and surface mixed layers can directly interact. Bottom-driven tidal mixing increases primary production by replenishing nutrients in the surface mixed layer (Hu et al., 2008; Sharples, 2008) but also decreases productivity by degrading light conditions through upward mixing of resuspended sediments (Porter et al., 2010; Capuzzo et al., 2013; Capuzzo et al., 2018) and by promoting dilution that hinders phytoplankton growth (Cloern, 1991). Numerous studies have established local effects of bottom-driven vertical mixing by tides on primary production on the NWES and regionally differing responses to tidal forcing (e.g., Cloern, 1991; Richardson et al., 2000; Sharples, 2008). In their comprehensive modeling study that accounted for tide-modulated benthic–pelagic coupling and lower trophic-level dynamics, Zhao et al. (2019) found a considerable, but spatially heterogeneous, tidal response of primary production in the North Sea. To date, there however is no comparable study that quantifies the tidal response of primary production for the entire NWES while accounting for the spatial heterogeneity of the shelf system.

In addition to bottom-driven vertical mixing, tides can also generate vertical mixing in stratified shelf regions by causing intermittent shear instabilities within the pycnocline (Rippeth, 2005). Tide-related shear instabilities in the pycnocline can be caused by breaking internal tides (Whalen et al., 2020), the interaction of wind-induced inertial oscillations with internal tides (van Haren et al., 1999; Hopkins et al., 2014), or the barotropic tide itself (Becherer et al., 2022). Such pycnocline mixing is crucial for the supply of nutrients for biological productivity in the subsurface biomass maximum (SBM) at the base of the pycnocline (Cullen, 2015). It is suggested that primary production in the SBM is predominantly new production (Hickman et al., 2012), i.e., sustained by allochthonous nutrient sources, and accounts for up to 50% of annual carbon fixation on the NWES

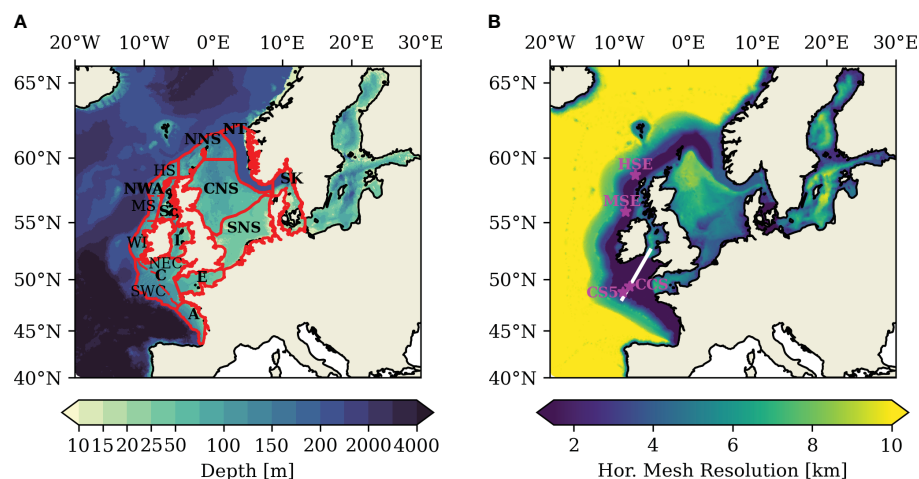


FIGURE 1

(A) Bathymetry in the model domain; red lines delineate subareas. (B) Horizontal model resolution of the unstructured triangular grid of the NWES-IT configuration. Magenta stars in (B) indicate positions of stations used for validation and analysis. White line in (B) indicates transect used in Sect. 3.3.

(Richardson et al., 2000; Rippeth et al., 2009; Hickman et al., 2012). This makes pycnocline mixing a potentially important component of the continental shelf sea pump on the NWES (Rippeth et al., 2014).

Baroclinic tides, also termed internal tides, are generated by a transfer of energy from the barotropic tide to the baroclinic tide through interaction of stratified flow with extreme topography like the shelf break (Baines, 1982). The NWES is a hotspot of internal tide generation, and particularly high tidal energy conversion has been reported for the steep Celtic Sea shelf break (Baines, 1982; Vlasenko et al., 2014). Observational studies have shown intensified pycnocline mixing associated with the internal tide at the shelf break of the NWES (New and Pingree, 1990; Rippeth and Inall, 2002). Low-mode internal tides propagate coherently for hundreds of kilometers across the Celtic Sea (Pingree and New, 1995; Green et al., 2008) and generate shear instabilities in the pycnocline when dissipating. Mixing by internal tides was shown to impact nutrient fluxes and biological productivity in the Celtic Sea (Pingree and Mardell, 1981; Sharples et al., 2007; Sharples et al., 2009; Tweddle et al., 2013). Sparse observations and the high spatial variability and episodic nature of mixing by internal tides however impede a comprehensive analysis and quantification of the role of internal tides for biological carbon fixation on the shelf.

Model-based studies on the other hand face the problem that the reproduction of realistic levels of pycnocline mixing in state-of-the-art numerical ocean models is a difficult task. Commonly implemented turbulence closures only crudely account for the contribution of high-frequency internal waves (Simpson et al., 1996; Burchard et al., 2002; Rippeth, 2005). Recent advances in high-resolution regional ocean modeling have however demonstrated the reproduction of the kilometrical-scale internal tide field on the NWES (Guihou et al., 2018). Graham et al. (2018a) further suggest that increased pycnocline mixing in a kilometrical-scale model configuration improved a bias in the representation of sea surface temperature at the shelf break of the NWES present in a coarser model configuration. Until now, no study has however addressed the implications of the improved representation of the internal tide field for primary production on the shelf.

In this paper, we present a novel coupled physical–biogeochemical regional model framework with kilometrical-scale horizontal resolution for the NWES. The model employs a flexible unstructured horizontal grid that explicitly resolves the low-mode internal tide field generated by the regionally dominant M2 tide in the Celtic Sea and shelf areas along the shelf break. The flexible horizontal grid facilitates coupled physical–biogeochemical simulations at reasonable computational cost and thus enables multiyear model integrations of the entire NWES and adjacent regions in the northeastern Atlantic. We apply the model to for the first time quantify tidal impacts on primary production on the entire NWES and provide a first estimate for the role of internal tides for biological carbon fixation along the shelf break of the NWES. We present the details of the applied model configurations and assess overall model performance in Section 2. In Section 3, we investigate the tidal

impacts on primary production and disentangle the contribution of barotropic and baroclinic tides to vertical mixing of nutrients.

2 Materials and methods

2.1 Regional ocean circulation model SCHISM

The open-source community-supported 3D physical modeling system SCHISM (Zhang et al., 2016b) is used in this study. SCHISM is a derivative product built from the original SELFE (Zhang and Baptista, 2008) and distributed with an open-source Apache v2 license. SCHISM is a numerically efficient and robust modeling system designed for the effective cross-scale simulation of 3D baroclinic ocean circulation. SCHISM has been used in multiple studies that span from shallow coastal areas to the deep open ocean (Yu et al., 2017; Ye et al., 2020; Wang Z. et al., 2022), as well as in a study of up/downwelling in shelf break canyons (Wang H. et al., 2022).

SCHISM is based on a customizable triangular–quadrangular unstructured horizontal grid. Flexible local refinement of the unstructured grid allows telescoping high horizontal resolution in areas of specific interest, and vice versa a low resolution in other parts of the domain. This feature facilitates high-resolution coupled ocean-ecosystem simulations at reasonable computational costs. The vertical coordinate is discretized with flexible hybrid Localized Sigma Coordinates with Shaved Cells (LSC²; Zhang et al., 2015). The LSC² vertical coordinate effectively reduces the pressure gradient force error (Zhang et al., 2016b). The LSC² vertical coordinate further enables the accurate representation of bathymetry without requiring bathymetry smoothing, which improves model accuracy at steep bathymetric slopes and sites of complex 3D bathymetry (Yu et al., 2017; Ye et al., 2018).

SCHISM solves the Reynolds-averaged Navier–Stokes equations in hydrostatic and Boussinesq approximated form with a semi-implicit finite-element/finite-volume method and an Eulerian–Lagrangian method (ELM) for momentum advection. The transport equations are solved with a robust third-order Weighted Essentially Non-Oscillatory (WENO) solver in the horizontal and an implicit Total Variation Diminishing (TVD) scheme in the vertical dimension. The advanced transport schemes are crucial for the simulation of baroclinic circulation and mesoscale dynamics in cross-scale applications (Ye et al., 2019). Density is calculated with the non-linear International Equation of State for Seawater (Fofonoff and Millard, 1983). Exchange with the atmosphere is computed with a bulk aerodynamic model (Zeng et al., 1998). Bottom drag is parameterized with the log law drag formula by Blumberg and Mellor (1987) and the use of a constant bottom roughness of 0.5 mm in this study. More detailed descriptions of the SCHISM model are given in Zhang et al. (2016a) and Zhang et al. (2016b).

Turbulence in form of eddy viscosities and eddy diffusivities is computed in SCHISM using the Generic Length-Scale formulation (GLS; Umlauf and Burchard, 2003). The specific parameterization

of the GLS turbulence closure is set according to the k - kl model with KC94 stability functions (Kantha and Clayson, 1994). In this parameterization, the critical gradient Richardson number is $Ri_C = 0.25$, in accordance with linear stability theory. The background diffusivity is set to $10^{-6} \text{ m}^2\text{s}^{-1}$. The maximum cutoff eddy diffusivity is set to $1 \text{ m}^2\text{s}^{-1}$.

SCHISM further adds bi-harmonic viscosity to the horizontal momentum equation to effectively remove spurious modes (Zhang et al., 2016b). The domain simulated in this study covers the deep ocean (e.g., eddy regime) and steep bathymetry at the shelf break that particularly exacerbates spurious modes (Yu et al., 2017; Ye et al., 2020). SCHISM augments the dissipation for such conditions by an additional Laplacian viscosity in the form of a spatially variable Shapiro filter (Zhang et al., 2016b; Ye et al., 2020). The local strength of the Shapiro filter is derived as a function of the local bathymetric slope α given by $\gamma = 0.5 \tanh(2\alpha/\alpha_0)$ with a reference slope of $\alpha_0 = 0.5$.

2.2 Ecosystem model ECOSMO

SCHISM is coupled to the biogeochemical model ECOSMO II (Daewel and Schrum, 2013) via the FABM framework (Bruggeman and Bolding, 2014). ECOSMO II is a further developed version of the ecosystem model ECOSMO first introduced for the North Sea (Schrum et al., 2006). ECOSMO II uses a nutrient-phytoplankton-zooplankton-detritus (NPZD) conceptual model approach, and its extended formulation allows the simulation of lower trophic-level dynamics in a wide range of ecosystems (Daewel and Schrum, 2013; Pein et al., 2021; Yumruktepe et al., 2022).

ECOSMO II solves prognostic equations for a total number of 16 state variables. It simulates three separate nutrient cycles for nitrogen, phosphorous, and silicate. Oxygen is solved as an additional tracer. Primary production in ECOSMO II is divided into three phytoplankton functional groups (diatoms, flagellates, and cyanobacteria) and is limited by either nutrients or light. ECOSMO further includes two zooplankton functional groups (herbivorous and omnivorous) and three functional groups for detritus (particulate organic matter, dissolved organic matter, biogenic opal). Benthic-pelagic coupling is considered, as described in Daewel and Schrum (2013). The model considers three different integrated surface sediment pools for each of the three nutrient cycles, one for opal, one for particular organic material consisting of N and C at a Redfield ratio, and one for iron-bound phosphorous. Sediment processes include sediment nutrient release as well as sinking, deposition, and resuspension of POM depending on a critical bottom shear stress.

Light attenuation in ECOSMO II includes phytoplankton self-shading as well as shading by particulate organic matter (POM) and dissolved organic matter (DOM), as proposed by Nissen (2014) and implemented in Zhao et al. (2019). With this dynamical coupling of turbidity to the seasonal primary production cycle, the model explicitly resolves the competing major bottom-up tidal processes controlling primary production, namely, the reduction of light availability by resuspension and mixing of organic matter into the euphotic zone and the supply of nutrients by tidal mixing.

A detailed description of the ecosystem model as well as a validation against observations are given in Daewel and Schrum (2013). The parameter set used in this study is documented in the Supplementary Material (Table S1).

2.3 Model configurations and experiments

The unstructured horizontal grid for the North-West European Shelf-Internal Tide (NWES-IT) model configuration used in this study was constructed with the Surface-water Modeling System software (SMS; Aquaveo, 2019). The NWES-IT domain spans 40°N – 66°N and 20°W – 30°E and thus covers the entire NWES and a part of the northeast Atlantic (see Figure 1). The Baltic Sea is included to adequately resolve basin-exchange processes but is not particularly attended to in this study as it does not feature relevant tidal energy. Sea ice, which usually develops seasonally in the Baltic Sea, is neglected for this study.

SCHISM's cross-scale capabilities are used to achieve telescoping high horizontal resolution in regions affected by internal tide generation at the shelf break and at other extreme bathymetric slopes. The high horizontal resolution of 1.5 km is realized throughout the Celtic Sea and Armorican Shelves and in a 75-km-wide band delimited in an off-shelf direction by the 200-m isobath. The on-shelf extent of 75 km was chosen against the backdrop that most internal tide energy is dissipated within tens of kilometers of their generation site (Pingree et al., 1986; Inall et al., 2011). The horizontal resolution of 1.5 km resolves internal tides with wave lengths of 12–25 km generated by the regionally dominant M2 tide (Guihou et al., 2018). In order to accommodate numerical constraints on model accuracy, the horizontal resolution in the rest of the model domain is determined relative to local water depth and the model time step of 100 s used in this study. This yields a horizontal resolution that smoothly varies from a minimum of ~ 2.5 km in the shallow coastal zones, or even 500 m at finely resolved areas like the Danish Straits, to a maximum resolution of ~ 10 km in the deepest parts of the shelf (see Figure 1B). At the shelf break, defined as the 200-m isobath, horizontal grid size smoothly transitions from 1.5 km to a quasi-uniform horizontal resolution of 10 km in the open Atlantic. The NWES-IT horizontal grid comprises a total number of $\sim 386\text{k}$ grid nodes and $\sim 758\text{k}$ triangular grid elements. A model configuration with a uniform horizontal resolution of 1.5 km would require approximately 2.3 million grid nodes. The coupled SCHISM-ECOSMO NWES-IT configuration runs ~ 170 times faster than real time with 36 CPUs on the Levante HPC-System at the German Climate Computing Center (DKRZ; <https://www.dkrz.de>, last accessed March 2023).

The coastline for the unstructured horizontal grid was derived from the GSHHS shoreline database at 5-km resolution (Wessel and Smith, 1996). The bathymetry for the domain was interpolated from the EMODnet Digital Bathymetry Digital Terrain Model (version 2018) dataset derived from the EMODnet Bathymetry portal (<http://www.emodnet-bathymetry.eu>; accessed 04/2020). The bathymetry in the model domain is documented in Figure 1A. The minimum water depth in the domain was set to 10 m to reduce

computational demand. The bathymetry was modified at deep fjords along the Norwegian coast to simplify the horizontal and vertical gridding processes. No other bathymetry smoothing was applied.

The LSC² vertical grid designed for the NWES-IT model configuration realizes a high vertical resolution of 2.5–6 m from the surface to ~60-m depth in order to highly resolve the regional thermocline. The number of layers in the vertical grid varies from three layers for the minimum depth of 10 m to 53 layers for water depths larger than 6,000 m.

Model forcing for temperature and salinity, and ECOSMO state variables nitrate, phosphate, silicate, and oxygen, is provided from WOA2018 climatological data (Boyer et al., 2018). Open boundary conditions for the remaining ECOSMO state variables are taken from a HYCOM–ECOSMO hindcast simulation of the North Atlantic (Samuelson et al., 2022). Dynamic oceanic forcing is provided twofold. Subtidal SSH and horizontal velocities are provided using daily averages from Samuelson et al. (2022). The harmonic tidal signal is added to both SSH and the horizontal velocities from the FES2014 product (Lyard et al., 2021) for 15 tidal constituents (Q1, O1, P1, S1, K1, 2N2, MU2, N2, NU2, M2, L2, T2, S2, K2, M4). Corrections for multiyear tidal cycles like the lunar nodal and lunar perigee tide are applied. Tidal potential is applied for the partial tides in the model domain; the effects of self-attraction and loading are neglected. We provide daily river forcing in form of river discharge and nutrient loads for the 172 largest rivers in the domain. River discharge and nitrate, ammonium, phosphate, and silicate loads represent daily mean climatological values computed for the period 1986–2015 from a regional river dataset compiled and used by Daewel and Schrum (2013) and further updated as described by Zhao et al. (2019). We assume ambient temperatures for river discharge. At the sea surface, boundary conditions are provided from a hindcast simulation with the regional atmospheric model COSMO-CLM version 5 with 0.11° horizontal resolution (Geyer, 2017). The atmospheric forcing is provided at an hourly time step. A domain wide bias correction of +15% is applied to shortwave radiation in COSMO-CLM to account for a domain-wide sea surface temperature (SST) bias. Surface albedo is globally set to 0.06, and SCHISM light attenuation parameters are set to Jerlov type IA.

A faster coarse resolution SCHISM–ECOSMO NWES-LR configuration was used to run a 10 year spin-up simulation from which the initial conditions for the NWES-IT configuration are interpolated. The separate coarser resolution NWES-LR configuration was co-developed in the same manner as the NWES-IT configuration. Horizontal- grid resolution in the NWES-LR configuration ranges from 4.5 km in shallow coastal regions to approximately 10 km in deep central shelf areas and reaches 15 km in the open ocean (Supplementary Material Figure S1). The LSC² vertical grid in NWES-LR is the equivalent of the one used in NWES-IT. Temperature, salinity, nitrate, phosphate, silicate, and oxygen for the NWES-LR configuration were initialized from WOA2018 (Boyer et al., 2018). ECOSMO sediment fields for NWES-LR were interpolated from long-term ECOSMO simulations provided by F. Werner (in prep.) and

Samuelson et al. (2022). Forcing data for the spin-up simulations is equivalent to the NWES-IT configuration.

We perform two numerical experiments with the NWES-IT model configuration to assess the impact of tides on NWES primary production. The TIDE experiment includes tidal forcing at the lateral open boundaries and tidal potential in the domain. In the NOTIDE experiment, the same model configuration is run completely without tidal forcing. Both experiments are integrated for a period of 6 years from 2010 to 2015 with hourly instantaneous model output. Model output is averaged to daily means and only saved in full temporal resolution for specified months to reduce memory use. The first year of the TIDE/NOTIDE experiments is treated as a secondary spin-up period and omitted from the analysis.

2.4 Analysis methods for the internal tide field and turbulent mixing

Seasonal stratification on the NWES leads to a quasi two-layer system in spring and summer, with a warm wind-mixed surface layer formed over cold deeper water masses. The pycnocline separates the two layers. Internal tides propagate in the horizontal direction along the pycnocline. In order to achieve realistic bulk mixing, the model needs to adequately represent the properties of the surface and bottom layers, as well as the depth of the layer interface.

We use the potential energy anomaly (PEA, Simpson et al., 1981) to characterize the stratification of the water column. The potential energy anomaly is a measure of the amount of work required to vertically mix the entire water column and is calculated as:

$$\frac{1}{D} \int_{-H}^{\eta} gz(\bar{\rho} - \rho) dz \quad (1)$$

with the depth mean density $\bar{\rho} = \frac{1}{H} \int_{-H}^{\eta} \rho dz$, the mean water depth H , the sea surface elevation η , the actual water depth $D = h + \eta$, and the gravitational acceleration g .

In order to assess stratification in vertical temperature profiles, we define the thermocline depth following Guihou et al. (2018) as a normalized first moment of stratification:

$$\delta(t) = H \frac{T_{bed}(t) - \bar{T}(t)}{T_{top}(t) - T_{bed}(t)} \quad (2)$$

Here, H is the depth of the water column, T_{top} and $T_{bed}(t)$ are the surface and bed temperatures at a given time, and $\bar{T}(t)$ is the depth-averaged temperature. The thermocline depth is represented by $\delta(t)$ in the limit of a two-layer vertical density structure. The pycnocline depth is derived in the same manner using density instead of temperature.

Internal waves that propagate along the layer interface lead to oscillatory vertical displacements of the pycnocline. We analyze the variability due to tidally generated internal waves with the help of the tidally filtered interface depth $\langle \delta \rangle$ computed with a Doodson X0 filter (Intergovernmental Oceanographic Commission, 1985). The pycnocline depth variability is then defined as:

$$\tilde{\delta} = \delta - \langle \delta \rangle. \quad (3)$$

The standard deviation of the tidal fluctuations in pycnocline depth can then be calculated as an estimate of the internal tide activity on shelf scale:

$$\text{std}(\tilde{\delta}(t)) = \sqrt{\frac{1}{72} \sum_{t-36h}^{t+36h} (\tilde{\delta}(t) - \frac{1}{72} \sum_{t-36h}^{t+36h} \tilde{\delta}(t))^2} \quad (4)$$

The standard deviation of $\tilde{\delta}$ is calculated over a moving 3×24 -h window to avoid aliasing from the spring-neap cycle while retaining sufficient data to isolate a clear signal. The standard deviation of $\tilde{\delta}$ represents a conservative estimate of the tidal variability in the vertical pycnocline displacements (Guihou et al., 2018).

Dissipation of the energy of baroclinic and barotropic tides induces turbulence that mixes nutrients and other tracers in the water column. To assess the ecosystem-relevant turbulent mixing associated with tides, we compute the turbulent nitrate flux in the water column following Sharples et al. (2001) as:

$$J_{NO_3} = -K_V \left(\frac{\Delta NO_3}{\Delta z} \right), \quad (5)$$

with the (vertical) eddy diffusivity K_V computed by the model turbulence closure, the difference in nitrate concentration between the respective discretized vertical model layers ΔNO_3 , and the vertical model layer thickness Δz in meters. The turbulent nitrate flux J_{NO_3} can be used to estimate the potential for new production (Dugdale and Goering, 1967) fueled by allochthonous nitrate from the bottom layer. Assuming full utilization of the vertically mixed nitrate by phytoplankton, we compute potential new production as:

$$PNP = J_{NO_3}(z_E) R_N M_C, \quad (6)$$

where $J_{NO_3}(z_E)$ is the turbulent nitrate flux evaluated at the base of the euphotic zone, R_N is the standard N:C Redfield ratio, and M_C is the molar mass of carbon.

2.5 Model validation

We evaluate the newly developed NWES-IT configuration's ability to reproduce general hydrographic and biogeochemical conditions on the NWES and specifically assess its skill in regard to tidal processes. We evaluate the results of the TIDE experiment on the western part of the NWES (i.e., the Celtic Seas and greater North Sea) over the 5-year period from 2011 to 2015.

To facilitate model validation, we divide the NWES into subareas (see Figure 1A) following a combination of bathymetric, geographic, and physical and ecosystem considerations based on Holt et al. (2012) and the ICES subareas (ICES, 1983). The greater North Sea is divided into the southern North Sea (SNS), the central North Sea (CNS), the northern North Sea (NNS), the English Channel (EC), the Norwegian Trench (NT), and the Kattegat/Skagerrak (SK) subareas. The Celtic Seas are divided into the Armorican Shelf (A), the Celtic Sea (C), the Irish Sea (I), the Inner Seas off the West Coast of Scotland (Sc), and the North-Western Approaches (NWA). The Celtic Sea and the North-

Western Approaches are further separated into smaller subareas for a more detailed analysis of tidal impacts. The northeastern inner shelf region (NEC) and the southwestern outer shelf region (SWC) of the Celtic Sea are separated by the approximate 130-m isobath. The North-Western Approaches subarea is divided into the Western Irish Shelf (WI), the Malin Shelf (MS), and the Hebrides Shelf (HS).

2.5.1 Tides

The NWES-IT model configuration's ability to simulate barotropic tides is evaluated against observational data from tide gauges and tidal current meters. Tide gauge data are compiled from CMEMS *In Situ* TAC (<http://www.marineinsitu.eu>; last accessed 08/2022), UHSLC tide gauge data (Caldwell et al., 2015), and the UK Tide Gauge Network provided by the British Oceanographic Data Centre (https://www.bodc.ac.uk/data/hosted_data_systems/sea_level/uk_tide_gauge_network; last accessed 08/2022). Simulated tidal currents are compared against observational data from the British Oceanographic Data Centre (made available by Karen Guihou under a CECILL license at https://github.com/Karen-Guihou/tidal_analysis; last accessed 08/2022).

Hourly model output from the TIDE experiment in July and August 2014 is used for the harmonic analysis of the tidal signal. Statistics are computed for the eight major constituents and shown in Table 1. For the regionally dominant M2 constituent, tidal elevations yield an RMSE of 33.15 cm and a mean error of -7.33 cm. The RMSE for the maximum M2 tidal current velocities is 13.42 cm/s, with a mean error of 3.5 cm/s. Mean errors in both tidal elevations and maximum tidal current velocities of the regionally dominant M2 constituent compare well with the performance of established NEMO AMM7 configurations (O'Dea et al., 2012; Guihou et al., 2018). RMSE for the M2 constituent in the SCHISM NWES-IT configuration is somewhat higher than in NEMO AMM7, which might be related to model boundary forcing and the implemented 10-m minimum water depth. Overall, Table 1 documents generally good comparability between model and observations and underlines adequate model performance in regard to tides.

2.5.2 General hydrography

We assess the adequate representation of the spatial, seasonal, and interannual variability of temperature by co-locating observation and model data in space and time against *in situ* temperature data obtained for the period 2011–2015 from the ICES database (<https://data.ices.dk>; downloaded 12/2022). The ICES data comprises a total number of 17,420 temperature profiles from CTD casts. Each CTD cast is depth-averaged for comparison against model data to account for differing vertical discretization. The Taylor diagram shown in Figure 2A demonstrates a good fit between the model and observational data for the defined subareas. Centered RMSE (CRMSE) errors are low (≤ 0.5), and the correlation between model and observational data is high ($R > 0.85$) except for the Norwegian Trench area (excluded in Figure 2A). The mean temperature bias calculated for the co-located data included in the Supplementary Material (Table S2) further underlines the good model performance.

TABLE 1 RMSE and mean error for comparison (model-obs) of model results against harmonic analysis from tide gauge data and tidal current semi-major axis from historical current meter data for the NWES.

Constituent	Elevation [cm]			Current [cm/s]		
	RMSE	Mean error	N	RMSE	Mean error	N
Q1	1.67	-0.47	120	–	–	–
O1	1.88	-0.17	120	0.91	-0.04	269
K1	2.77	+0.45	120	0.99	-0.05	269
N2	6.86	+2.33	c120	3.93	+2.33	261
M2	33.15	-7.33	120	13.42	+3.05	270
S2	14.48	-4.5	120	4.95	+2.01	272
M4	5.04	1.63	120	1.23	-0.55	262

Harmonic analysis is computed from hourly model data for July and August 2014. Outliers are removed (>2.58 STD), N shows number of valid data used in the comparison.

We further compare mean summer (JJA) sea surface temperatures (2011–2015) against satellite observations obtained from the European Space Agency SST Climate Change Initiative (ESA SST CCI) reprocessed sea surface temperature analysis (<https://doi.org/10.48670/moi-00169>; downloaded 11/2022). Figure 3A shows simulated mean summer SST for 2011–2015. SST on the NWES has a latitudinal gradient. It is highest in the Celtic Sea (16°C–18°C), followed by the shallow southern North Sea (15°C–17°C). Surface temperature then decreases with latitude and reaches temperatures around 12°C in the northern North Sea. The model configuration reproduces a cool band of summer SST with a distinct difference of 1°C – 2°C to adjacent areas along the shelf break of the Armorican and Celtic Sea. Such a band of cold SST is frequently documented in observations (Pingree et al., 1982; Sharples et al., 2007). Comparison with the observed SST field from ESA SST CCI satellite data in Figure 3B shows high agreement between the two fields. The mean bias is below $\pm 0.5^\circ\text{C}$ in most of

the domain. Too warm temperatures along the Celtic Sea shelf break suggest underestimated mixing in the region, and too cold temperatures along the northwestern GB coast conversely suggests minor overmixing.

Stratification is evaluated by a direct comparison of vertical temperature structure against observations from a mooring station in the Celtic Sea. Data for the CSE5 mooring station in the Celtic Sea was obtained from the UK FASTnet project (https://www.bodc.ac.uk/projects/data_management/uk/fastnet, downloaded 08/2022). The CSE5 mooring station was deployed at a distance of approximately 40 km to the Celtic Sea shelf break in a mean water depth of 184 m. The nominal position of the CS5 station is 48.77° N and 9.41° W. The CSE5 station is marked in Figure 1B. The water column at the CSE5 station shown in Figure 4 features a well-established two-layer system in June 2012. Simulated temperatures of 13.5°C–15°C in the surface mixed layer match observations, and the model resolves the cooling of the surface layer during a wind event on 14–18 June. The

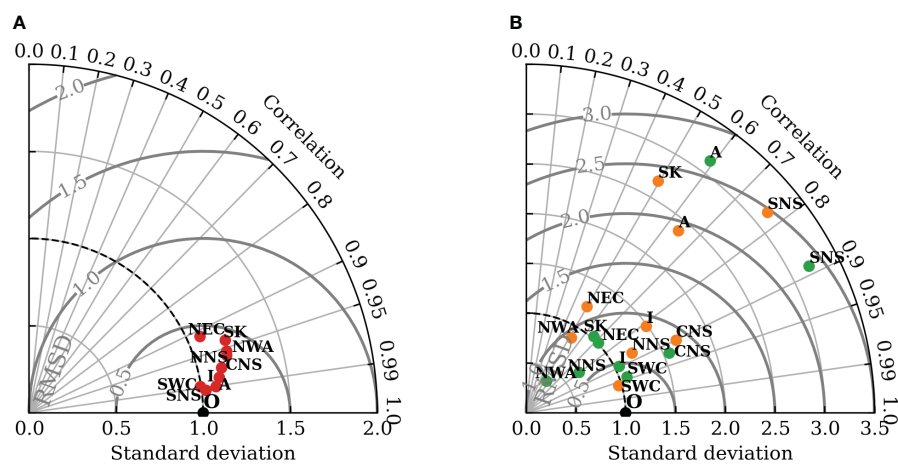


FIGURE 2

(A) Taylor diagram of depth-averaged model temperature co-located against observational data (2011–2015) downloaded from the ICES database (<https://data.ices.dk>; downloaded December 2022). Data are co-located in time and space for a total number of 17,420 temperature profiles from CTD casts. (B) Taylor diagram for surface (<20 m) nitrate (orange) and phosphate (green) concentrations co-located to ICES observational data (2011–2015). We use a total number of 6,045 stations for nitrate and 6,083 stations for phosphate.

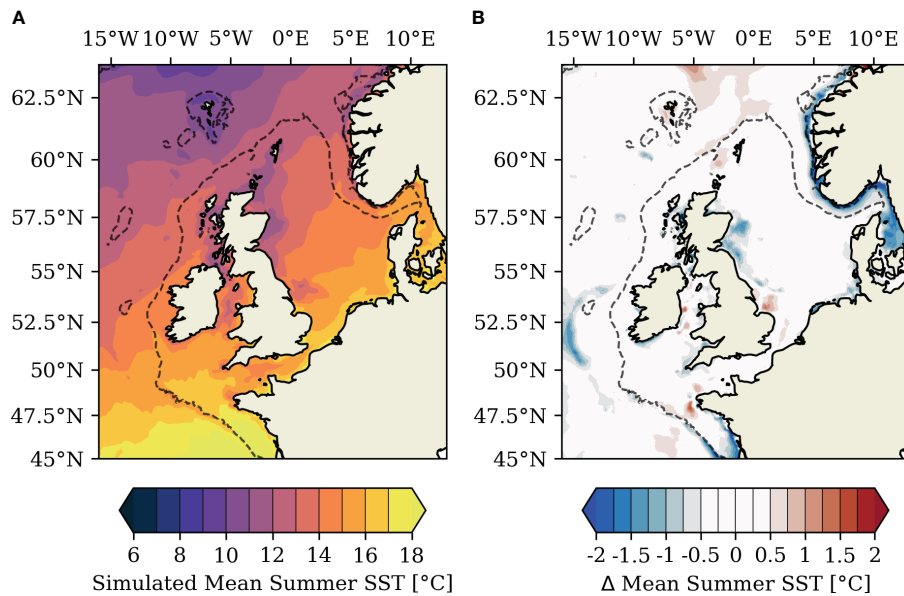


FIGURE 3

Simulated mean summer (JJA) SST for 2011–2015 (A) and temperature bias for simulated mean summer SST (2011–2015) against ESA SST CCI satellite observations (B).

thermocline depth is captured well in the model. Bottom temperatures at the CSE5 station are marginally overestimated by 0.25°C–0.5°C in the model.

The presented validation of temperature indicates an overall good representation of the spatial, seasonal, and interannual variability of temperature and the associated mixing-stratification status on the shelf. An additional comparison of mean sea surface salinity to climatological data from the Baltic and North Seas climatology (BNSC; Hinrichs and Gouretski, 2019) is included in the Supplementary Material (Figure S2). The model configuration

enables the efficient simulation of the general hydrography of the NWES required to capture relevant coupled physical–biogeochemical circulation features (Pätsch et al., 2017).

2.5.3 Internal tides

The vertical temperature profile in Figure 4 shows high-frequency oscillatory vertical displacements of the thermocline also documented in observations. Such thermocline depth variability indicates the presence of internal tides. We use the

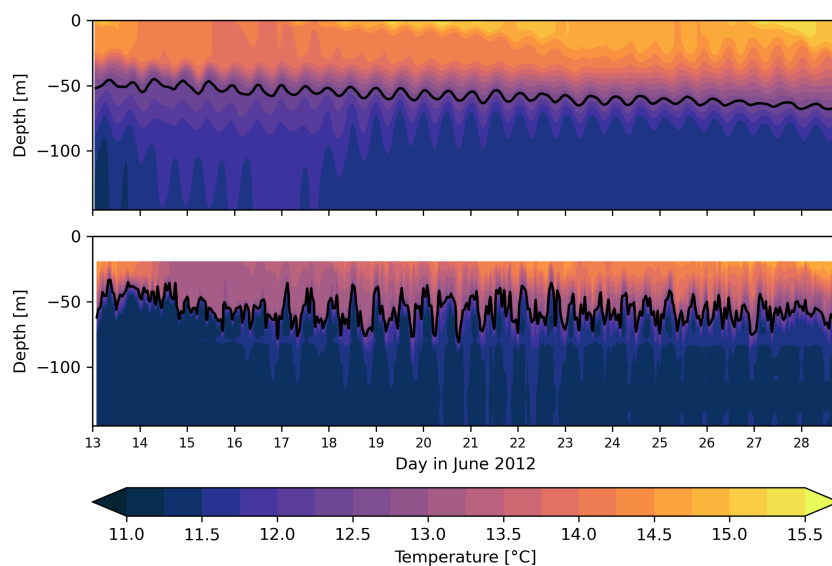


FIGURE 4

Time series of temperature at the CS5 station at 48.77°N, 9.4°W from model (top) and observations (bottom). Black contour indicates thermocline depth computed with Eq. 2.

tidal thermocline depth variability defined in Eq. 3 to evaluate the model's ability to reproduce internal tides in more detail. We extract the tidal thermocline depth variability at the CS5 station as well as at the CCS, MSE, and HSE stations on the NWES (all stations are marked in Figure 1B). The CS5 station features low-mode internal tides but is positioned well out of the complex internal tide generation zone at the shelf break (Hopkins et al., 2014). The CCS station is located in the central Celtic Sea at a nominal position of 49.32° N and 8.49°W with a mean water depth of 145.4 m. Observational data at the CCS station are available for August 2014 from the UK Shelf Sea Biogeochemistry project (Wihsgott et al., 2016). The MSE station is located at the shelf break of the Malin Shelf at 55.87° N and 9.06° W with a mean water depth of 149 m. The HSE station is positioned at 58.7°N and 7.6°W in proximity of the shelf break of the Hebrides shelf and has a mean water depth of 153 m.

At the CCS and CS5 stations, we extract the tidal thermocline depth variability for the respective observational periods to allow evaluation against observations. At the MSE and HSE stations, we extract data in August 2014 to evaluate stratified conditions. The fast Fourier transform spectral (FFT) analysis of the thermocline depth signal in Figure 5 shows that the thermocline depth variability at all stations clearly shows frequency banding that is best captured by regionally relevant M2, M4, and S1 tidal harmonic bands. The frequency banding fits well with observations at the CS5 and CCS stations. The M2 frequency band holds the most energy at all four stations. The model underestimates the energy in the M2 tidal frequency band at the CS5 station close to the shelf break. The simulated energy in the M2 frequency band fits with observations at the CCS station in the central Celtic Sea. The model further generally underestimates energy in higher frequency bands, e.g., for the M4 and M6 overtides, at both the CS5 and CCS stations.

2.5.4 Biogeochemistry

We assess the model's consistency with large-scale nutrient distributions and seasonality against *in situ* data of nutrients obtained from the ICES database (<https://data.ices.dk>; downloaded 11/2022) for the period 2011–2015. Similar to Daewel and Schrum (2013), we compute the vertical integral of the observational data in the top 20 m if observations at different depth levels are available. For stations with surface values only

(max. depth < 5m), we use the shallowest observation for direct collocation, as the thickness of the surface layer in the model ranges between 2.5 and 5 m. The observational data is co-located in time and space against daily mean model output of the TIDE experiment, and we visualize the normalized statistics for the different subareas with the help of a Taylor diagram in Figure 2B.

For nitrate, the Taylor diagram in Figure 2B shows centered RMSE values < 1 for all subareas except the Armorican shelf (CRMSE \approx 1.9), the Skagerrak/Kattegat region (CRMSE \approx 2.4), the southern North Sea (CRMSE \approx 2.5), and the northeastern Celtic Sea (CRMSE \approx 1.2). Normalized standard deviation is slightly below 1 for the NWA and SWC subareas and between 1 and 1.75 for NEC, I, NNS, and CNS subareas, indicating a slightly underestimated/overestimated representation of nitrate variability in the respective subareas. The SNS, A, and SK subareas have high standard deviation (> 2). The correlation is > 0.5 for all subareas except SK (\approx 0.49). The correlation is > 0.8 for the CNS, NNS, and SWC subareas.

Model performance for phosphate is slightly better than for nitrate (Figure 2B) but also shows reduced performance for the A and SNS subareas. Centered RMSE is high for the southern North Sea and Armorican Shelf but < 1 for the other subareas. The standard deviation shows a pattern similar to CRMSE; it is high for the SNS and A subareas, intermediate for the CNS (\approx 1.6), and around 1 for SK, NEC, SWC, and I. The standard deviation is < 1 for NNS and NWA. The correlation is higher than for nitrate, with all subareas showing correlation > 0.6 except for the NWA (\approx 0.54) and A subareas (\approx 0.59). The correlation is particularly high (>0.8) for SWC, I, SNS, and CNS subareas.

We complement the normalized and centered statistics with the percentage bias (Allen et al., 2007) documented in Table S2 in the Supplementary Material. The percentage bias shows decent model performance on the NWES but again shows a reduced model skill particularly in shallow subareas like the southern North Sea, northeastern Celtic Sea, or the Irish Sea. The model's particular difficulties in reproducing low summer nutrient concentrations in shallow regions is a common issue with ECOSMO. Daewel and Schrum (2013) relate the reduced model skill in shallow coastal regions to unconsidered impacts of near-coast ecosystems (e.g., the Wadden Sea) and the utilization of Redfield stoichiometry in the model. Other aspects of the presented nutrient validation, like

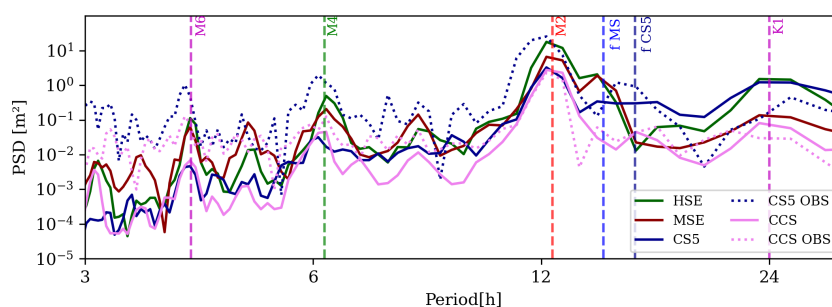


FIGURE 5

Frequency analysis of thermocline depth signal at CCS, CS5, MSE, and HSE stations. The FFT is implemented with a Welch filter (with 192h segments) and a Hanning window (with 50% overlap). Dotted lines show frequency analysis of available observational data.

the better model performance in regard to phosphate, show promising consistency with previous model studies based on smaller domain sizes and different physical model components (Daewel and Schrum, 2013; Zhao et al., 2019).

Mean annual primary production in the TIDE experiment (2011–2015) shown in Figure 6A reproduces the characteristic spatial pattern of primary production on the NWES (e.g., Holt et al., 2012; Holt et al., 2016). Shallow and coastal regions feature high primary production, whereas NPP is substantially lower in the deeper central basins of the shelf where seasonal stratification limits vertical nutrient supply. NPP simulated with ECOSMO is typically in the lower range of what is reported in literature for the region (Daewel and Schrum, 2013; Zhao et al., 2019). Productivity is particularly low along the European continental coast, where observations suggest NPP to range from 199 to 261 $\text{gCm}^{-2}\text{yr}^{-1}$ (Joint and Pomroy, 1993). Simulated annual NPP of 70–85 $\text{gCm}^{-2}\text{yr}^{-1}$ in the stratified central Celtic Sea fits well with published estimates of 80 $\text{gCm}^{-2}\text{yr}^{-1}$ based on *in situ* incubations (Joint and Groom, 2000). The model also resolves intensified biological productivity in tidal frontal zones (Mann and Lazier, 2013), e.g., in the southern North Sea, along the western British coast, the English Channel, or between the Irish and Celtic Seas. A qualitative comparison of mean seasonal phytoplankton biomass to a

chlorophyll-*a* Copernicus Global Colour satellite product (<https://doi.org/10.48670/moi-00281>, downloaded 5/2023) in Figure S3 shows the adequate seasonal evolution of phytoplankton biomass in the model. The model reproduces a pronounced bloom in spring and subsequent bloom progression from south to north in summer also documented in the satellite chlorophyll-*a* product. Phytoplankton biomass and chlorophyll-*a* are high in the shallow coastal areas throughout the summer, whereas the seasonally stratified central basins of the North Sea and Celtic Sea show low values due to nutrient limitation in the surface layer in summer.

Light attenuation in ECOSMO II explicitly includes phytoplankton self-shading as well as shading by POM and DOM. In combination with resolved benthic–pelagic coupling by sedimentation and resuspension of POM, this allows the representation of the spatially diverse primary production dynamics in turbid coastal regions of the NWES (Capuzzo et al., 2013; van Leeuwen et al., 2015; Taylor et al., 2021). Figure S4 shows a qualitative comparison of simulated mean seasonal surface organic detrital matter concentration (DOM + POM) with the volume absorption coefficient of radiative flux in sea water due to dissolved organic matter and other detrital organic particles obtained from a Copernicus Global Colour satellite product (<https://doi.org/10.48670/moi-00281>, downloaded 5/2023). Figure

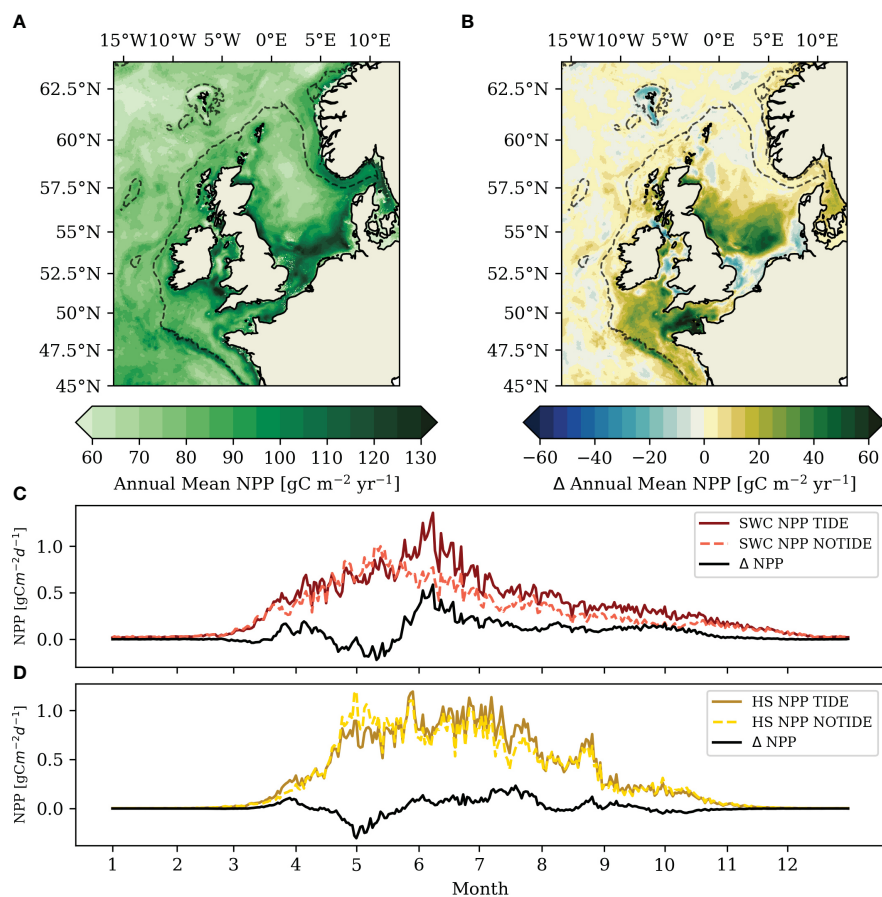


FIGURE 6

(A) Mean annual primary production (2011–2015) in TIDE experiment and (B) difference in mean annual primary production for 2011–2015 between the experiments (TIDE–NOTIDE). Dashed black contour shows the 200-m isobath. Daily primary production computed for period 2011–2015 for the southwestern Celtic Sea (C) and Hebrides Shelf subareas (D).

S4 documents the adequate spatial distribution of DOM and POM in the model. Maximum DOM and POM concentrations and associated light absorption occur in the shallow near-coast areas, especially in permanently mixed regions with strong resuspension of POM. The seasonality of DOM and POM varies with the seasonal cycle of primary productivity, which is also present in the satellite-derived absorption coefficient.

The consistency across model configurations and the overall good agreement between simulated nutrient fields and ICES observation data affirm overall adequate SCHISM–ECOSMO performance in regard to simulated biogeochemical cycles. SCHISM–ECOSMO resolves key processes regarding the effects of tidal forcing on nutrients and light, and the presented validation analysis encourages the use of SCHISM–ECOSMO for the investigation of tidal impacts on primary production on the entire shelf.

3 Results and discussion

3.1 Tidal mixing and the internal tide field in the NWES-IT model configuration

The signature of tidal mixing is illustrated in Figure 7A by means of the annual mean Potential Energy Anomaly (PEA; Eq. 1) computed for the period of maximum stratification from mid-June to mid-August (2011–2015). Permanently mixed areas ($PEA < 20 \text{ Jm}^{-3}$) are separated from seasonally stratified areas by tidal mixing fronts, e.g., in the southern North Sea, the western approaches of the English Channel or the St. George front separating the Celtic and Irish Seas. PEA magnitude and the

positions of the tidal fronts match results of previous studies and observations (Holt and Umlauf, 2008; Pätsch et al., 2017; Graham et al., 2018a) and thus further substantiate the adequate simulation of the mixing-stratification status on the NWES outlined in Sect. 2.5.

The refined horizontal grid resolution in the NWES-IT configuration reproduces pycnocline depth variability at tidal frequencies that suggests the presence of kilometrical-scale internal tides (Sect. 2.5.3). We compute the pycnocline depth tidal standard deviation $std(\tilde{\delta})$ (Eq. 4) for a spring tide period from 11 to 14 August 2014 to evaluate the resolved internal tide activity on the entire NWES. We chose a period in early August because the vertical temperature gradients, which mainly control stratification on the NWES, are largest in late July and early August.

The computed $std(\tilde{\delta})$ in Figure 7B shows high spatial variability on the NWES; it ranges from 0 to over 8 m at sites along the shelf break. The results from the NWES-IT configuration show high consistency with kilometrical-scale regional model results presented by Guihou et al. (2018). The $std(\tilde{\delta})$ along the shelf break of the northern North Sea, where the continental slope is subcritical for internal tide generation (Huthnance et al., 2022), is low. The local horizontal grid resolution (6–10 km; see Figure 1B) does not resolve kilometrical-scale processes in the central North Sea, and the NWES-IT configuration consequently does not reproduce internal tides in this region. The study of Guihou et al. (2018) shows only very low internal tide activity in the central North Sea, so that the low internal tide activity in the NWES-IT configuration fits with the expected internal tide activity in the region. The $std(\tilde{\delta})$ in Figure 7B is significantly elevated along the steep shelf break of the Celtic Sea, in line with multiple observational studies that show high internal tide activity in this region (Pingree and Mardell, 1985; New and Pingree, 1990; Sharples et al., 2007; Green et al., 2008; Inall et al., 2011). The $std(\tilde{\delta})$

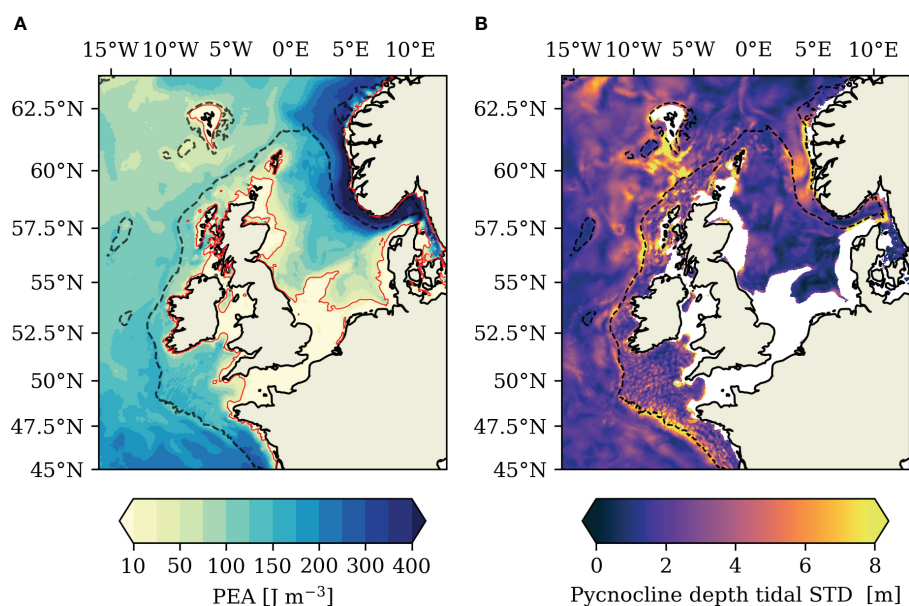


FIGURE 7

Mean Potential Energy Anomaly for period of highest stratification in TIDE experiment (15 July – 15 August; mean for 2011–2015) computed for top 200 m (A). Pycnocline standard deviation in TIDE experiment computed for spring tide period 11 – 14 August 2014 for top 200 m (B). Permanently mixed regions ($PEA < 20 \text{ Jm}^{-3}$) are masked out in (B). Please note the non-proportional color bar discretization in (A).

is also elevated on the Malin Shelf and its continental slope, where on-shelf propagation of internal tides has also been observed (Sherwin, 1988; Rippeth and Inall, 2002). The $std(\tilde{\delta})$ is intermediate on the narrow Hebrides Shelf but is elevated on the continental slope close to the Wyville Thomson Ridge known for internal tide generation (Sherwin, 1991; Hall et al., 2019).

The fine-scale structure of $std(\tilde{\delta})$ throughout the Celtic Sea further suggests a complex and spatially variable internal tide field with internal tide generation at small-scale bathymetric features like canyon ridges and sea banks. Increases of $std(\tilde{\delta})$ at the edge of the permanently mixed areas on the shelf do not indicate increased internal tide activity but reflect reduced stratification. The resolved spatial variability of internal tide activity in the Celtic Sea is consistent with the results of Guihou et al. (2018) and non-hydrostatic simulations in smaller areas of the Celtic Sea (Vlasenko et al., 2013; Vlasenko et al., 2014).

3.2 Tidal impacts on primary production on the NWES

We investigate the impact of tidal forcing on primary production on the NWES by comparing the mean annual primary production (2011–2015) from the NWES-IT experiments with and without tidal forcing. Figure 6A shows mean annual net primary production (NPP) in the TIDE experiment with tidal forcing. Figure 6B shows the respective difference in mean annual NPP between the TIDE experiment and the NOTIDE experiment.

Table 2 further documents the NPP response to tidal forcing for the subareas introduced in Sect. 2.5. Note that the Celtic Sea and the North-Western Approaches are separated into smaller subareas for a more detailed analysis of tidal impacts, as described in Sect. 2.5.2 and documented in Figure 1B.

The comparison of mean annual NPP in the two experiments in Figure 6B shows that tidal forcing extensively structures biological productivity on the NWES. Tidal forcing substantially increases mean annual primary production on the shelf by around 16% (~14.47 Mt C; Table 2). The tidal response of primary production on the inner shelf found in this study is similar to results obtained by Zhao et al. (2019) for the central and southern North Sea. Tidal impacts on the inner shelf can largely be classified based on stratification characteristics and water depths. Tidal forcing decreases productivity in the majority of the shallow permanently mixed regions of the NWES (see PEA in Figure 7A). The tidal NPP response is also negative in the tidally energetic North Channel between Ireland and the UK. Shallow stratified areas of the NWES in turn are particularly responsive to tidal mixing of nutrients and show strong productivity increases. The dynamic tidal frontal systems in the southern North Sea, northeastern Celtic Sea, or western English Channel particularly invigorate local primary production in the TIDE experiment.

The tidal NPP response is generally lower in the deep outer shelf regions of the NWES. The northern North Sea shows a minor positive response to tidal forcing (+2%; Table 2) but features local reductions of up to $-10 \text{ gCm}^{-2}\text{yr}^{-1}$. Tidal NPP response on the northern North Sea continental slope is neutral or marginally

TABLE 2 Annual mean primary production (2011–2015) on the NWES in NOTIDE and TIDE experiments.

Subarea	NOTIDE	TIDE	Difference
	Total [$Mt \text{ C yr}^{-1}$] (Mean [$gC \text{ m}^2 \text{ yr}^{-1}$])	Total [$Mt \text{ C yr}^{-1}$] (Mean [$gC \text{ m}^2 \text{ yr}^{-1}$])	
S. North Sea (SNS)	17.48 (85.7)	19.9 (97.5)	+ 14%
C. North Sea (CNS)	16.44 (67.7)	19.33 (79.6)	+18%
N. North Sea (NNS)	5.89 (74.4)	6.02 (76.0)	+2%
Skag./Kattegat (SK)	5.16 (66.3)	5.77 (74.2)	+12%
Norwegian Trench (NT)	6.44 (82.9)	6.57 (84.6)	+2%
English Channel (EC)	4.82 (58.6)	7.49 (91.1)	+55%
Armorican Shelf (A)	5.36 (76.3)	6.21 (88.4)	+16%
N-E Celtic Sea (NEC)	7.66 (71.4)	9.86 (91.9)	+29%
S-W Celtic Sea (SWC)	6.16 (67.5)	7.69 (84.3)	+25%
Irish Sea (I)	4.04 (84.7)	4.27 (84.5)	+6%
I. Sea W. of Scotl. (Sc)	3.24 (73.3)	3.63 (82.2)	+12%
West Irish Shelf (WI)	3.67 (78.2)	3.89 (82.9)	+6%
Malin Shelf (MS)	1.64 (77.1)	1.74 (81.5)	+6%
Hebrides Shelf (HS)	2.73 (77.4)	2.84 (80.4)	+4%
Sum for NWES	90.74 $Mt \text{ C yr}^{-1}$	105.21 $Mt \text{ C yr}^{-1}$	+16%

Difference between experiments computed relative to NOTIDE experiment.

negative. Tidal forcing also locally decreases NPP on the Hebrides shelf, but the HS subarea still shows an aggregated increase of +4%. At around 58°N, tidal forcing locally increases NPP by 10–15 $\text{gCm}^{-2}\text{yr}^{-1}$ in a patch on the continental slope. The tidal NPP response further increases southward and yields +6% for the Malin Shelf subarea, where NPP is particularly enhanced by tidal forcing in a small region that also features high internal tide activity in Figure 7B. NPP is also increased by 10–15 $\text{gCm}^{-2}\text{yr}^{-1}$ on the continental slope of the Malin Shelf at around 55.5°N and on the northern flank of the Porcupine Seabank.

The Celtic Sea in the southwest of the NWES stands in stark contrast to the North-Western Approaches, highlighting substantial regional differences in the impact of tidal forcing on primary production along the NWES shelf break. Although the water depth in the southwestern Celtic Sea (SWC) subarea is comparable with, e.g., the NNS (> 130 m), the SWC subarea still shows a substantial NPP increase of +25% with tidal forcing (Table 2). Highest NPP increases (locally up to 50 $\text{gCm}^{-2}\text{yr}^{-1}$) occur on the continental slope of the Celtic Sea in the English Channel tidal flux window at around 5.5–8.5°W. Tidal forcing moreover substantially increases NPP in the deep outer shelf area along the Celtic Sea shelf break (up to 30 $\text{gCm}^{-2}\text{yr}^{-1}$) and the central Celtic Sea (up to 35 $\text{gCm}^{-2}\text{yr}^{-1}$). The deep water column limits the impact of the barotropic tide in the region. Figure 7B however indicates high internal tide activity.

We turn to the seasonal cycle of NPP to examine the regional differences of the tidal NPP response in the deep shelf areas along the shelf break in more detail. Figures 6C, D show the mean seasonal cycle of NPP (2011–2015) averaged for the southwestern Celtic Sea (SWC, Figure 6C) and the Hebrides Shelf (HS, Figure 6D) subareas. The seasonal cycle of NPP in the TIDE experiment in Figure 6C fits with observations by Joint et al. (2001), who found an extended spring bloom from March to June in the Chappelle Bank region on the Celtic Sea shelf break. Tidal forcing marginally increases spring NPP in the HS subarea in March and then decreases from April to early June (Figure 6D). In the Celtic Sea, tidal forcing similarly increases NPP in late March/early April and then reduces NPP until late May. The decrease of spring NPP by tidal forcing is more pronounced in the HS subarea than in the SWC subarea. We attribute the reduction in spring NPP to a delay of the spring bloom that is caused by the deepening of the mean spring surface mixed layer in the TIDE experiment by 8 and 4 m in the HS and SWC subareas, respectively. In a deeper mixed layer, phytoplankton spends less time in favorable light conditions close to the surface, which hinders the buildup of spring bloom biomass in this period. This mechanism was also identified for the northern North Sea in Zhao et al. (2019).

Tidal forcing continuously enhances NPP during the summer bloom period in the southwestern Celtic Sea. The largest tidally induced increase in NPP in the SWC occurs in late spring/early summer; the averaged NPP in the SWC is up to 6 $\text{gCm}^{-2}\text{d}^{-1}$ higher in the TIDE experiment in late May/early June. Tidal forcing moreover marginally increases autumn NPP in the SWC. Tidal forcing also increases summer NPP in the HS subarea, but the magnitude of the increase is substantially lower (only up to 2 $\text{gCm}^{-2}\text{d}^{-1}$) than in the SWC. In the HS subarea, the largest

difference between the TIDE and NOTIDE experiment occurs in July.

Tinker et al. (2022) have shown significant tidal impacts on the residual circulation on the NWES, which are reproduced in our study (Figure S5 Supplementary Material). Tidal phase-driven transport can locally increase residual shelf circulation. Tides also increase bed friction on the shelf, which in turn can decrease the residual shelf circulation. The latter tidal impact particularly affects regions of freshwater influence (Lin et al., 2022; Tinker et al., 2022). A tidal slowing of river water export may contribute to the decrease in mean (summer) surface nutrient concentrations found in ROFIs along the Dutch and German continental coast or in the English Channel (see Figure 8). The (permanently mixed) near-coast areas however are not nutrient limited but light limited (Tett and Walne, 1995) because of intense vertical mixing, high riverine nutrient inputs, and on-shore transport of nutrients and organic matter by estuarine-type circulation (Hofmeister et al., 2017). The reduction of the residual circulation along the continental coast is thus not the decisive factor for the negative near-coast NPP response to tidal forcing. Instead, in line with Zhao et al. (2019), we find that this impact is caused by the degradation of local light conditions due to tidally enhanced resuspension and vertical mixing of POM. Zhao et al. (2019) further established that the major tidal impact on NPP in the seasonally stratified and tidal frontal regions of the North Sea is *via* vertical mixing of nutrients. We therefore focus our analysis of tidal impacts on vertical mixing in the following sections.

The presented study considers major bottom-up processes controlling the tidal impact on primary production, including the tidal mixing of nutrients and organic matter, as well as the resuspension of POM. The 10-m minimum water depths used in this study however limits the representation of particularly shallow coastal regions, as a wetting and drying scheme is not implemented in the model configuration. River plumes and related near-coastal currents may therefore be underrepresented. Moreover, the identified sensitivity of primary production to tidal forcing could be affected by sediment retention by macrobenthos (Prins et al., 1996; Kamp and Witte, 2005; Le Guitton et al., 2017) and its impact on water column turbidity through reduced POM resuspension. The influence of inorganic suspended particulate matter on tidal impacts on NPP is another source of uncertainty in the presented approach that needs to be addressed in future research.

3.3 Vertical mixing by the barotropic and baroclinic tide

We investigate the tidal impact on vertical mixing of nutrients to evaluate its role for the tidal NPP response shown in the previous section. In light of the substantial positive NPP responses found in areas of internal tide activity, we will particularly evaluate the impact of internal tides on vertical mixing. We focus on nitrate in the following, as it is the main limiting nutrient for primary production in the stratified regions of the NWES. We compute the mean turbulent nitrate flux $\overline{J_{\text{NO}_3}}$ (Eq. 5) during the period of strongest stratification (15 July–15 August; mean for 2011–2015) to assess how effective turbulence in the water column mixes across

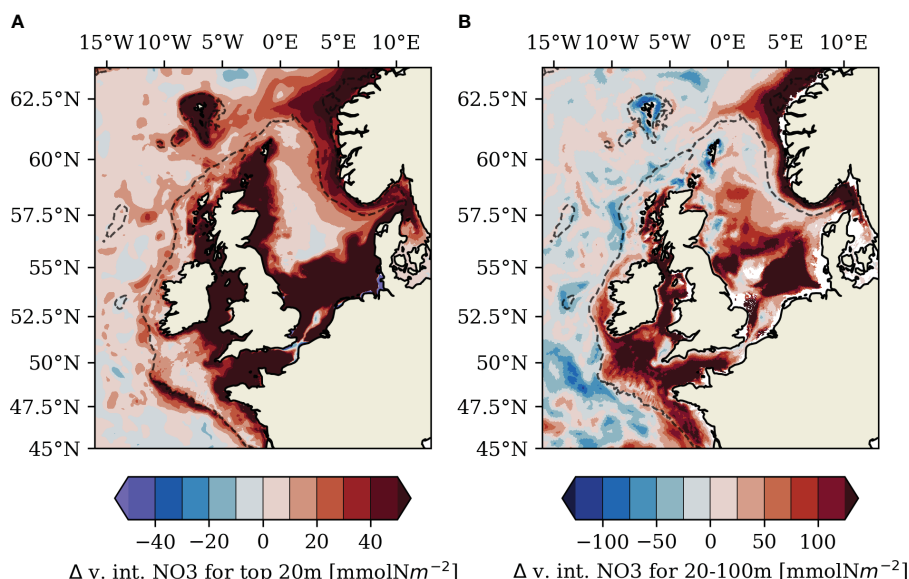


FIGURE 8
Difference (TIDE–NOTIDE) of mean nitrate concentration in June (2011–2015) vertically integrated over (A) the surface layer (top 20 m) and (B) over internal depths (20–100 m).

the nitrate gradient and replenishes nutrients in the euphotic zone. **Figure 9A** shows the difference in $\overline{J_{NO_3}}$ between the TIDE experiment and the NOTIDE experiment along a vertical transect that spans from the tidal frontal region in the Irish Sea to the shelf break of the Celtic Sea. The transect is marked in **Figure 1B**. The corresponding vertical transect of mean eddy diffusivity $\overline{K_V}$ from the TIDE experiment is shown in **Figure 9B**.

In shallow regions with strong tidal currents, like the Irish Sea on the left-hand side of **Figure 9**, tides and wind generate turbulence in the entire water column (**Figure 9B**). In transitional tidal frontal areas, the surface and bottom layer strongly interact and wind forcing or the spring-neap tidal cycle can laterally move the tidal front. The persistent competition between tidal mixing and thermal stratification generates intense turbulent mixing of nutrients into the upper water column on the stratified side of the front (e.g., **Pingree et al., 1975**). Changes in stratification and/or the vertical nitrate gradient by tidal stirring in the bottom boundary layer can also decrease turbulent transports in some regions (see **Figure 9A**).

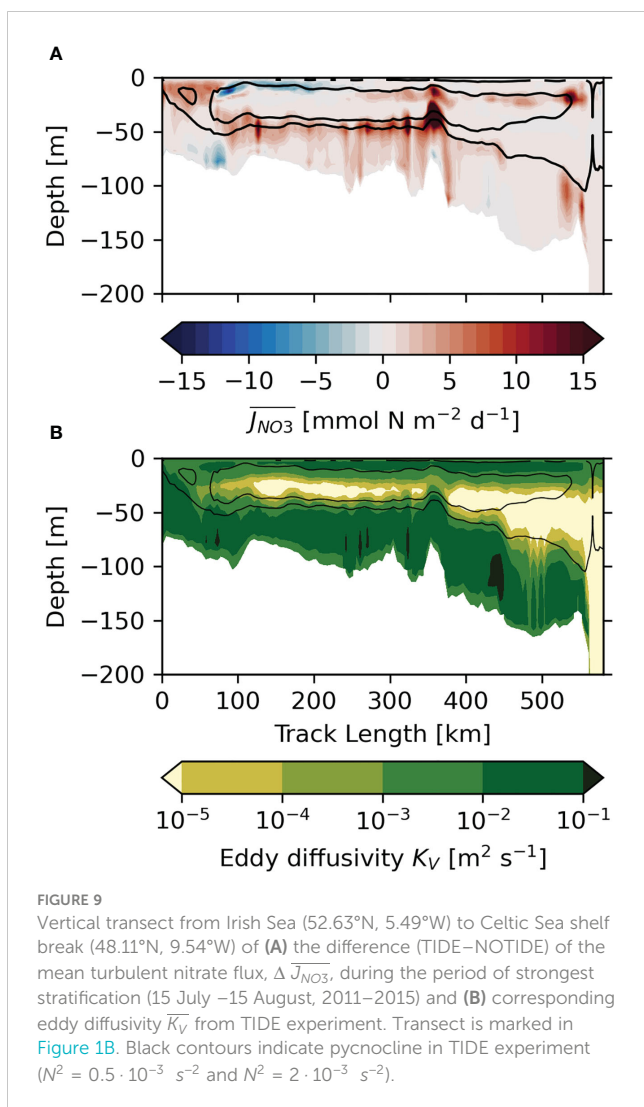
In the stably stratified section of **Figure 9**, the pycnocline (marked by the N^2 contours) suppresses turbulence and acts as a flux barrier. Tidal forcing can however also generate turbulence within the pycnocline, where turbulence has a particularly high mixing efficiency due to stronger vertical gradients (**Rippeth, 2005**). **Figure 9A** accordingly shows high tidally generated $\overline{J_{NO_3}}$ at the base of the pycnocline in the northeastern Celtic Sea (water depth < 130m). Pycnocline mixing is elevated at bathymetric features and particularly high at the Jones Bank (approx. 350km in **Figure 9**).

Pycnocline mixing requires shear to be produced in the pycnocline, either directly by the barotropic tide, internal waves, or wind-induced inertial oscillations. **Becherer et al. (2022)** found the barotropic tide alone to produce sufficient shear at the base of pycnocline to generate observed diapycnal mixing in the shallow

southern North Sea. In the Celtic Sea, with its energetic internal tide field, internal wave breaking will contribute as well. The separation of the surface and boundary mixed layers increases in the deeper water column in the southwestern part of the transect shown in **Figure 9** (beyond the Jones Bank). Here, the impact of the barotropic tide becomes negligible and pycnocline mixing relies on shear instabilities produced by inertial oscillations and internal waves. **Figure 9A** shows tidal forcing enhances $\overline{J_{NO_3}}$ within the pycnocline in the deep southwestern section of the transect. Tidal forcing particularly enhances $\overline{J_{NO_3}}$ within the pycnocline in the region close at the shelf break. Turbulent mixing of nitrate across the pycnocline has been observed in the shelf regions along the Celtic Sea shelf break and is attributed to mixing by the energetic internal tide field (**Sharples et al., 2007; Sharples et al., 2009**). Tidally elevated $\overline{J_{NO_3}}$ in the pycnocline in proximity to the Jones Bank further suggests mixing by internal tides generated at the local extreme bathymetry, which also fits with observations (**Palmer et al., 2013; Tweddle et al., 2013**).

3.4 Tide-generated vertical mixing of nutrients across the pycnocline

To obtain a shelf-wide estimate of the turbulent transport that can sustain (new) primary production in the stratified system during summer, we evaluate the mean turbulent nitrate flux at the nutricline (denoted as $\overline{J_{NO_3}(z_N)}$ in the following). We define the nutricline as the maximum vertical nitrate gradient in the water column. We here follow **Sharples et al. (2001)** and utilize the condition that primary production sets up the nutricline at the base of the euphotic zone below the subsurface biomass maximum in the pycnocline. We show $\overline{J_{NO_3}(z_N)}$ averaged for the period of maximum stratification from the 15 July to 15 August for the entire



NWES in Figure 10A and for the Celtic Sea in Figure 10C. To understand the impact of tides on vertical mixing, we further compute the difference between $\overline{J_{NO_3}(z_N)}$ in the TIDE and NOTIDE experiments. The proportional difference between the two experiments, expressed as $\Delta \overline{J_{NO_3}(z_N)}$, is shown in Figure 10B.

$\overline{J_{NO_3}(z_N)}$ in Figure 10A, C is zero if there is no vertical nitrate gradient, like in the permanently mixed regions along the coasts. In the northeastern Celtic Sea, the fresh and nutrient-rich river outflow from the Bristol Channel obscures the mixing signal. Figure 10A shows that turbulent transports are high in the tidal frontal regions and weakly stratified shallow regions (delineated by $PEA = 50 \text{ Jm}^{-3}$ in Figure 10A). The high turbulent nutrient supply to the surface sustains particularly high NPP rates in the transitional regimes, as can be seen by the spatial coherence of high NPP in Figure 6A and the high $\overline{J_{NO_3}(z_N)}$ found along tidal frontal zones in the NWES (e.g., in the western English Channel or southern North Sea).

Turbulent nitrate fluxes across the nutricline are generally low in the stably stratified regions of the NWES ($PEA > 50 \text{ Jm}^{-3}$). Figure 10A shows $\overline{J_{NO_3}(z_N)} < 0.5 \text{ mmol N m}^{-2} \text{ d}^{-1}$ in most of the central areas of the Celtic Sea and North Sea basins. Observations of diapycnal nutrient fluxes on the NWES are sparse and limited in time, making a direct comparison difficult. Observational estimates

suggest a background flux of $1 - 2 \text{ mmol N m}^{-2} \text{ d}^{-1}$ for the wider Celtic Sea region (Sharples et al., 2001; Williams et al., 2013b). A general underestimation of pycnocline mixing in stratified shelf areas is common for turbulence closures like the GLS k–kl closure used in this study. The deficiency in the representation of pycnocline mixing is attributed to the fact that the parameterizations do not include all physical processes that contribute to pycnocline mixing on the shelf (Simpson et al., 1996; Rippeth, 2005). Observational estimates close to the Norwegian Trench region of the North Sea ($< 0.5 \text{ mmol N m}^{-2} \text{ d}^{-1}$; Bendtsen and Richardson, 2018) and the Western Irish Sea ($0.31 \text{ mmol N m}^{-2} \text{ d}^{-1}$; Williams et al., 2013a) however fit better with the mixing reproduced by the model.

The difference in $\overline{J_{NO_3}(z_N)}$ between the NOTIDE and TIDE experiments in Figure 10B shows that tidal impacts explain almost all turbulent mixing across the nutricline in the shallow stratified regions of the NWES and a relevant proportion of $\overline{J_{NO_3}(z_N)}$ in the central basins of the North Sea and Celtic Sea. Tidal impacts on $\overline{J_{NO_3}(z_N)}$ clearly depend on local water depths and mirror the decreasing positive tidal NPP response with water depths in Figure 6B. $\overline{J_{NO_3}(z_N)}$ decreases with water depths as mixing driven by the barotropic tide loses the potential to affect the euphotic zone. To effectively differentiate between turbulent mixing induced by the barotropic tide and by baroclinic processes like internal tides, we compute the distance ΔZ_{NB} between the nutricline, as a proxy for the euphotic depth, and the depth at which the eddy diffusivity $\overline{K_V}$ falls below $10^{-3} \text{ m}^2 \text{ s}^{-1}$ in the bottom layer as a proxy for the extent of the bottom boundary layer.

Figure 10D shows mean ΔZ_{NB} on the NWES for the period of maximum stratification from the 15 July to 15 August (mean for 2011–2015). The visual comparison with $\Delta \overline{J_{NO_3}(z_N)}$ in Figure 10B indicates that in the North Sea, where there is low internal tide activity, $\Delta Z_{NB} = 30 \text{ m}$ approximately concurs with the extent of positive (i.e., tide-induced) $\Delta \overline{J_{NO_3}(z_N)}$. The comparison with the tidal NPP response in Figure 6B supports this assumption; here, $\Delta Z_{NB} = 30 \text{ m}$ approximately corresponds to the boundary of the positive tidal NPP response. We use this simplified approximation to define that at $\Delta Z_{NB} > 30 \text{ m}$, the impact of the barotropic tide on pycnocline mixing becomes negligible and baroclinic processes like internal tides are the dominant drivers of pycnocline mixing.

As already indicated in Figure 9A, turbulent nitrate fluxes across the nutricline are enhanced in a distinct band along the Celtic Sea shelf break (Figures 10A–C). The barotropic tide plays a role in the EC tidal flux window ($5.5 - 8.5^\circ \text{W}$), where tidal energy dissipation is very high (Pingree et al., 1982) and $\Delta Z_{NB} < 30 \text{ m}$ extends nearly up to the shelf break (Figure 10D). $\overline{J_{NO_3}(z_N)}$ is particularly high at the shelf break part of the EC tidal flux window (locally up to $5 \text{ mmol N/m}^2 \text{ d}$). The remaining area of elevated $\overline{J_{NO_3}(z_N)}$ along the shelf break shows pronounced separation of bottom and surface mixed layers ($\Delta Z_{NB} \gg 30 \text{ m}$). In the sector of the Celtic Sea shelf break north of 8.5°W , Figures 10A, C show elevated $\overline{J_{NO_3}(z_N)}$ with values in the range of $\sim 0.5 - 2 \text{ mmol N m}^{-2} \text{ d}^{-1}$. Local mixing hotspots with $\overline{J_{NO_3}(z_N)}$ of up to $5 \text{ mmol N m}^{-2} \text{ d}^{-1}$ are also evident on the northern sector of the Celtic Sea shelf break. The elevated average turbulent nitrate fluxes fit with the observed range of $1 - 9 \text{ mmol N m}^{-2} \text{ d}^{-1}$ reported for the northern sector of the Celtic Sea shelf break by Sharples et al. (2007). The area of tidally enhanced

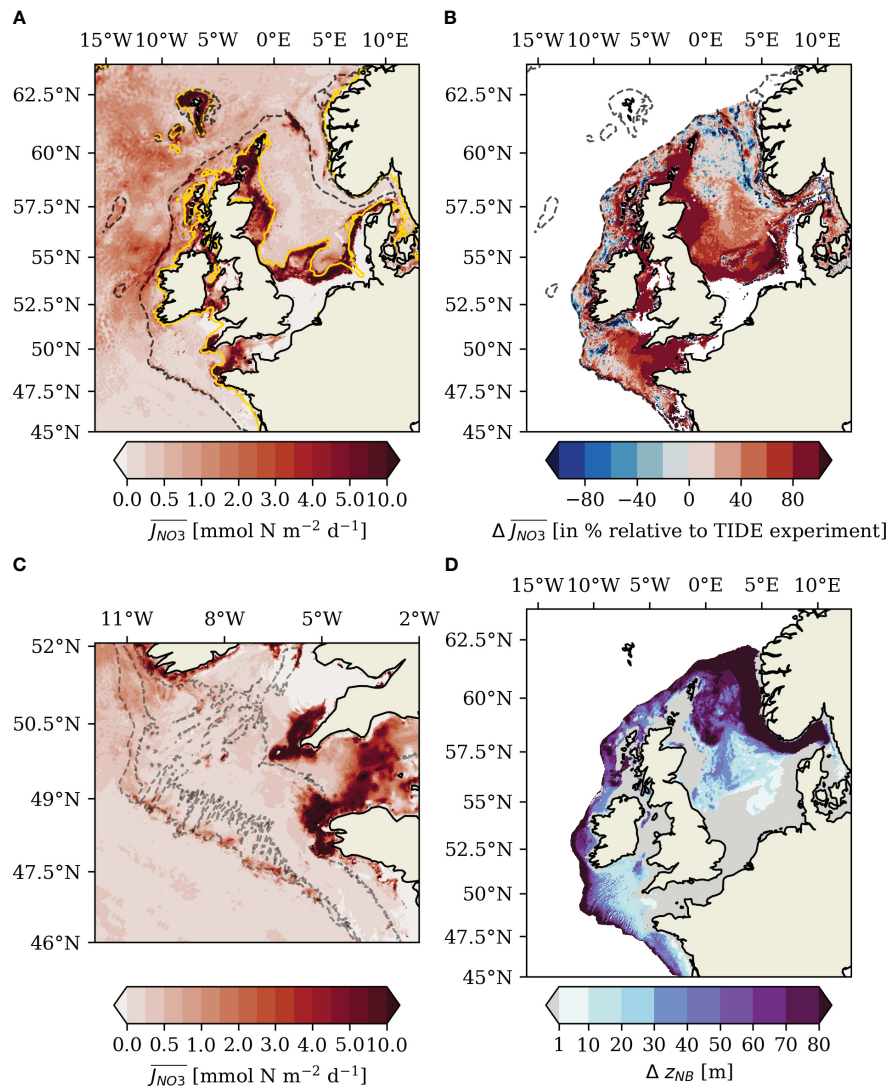


FIGURE 10

(A) Mean turbulent nitrate flux evaluated at nutricline, $\overline{J_{NO_3}(z_N)}$, during period of strongest stratification (15 July – 15 August, mean for 2011–2015). Yellow contour in (A) shows $PEA = 50 \text{ Jm}^{-3}$. (B) Proportional difference $\Delta \overline{J_{NO_3}(z_N)}$ ((TIDE–NOTIDE)/TIDE) of the mean turbulent nitrate flux in percent relative to TIDE experiment. Areas where $\overline{J_{NO_3}(z_N)}$ is zero masked for clarity. (C) $\overline{J_{NO_3}(z_N)}$ during the period of strongest stratification (15 July – 15 August, mean for 2011–2015) in Celtic Sea. Dashed black contours indicate 100-, 150-, and 200-m isobaths. (D) Mean distance Δz_{NB} between the nutricline and the depth at which the eddy diffusivity $\overline{K_V}$ falls below $10^{-3} \text{ m}^2 \text{ s}^{-1}$ in the bottom layer for 15 July – 15 August (mean for 2011–2015). Please note non-proportional colorbar discretization in (A, C).

nitrate fluxes along the Celtic Sea shelf break in Figures 10A–C extends approximately 10–40 km onto the shelf. This also agrees with the observed dissipation of the majority of baroclinic energy within tens of kilometers of the generation site (Pingree et al., 1986; Inall et al., 2011).

Figure 10C further indicates elevated $\overline{J_{NO_3}(z_N)}$ at small-scale bathymetric features throughout the Celtic Sea, with mean mixing rates of $0.5 - 3 \text{ mmol N m}^{-2} \text{ d}^{-1}$ at the respective ridges and sea banks. $\overline{J_{NO_3}(z_N)}$ shown in Figure 10C reaches values of up to $10 \text{ mmol N m}^{-2} \text{ d}^{-1}$ at the distinct Jones Bank, which is well within the range of observed mixing rates attributed to local internal lee wave generation (Tweddle et al., 2013; $0.8 - 52 \text{ mmol N m}^{-2} \text{ d}^{-1}$).

Background turbulent nitrate fluxes across the nutricline are overall higher on the narrow North-Western Approaches than in

the southwestern Celtic Sea. Figure 10A shows elevated $\overline{J_{NO_3}(z_N)}$ in some areas along the shelf break of the NWA where the surface and bottom layer are well separated ($\Delta z_{NB} \gg 30 \text{ m}$). $\overline{J_{NO_3}(z_N)}$ is up to $15 \text{ mmol N m}^{-2} \text{ d}^{-1}$ along the shelf break northwest of Ireland at around $54.5 - 55.5^\circ \text{N}$, where upper-slope bathymetry is irregular and features a distinct canyon (Huthnance et al., 2022). $\overline{J_{NO_3}(z_N)}$ is also elevated ($1 - 4 \text{ mmol N m}^{-2} \text{ d}^{-1}$, locally up to $18 \text{ mmol N m}^{-2} \text{ d}^{-1}$) along the shelf break of and on the Malin Shelf at around $56 - 57^\circ \text{N}$, in an area where Figure 7B shows high internal tide activity and mixing by internal tides has been observed (Sherwin, 1988; Rippeth and Inall, 2002). A small area of high $\overline{J_{NO_3}(z_N)}$ further occurs on the shelf break of Hebrides Shelf at around $7 - 8^\circ \text{W}$; here, Figure 10A shows values of up to $20 \text{ mmol N m}^{-2} \text{ d}^{-1}$. $\overline{J_{NO_3}(z_N)}$ on the northern North Sea shelf and shelf break is comparatively low.

Small patches of elevated $\overline{J_{NO_3}(z_N)}$ with up to 5 mmol N m⁻²d⁻¹ occur at the shelf break north of the Fair Isle Channel and the Shetland islands. A small area at northwestern edge of the Norwegian Trench potentially affected by the low salinity Baltic Sea outflow also shows $\overline{J_{NO_3}(z_N)}$ of up to 20 mmol N m⁻²d⁻¹.

The impact of the barotropic tide in the deep regions along the shelf break of the NWES is negligible ($\Delta Z_{NB} \gg 30$ m in Figure 10D). Figure 10B nevertheless shows that tidal forcing accounts for >60% of locally elevated $\overline{J_{NO_3}(z_N)}$ in the region along the Celtic Sea shelf break during the investigated period of strongest stratification. Tidal forcing also accounts for >40%–60% of the locally elevated $\overline{J_{NO_3}(z_N)}$ on the Malin Shelf. Positive $\Delta \overline{J_{NO_3}(z_N)}$ further correlates with elevated $\overline{J_{NO_3}(z_N)}$ on the northern flank of the Porcupine Bank, the Hebrides Shelf at around 7–8°W and the shelf break section north of the Fair Isle Channel. Sites of positive $\Delta \overline{J_{NO_3}(z_N)}$ generally feature relevant internal tide activity (Figure 7B), whereas regions of low internal tide activity along the shelf break of the NWES partially feature low or negative $\Delta \overline{J_{NO_3}(z_N)}$. The finding that $\Delta \overline{J_{NO_3}(z_N)}$ predominantly explains locally elevated $\overline{J_{NO_3}(z_N)}$ along the shelf break and the coherence with sites of high internal tide activity shows that the vertical mixing along the shelf break is caused by the resolved kilometrical-scale internal tide field in the region. The dissipation of on-shelf propagating low-mode internal tides vertically mixes nutrients into the euphotic zone and can contribute to the positive tidal NPP response identified for the shelf break regions in Figures 6B–D.

The emergence of substantially tidally elevated pycnocline mixing rates in proximity to internal tide generation sites suggests that resolving kilometrical-scale internal tides locally reduces the mid-water mixing deficiency commonly identified for stratified shelf regimes in ocean models (Simpson et al., 1996; Burchard et al., 2002; Rippeth, 2005). Our results here support Graham et al. (2018a), who suggested that a reduction of a warm SST bias along the Celtic Sea shelf break in their kilometrical-scale AMM15 NEMO model configuration was due to enhanced mixing by resolved internal tides. Pycnocline mixing simulated with a hydrostatic model like SCHISM will still likely underestimate mixing by the fully non-hydrostatic internal wave field (Vlasenko et al., 2014). Our results thus only constitute a lower bound for the impact of internal tides on shelf primary production. An improved representation of the non-linear interaction of wind-generated inertial oscillations and internal tides would also further improve the parameterization

of the magnitude and episodic nature of mixing within the pycnocline (Davies and Xing, 2003; Hopkins et al., 2014), with potential impacts in central shelf areas as well. The representation and potentials for such non-linear interaction in kilometrical-scale regional ocean models is particularly interesting in this regard.

3.5 Impact of tide-generated pycnocline mixing on summer primary productivity

We further assess the contribution of tide-induced vertical mixing to the overall tidal NPP response in summer for the shelf areas along the shelf break. We compute tidally generated potential new production (PNP; Eq. 6) using the sum of tide-generated mean turbulent nitrate fluxes across the nutricline, i.e., $\Delta J_{NO_3}(z_N)$, over the summer months (JJA; mean for 2011–2015). We only consider stably stratified areas with $PEA > 50$ Jm⁻³, which explicitly excludes the tidal frontal areas. We further isolate the contribution of the internal-tide field from $\Delta J_{NO_3}(z_N)$ by masking regions with $\Delta Z_{NB} < 30$ m and only considering the shelf area resolved at kilometrical-scale horizontal resolution. The results are summarized in Table 3.

Tide-generated potential new production sustained by vertical mixing across the pycnocline explains 20% (0.23 Mt C) of the mean tidal summer NPP response (JJA; 2011–2015) in the SWC subarea, with around 50% of PNP attributable to mixing by the internal tide alone (Table 3). Tide-generated pycnocline mixing in summer therefore only sustains ~ 3% of mean annual primary production in the SWC subarea. The remaining difference in mean summer NPP between the TIDE and NOTIDE experiments in the southwest Celtic Sea (0.92 Mt C; 80%) suggests that other tidally modulated processes are relevant for local primary production as well.

An intensification of regenerated primary production in the surface layer with tidal forcing, potentially associated with the delay of the spring bloom with tidal forcing (see Sect. 3.2) or re-entrainment of organic matter into the surface layer, could also play a role in the tidal NPP response in the Celtic Sea. Huthnance et al. (2022) further showed baroclinic on-shelf transport by internal tides at mooring stations at the Celtic Sea shelf break in summer. Graham et al. (2018b) also found substantial on-shelf transports along the pycnocline and in the surface layer at the Celtic Sea shelf break in late spring and summer and attributed the on-

TABLE 3 Overview of tidal impacts on summer net primary production in subareas along the shelf break.

Subarea	Internal-tide-generated summer PNP	Tide-generated summer PNP	Tidal summer NPP response	Ratio of tide-generated PNP to tidal summer NPP response
	[Mt C]	[Mt C]	[Mt C]	
SWC	0.12	0.23	1.15	20%
MS	0.03	0.08	0.08	92%
HS	0.03	0.06	0.09	65%
NNS	0.04	0.04	0.13	30%

Only stably stratified ($PEA > 50$ Jm⁻³) segments of the subareas are considered. Tidal summer NPP response is computed as the sum of vertically integrated mean NPP for summer months (JJA; 2011–2015). Potential new production (PNP) is calculated with Eq. 6 using the sum of mean summer (JJA; 2011–2015) tide-generated turbulent nitrate fluxes across nutricline ($\Delta \overline{J_{NO_3}(z_N)}$). Isolation of internal-tide-generated PNP is described in Sect. 3.5.

shelf transport at internal depths to internal tides resolved in their kilometrical-scale NEMO AMM15 model configuration. Tide-driven on-shelf transport would explain higher early summer nutrient concentrations in the TIDE experiment found in the outer shelf regions along the Celtic Sea shelf break for both the surface layer (>20 m; Figure 8A) and at internal depths (20–100 m; Figure 8B) in our study. In combination, the increased lateral on-shelf transport of nutrients from the tidally enhanced shelf break front (Figures 6B, 8A) and vertical mixing by internal tides likely account for the majority of the tidal response of summer NPP in the region. Recent work by Tinker et al. (2022) has also shown an impact of tidal forcing on the residual circulation on the NWES, with a pronounced tidal impact on the continental slope current. Tidal flow can additionally influence local circulation through topographically driven residual eddies, which are resolved at kilometrical-scale horizontal resolution in the Celtic Sea (Polton, 2015). Changes in the residual circulation potentially affect the nutrient distribution and biological productivity in the southwestern Celtic Sea. A detailed analysis of the different tidal impacts on cross-shelf horizontal transports is however beyond the scope of this study.

Analysis of potential new production driven by vertical mixing is more complex on the narrow shelves of the North-Western Approaches. The surface layer on the North-Western Approaches is not nutrient depleted in summer (Savidge and Lennon, 1987; Painter et al., 2017) because of cross-shelf exchange with nutrient-rich North Atlantic current water masses and upwelling at the shelf break (Huthnance et al., 2022). The persistent availability of nutrients in the surface layer throughout summer effectively limits the local NPP response to additional nutrient supply by tidal processes, which is particularly evident in tidal frontal zones (see Figure 6B). Table 3 nevertheless shows that tide-generated potential new production supplied by vertical mixing across the pycnocline can explain most of the low tidal response of summer NPP in the stratified areas of the Malin Shelf (92%) and Hebrides Shelf (65%). Tide-generated potential new production however only accounts for 30% of the tidal summer NPP response in the northern North Sea, suggesting relevant contributions of other tidally modulated processes here as well.

4 Conclusions

We introduce the flexible SCHISM-ECOSMO NWES-IT configuration and apply it to quantify the impact of barotropic and baroclinic tides on primary production on the NWES. The model validation demonstrates the reasonable simulation of the general hydrography and relevant biogeochemical cycles on the NWES. The applied strategy of local grid refinement shows high efficiency in computational cost and storage requirements, as the number of grid nodes is reduced by a factor of ~6 compared with a uniform high-resolution configuration. This makes the NWES-IT configuration a powerful tool for the investigation of kilometrical-scale physical processes relevant for shelf ecosystems and the continental shelf carbon pump.

Our results suggest that tidal forcing increases biological productivity on the NWES and that around 16% (14.47 Mt C) of annual mean primary production on the shelf is related to tidal forcing. Our study explored the hydrodynamic control of primary production on the shelf and identified a dominant role of tides for structuring primary production in shallow inner shelf regions like the southern and central North Sea, the English Channel, and the Irish Sea. Vertical mixing of nutrients by the barotropic tide particularly invigorates primary production in the tidal frontal regions of the NWES. Tidal mixing and the resuspension of suspended matter however also decrease primary production in shallow permanently mixed regions of the NWES.

A substantial increase of mean annual primary productivity by +25% (1.53 Mt C) was shown for the deep southwestern Celtic Sea. Tidal forcing mainly enhanced NPP in the southwestern Celtic Sea during the summer productive period. Tide-generated turbulent nutrient mixing across the pycnocline explains approximately one-fifth of the tidal response of summer NPP in the southwestern Celtic Sea. The overall contribution of tide-generated pycnocline mixing to mean annual primary production in the southwestern Celtic Sea is small (only around ~3%). Around 50% of the tide-generated pycnocline mixing in the southwestern Celtic Sea is attributed to the kilometrical-scale internal tide field resolved in the NWES-IT configuration. The large unaccounted remainder of the tidal response of summer NPP found in this study suggests that the tidal NPP response in the southwestern Celtic Sea is caused by a combination of processes. The enhancement of lateral on-shelf transport by tidal forcing, e.g., by internal tides along the pycnocline, is likely particularly important for primary production in the southwestern Celtic Sea. Tidal forcing only plays a minor role for primary production along the shelf break of the North-Western Approaches and the northern North Sea. The high productivity in these regions is rather due to nutrients supplied by cross-shelf exchange with nutrient-rich North Atlantic current water masses and upwelling at the shelf break.

Tidally enhanced turbulent mixing of nutrients across the pycnocline will likely affect the *f* ratio of summer primary production in the stratified regions of the NWES. The *f* ratio, which is the rate of new production to total primary production, is a relevant control for the oceanic uptake of atmospheric CO₂. A tidally enhanced biological carbon pump may increase sequestration of atmospheric CO₂ in shelf sediments or *via* off-shelf transport in the continental shelf carbon pump. As much of the tidal NPP response occurs in the frontal areas of the NWES, the particular dynamics of primary production in and adjacent to tidal fronts merit careful consideration in future work on the shelf carbon cycle. The substantial overall tidal impact on primary production on the NWES could potentially lead to a contribution of long-term tidal variations (e.g., the 18.61-year nodal cycle or the 8.85-year lunar perigee cycle) to long-term variability of marine ecosystem dynamics and oceanic CO₂ uptake.

The significant contribution of the barotropic and baroclinic tide to primary production on the NWES identified in this study further underlines the need to accurately assess and constrain tidal impacts on oceanic uptake of atmospheric CO₂. Further research

should also address the potential sensitivity of pycnocline mixing to the increase in thermal stratification in a warming climate (Holt et al., 2010; Mathis et al., 2019). The impact of barotropic and baroclinic tides on primary production found in this study moreover highlights the necessity of their representation in regional and global ocean models. This particularly applies to modeling studies that address regional and global marine carbon cycle dynamics. Kilometrical-scale horizontal resolution will likely remain beyond computational feasibility for large-scale model applications in the near future, although advances in model development were recently made to overcome such conceptual limitations (Mathis et al., 2022). Therefore, further work is required to improve the parameterization of kilometrical-scale physical processes like internal tides.

Data availability statement

The raw data supporting the conclusions of this article will be made available by the authors, without undue reservation.

Author contributions

JK generated the data set, performed the data analysis, and wrote the manuscript. MM, YZ, and CS provided essential background knowledge and advised the study. CS initiated the idea of the study. All authors contributed to conception and design of the study and manuscript revision, and read and approved the submitted version.

Acknowledgments

We would like to acknowledge the contribution by Richard Hofmeister to the development of SCHISM-ECOSMO. We would like to thank Benjamin Jacob and Johannes Pein for helpful advice regarding the SCHISM model. Computational resources were made available by the German Climate Computing Center (DKRZ) through support from the German Federal Ministry of Education and Research (BMBF). We would like to thank the reviewers for

References

- Allen, J. I., Holt, J. T., Blackford, J., and Proctor, R. (2007). Error quantification of a high-resolution coupled hydrodynamic-ecosystem coastal-ocean model: part 2. chlorophyll-a, nutrients and SPM. *J. Mar. Syst.* 68, 381–404. doi: 10.1016/j.jmarsys.2007.01.005
- Aquaveo, L. L. C. (2019). *Surface-water modeling system: reference manual & tutorials* (LLC, Provo, Utah: Aquaveo LLC).
- Baines, P. G. (1982). On internal tide generation models. *Deep Sea Res. Part A. Oceanographic Res. Papers* 29, 307–338. doi: 10.1016/0198-0149(82)90098-X
- Becherer, J., Burchard, H., Carpenter, J. R., Graewe, U., and Merckelbach, L. M. (2022). The role of turbulence in fueling the subsurface chlorophyll maximum in tidally dominated shelf seas. *J. Geophys. Res. Oceans* 127, e2022JC018561. doi: 10.1029/2022JC018561
- Bendtsen, J., and Richardson, K. (2018). Turbulence measurements suggest high rates of new production over the shelf edge in the Northeastern North Sea during summer. *Biogeosciences* 15, 7315–7332. doi: 10.5194/bg-15-7315-2018
- Blumberg, A. F., and Mellor, G. L. (1987). A description of a three-dimensional coastal ocean circulation model. In *Three-Dimensional Coastal Ocean Models*, N.S. Heaps (Ed.), 1–16. doi: 10.1029/CO004p0001
- Boyer, T. P., Garcia, H. E., Locarnini, R. A., Zweng, M. M., Mishonov, A. V., Reagan, J. R., et al. (2018) *World ocean atlas 2018*. Available at: <https://www.ncei.noaa.gov/archive/accession/NCEI-WOA18> (Accessed 29, 2022).
- Bruggeman, J., and Bolding, K. (2014). A general framework for aquatic biogeochemical models. *Environ. Model. Software* 61, 249–265. doi: 10.1016/j.envsoft.2014.04.002
- Burchard, H., Bolding, K., Rippeth, T. P., Stips, A., Simpson, J. H., and Sündermann, J. (2002). Microstructure of turbulence in the Northern North Sea: a comparative study of observations and model simulations. *Processes Vertical Exchange Shelf Seas (PROVEX) Part I* 47, 223–238. doi: 10.1016/S1385-1101(02)00126-0

their time and insights. They have helped improve the manuscript. We would like to thank ICDC, CEN, University Hamburg, for data support. This study has been conducted using E.U. Copernicus Marine Service Information; <https://doi.org/10.48670/moi-00169>; <http://dx.doi.org/10.17183/REFMAR>; <https://doi.org/10.48670/moi-00281>. The manuscript contains data supplied by the Natural Environmental Research Council (NERC). The tidal validation and analysis in this manuscript used tools and open data sets made publicly available under a CECILL license at https://github.com/KarenGuihou/tidal_analysis. The research was funded by the Deutsche Forschungsgemeinschaft (DFG, German Research Foundation) under Germany's Excellence Strategy – EXC 2037 'CLICCS - Climate, Climatic Change, and Society' – Project Number: 390683824 and contributes to the CLICCS subproject A5 – The Land-Ocean Transition Zone. The article processing charges for this open-access publication were covered by the Helmholtz-Zentrum Hereon.

Conflict of interest

The authors declare that the research was conducted in the absence of any commercial or financial relationships that could be construed as a potential conflict of interest.

Publisher's note

All claims expressed in this article are solely those of the authors and do not necessarily represent those of their affiliated organizations, or those of the publisher, the editors and the reviewers. Any product that may be evaluated in this article, or claim that may be made by its manufacturer, is not guaranteed or endorsed by the publisher.

Supplementary material

The Supplementary Material for this article can be found online at: <https://www.frontiersin.org/articles/10.3389/fmars.2023.1206062/full#supplementary-material>

- Caldwell, P. C., Merrifield, M. A., and Thompson, P. R. (2015) Sea Level measured by tide gauges from global oceans — the joint archive for Sea level holdings (NCEI accession 0019568): version 5.5. In: *Dataset* (Accessed 02, 2022).
- Capuzzo, E., Lynam, C. P., Barry, J., Stephens, D., Forster, R. M., Greenwood, N., et al. (2018). A decline in primary production in the North Sea over 25 years, associated with reductions in zooplankton abundance and fish stock recruitment. *Global Change Biol.* 24, e352–e364. doi: 10.1111/gcb.13916
- Capuzzo, E., Painting, S. J., Forster, R. M., Greenwood, N., Stephens, D. T., and Mikkelsen, O. A. (2013). Variability in the sub-surface light climate at ecohydrodynamically distinct sites in the North Sea. *Biogeochemistry* 113, 85–103. doi: 10.1007/s10533-012-9772-6
- Cloern, J. E. (1991). Tidal stirring and phytoplankton bloom dynamics in an estuary. *J. Mar. Res.* 49, 203–221. doi: 10.1357/002224091784968611
- Cullen, J. J. (2015). Subsurface chlorophyll maximum layers: enduring enigma or mystery solved? *Annu. Rev. Mar. Sci.* 7, 207–239. doi: 10.1146/annurev-marine-010213-135111
- Daewel, U., and Schrum, C. (2013). Simulating long-term dynamics of the coupled North Sea and Baltic Sea ecosystem with ECOSMO II: model description and validation. *J. Mar. Syst.* 119–120, 30–49. doi: 10.1016/j.jmarsys.2013.03.008
- Davies, A. M., and Xing, J. (2003). On the interaction between internal tides and wind-induced near-inertial currents at the shelf edge. *J. Geophys. Res.* 108(C3). doi: 10.1029/2002JC001375
- Dugdale, R. C., and Goering, J. J. (1967). UPTAKE OF NEW AND REGENERATED FORMS OF NITROGEN IN PRIMARY PRODUCTIVITY I. *Limnol. Oceanogr.* 12, 196–206. doi: 10.4319/lo.1967.12.2.0196
- Fofonoff, N. P., and Millard, R. C. (1983). Algorithms for computation of fundamental properties of seawater. *Unesco Tech. papers Mar. Sci.* 44. doi: 10.25607/OBP-1450
- Frankignoulle, M., and Borges, A. V. (2001). European Continental shelf as a significant sink for atmospheric carbon dioxide. *Global Biogeochem. Cycles* 15, 569–576. doi: 10.1029/2000GB001307
- Geyer, B. (2017). *coastDat-3_COSMO-CLM_ERAI* (World Data Center for Climate (WDCC) at DKRZ). Available at: http://cera-www.dkrz.de/WDCC/ui/Compact.jsp?acronym=coastDat-3_COSMO-CLM_ERAI.
- Graham, J. A., O'Dea, E., Holt, J., Polton, J., Hewitt, H. T., Furner, R., et al. (2018a). AMM15: a new high-resolution NEMO configuration for operational simulation of the European north-west shelf. *Geosci. Model. Dev.* 11, 681–696. doi: 10.5194/gmd-11-681-2018
- Graham, J. A., Rosser, J. P., O'Dea, E., and Hewitt, H. T. (2018b). Resolving shelf break exchange around the European Northwest shelf. *Geophys. Res. Lett.* 45, 12,386–12,395. doi: 10.1029/2018GL079399
- Green, J. A. M., Simpson, J. H., Legg, S., and Palmer, M. R. (2008). Internal waves, baroclinic energy fluxes and mixing at the European shelf edge. *Continental Shelf Res.* 28, 937–950. doi: 10.1016/j.csr.2008.01.014
- Guihou, K., Polton, J., Harle, J., Wakelin, S., O'Dea, E., and Holt, J. (2018). Kilometric scale modeling of the North West European shelf seas: exploring the spatial and temporal variability of internal tides. *J. Geophys. Res. Oceans* 123, 688–707. doi: 10.1002/2017JC012960
- Hall, R. A., Berx, B., and Damerell, G. M. (2019). Internal tide energy flux over a ridge measured by a co-located ocean glider and moored acoustic Doppler current profiler. *Ocean Sci.* 15, 1439–1453. doi: 10.5194/os-15-1439-2019
- Hickman, A. E., Moore, C. M., Sharples, J., Lucas, M. I., Tilstone, G. H., Krivtsov, V., et al. (2012). Primary production and nitrate uptake within the seasonal thermocline of a stratified shelf sea. *Mar. Ecol. Prog. Ser.* 463, 39–57. doi: 10.3354/meps09836
- Hinrichs, I., and Gouretski, V. (2019). *Baltic And north Sea climatology hydrographic part (Version 1.1)* (World Data Center for Climate (WDCC) at DKRZ). doi: 10.26050/WDCC/BNSClimHydrov1.1
- Hofmeister, R., Flöser, G., and Schartau, M. (2017). Estuary-type circulation as a factor sustaining horizontal nutrient gradients in freshwater-influenced coastal systems. *Geo-Marine Lett.* 37, 179–192. doi: 10.1007/s00367-016-0469-z
- Holt, J., Butenschön, M., Wakelin, S. L., Artioli, Y., and Allen, J. I. (2012). Oceanic controls on the primary production of the Northwest European continental shelf: model experiments under recent past conditions and a potential future scenario. *Biogeosciences* 9, 97–117. doi: 10.5194/bg-9-97-2012
- Holt, J., Schrum, C., Cannaby, H., Daewel, U., Allen, I., Artioli, Y., et al. (2016). Potential impacts of climate change on the primary production of regional seas: a comparative analysis of five European seas. *Prog. IN OCEANOGRAPHY* 140, 91–115. doi: 10.1016/j.pocean.2015.11.004
- Holt, J., and Umlauf, L. (2008). Modelling the tidal mixing fronts and seasonal stratification of the Northwest European continental shelf. *Continental Shelf Res.* 28, 887–903. doi: 10.1016/j.csr.2008.01.012
- Holt, J., Wakelin, S., Lowe, J., and Tinker, J. (2010). The potential impacts of climate change on the hydrography of the Northwest European continental shelf. *Prog. IN OCEANOGRAPHY* 86, 361–379. doi: 10.1016/j.pocean.2010.05.003
- Hopkins, J. E., Stephenson, G. R., Green, J. A. M., Inall, M. E., and Palmer, M. R. (2014). Storms modify baroclinic energy fluxes in a seasonally stratified shelf sea: inertial-tidal interaction. *J. Geophys. Res. Oceans* 119, 6863–6883. doi: 10.1002/2014JC010011
- Hu, S., Townsend, D. W., Chen, C., Cowles, G., Beardsley, R. C., Ji, R., et al. (2008). Tidal pumping and nutrient fluxes on Georges bank: a process-oriented modeling study. *J. Mar. Syst.* 74, 528–544. doi: 10.1016/j.jmarsys.2008.04.007
- Huthnance, J., Hopkins, J., Berx, B., Dale, A., Holt, J., Hosegood, P., et al. (2022). Ocean shelf exchange, NW European shelf seas: measurements, estimates and comparisons. *Prog. IN OCEANOGRAPHY* 202, 102760. doi: 10.1016/j.pocean.2022.102760
- ICES (1983). Flushing times of the North Sea. *ICES Cooperative Res. Rep.* 123, 153.
- Inall, M., Aleynik, D., Boyd, T., Palmer, M., and Sharples, J. (2011). Internal tide coherence and decay over a wide shelf sea. *Geophys. Res. Lett.* 38, n/a–n/a. doi: 10.1029/2011GL049943
- Intergovernmental Oceanographic Commission (1985). “Manual on sea level measurement and interpretation,” in *Volume I - basic procedures* (Paris, France: UNESCO) 1, 83. doi: 10.25607/OBP-1420
- Joint, I., and Groom, S. B. (2000). Estimation of phytoplankton production from space: current status and future potential of satellite remote sensing. *J. Exp. Mar. Biol. Ecol.* 250, 233–255. doi: 10.1016/S0022-0981(00)00199-4
- Joint, I., and Pomroy, A. (1993). PHYTOPLANKTON BIOMASS AND PRODUCTION IN THE SOUTHERN NORTH-SEA. *Mar. Ecol. Prog. Ser.* 99, 169–182. doi: 10.3354/meps099169
- Joint, I., Wollast, R., Chou, L., Batten, S., Elskens, M., Edwards, E., et al. (2001). Pelagic production at the Celtic Sea shelf break. *DEEP-SEA Res. Part II-TOPICAL Stud. IN OCEANOGRAPHY* 48, 3049–3081. doi: 10.1016/S0967-0645(01)00032-7
- Kamp, A., and Witte, U. (2005). Processing of ¹³C-labelled phytoplankton in a fine-grained sandy-shelf sediment (North Sea): relative importance of different macrofauna species. *Mar. Ecol. Prog. Ser.* 297, 61. doi: 10.3354/meps297061
- Kantha, L. H., and Clayson, C. A. (1994). An improved mixed layer model for geophysical applications. *J. Geophys. Res.* 99, 25235–25266. doi: 10.1029/94JC02257
- Laruelle, G. G., Lauerwald, R., Pfeil, B., and Regnier, P. (2014). Regionalized global budget of the CO₂ exchange at the air-water interface in continental shelf seas. *Global Biogeochem. Cycles* 28, 1199–1214. doi: 10.1002/2014GB004832
- Legge, O., Johnson, M., Hicks, N., Jickells, T., Diesing, M., Aldridge, J., et al. (2020). Carbon on the Northwest European shelf: contemporary budget and future influences. *Front. Mar. Sci.* 7. doi: 10.3389/fmars.2020.00143
- Le Guitton, M., Soetaert, K., Sinninghe Damsté, J. S., and Middelburg, J. J. (2017). A seasonal study of particulate organic matter composition and quality along an offshore transect in the Southern North Sea. *Estuarine Coast. Shelf Sci.* 188, 1–11. doi: 10.1016/j.eccs.2017.02.002
- Lin, L., Liu, H., Huang, X., Fu, Q., and Guo, X. (2022). Effect of tides on river water behavior over the eastern shelf seas of China. *Hydrology Earth System Sci.* 26, 5207–5225. doi: 10.5194/hess-26-5207-2022
- Lyard, F. H., Allain, D. J., Cancet, M., Carrère, L., and Picot, N. (2021). FES2014 global ocean tide atlas: design and performance. *Ocean Sci.* 17, 615–649. doi: 10.5194/os-17-615-2021
- Mann, K. H., and Lazier, J. R. (2013). *Dynamics of marine ecosystems: biological-physical interactions in the oceans. 3rd ed.* (John Wiley & Sons, Ltd).
- Mathis, M., Elizalde, A., and Mikolajewicz, U. (2019). The future regime of Atlantic nutrient supply to the Northwest European shelf. *J. Mar. Syst.* 189, 98–115. doi: 10.1016/j.jmarsys.2018.10.002
- Mathis, M., Logemann, K., Maerz, J., Lacroix, F., Hagemann, S., Chegini, F., et al. (2022). Seamless integration of the coastal ocean in global marine carbon cycle modeling. *J. Adv. Model. Earth Syst.* 14, e2021MS002789. doi: 10.1029/2021MS002789
- New, A. L., and Pingree, R. D. (1990). Evidence for internal tidal mixing near the shelf break in the Bay of Biscay. *Deep Sea Res. Part A. Oceanographic Res. Papers* 37, 1783–1803. doi: 10.1016/0198-0149(90)90078-A
- Nissen, C. (2014). *Physical-biogeochemical couplings in the land-ocean transition zone* (Bergen: The University of Bergen).
- O'Dea, E. J., Arnold, A. K., Edwards, K. P., Furner, R., Hyder, P., Martin, M. J., et al. (2012). An operational ocean forecast system incorporating NEMO and SST data assimilation for the tidally driven European North-West shelf. *J. OF OPERATIONAL OCEANOGRAPHY* 5, 3–17. doi: 10.1080/1755876X.2012.11020218
- Painter, S. C., Hartman, S. E., Kivimäe, C., Salt, L. A., Clargo, N. M., Daniels, C. J., et al. (2017). The elemental stoichiometry (C, Si, n, p) of the Hebrides shelf and its role in carbon export. *Prog. IN OCEANOGRAPHY* 159, 154–177. doi: 10.1016/j.pocean.2017.10.001
- Palmer, M. R., Inall, M. E., and Sharples, J. (2013). The physical oceanography of Jones bank: a mixing hotspot in the Celtic Sea. *Prog. IN OCEANOGRAPHY* 117, 9–24. doi: 10.1016/j.pocean.2013.06.009
- Pätsch, J., Burchard, H., Dieterich, C., Gräwe, U., Gröger, M., Mathis, M., et al. (2017). An evaluation of the North Sea circulation in global and regional models relevant for ecosystem simulations. *Ocean Model.* 116, 70–95. doi: 10.1016/j.ocemod.2017.06.005
- Pein, J., Eisele, A., Sanders, T., Daewel, U., Stanev, E. V., van Beusekom, J. E. E., et al. (2021). Seasonal stratification and biogeochemical turnover in the freshwater reach of a partially mixed dredged estuary. *Front. Mar. Sci.* 8. doi: 10.3389/fmars.2021.623714
- Pingree, R. D., and Mardell, G. T. (1981). Slope turbulence, internal waves and phytoplankton growth at the Celtic Sea shelf-break. *Philos. Trans. R. Soc. London. Ser. A Math. Phys. Sci.* 302(1472), 663–682. doi: 10.1098/rsta.1981.0191

- Pingree, R. D., and Mardell, G. T. (1985). Solitary internal waves in the Celtic Sea. *Prog. IN OCEANOGRAPHY* 14, 431–441. doi: 10.1016/0079-6611(85)90021-7
- Pingree, R. D., Mardell, G. T., Holligan, P. M., Griffiths, D. K., and Smithers, J. (1982). Celtic Sea and armorican current structure and the vertical distributions of temperature and chlorophyll. *Continental Shelf Res.* 1, 99–116. doi: 10.1016/0278-4343(82)90033-4
- Pingree, R. D., Mardell, G. T., and New, A. L. (1986). Propagation of internal tides from the upper slopes of the bay of Biscay. *Nature* 321, 154–158. doi: 10.1038/321154a0
- Pingree, R. D., and New, A. L. (1995). Structure, seasonal development and sunglint spatial coherence of the internal tide on the celtic and armorican shelves and in the bay of Biscay. *Deep Sea Res. Part I: Oceanographic Res. Papers* 42, 245–284. doi: 10.1016/0967-0637(94)00041-P
- Pingree, R. D., Pugh, P. R., Holligan, P. M., and Forster, G. R. (1975). Summer phytoplankton blooms and red tides along tidal fronts in the approaches to the English channel. *Nature* 258, 672–677. doi: 10.1038/258672a0
- Polton, J. A. (2015). Tidally induced mean flow over bathymetric features: a contemporary challenge for high-resolution wide-area models. *Geophysical Astrophysical Fluid Dynamics* 109, 207–215. doi: 10.1080/03091929.2014.952726
- Porter, E. T., Mason, R. P., and Sanford, L. P. (2010). Effect of tidal resuspension on benthic–pelagic coupling in an experimental ecosystem study. *Mar. Ecol. Prog. Ser.* 413, 33–53. doi: 10.3354/meps08709
- Prins, T., Smaal, A. C., Pouwer, A. J., and Dankers, N. (1996). Filtration and resuspension of particulate matter and phytoplankton on an intertidal mussel bed in the oosterschelde estuary (SW Netherlands). *Mar. Ecol. Prog. Ser.* 142, 121–134. doi: 10.3354/meps142121
- Richardson, K., Visser, A. W., and Pedersen, F. B. (2000). Subsurface phytoplankton blooms fuel pelagic production in the North Sea. *J. Plankton Res.* 22, 1663–1671. doi: 10.1093/plankt/22.9.1663
- Rippeth, T. P. (2005). Mixing in seasonally stratified shelf seas: a shifting paradigm. *Philos. Trans. Ser. A Mathematical physical Eng. Sci.* 363, 2837–2854. doi: 10.1098/rsta.2005.1662
- Rippeth, T. P., and Inall, M. E. (2002). Observations of the internal tide and associated mixing across the malin shelf. *J. Geophys. Res.* 107, 928. doi: 10.1029/2000JC000761
- Rippeth, T. P., Lincoln, B. J., Kennedy, H. A., Palmer, M. R., Sharples, J., and Williams, C. A. J. (2014). Impact of vertical mixing on sea surface pCO₂ in temperate seasonally stratified shelf seas. *J. Geophys. Res. Oceans* 119, 3868–3882. doi: 10.1002/2014JC010089
- Rippeth, T. P., Wiles, P., Palmer, M. R., Sharples, J., and Tweddle, J. (2009). The diapycnal nutrient flux and shear-induced diapycnal mixing in the seasonally stratified Western Irish Sea. *Continental Shelf Res.* 29, 1580–1587. doi: 10.1016/j.csr.2009.04.009
- Samuelsen, A., Schrum, C., Yumruketepe, V.Ç., Daewel, U., and Roberts, E. M. (2022). Environmental change at deep-sea sponge habitats over the last half century: a model hindcast study for the age of anthropogenic climate change. *Front. Mar. Sci.* 9. doi: 10.3389/fmars.2022.737164
- Savidge, G., and Lennon, H. J. (1987). Hydrography and phytoplankton distributions in North-west Scottish waters. *Continental Shelf Res.* 7, 45–66. doi: 10.1016/0278-4343(87)90063-X
- Schrum, C., Alekseeva, I., and St. John, M. (2006). Development of a coupled physical–biological ecosystem model ECOSMO. *J. Mar. Syst.* 61, 79–99. doi: 10.1016/j.jmarsys.2006.01.005
- Sharples, J. (2008). Potential impacts of the spring-neap tidal cycle on shelf sea primary production. *J. Plankton Res.* 30, 183–197. doi: 10.1093/plankt/fbm088
- Sharples, J., Moore, C. M., Hickman, A. E., Holligan, P. M., Tweddle, J. F., Palmer, M. R., et al. (2009). Internal tidal mixing as a control on continental margin ecosystems. *Geophys. Res. Lett.* 36, 249. doi: 10.1029/2009GL040683
- Sharples, J., Moore, M. C., Rippeth, T. P., Holligan, P. M., Hydes, D. J., Fisher, N. R., et al. (2001). Phytoplankton distribution and survival in the thermocline. *Limnol. Oceanogr.* 46, 486–496. doi: 10.4319/lo.2001.46.3.0486
- Sharples, J., Tweddle, J. F., Mattias Green, J. A., Palmer, M. R., Kim, Y.-N., Hickman, A. E., et al. (2007). Spring-neap modulation of internal tide mixing and vertical nitrate fluxes at a shelf edge in summer. *Limnol. Oceanogr.* 52, 1735–1747. doi: 10.4319/lo.2007.52.5.1735
- Sherwin, T. (1988). Analysis of an internal tide observed on the malin shelf, north of Ireland. *J. Phys. Oceanography - J. Phys. OCEANOGR* 18, 1035–1050. doi: 10.1175/1520-0485(1988)018<1035:AOAITO>2.0.CO;2
- Sherwin, T. J. (1991). “Evidence of a deep internal tide in the Faeroe-Shetland channel,” in *Tidal hydrodynamics*, vol. 469–488. Ed. B. B. Parker (New York: John Wiley).
- Simpson, J. H., Crawford, W. R., Rippeth, T. P., Campbell, A. R., and Cheok, J. V. S. (1996). The vertical structure of turbulent dissipation in shelf seas. *J. Phys. Oceanography* 26, 1579–1590. doi: 10.1175/1520-0485(1996)026<1579:TVSOTD>2.0.CO;2
- Simpson, J. H., Crisp, D. J., Hearn, C., Swallow, J. C., Currie, R. I., and Gill, A. E. (1981). The shelf-sea fronts: implications of their existence and behaviour. *Philos. Trans. R. Soc. London. Ser. A Math. Phys. Sci.* 302, 531–546. doi: 10.1098/rsta.1981.0181
- Simpson, J. H., and Hunter, J. R. (1974). Fronts in the Irish Sea. *Nature* 250, 404–406. doi: 10.1038/250404a0
- Taylor, M. H., Akimova, A., Bracher, A., Kempf, A., Kühn, B., and Hélaouié, P. (2021). Using dynamic ocean color provinces to elucidate drivers of North Sea hydrography and ecology. *J. Geophys. Res. Oceans* 126, e2021JC017686. doi: 10.1029/2021JC017686
- Tett, P., and Walne, A. (1995). Observations and simulations of hydrography, nutrients and plankton in the southern north Sea. *Ophelia* 42, 371–416. doi: 10.1080/00785326.1995.10431514
- Thomas, H., Bozec, Y., Elkalay, K., and Baar, H.J.W.de (2004). Enhanced open ocean storage of CO₂ from shelf sea pumping. *Sci. (New York N.Y.)* 304, 1005–1008. doi: 10.1126/science.1095491
- Tinker, J., Polton, J. A., Robins, P. E., Lewis, M. J., and O’Neill, C. K. (2022). The influence of tides on the North West European shelf winter residual circulation. *Front. Mar. Sci.* 9. doi: 10.3389/fmars.2022.847138
- Tsunogai, S., Watanabe, S., and Sato, T. (1999). Is there a “continental shelf pump” for the absorption of atmospheric CO₂? *Tellus B* 51, 701–712. doi: 10.1034/j.1600-0889.1999.t01-2-00010.x
- Tweddle, J. F., Sharples, J., Palmer, M. R., Davidson, K., and McNeill, S. (2013). Enhanced nutrient fluxes at the shelf sea seasonal thermocline caused by stratified flow over a bank. *Prog. IN OCEANOGRAPHY* 117, 37–47. doi: 10.1016/j.ocean.2013.06.018
- Umlauf, L., and Burchard, H. (2003). A generic length-scale equation for geophysical turbulence models. *J. Mar. Res.* 61, 235–265. doi: 10.1357/002224003322005087
- van Haren, H., Maas, L., Zimmerman, J. T. F., Ridderinkhof, H., and Malschaert, H. (1999). Strong inertial currents and marginal internal wave stability in the Central North Sea. *J. Geophys. Res. Lett.* 26, 2993–2996. doi: 10.1029/1999GL002352
- van Leeuwen, S., Tett, P., Mills, D., and van der Molen, J. (2015). Stratified and nonstratified areas in the North Sea: long-term variability and biological and policy implications. *J. Geophys. Res. Oceans* 120, 4670–4686. doi: 10.1002/2014JC010485
- Vlasenko, V., Stashchuk, N., Inall, M. E., and Hopkins, J. E. (2014). Tidal energy conversion in a global hot spot: on the 3-d dynamics of baroclinic tides at the Celtic Sea shelf break. *J. Geophys. Res. Oceans* 119, 3249–3265. doi: 10.1002/2013JC009708
- Vlasenko, V., Stashchuk, N., Palmer, M. R., and Inall, M. E. (2013). Generation of baroclinic tides over an isolated underwater bank. *J. Geophys. Res. Oceans* 118, 4395–4408. doi: 10.1002/jgrc.20304
- Wang, H., Gong, D., Friedrichs, M. A. M., Harris, C. K., Miles, T., Yu, H.-C., et al. (2022). A cycle of wind-driven canyon upwelling and downwelling at Wilmington canyon and the evolution of canyon-upwelled dense water on the MAB shelf. *Front. Mar. Sci.* 9. doi: 10.3389/fmars.2022.866075
- Wang, Z., Li, D., Xue, H., Thomas, A. C., Zhang, Y. J., and Chai, F. (2022). Freshwater transport in the scotian shelf and its impacts on the gulf of Maine salinity. *JGR Oceans* 127, 16. doi: 10.1029/2021JC017663
- Wessel, P., and Smith, W. H. F. (1996). A global, self-consistent, hierarchical, high-resolution shoreline database. *J. Geophys. Res.* 101, 8741–8743. doi: 10.1029/96JB00104
- Whalen, C. B., Lavergne, C., Naveira Garabato, A. C., Klymak, J. M., MacKinnon, J. A., and Sheen, K. L. (2020). Internal wave-driven mixing: governing processes and consequences for climate. *Nat. Rev. Earth Environ.* 1, 606–621. doi: 10.1038/s43017-020-0097-z
- Whiggott, J., Hopkins, J., Sharples, J., Jones, E., and Balfour, C. (2016). Long-term mooring observations of full depth water column structure spanning 17 months, collected in a temperate shelf sea (Celtic Sea) British Oceanographic Data Centre - Natural Environment Research Council, UK. doi: 10.5285/389fe406-ebd9-74fl-e053-6c86abc032a4
- Williams, C., Sharples, J., Green, M., Mahaffey, C., and Rippeth, T. (2013a). The maintenance of the subsurface chlorophyll maximum in the stratified Western Irish Sea. *Limnol. Oceanogr.* 3, 61–73. doi: 10.1215/21573689-2285100
- Williams, C., Sharples, J., Mahaffey, C., and Rippeth, T. (2013b). Wind-driven nutrient pulses to the subsurface chlorophyll maximum in seasonally stratified shelf seas. *Geophys. Res. Lett.* 40, 5467–5472. doi: 10.1002/2013GL058171
- Ye, F., Zhang, Y. J., He, R., Wang, Z., Wang, H. V., and Du, J. (2019). Third-order WENO transport scheme for simulating the baroclinic eddy on an unstructured grid. *Ocean Model.* 143, 101466. doi: 10.1016/j.ocemod.2019.101466
- Ye, F., Zhang, Y. J., Wang, H. V., Friedrichs, M. A., Irby, I. D., Altjeljevic, E., et al. (2018). A 3D unstructured-grid model for Chesapeake bay: importance of bathymetry. *Ocean Model.* 127, 16–39. doi: 10.1016/j.ocemod.2018.05.002
- Ye, F., Zhang, Y. J., Yu, H., Sun, W., Moghimi, S., Myers, E., et al. (2020). Simulating storm surge and compound flooding events with a creek-to-ocean model: importance of baroclinic effects. *Ocean Model.* 145, 101526. doi: 10.1016/j.ocemod.2019.101526
- Yu, H.-C., Zhang, Y. J., Yu, J. C., Terng, C., Sun, W., Ye, F., et al. (2017). Simulating multi-scale oceanic processes around Taiwan on unstructured grids. *Ocean Model.* 119, 72–93. doi: 10.1016/j.ocemod.2017.09.007
- Yumruketepe, V.Ç., Samuelsen, A., and Daewel, U. (2022). ECOSMO II(CHL): a marine biogeochemical model for the north Atlantic and the Arctic. *Geosci. Model. Dev.* 15, 3901–3921. doi: 10.5194/gmd-15-3901-2022
- Zeng, X., Zhao, M., and Dickinson, R. E. (1998). Intercomparison of bulk aerodynamic algorithms for the computation of Sea surface fluxes using TOGA COARE and TAO data. *J. Climate* 11, 2628–2644. doi: 10.1175/1520-0442(1998)011%3C2628:IOBAAF%3E2.0.CO;2
- Zhang, Y. J., Ateljevic, E., Yu, H.-C., Wu, C. H., and Yu, J. C. (2015). A new vertical coordinate system for a 3D unstructured-grid model. *Ocean Model.* 85, 16–31. doi: 10.1016/j.ocemod.2014.10.003

Zhang, Y., and Baptista, A. M. (2008). SELFE: a semi-implicit eulerian–Lagrangian finite-element model for cross-scale ocean circulation. *Ocean Model.* 21, 71–96. doi: 10.1016/j.ocemod.2007.11.005

Zhang, Y. J., Stanev, E. V., and Grashorn, S. (2016a). Unstructured-grid model for the North Sea and Baltic Sea: validation against observations. *Ocean Model.* 97, 91–108. doi: 10.1016/j.ocemod.2015.11.009

Zhang, Y. J., Ye, F., Stanev, E. V., and Grashorn, S. (2016b). Seamless cross-scale modeling with SCHISM. *Ocean Model.* 102, 64–81. doi: 10.1016/j.ocemod.2016.05.002

Zhao, C., Daewel, U., and Schrum, C. (2019). Tidal impacts on primary production in the North Sea. *Earth Syst. Dynam.* 10, 287–317. doi: 10.5194/esd-10-287-2019

Supplementary Material

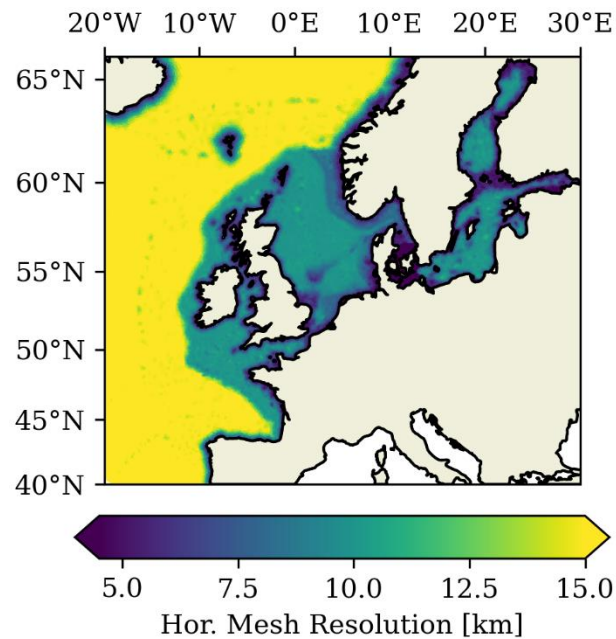
Barotropic and baroclinic tides increase primary production on the North-West European Shelf

Jan Kossack*, Moritz Mathis, Ute Daewel, Yinglong Joseph Zhang, Corinna Schrum

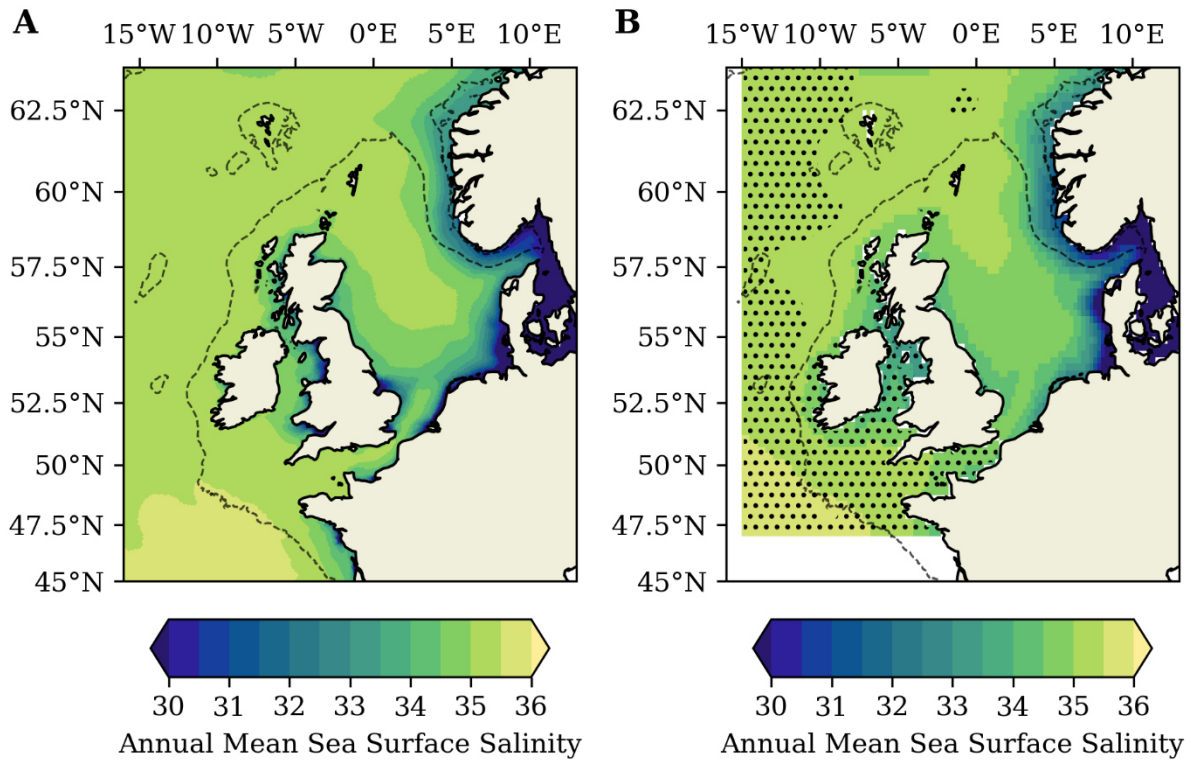
* Correspondence: Jan Kossack: jan.kossack@hereon.de

1 Supplementary Figures and Tables

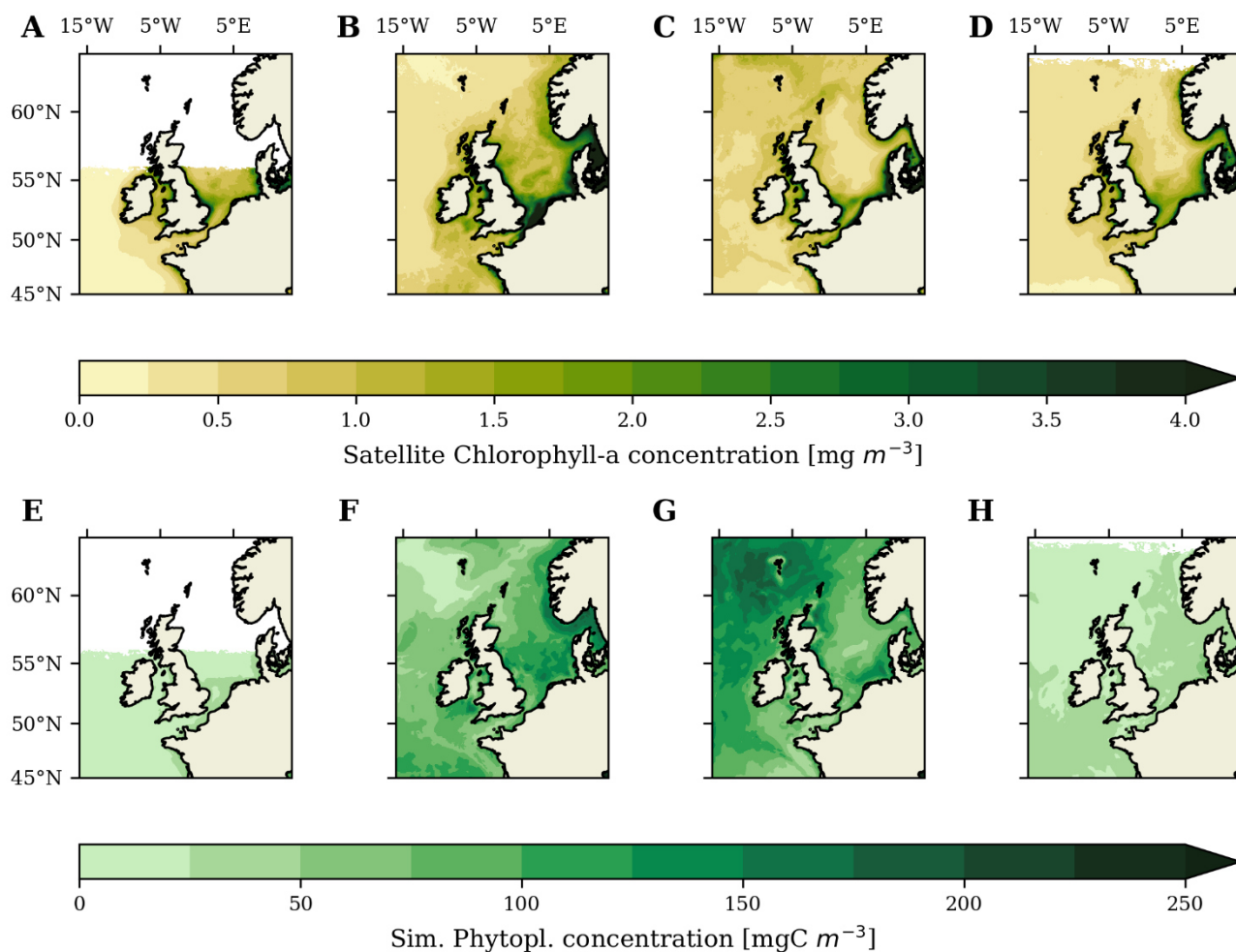
1.1 Supplementary Figures



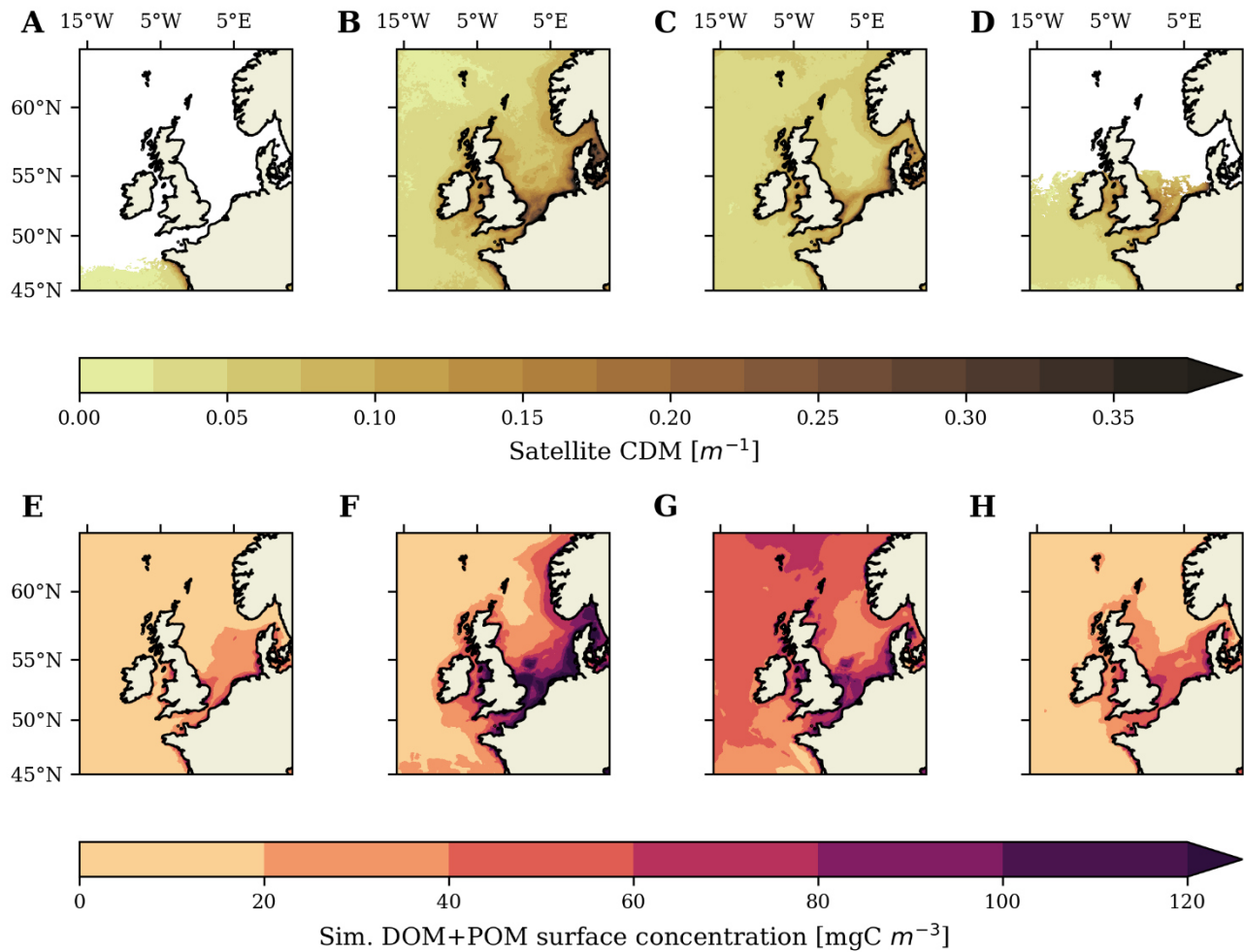
Supplementary Figure S1. Horizontal grid resolution of coarse NWES-LR configuration.



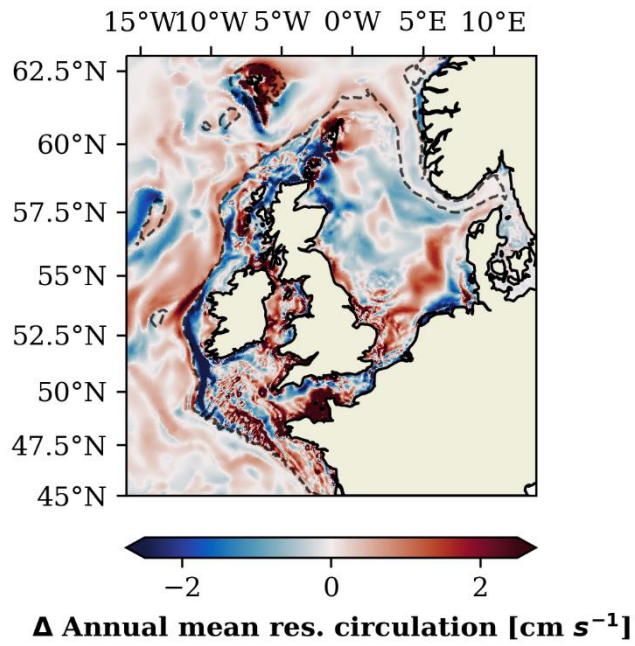
Supplementary Figure S2. Simulated mean annual sea surface salinity for the period 2011-2015 (A) and annual sea surface salinity (1985-2015) from BNSC climatology (B). Patched area indicates interpolation error > 0.4 in BNSC.



Supplementary Figure S3. Seasonal mean (2011-2015) chlorophyll-a concentration in sea water from Copernicus Global Color Satellite Product for winter (A), spring (B), summer (C) and autumn (D). E-H show respective seasonal mean phytoplankton concentration (diatoms + flagellates; 2011-2015) from simulation. The simulated phytoplankton concentration has been depth averaged over the optical depth as described in the Global Color Manual (<https://doi.org/10.48670/moi-00281>, last accessed 06/2023).



Supplementary Figure S4. Seasonal mean volume absorption coefficient of radiative flux in sea water due to dissolved organic matter and other detrital organic particles (CDM, 2011-2015) from Copernicus Global Color Satellite Product for winter (A), spring (B), summer (C) and autumn (D). E-H show respective seasonal mean organic detrital matter (DOM+POM; 2011-2015) concentration in the surface layer from simulation.



Supplementary Figure S5. Difference in annual mean velocity magnitude of the residual circulation (TIDE-NOTIDE; 2011-2015).

1.2 Supplementary Tables

Supplementary Table S1: ECOSMO parameter set used in study.

Definition	Abbr.	Value	Unit
Max. growth rate for Pl	σ_{Pl}	1.30	1/d
Max. growth rate for Ps	σ_{Ps}	1.10	1/d
Photosynthet. effic.	α	0.01	m^2/W
Phyto. self-shading	κ_{phyto}	0.03	$m^2/mmolC$
Detr. self-shading	κ_{det}	0.20	$m^2/mmolC$
DOM self-shading	κ_{DOM}	0.29	$m^2/mmolC$
Water ext. coefficient	κ_W	0.05	1/m
External SPM ext. coeff.	κ_{SPM}	0.0	1/m/(mg/l)
PAR fraction of incident light	par_fraction	0.6	-
NH4 half saturation const.	r_{NH4}	0.20	$mmolN/m^3$
NO3 half saturation const.	r_{NO3}	0.5	$mmolN/m^3$
NH4 inhibition parameter	ψ	3.0	$m^3/mmolN$
Pl mortality rate	m_{Pl}	0.04	1/d
Ps mortality rate	m_{Ps}	0.08	1/d
Graz. r. Zl on Phytopl.	$\sigma_{Zl,P}$	0.8	1/d
Graz. r. Zs on Phytopl.	$\sigma_{Zs,P}$	1.0	1/d
Grazing rate Zl on Zs	$\sigma_{Zl,Zs}$	0.5	1/d
Zs, Zl half saturation const.	r_Z	0.5	$mmolC/m^3$
Zl mortality rate	m_{Zl}	0.1	1/d
Zs mortality rate	m_{Zs}	0.2	1/d
Zl excretion rate	μ_{Zl}	0.06	1/d
Zs excretion rate	μ_{Zs}	0.08	1/d
Zl assim. eff. on plankton	$\gamma_{Zl,P}$	0.75	-

Zs assim. eff. on plankton	$\gamma_{Zs,P}$	0.75	-
Zl & Zs assim. eff. on detr.	$\gamma_{Z,D}$	0.75	-
Detritus remineralization rate	ϵ_D	0.003	1/d
Detritus sinking rate	w_D	5.0	m/d
PO4 half saturation const.	r_{PO4}	0.05	$mmolP/m^3$
SiO2 half saturation const.	r_{Si}	0.5	$mmolSi/m^3$
Si remineralization rate	ϵ_{Si}	0.015	1/d
Max. growth rate for BG	σ_{BG}	1.0	1/d
BG Temp. control	$T_{ctrl,BG}$	1.0	1/°C
BG reference temperature	$T_{ref,BG}$	0.0	
BG max. grazing rate	β_{BG}	0.3	1/d
BG mortality rate	m_{BG}	0.08	1/d
Critic. bot. stress for resusp.	τ_{crit}	0.007	N/m^2
Resuspension rate	λ_{s2d}	25.	1/d
Sedimentation rate	λ_{d2s}	3.5	m/d
Burial rate	δ_{bur}	0.00001	1/d
Sed. remineralization rate	ϵ_{Sed}	0.001	1/d
Temp. control denitrification	$T_{ref,denit}$	0.15	1/°C
P sedim. rel. p1	RelSEDp1	0.15	-
P sedim. rel. p2	RelSEDp2	0.10	-
Sed. remineralization rate Si	ϵ_{Sed3}	0.0002	1/d
Opal sinking rate	w_{Opal}	5.0	m/d
BG sinking rate	w_{BG}	-1.0	m/d
Diatom sinking rate	w_{Pl}	0.0	m/d
Grazing preference Zs on Ps	$a_{Zs,Ps}$	0.7	-
Grazing preference Zs on Pl	$a_{Zs,Pl}$	0.25	-
Graz. preference Zs on Det.	$a_{Zs,Det}$	0.1	-
Grazing preference Zs on BG	$a_{Zs,BG}$	0.3	-
Grazing preference Zl on Ps	$a_{Zl,Ps}$	0.1	-

Supplementary Material

Grazing preference Zl on Pl	$a_{Zl,Pl}$	0.85	-
Grazing preference Zl on Zs	$a_{Zl,Zs}$	0.15	-
Grazing preference Zl on Det.	$a_{Zl,Det}$	0.1	-
Grazing preference Zl on BG	$a_{Zl,BG}$	0.3	-
Fract. of dissolved from detr.	a_{DOM}	0.4	-
Surface deposition NO3	surface_deposition_no3	0.0	$mmolN/m^2d$
Surface deposition NH4	surface_deposition_nh4	0.0	$mmolN/m^2d$
Surface deposition PHO	surface_deposition_pho	0.0	$mmolP/m^2d$
Surface_deposition SIL	surface_deposition_sil	0.0	$mmolSi/m^2d$
Min. daily rad. for BG growth	I_{BG}	120.	W/m^2
Min. daily PAR N fixation	PAR_{BG}	120.	W/m^2

Supplementary Table S2: Statistics from validation against observations. Mean temperature bias of depth-averaged model temperature co-located in time and space against ICES data (2011-2015). Percentage bias (model-obs) for model data co-located to ICES observational data (2011-2015). The Percentage bias is defined following Allen et al. (2007) as $Pbias = \frac{\sum_{n=1}^N (M_n - O_n)}{\sum_{n=1}^N O_n} * 100$.

Subarea	Temperature mean bias [°C]	Nitrate percentage bias	Phosphate percentage bias
S. North Sea (SNS)	0.44	+225 %	+136 %
C. North Sea (CNS)	-0.34	+79 %	+57 %
N. North Sea (NNS)	-0.2	+ 27 %	+1 %
Skag./ Kategatt (SK)	-0.03	+165 %	+61 %
N-W Approach (NWA)	0.03	+7 %	-52 %
Irish Sea (I)	0.27	+87 %	+6 %
Celtic Sea (C)	-0.21	-	-
N-E Celtic Sea (NEC)	-	+116 %	+24 %
S-W Celtic Sea (SWC)	-	+25 %	+1 %
Armorican Shelf (A)	-	+171 %	+271 %
English Channel (E)	0.47	-	-
Norwegian Trench (NT)	1.15	-	-
I. Seas W. of Sc. (Sc)	0.21	-	-

2 REFERENCES

Allen, J. I., Holt, J. T., Blackford, J., and Proctor, R. (2007). Error quantification of a high-resolution coupled hydrodynamic-ecosystem coastal-ocean model: Part 2. Chlorophyll-a, nutrients and SPM. *Journal of Marine Systems* 68, 381–404. doi: 10.1016/j.jmarsys.2007.01.005

Appendix C – Tidal impacts on air-sea CO₂ exchange on the Northwest European Shelf

This appendix contains a paper, which is under review in *Frontiers in Marine Science – Marine Biogeochemistry* and was submitted as:

Kossack, J., Mathis, M., Daewel, U., Liu, F., Demir, K. T., Thomas, H., Schrum, C. (2024). Tidal impacts on air-sea CO₂ exchange on the Northwest European Shelf. *Frontiers in Marine Science* (under review)

The contribution of Jan Felix Gottlieb Kossack (JK) and others to this paper is as follows:

JK performed the model experiments and generated the data set, performed the data analysis, and wrote the manuscript. UD, CS, JK, FL and KD contributed to model development. MM, UD, HT and CS provided essential background knowledge and advised the study. CS initiated the idea of the study. All authors contributed to conception and design of the study and read and approved the submitted version.

Tidal impacts on air-sea CO₂ exchange on the North-West European Shelf

1 Jan Kossack^{1*}, Moritz Mathis¹, Ute Daewel¹, Feifei Liu¹, Kubilay Timur Demir¹, Helmuth
2 Thomas^{2,3}, Corinna Schrum⁴

3 ¹Institute of Coastal Systems, Helmholtz-Zentrum Hereon, Geesthacht, Germany

4 ²Institute of Carbon Cycles, Helmholtz-Zentrum Hereon, Geesthacht, Germany

5 ³Institute for Chemistry and Biology of the Sea, Carl von Ossietzky University Oldenburg,
6 Oldenburg, 26129, Germany

7 ⁴Institute of Oceanography, University of Hamburg, Hamburg, Germany

8

9 * **Correspondence:**

10 Jan Kossack

11 jan.kossack@hereon.de

12 **Keywords:** NW Europe; tides; internal tides; marine carbon cycle; 3D coupled hydrodynamic-
13 biogeochemical modeling; air-sea CO₂ exchange

14 Abstract

15 Tidal forcing is a dominant physical forcing mechanism on the Northwest European Shelf (NWES)
16 that regulates the mixing-stratification status of the water column and thus acts as a major control for
17 biological productivity and air-sea CO₂ exchange. Tides further influence the marine carbon cycle on
18 the shelf by affecting benthic-pelagic coupling, vertical mixing and the large-scale residual
19 circulation. The cumulative tidal impact on oceanic uptake of atmospheric CO₂ on the NWES
20 however remains largely unexplored. We use a coupled physical-biogeochemical ocean model to
21 gain quantitative understanding of the tidal impacts on the air-sea CO₂ exchange of the NWES by
22 comparing hindcast simulations with and without tidal forcing. Our results show that tidal forcing
23 weakens the annual oceanic CO₂ uptake on the NWES by 0.15 *Tmol C yr⁻¹*, corresponding to a
24 ~13% stronger CO₂ sink in the experiment without tidal forcing. This impact contrasts with the tide-
25 induced increase in marine primary production demonstrated in earlier studies, which primarily
26 enhances biological carbon fixation in shallow inner-shelf regions of the NWES. Instead, we find
27 tidal mixing, tide-induced baroclinic circulation and the tidal impact on benthic-pelagic coupling to
28 be dominant controls of air-sea CO₂ exchange. Tidal mixing in the permanently mixed shelf regions
29 accounts for the majority (~40%) of the weakening effect on CO₂ uptake, while the modulation of
30 water mass composition in the Celtic Sea by tide-induced baroclinic circulation reduces the uptake
31 further (~33% of the difference in annual mean CO₂ uptake). In terms of the shelf carbon budget, the
32 tidal response of air-sea CO₂ exchange is primarily mediated by changes to the pelagic DIC reservoir
33 (~73%; -0.11 *Tmol C yr⁻¹*). Tidal impacts on off-shelf carbon export to the North Atlantic only
34 account for ~20% (-0.03 *Tmol C yr⁻¹*) of the tidal impact on shelf CO₂ uptake, and changes in
35 sedimentation of particulate organic carbon account for the remaining ~7% (-0.01 *Tmol C yr⁻¹*).

36

37 1 Introduction

38 Tidal forcing is one of the dominant physical forcing mechanisms on the Northwest European Shelf
39 (NWES) and affects turbulent mixing, stratification and circulation on the shelf. Being a broad mid-
40 latitude continental shelf, the NWES forms a highly dynamic land-ocean transition zone that
41 connects the terrestrial and ocean carbon reservoirs (Bauer et al., 2013). The continental shelf pump
42 mechanism (Tsunogai et al., 1999), which efficiently exports carbon-enriched subsurface waters from
43 the shelf into the deep North Atlantic, further makes the NWES a vital part of the global ocean
44 carbon sink (Thomas et al., 2004; Legge et al., 2020). Large uncertainties however persist regarding
45 the role of tides and other shelf-specific processes for the magnitude, variability and future
46 development of carbon sequestration on the NWES (Ward et al., 2020; Dai et al., 2022). Global
47 circulation models used in earth system science also only poorly represent shelf-specific processes
48 and commonly neglect tides, which significantly limits our current understanding of the coastal ocean
49 in the marine carbon cycle (Holt et al., 2017; Resplandy et al., 2024).

50 Bottom-driven tidal mixing structures the NWES into shallow permanently mixed regions,
51 transitional regions with tidal fronts and weak stratification and seasonally stratified deep regions
52 (Simpson and Hunter, 1974). Tides can also generate vertical mixing in stratified shelf regions by
53 causing intermittent shear instabilities within the pycnocline (Rippeth, 2005; Becherer et al., 2022).
54 Several studies report elevated pycnocline mixing associated with the internal tide at the shelf break
55 and adjacent outer shelf regions of the NWES (New and Pingree, 1990; Rippeth and Inall, 2002;
56 Sharples et al., 2007). Tides further contribute to the large-scale residual circulation on the NWES by
57 generating baroclinic residual currents (Hill et al., 2008) and also by directly affecting the barotropic
58 residual circulation on the NWES (Tinker et al., 2022). Tides also induce residual mean flow at
59 small-scale bathymetric features, which has been hypothesized to affect the large-scale circulation on
60 the NWES (Polton, 2015).

61 Tidal forcing has been shown to substantially affect biological productivity on the NWES
62 (Richardson et al., 2000; Sharples, 2008; Zhao et al., 2019; Kossack et al., 2023). Observations
63 further suggest that tidal mixing acts as a major control for air-sea CO₂ exchange on the NWES
64 (Thomas et al., 2004; Thomas et al., 2005b; Bozec et al., 2006; Prowe et al., 2009). Diapycnal
65 nutrient fluxes induced by internal tides or other tidal processes (e.g. Sharples et al., 2007; Becherer
66 et al., 2022) sustain relevant subsurface primary production on the NWES that is suggested to be
67 relevant for air-sea CO₂ exchange (Richardson et al., 2000; Hickman et al., 2012; Rippeth et al.,
68 2014). Tidal impacts on the residual circulation (e.g. Hill et al., 2008; Tinker et al., 2022) also affect
69 the large-scale spatial distribution of the carbonate system and thus air-sea CO₂ exchange. To our
70 knowledge, no study has so far addressed the cumulative impact of the multifaceted tidal processes
71 on air-sea CO₂ exchange on the NWES.

72 In this paper, we evaluate tidal impacts on air-sea CO₂ exchange by comparing two separate multi-
73 year numerical model experiments with and without any tidal forcing. We extend the high-resolution
74 coupled physical-biogeochemical regional model framework introduced in Kossack et al. (2023) for
75 the investigation of the marine carbon cycle by incorporating an additional carbonate system model.
76 The model system is based on a flexible unstructured grid that realizes kilometrical-scale horizontal
77 model resolution on the NWES, which for the first time allows an investigation of the impacts of the
78 regionally important internal tide field on air-sea CO₂ exchange in a fully coupled physical-
79 biogeochemical model framework.

80 We present the details of the applied model configuration, and assess the performance of the
81 carbonate system model in Section 2. In Section 3, we investigate the tidal impacts on air-sea CO₂
82 exchange and elucidate the role of tidal processes for the shelf carbon cycle. Section 4 discusses the
83 presented results and provides conclusions on the role of tidal forcing for the shelf carbon cycle.

84

85

86 **2 Materials and methods**

87 **2.1.1 SCHISM-ECOSMO model configuration**

88 We apply the coupled physical-biogeochemical regional model framework SCHISM-ECOSMO
89 introduced in Kossack et al. (2023) in this study. The 3D hydrodynamic model SCHISM (Zhang et
90 al., 2016) is coupled to the lower trophic level ecosystem model ECOSMO II (Daewel and Schrum,
91 2013) via the FABM framework (Bruggeman and Bolding, 2014). The additional coupling to a
92 carbonate system model is described in Sect. 2.1.2. The model domain extends from 40°N – 66 °N
93 and 20° W – 30°E and thus covers the entire NWES and a part of the north-east Atlantic (see Fig. 1).
94 We impose a minimum water depths of 10 m in the model domain. The Baltic Sea is included to
95 adequately resolve basin-exchange processes, but is not particularly attended to in this study, as it
96 does not feature relevant tidal energy.

97 The physical model component SCHISM is a numerically efficient and robust modelling system
98 based on an unstructured horizontal grid. SCHISM is specifically designed for cross-scale simulation
99 of 3D baroclinic ocean circulation from shallow coastal areas to the deep open ocean (Yu et al., 2017;
100 Ye et al., 2020; Wang et al., 2022). The applied NWES-IT model configuration realizes a telescoping
101 high horizontal resolution of 1.5km in the Celtic Sea and in a 75km wide band delimited in off-shelf
102 direction by the 200m isobath. The high-resolution model grid explicitly resolves the kilometrical-
103 scale internal tide field on the NWES (Guihou et al., 2018) and the generation of tide-induced
104 residual mean flow at small-scale bathymetric features (Polton, 2015). The horizontal resolution in
105 the remaining model domain smoothly varies from a maximum of ~2.5km in the shallow coastal
106 zones, or even 500m at the Danish Straits, to a maximum resolution of ~10km in the deepest parts of
107 the shelf. In the vertical, the model applies a flexible Localized Sigma Coordinate with shaved cells
108 (LSC²) with a maximum of 53 vertical layers. The specific implementation of the physical SCHISM
109 setup and an extensive model validation is provided in Kossack et al. (2023).

110 The biogeochemical model ECOSMO II uses a nutrient-phytoplankton-zooplankton-detritus (NPZD)
111 conceptual model approach with a total number of 16 state variables (see Fig. 2), including three
112 phytoplankton functional groups (diatoms, flagellates and cyanobacteria), two zooplankton
113 functional groups (herbivorous and omnivorous) and three functional groups for detritus (particulate
114 organic matter, dissolved organic matter, biogenic opal). All organic matter pools contain carbon,
115 nitrogen and phosphorous in elemental Redfield ratios of 106:16:1 (Redfield et al., 1963). Benthic-
116 pelagic coupling is implemented as described in Daewel and Schrum (2013). The model considers
117 three different integrated surface sediment pools for each of the three nutrient cycles, one for opal/
118 silicate, one for particulate organic material consisting of carbon, nitrogen and phosphorous at a
119 Redfield ratio, and one for iron-bound phosphorous. Sediment processes include sinking, deposition,
120 and resuspension of particulate organic matter (POM) and opal depending on a critical bottom shear
121 stress, as well as benthic remineralisation of POM and opal. The extended formulation of ECOSMO
122 II allows the simulation of lower trophic level dynamics in a wide range of ecosystems and resolves

123 pelagic and benthic biological processes that affect the marine carbon cycle. The coupled SCHISM-
124 ECOSMO system is introduced and validated by Kossack et al. (2023). The parameter set used here
125 is documented in Table ST1 in the supplementary material.

126

127 **2.1.2 Carbonate system model**

128 We employ the FABM framework to further couple the SCHISM-ECOSMO model configuration to
129 the carbonate system model introduced by Blackford and Gilbert (2007). The carbonate system
130 model simulates the carbonate chemistry in seawater based on four state variables: pH, the partial
131 pressure of CO₂ (pCO₂), dissolved inorganic carbon (DIC) and total alkalinity (TA). When two of the
132 four state variables are known, the model estimates the other two iteratively. In the subsequent text,
133 the used model configuration is referred to as SCHISM-ECOSMO-CO₂.

134 Different adaptations of the implemented carbonate system model component have been employed to
135 investigate carbonate chemistry on the NWES in several previous studies (Artioli et al., 2012;
136 Wakelin et al., 2012; Artioli et al., 2014; Blackford et al., 2017). In this study, DIC and TA are
137 provided as prognostic state variables from the ecosystem model component ECOSMO II. The
138 carbonate system model then uses DIC and TA, along with temperature, pressure and salinity, to
139 derive the speciation of DIC in seawater and iteratively solve for pH and pCO₂. The applied
140 carbonate system dissociation constants are taken from Millero et al. (2006). Air-sea CO₂ exchange is
141 calculated based on the pCO₂ gradient between the ocean and prescribed atmospheric pCO₂^{air} using
142 the gas transfer parameterization of Wanninkhof (2014).

143 Fig. 2 illustrates the coupling of ECOSMO II and the carbonate system model. Simulated DIC is
144 influenced by organic carbon production by net primary production by the three phytoplankton
145 groups ($NPP_{P1,P2,P3}$), and by organic carbon decomposition by pelagic remineralization of DOM and
146 POM, zooplankton excretion and DIC release from benthic remineralization ($F_{DIC,benthic}$):

$$147 \quad F_{DIC,bio} = \varepsilon_{DOM}C_{DOM} + \varepsilon_{POM}C_{POM} + \mu_1C_{Z1} + \mu_2C_{Z2} + F_{DIC,benthic} - NPP_{P1,P2,P3}. \quad (1)$$

148 Here C_X denotes the respective biomass of DOM, POM, herbivorous zooplankton (Z1) and
149 omnivorous zooplankton (Z2). $\varepsilon_{DOM,POM}$ denotes the respective remineralization rates for DOM and
150 POM, and $\mu_{1,2}$ the excretion rates $\mu_{1,2}$ for the two zooplankton groups. We do not simulate a
151 sediment DIC pool and consequently do not include a DIC flux to the sediment.

152 We implement TA as a fully prognostic variable that is influenced by benthic and pelagic biological
153 processes as described by Wolf-Gladrow et al. (2007) and Gustafsson (2013). TA is explicitly
154 affected by nitrate and ammonium based primary production, aerobic remineralization of organic
155 matter and anaerobic denitrification in ECOSMO II.

156

157 **2.1.3 Model forcing and experiments**

158 Atmospheric forcing and SCHISM-ECOSMO forcing at the open boundaries used in this study are
159 equivalent to Kossack et al. (2023). Boundary conditions for temperature, salinity, nitrate, phosphate,
160 silicate and oxygen are provided from monthly mean WOA2018 climatological data (Boyer et al.,
161 2018) and thus do not include inter-annual variability. The model configuration used in this study

162 includes spatial varying surface deposition of nitrate and ammonium based on EMEP MSC-W data
163 from MET Norway (https://emep.int/mscw/mscw_moddata.html; downloaded 09/2023), which was
164 not yet implemented in Kossack et al. (2023). Boundary conditions for TA are provided from the
165 global 3D NNGv2LDEO TA climatology (Broullón et al., 2019). Boundary conditions for DIC are
166 provided from the global NNGv2LDEO DIC climatology (Broullón et al., 2020). We add an
167 additional trend for the simulation period derived from a global ICON-coast simulation (Mathis et al.,
168 2022) to account for the effect of rising atmospheric CO₂. Atmospheric pCO₂ is prescribed from
169 monthly mean atmospheric pCO₂ data measured at the Mace Head station (Lan et al., 2022).

170 River forcing is provided in form of daily river discharge and nutrient, DIC and TA loads for the 172
171 largest rivers in the domain. River input for ECOSMO state variables other than nutrients are set to
172 zero. River discharge as well as nitrate, ammonium, phosphate and silicate loads represent multi-year
173 daily mean values computed for the period 2000-2015 from a regional river dataset compiled and
174 used by Daewel and Schrum (2013) and further updated by Zhao et al. (2019). We use annual mean
175 concentrations compiled by Pätsch and Lenhart (2008) for riverine DIC, DOM and TA input via the
176 Scheldt, Meuse, Rhine, Ems and Elbe on the European continental coast. We use annual mean
177 concentrations compiled in Neal and Davies (2003) for riverine DIC, DOM and TA input via the
178 Humber estuary, Wear, Tweed, Great Ouse and Thames on the eastern UK coast. As done in Kühn et
179 al. (2010), we assume that only 10% of the riverine DOM is bioavailable and, assuming rapid
180 remineralization in the land-ocean transition zone, directly add it to riverine DIC. We prescribe an
181 average DIC concentration of 2700 mmol C m⁻³ computed from Pätsch and Lenhart (2008) for the
182 remaining rivers on the NWES with no available DIC. For missing DOM concentrations, we assume
183 a DOM/DIC ratio of 1/10, of which only 10% is considered bio-available and added to riverine DIC.
184 Due to the overall lack of riverine TA data, we use the end member approach following Hjalmarsson
185 et al., (2008) and Artioli et al. (2012) to estimate riverine TA concentrations for the rivers on the
186 NWES with no available data. For rivers not included in the resulting geographic groupings, we use
187 the average of the estimated riverine TA on the NWES (2050 mmol m⁻³).

188 As done in Kossack et al. (2023), a faster coarse resolution SCHISM-ECOSMO-CO₂ NWES-LR
189 configuration was used to run a 5 year spin-up simulation from which the initial conditions for the
190 high-resolution configuration used in this study are interpolated. The separate coarser resolution
191 NWES-LR configuration is described in Kossack et al. (2023). Temperature, salinity, nitrate,
192 phosphate, silicate and oxygen for the spin-up simulation were initialized from WOA2018 (Boyer et
193 al., 2018). Initial conditions for DIC and TA are interpolated from the respective NNGv2LDEO
194 climatologies (Broullón et al., 2019; Broullón et al., 2020), except for the Baltic, where TA initial
195 conditions are generated using the end-member approach following Hjalmarsson et al. (2008).
196 ECOSMO sediment fields for NWES-LR were interpolated from long-term ECOSMO simulations
197 provided by F. Werner (in pers. comm.) and Samuelsen et al. (2022). Forcing data for the spin-up
198 simulation is equivalent to the high-resolution model configuration described above.

199 We perform two numerical experiments with the high-resolution SCHISM-ECOSMO-CO₂ model
200 configuration to assess the impact of tides on air-sea CO₂ exchange on the NWES. The TIDE
201 experiment includes tidal forcing at the lateral open boundaries and tidal potential in the domain. In
202 the NOTIDE experiment, the same model configuration is run completely without tidal forcing. Both
203 experiments are integrated for a period of 5 years from 2000 to 2005 with hourly instantaneous
204 model output that is averaged to daily means. The first year of the TIDE/ NOTIDE experiments is
205 treated as a secondary spin-up period and omitted from the analysis.

206

207 2.2 Analysis methods for the carbonate system

208 2.2.1 Biological and temperature control of pCO₂ in the ocean

209 We assess the temperature and biological control of surface pCO₂ following the approach proposed
210 by Takahashi et al. (2002), which uses a linearization of the temperature dependency of pCO₂ to
211 differentiate between temperature and biologically driven changes of pCO₂. We calculate the effect
212 of temperature and biology on pCO₂ over an annual cycle as

$$213 \quad pCO_{2T} = \overline{pCO_2} \times e^{(0.0423(T-\bar{T}))} \quad (2)$$

$$214 \quad pCO_{2bio} = pCO_2 \times e^{(0.0423(\bar{T}-T))}, \quad (3)$$

215 where pCO_2 and T are in-situ pCO₂ and temperature, and $\overline{pCO_2}$ and \bar{T} denote annual means. pCO_{2T}
216 here estimates the pCO₂ values expected from changes in sea surface temperature alone. The
217 biological signal pCO_{2bio} in this approach inherently comprises all non-temperature related effects
218 on pCO₂ (e.g. also changes in TA).

219 Again following Takahashi et al. (2002), the ratio of the effects of temperature and biology on
220 surface pCO₂ was calculated to assess the relative importance of biology and temperature over the
221 annual cycle:

$$222 \quad T/B = \Delta pCO_{2T} / \Delta pCO_{2bio}, \quad (4)$$

223 with the seasonal amplitudes of the change in pCO₂ related to temperature and biological effects:

$$224 \quad \Delta pCO_{2T} = \max(pCO_{2T}) - \min(pCO_{2T}) \quad (5)$$

$$225 \quad \Delta pCO_{2bio} = \max(pCO_{2bio}) - \min(pCO_{2bio}) \quad (6)$$

226 Regions with annually strong biological effects on pCO₂ will show a smaller T/B ratio, while
227 regions with weaker biological effects on pCO₂ show a higher T/B ratio.

228

229 2.2.2 Net community production

230 We calculate net community production (NCP), i.e. the difference between net primary production
231 and heterotrophic pelagic and benthic remineralization, to evaluate the net change of DIC in the
232 water column evoked by biological processes. We calculate net community production as

$$233 \quad NCP = \int_{-H}^{\eta} (NPP_{P1,P2,P3} - HR_P) - F_{DIC,benthic}, \quad (7)$$

234 where $NPP_{P1,P2,P3}$ is net primary production by the three phytoplankton functional groups, $HR_P =$
235 $\epsilon_{DOM}C_{DOM} + \epsilon_{POM}C_{POM} + \mu_1C_{Z1} + \mu_2C_{Z2}$ is pelagic heterotrophic remineralization comprising
236 DOM and POM remineralization and zooplankton excretion (see Eq. 1) and $F_{DIC,benthic}$ is the DIC
237 release from benthic remineralization.

238

239 2.2.3 Diapycnal fluxes driven by turbulent mixing across the pycnocline

240 To assess turbulent mixing relevant for the carbonate system, we compute turbulent fluxes of DIC
241 and nitrate following Sharples et al. (2001) and in line with Kossack et al. (2023) as

$$242 J_{NO_3} = -K_V \left(\frac{\Delta NO_3}{\Delta z} \right) \quad (8)$$

$$243 J_{DIC} = -K_V \left(\frac{\Delta DIC}{\Delta z} \right) \quad (9)$$

244 with the (vertical) eddy diffusivity K_V computed by the model turbulence closure, the difference in
245 nitrate and DIC concentrations between the respective discretized vertical model layers ΔNO_3 and
246 ΔDIC , and the vertical model layer thickness Δz in meters. To get the diapycnal fluxes into the
247 euphotic zone at the surface, we evaluate the diapycnal fluxes at the nutricline z_N (defined as the
248 maximum vertical nitrate gradient in the water column).

249 The turbulent nitrate flux J_{NO_3} into the surface mixed layer can be used to estimate a potential for
250 subsurface primary production, which constitutes a DIC sink in the surface mixed layer. Assuming
251 full utilization of the vertically mixed nitrate by phytoplankton, we compute potential subsurface
252 primary production as

$$253 PSP = J_{NO_3}(z_N)R_N, \quad (10)$$

254 where $J_{NO_3}(z_N)$ is the turbulent nitrate flux evaluated at the base of the euphotic zone and R_N the
255 standard N:C Redfield ratio.

256

257 2.3 Carbonate system model validation

258 We validate the model results against different observational products to evaluate the model's
259 performance in reproducing the marine carbon cycle on the NWES. We focus on the results of the
260 carbonate system component of the model system. The model performance with respect to general
261 hydrographic conditions and lower trophic level ecosystem dynamics has already been evaluated for
262 the NWES (excluding the Baltic) in Kossack et al. (2023). The subareas used to evaluate model
263 performance in this section (see Fig. 1) are chosen as in Kossack et al. (2023) and account for the
264 spatial heterogeneity of physical and biogeochemical processes on the NWES.

265 DIC and TA are validated against observational data obtained from the Global Ocean Data Analysis
266 Project version 2 data product (GLODAPv2.2022; Key et al., 2015; Olsen et al., 2016).
267 GODAPv2.2022 comprises a total number of 4283 quality controlled in situ seawater samples for
268 DIC and 3824 samples for TA on the NWES in the simulated time period from 2001-2005, the
269 majority of which are from the greater North Sea area. Simulated pCO₂ is validated against
270 observational data obtained from the Surface Ocean CO₂ Atlas version 2023 data product (Bakker et
271 al., 2016). SOCATv2023 contains a total number of 786018 in situ surface ocean fCO₂ (CO₂
272 fugacity) measurements collected on the NWES in the simulated time period from 2001-2005. Ocean
273 surface fCO₂ is converted to pCO₂ using the PyCO2SYS v1.8.2 software (Humphreys et al., 2023).
274 The SOCATv2023 data has high temporal and spatial resolutions, but the coverage of the NWES is
275 irregular. Data coverage is high for the greater North Sea region, intermediate in the Celtic Sea and
276 sparse on the North Western Approaches.

277 **2.3.1 DIC and TA validation**

278 We co-locate the observational DIC and TA samples from the GLODAPv2.2022 data product and
279 daily mean model output in time and space for each subarea to quantitatively assess the model's
280 consistency with the spatial and temporal variability of the large-scale carbonate system. Data
281 sparsity limits the quantitative validation of DIC and TA to the greater North Sea area (i.e. the SNS,
282 CNS, NNS, SK and NT subareas in Fig. 1). The direct co-location of observational data and model
283 results is a rigorous test for the model and sensitive to relatively minor spatial and temporal
284 mismatches between model and observations (Allen et al., 2007; Artioli et al., 2012).

285 Fig. 3 shows the statistics of the centered co-located data for the greater North Sea subareas in form
286 of a Taylor diagram. Correlation coefficients are > 0.8 for the NNS, NT and SK subareas and 0.79 in
287 the central North Sea. The southern North Sea shows the lowest correlation coefficient (SNS \approx
288 0.52). The centered standard deviation is below 1 in all evaluated subareas and lowest in the CNS,
289 indicating an underestimation of the amplitude of DIC variability (in time and space) in the model.
290 Centered root mean square errors (CRMSE) for the subareas are between 0.5 and 1, which suggests a
291 good fit between the model data and observations. The SNS shows the highest CRMSE, which again
292 underlines slightly reduced model performance in the shallow SNS compared to the deeper North Sea
293 areas.

294 The Taylor plot in Fig. 3 illustrates that TA shows poorer agreement with observations than DIC,
295 particularly in the northern North Sea subarea. The correlation coefficient between model results and
296 observations is moderately high for the NT (≈ 0.77) and SK (≈ 0.71) subareas, and ≈ 0.51 for the
297 SNS. Correlation is however low in the CNS (≈ 0.26) and statistically insignificant in the deep
298 NNS ($R \approx 0.05$ and p -value > 0.3). The centered standard deviation for TA is < 0.5 for all subareas
299 except the Skagerrak/ Kattegat subarea (CSTD ≈ 0.77), which suggests a general underestimation of
300 the amplitude of TA variability in the model. The centered standard deviation is particularly low for
301 the CNS (CSTD ≈ 0.37) and the NNS (CSTD ≈ 0.25). Centered root mean square errors (CRMSE)
302 are between 0.75 and 1 in the NT, SK, SNS and CNS subareas. The NNS subarea shows the highest
303 CRMSE (> 1).

304 The evaluation of the percentage bias (i.e. the sum of model error normalized by the data)
305 documented in Table 1 complements the normalized and centered statistics in Fig. 3 and provides a
306 measure for systematic over- or underestimation of observations (Allen et al., 2007). The percentage
307 biases for both DIC and TA in Table 1 are $\leq 1\%$ in all subareas except the SNS, where the
308 percentage bias is 1.7% for DIC and 1.1% for TA. The low percentage bias in Table 1 underlines the
309 good fit between model data and observations demonstrated by the centered statistics in Fig. 3, but
310 suggests a minor overestimation of both DIC and TA concentrations in the model. An additional
311 evaluation of the mean bias of seasonal surface DIC concentration (Fig. S1 in the supplementary
312 material) indicates that the model particularly overestimates surface DIC concentrations in spring and
313 summer.

314

315 **2.3.2 pCO₂ validation**

316 The evaluation of simulated surface pCO₂ against observational SOCATv2023, which provides data
317 coverage for more shelf regions than the greater North Sea, is an important indicator for the
318 representation of the air-sea CO₂ exchange on the NWES. We evaluate simulated pCO₂ by co-
319 locating it in time and space against surface in situ measurements obtained from the SOCATv2023

320 data product. Errors in the derived carbonate system variable $p\text{CO}_2$ will be larger than in TA and DIC,
321 as errors in DIC, TA and the applied parameterizations accumulate (Artioli et al., 2012; Wakelin et
322 al., 2012). Fig. 4 shows simulated mean seasonal surface $p\text{CO}_2$ for the period 2001-2005, as well as
323 the biases (model-observation) between simulated $p\text{CO}_2$ and co-located SOCATv2023 data
324 aggregated for the respective seasons. The annual mean percentage bias and normalized root mean
325 square error (NRMSE; calculated as RMS error divided by standard deviation of observations),
326 aggregated for subareas with relevant observational coverage, are further documented in Table 1.

327 Fig. 4 shows that the model both over- and underestimates surface $p\text{CO}_2$ over the course of the year
328 and that there is substantial temporal and spatial variability in the model bias. The bias in $p\text{CO}_2$ in
329 winter is relatively small in the deeper areas of the North Sea and Celtic Sea and indicates a minor
330 local underestimation of $p\text{CO}_2$ in the model. Shallow inner-shelf areas like the English Channel and
331 the southern North Sea in turn show stronger $p\text{CO}_2$ underestimation in winter.

332 High DIC consumption by the spring bloom induces a strong drawdown of surface $p\text{CO}_2$ that is
333 resolved by the model. The spring $p\text{CO}_2$ bias shown in Fig. 4 suggests an overestimation of simulated
334 surface $p\text{CO}_2$ on most of the NWES. The overestimation in spring is particularly high in the shallow
335 southern North Sea and the Skagerrak. Some shelf regions, for example in the English Channel,
336 however show a local underestimation of simulated $p\text{CO}_2$ in spring.

337 The higher temperature and heterotrophic remineralization of spring bloom remnants increase surface
338 $p\text{CO}_2$ again in summer, especially in permanently mixed shallow inner-shelf regions. The model
339 resolves the increase in surface $p\text{CO}_2$, but summer $p\text{CO}_2$ biases suggest that the model overestimates
340 summer $p\text{CO}_2$ nearly everywhere on the NWES. The positive bias in summer is particularly high in
341 the Southern Bight region of the North Sea, the Norwegian Trench and parts of the central North Sea.
342 Some shelf regions like the south-western North Sea however also show a local underestimation of
343 surface $p\text{CO}_2$ in summer.

344 In autumn, the majority of the co-located $p\text{CO}_2$ data again suggests a moderate underestimation of
345 simulated $p\text{CO}_2$ on most of the NWES. The underestimation of surface $p\text{CO}_2$ in autumn is
346 particularly pronounced in the coastal areas of the southern North Sea. The model nevertheless
347 locally also overestimates $p\text{CO}_2$, e.g. in a small area in the southern part of the central North Sea or in
348 the Norwegian Trench.

349 The percentage bias for $p\text{CO}_2$ in Table 1 shows that the model overestimates annual mean $p\text{CO}_2$ in all
350 subareas. The percentage bias is nevertheless low throughout the model domain. It is $< 5\%$ in the
351 CNS, NNS and English Channel, and slightly larger than 10% in the SNS, SK, NT and Celtic Sea
352 subareas. The NRMS errors documented in Table 1 range from 0.9 in the NNS and SNS subareas to
353 1.3 in the NT subarea. The low NRMSE values indicate that the difference between the model and
354 observations are small compared to the variability of the observations in the respective subarea, and
355 suggest good to fair agreement (Allen et al., 2007) between simulated and observed $p\text{CO}_2$.

356

357 **2.3.3 Air-Sea CO₂ flux validation**

358 We further assess the overall model performance by evaluating the simulated air-sea CO₂ flux in the
359 TIDE experiment with observation and model-based literature estimates for the NWES. The annual
360 air-sea CO₂ flux in Fig. 5A and Table 2 shows that most regions of the NWES are net sinks of CO₂.
361 Simulated oceanic CO₂ uptake is high in deep outer shelf areas and strongest on the Hebrides shelf

362 and in the northern North Sea. Simulated oceanic CO₂ uptake is substantially lower or nearly neutral
363 in shallow inner-shelf areas like the southern North Sea and English Channel. Permanently mixed
364 regions in the Irish Sea and along the German North Sea coast show neutral air-sea CO₂ exchange or
365 weak outgassing. The simulated annual CO₂ flux in the Irish Sea suggests the region is a minor
366 source of CO₂ to the atmosphere over the year (see Table 2). ROFIs close to the major rivers on the
367 continental and UK coasts also show outgassing of CO₂ to the atmosphere.

368 The decrease of the oceanic CO₂ sink from the deep northern North Sea to the shallow southern North
369 Sea qualitatively fits to the spatial structure of observations by Thomas et al. (2004) and the multi-year
370 mean air-sea CO₂ flux derived in Becker et al. (2021). Based on an extensive observational campaign
371 in 2001, Thomas et al. (2004) estimate annual oceanic CO₂ uptake of $1.5 - 2.5 \text{ mol C m}^{-2}\text{yr}^{-1}$ in
372 the northern North Sea, which compares well to the estimated annual mean flux of $2.1 \text{ mol C m}^{-2}\text{yr}^{-1}$
373 in our simulations. Our model shows a weak oceanic CO₂ sink in the Southern Bight of the North Sea
374 and the eastern English Channel. Thomas et al. (2004) and Becker et al. (2021) in contrast found the
375 region to be a weak source of CO₂ to the atmosphere. There however is large interannual variability in
376 the region and studies from different years and with different methodologies conflict in the direction
377 of the CO₂ flux in the region (Thomas et al., 2004; Schiettecatte et al., 2007; Omar et al., 2010; Kitidis
378 et al., 2019).

379 Simulated annual mean oceanic CO₂ uptake of $0.8 \text{ mol C m}^{-2}\text{yr}^{-1}$ in the north-eastern Celtic Sea
380 and $1.4 \text{ mol C m}^{-2}\text{yr}^{-1}$ in the south-western Celtic Sea are higher than respective estimates in
381 Marrec et al. (2015), who proposed $0.6 \text{ mol C m}^{-2}\text{yr}^{-1}$ for the north-eastern Celtic Sea and
382 $0.9 \text{ mol C m}^{-2}\text{yr}^{-1}$ for the south-western Celtic Sea. Frankignoulle and Borges (2001) however
383 estimated a higher oceanic CO₂ uptake of $1.7 - 2.9 \text{ mol C m}^{-2}\text{yr}^{-1}$ for the Celtic Sea and Bay of
384 Biscay region. Simulated area-mean weak outgassing of $-0.3 \text{ mol C m}^{-2}\text{yr}^{-1}$ in the Irish Sea
385 matches the estimate of $-0.3 \text{ mol C m}^{-2}\text{yr}^{-1}$ in Marrec et al. (2015).

386 The overall mean annual oceanic CO₂ uptake on the NWES (delineated by the 200m isobath plus the
387 Norwegian Trench) for the period 2001-2005 is $1.16 \text{ Tmol yr}^{-1}$, compared to the estimated range of
388 $1.3 - 3.3 \text{ Tmol yr}^{-1}$ proposed in Legge et al. (2020) based on two observational and two modelling
389 studies. The standard deviation of the simulated annual mean shelf CO₂ uptake, i.e. the interannual
390 variability for the simulation period 2001-2005, is $\pm 0.08 \text{ Tmol yr}^{-1}$. The overall mean net annual
391 oceanic CO₂ uptake in the North Sea (here defined as the SNS, CNS and NT subareas) is
392 $0.55 \text{ Tmol C yr}^{-1}$ in our simulations, with a standard deviation of $\pm 0.03 \text{ Tmol C yr}^{-1}$. Using a
393 slightly larger geographical definition of the North Sea, Thomas et al. (2005a) estimated an annual
394 oceanic CO₂ uptake of $0.794 \text{ Tmol yr}^{-1}$ for the North Sea based on observational surveys in 2001
395 and 2002, with an estimated range of uncertainty of 20-50% related to differences in gas transfer
396 parameterizations (Watson et al., 2009; Meyer et al., 2018).

397

398 **2.4 Validation summary**

399 The validation demonstrates that the applied SCHISM-ECOSMO-CO₂ model system reproduces key
400 features of the marine carbon cycle on the NWES. Simulated oceanic CO₂ uptake on the NWES
401 compares favourably with estimates from literature, but the model shows a tendency to underestimate
402 the shelf CO₂ sink. The validation of the carbonate system model state variables DIC and TA indicate
403 quantitative agreement between the model and observational data. Model performance for DIC is
404 better than for TA. The model biases for both DIC and TA indicate a minor overestimation against

405 observations in both variables. Errors for the derived carbonate system model variable $p\text{CO}_2$ show
406 reasonable model performance, but are larger than for DIC and TA and especially highlight model
407 limitations in the simulation of the full spatial heterogeneity and temporal variability of the shelf
408 carbonate system. The presented model validation aligns with the modelling studies by Artioli et al.
409 (2012) and Wakelin et al. (2012), who find comparable quantitative agreement to observations for
410 DIC and TA, and also poorer model performance for $p\text{CO}_2$.

411 The good quantitative validation results for DIC underline the model's general ability to reproduce the
412 spatial and temporal variability of DIC on the shelf. Model performance for DIC is slightly lower for
413 the shallow southern North Sea (SNS) compared to the deeper North Sea areas. The validation suggests
414 that the model underestimates DIC drawdown during the productive season, especially in summer.
415 Overestimated DIC is likely a dominant factor for the identified overestimation of surface $p\text{CO}_2$ in
416 spring and summer (Fig. 4), and therefore potentially contributes to the underestimation of the NWES
417 CO_2 sink in the model. The overestimation of DIC in spring and summer is presumably linked to an
418 underestimation of primary productivity commonly identified for ECOSMO II (Daewel and Schrum,
419 2013; Zhao et al., 2019). Small summer SST warm biases (documented in Kossack et al., 2023) might
420 also locally contribute to the overestimation of surface $p\text{CO}_2$. The strict application of Redfield
421 stoichiometry in ECOSMO II likely is a key factor that contributes to DIC overestimation in the model.
422 Non-Redfield DIC fixation has been observed on the NWES (e.g. Bozec et al., 2006; Humphreys et
423 al., 2019), and ecosystem models assuming Redfield stoichiometry in the production and
424 decomposition of organic matter generally tend to underestimate biological carbon fixation, especially
425 in summer (Prowe et al., 2009; Kühn et al., 2010).

426 Further model limitations arise from applied model parameterizations. POM is parameterized with a
427 constant sinking rate. POM and DOM remineralization in ECOSMO II are parameterized with only
428 temperature-dependent bulk remineralization rates that potentially contribute to the misrepresentation
429 of spatial and temporal variability of the shelf carbonate system. Further differentiation of size and
430 lability of the POM and DOM compartments, or the explicit parameterization of the microbial loop
431 (Azam et al., 1983) hold potential for further model improvement. Uncertainty in benthic carbon stocks
432 and parameterizations of benthic-pelagic coupling also restrict model performance on the NWES
433 (Legge et al., 2020). Benthic-pelagic coupling is particularly relevant in shelf settings where the
434 sediment and atmosphere can directly interact. Recent work has shown the importance of macrobenthos
435 and associated bioturbation for the sedimentary organic carbon budget and benthic-pelagic coupling
436 (Zhang et al., 2019). The inclusion of macrobenthos and associated bioturbation could potentially
437 improve the seasonal cycle of pelagic DIC concentrations (and associated air-sea CO_2 fluxes) by
438 modulating benthic remineralization and resuspension.

439 Given the substantial inter-annual variability of DIC concentrations in the eastern North Atlantic
440 (Thomas et al., 2008), the climatological forcing applied at the open boundary further impedes model
441 performance on the NWES. The river loads for DIC and TA also lack seasonal and inter-annual
442 variability. Given the general sparsity of adequate data for riverine and other coastal carbon inputs,
443 the applied riverine forcing is generally subject to particularly high uncertainty (Legge et al., 2020)
444 that limits model performance in the coastal regime. This likely contributes to the lower model
445 performance found for DIC in the southern North Sea.

446 The use of climatological data at the open boundary also likely limits model performance for TA and
447 potentially contributes to the low TA model skill in the northern North Sea. In contrast to other
448 approaches, the applied prognostic TA model enables the simulation of the highly heterogeneous
449 NWES including the Baltic Sea, for which no single reliable TA-salinity regression is applicable. The

450 complex biological dynamics and coastal processes and inputs that affect TA however are a
451 challenge for the fully prognostic simulation of TA. Benthic processes and associated TA fluxes have
452 been shown to be relevant on the NWES (Brenner et al., 2016), but are only partially reproduced in
453 the model system. Simulated TA will also be restricted by errors in the simulation of nutrient sources
454 and sinks in ECOSMO II (see Kossack et al., 2023). Another significant caveat is the large
455 uncertainty in riverine inputs of TA and the lack of adequate (basin-scale) data for additional coastal
456 TA inputs, for example from the Wadden Sea (Thomas et al., 2009). The moderate model
457 performance in the southern North Sea is therefore already promising. The comparatively high model
458 performance in the Skagerrak/ Kattegat and the Norwegian Trench further suggests a reasonable
459 representation of TA in the Baltic Sea outflow.

460 The dynamic shelf environment and the complexity of coastal ecosystems, as well as the large
461 uncertainty in riverine and other coastal inputs relevant to the carbonate system (Legge et al., 2020),
462 make modelling the coastal and shelf carbon cycle very challenging. Despite its limitations, the
463 presented SCHISM-ECOSMO-CO₂ model system is accepted to reproduce key features of the
464 marine carbon cycle on the NWES both qualitatively and with reasonable quantitative skill. The
465 moderate complexity of the biogeochemical components of the applied model configuration further
466 facilitates the use of a high horizontal model resolution of 1.5km required to resolve key tidal
467 processes on the NWES (Polton, 2015; Guihou et al., 2018) at reasonable computational cost (see
468 Kossack et al., 2023). The model validation therefore encourages the use of SCHISM-ECOSMO-
469 CO₂ for the investigation of tidal impacts on the air-sea CO₂ flux in the following sections of the
470 study.

471

472

473 **3 Results**

474 **3.1 Tidal impacts on air-sea CO₂ exchange**

475 We find that annual mean oceanic CO₂ uptake on the NWES (area delimited by the 200m isobath,
476 excluding the Baltic Sea) is $-0.15 \text{ Tmol C yr}^{-1}$ lower in the experiment with tidal forcing than in
477 the experiment without tidal forcing (Table 2). This amounts to a 13% higher annual mean oceanic
478 CO₂ uptake on the NWES in the NOTIDE experiment (Fig. 5B) compared to the TIDE experiment
479 (Fig. 5A).

480 The difference of mean annual air-sea CO₂ flux (2001-2005) between the two experiments
481 documented in Fig. 5C and Table 2 shows spatially heterogeneous tidal impacts on the air-sea CO₂
482 flux on the NWES. Tidal forcing substantially decreases oceanic CO₂ uptake in large parts of the
483 NWES, predominantly in shallow inner-shelf regions. The relative difference in the air-sea CO₂
484 exchange is particularly pronounced in the Irish Sea (-157%), which shows net CO₂ outgassing over
485 the annual cycle in the TIDE experiment but net oceanic CO₂ uptake in the NOTIDE experiment.
486 Inner-shelf subareas like the North-Eastern Celtic Sea (-44%) or the English Channel (-34%) also
487 show a relevant reduction of oceanic CO₂ uptake. Tidal forcing however also increases oceanic CO₂
488 uptake (up to $1 \text{ mol C m}^{-2} \text{ yr}^{-1}$), predominantly in seasonally stratified areas in the central and
489 northern North Sea. The northern North Sea is the only subarea in which tidal forcing marginally
490 increases mean annual oceanic CO₂ uptake (+5%). The seasonally stratified Celtic Sea in contrast
491 show a distinct reduction of mean annual oceanic CO₂ uptake. The tidal impacts on the air-sea CO₂
492 flux on the outer-shelf Western Irish, Malin and Hebrides Shelves are generally negligible, with only

493 small local decreases of oceanic CO₂ uptake in shallow near-coast areas. Fig. 5C however indicates
494 that tidal forcing substantially decreases oceanic CO₂ uptake on the continental slope along the Celtic
495 Sea and on adjacent outer-shelf areas of the south-western Celtic Sea.

496

497 **3.2 Understanding the mechanisms behind the tidal impacts on air-sea CO₂ exchange**

498 **3.2.1 Tidal impacts on sedimentation**

499 The net annual carbon flux from the water column to the sediment due to deposition of POC on the
500 NWES is small in the TIDE experiment (1 Gmol C yr^{-1} ; mean for 2001-2005). Neglecting tides,
501 and therefore primarily the tidal impact on benthic-pelagic coupling due to physical resuspension by
502 strong tidal currents, increases POC deposition and results in a higher annual mean sediment carbon
503 content on the NWES (Fig. 6). Over the annual cycle, benthic remineralization in the NOTIDE
504 experiment however also diffusively returns the bulk of the deposited POC back into the water
505 column as DIC. The resulting mean annual net carbon flux to the sediment is thus also only
506 $0.01 \text{ Tmol C yr}^{-1}$ in the NOTIDE experiment.

507

508 **3.2.2 Tidal impacts on net community production**

509 Tidal forcing has been shown to substantially increase net primary production (NPP) on the NWES
510 (by about 14%, see Kossack et al., 2023). Changes in heterotrophic remineralization however also
511 need to be considered to obtain the net tidal impact on biological carbon cycling on the NWES. We
512 directly evaluate tidal impacts on net community production (i.e. the metabolic balance between NPP
513 and heterotrophic remineralization) computed with Eq. 7 to assess tidal impacts on biological cycling
514 of carbon. Mean annual NCP in the TIDE experiment is shown in Fig. 7A. The difference in mean
515 annual NCP between the TIDE and NOTIDE experiments is shown in Fig. 7B and additionally
516 documented in Table 2.

517 Our results suggest that the entire NWES is net heterotrophic ($NCP = -0.62 \text{ Tmol C yr}^{-1}$) in the
518 TIDE experiment (mean for 2001-2005). The North Sea is also net heterotrophic ($NCP =$
519 $-0.32 \text{ Tmol C yr}^{-1}$) in the TIDE experiment, with particularly negative NCP (i.e. strong
520 heterotrophy) in the Norwegian Trench. Fig. 7B and Table 2 show a spatially heterogeneous tidal
521 response of NCP on the NWES, and suggest that tides make the NWES slightly more heterotrophic
522 (by $-0.04 \text{ Tmol C yr}^{-1}$). The difference between the experiments amounts to $\sim 7\%$ (relative to the
523 TIDE experiment). About $\frac{1}{4}$ of the increase in heterotrophy with tidal forcing can be explained by the
524 higher sequestration of POC in the sediment in the NOTIDE experiment (see Sect. 3.2.1). The
525 remaining $\frac{3}{4}$ imply higher organic carbon import onto the NWES. We therefore find that although
526 tides substantially increase net primary production on the NWES, this does not move the shelf system
527 closer to autotrophy.

528 The tidal impact on heterotrophic remineralization is primarily facilitated through the strong tidal
529 impact on benthic-pelagic coupling on the shelf (see Sect. 3.2.1). Higher sedimentation of POC in the
530 NOTIDE experiment redistributes heterotrophic remineralization from the water column into the
531 sediment. Benthic heterotrophic remineralization is also slower than pelagic heterotrophic
532 remineralization (e.g. Krumins et al., 2013). The difference in the parameterized remineralization
533 rates (see parameter set in Table ST1 in the supplementary material) therefore additionally affects the
534 timing of heterotrophic remineralization in the two experiments. Heterotrophic remineralization in

535 the TIDE experiment consequently occurs earlier in the annual cycle than in the NOTIDE
536 experiment. Compared to the TIDE experiment, the NOTIDE experiment is more autotrophic in
537 summer and more heterotrophic in autumn and winter (see Fig. S2 in the supplementary material).

538 Tidal impacts on mean annual NCP in Fig. 7B show large spatial heterogeneity on the NWES. Tidal
539 impacts on NCP are most pronounced in inner-shelf regions, where Fig. 7B shows areas with strong
540 increases of NCP with tidal forcing, but often also directly adjacent areas of strong decreases of NCP.
541 Tidal impacts on NCP in the deeper shelf regions are generally smaller, but also show a pattern of
542 local increases and local decreases. Only the northern North Sea shows a moderate net increase in
543 NCP with tidal forcing (Table 2), particularly in the region east of the Shetland Islands. The observed
544 spatial pattern in the tidal response of NCP in Fig. 7B, with local increases and often adjacent local
545 decreases of NCP, is consistent with the strong tidal impact on benthic-pelagic coupling and suggest
546 advective transport of tidally resuspended POM. The tidally resuspended POM is advected
547 downstream, for example with the cyclonic circulation in the North Sea, while the sedimented POM
548 in the NOTIDE experiment remains stationary. Advective transport of POM out of a specific area
549 decreases local heterotrophic remineralization relative to primary production, i.e. it increases local
550 autotrophy. Local increases in heterotrophy in turn suggests tides enhance advective transport of
551 organic matter into the the respective area. The substantial reduction of NCP with tidal forcing in the
552 Norwegian Trench ($-32.8 \text{ Gmol C yr}^{-1}$) suggests tides are particularly important for organic matter
553 transport from the North Sea shelf into the Norwegian Trench.

554 Tidal forcing therefore mainly laterally redistributes organic matter on the shelf, affects the balance
555 of benthic and pelagic heterotrophic remineralization and determines the timing of heterotrophic
556 remineralization. The large mismatches between the tidal impacts on the air-sea CO_2 flux and tidal
557 impacts on NCP shown in Table 2 however suggests there is no direct relationship between the tidal
558 impacts on NCP and air-sea CO_2 exchange. The discrepancies are particularly large in shallow inner-
559 shelf regions like the Irish Sea and English Channel, where tides decrease annual mean oceanic CO_2
560 uptake even though tidal forcing makes the subareas more autotrophic (which generally facilitates
561 more CO_2 uptake from the atmosphere). This indicates that other tidal processes are the prevailing
562 factor for the tidal impacts on air-sea CO_2 flux in shallow inner-shelf regions.

563

564 **3.2.3 Tidal impacts in permanently mixed regions**

565 Tidal mixing partitions the shelf into permanently mixed and seasonally stratified regions, which
566 both constitute distinct biogeochemical regimes with implications for air-sea CO_2 exchange (e.g.
567 Thomas et al., 2004). Seasonal stratification enables the drawdown of surface DIC concentrations by
568 means of the biological pump mechanism (Volk and Hoffert, 1985). The drawdown of surface DIC
569 in spring and summer counteracts the effect of seasonal warming, which drives up surface pCO_2 , and
570 thus facilitates net oceanic uptake of atmospheric CO_2 over the annual cycle. In permanently mixed
571 regions, primary production and heterotrophic remineralization are not vertically separated and
572 (respired) carbon in the water column can constantly exchange with the atmosphere. Strong tidal
573 resuspension of POM from the sediment additionally increases the organic carbon pool available for
574 pelagic heterotrophic remineralization and mixing in spring and summer. Permanently mixed regions
575 consequently generally exhibit weak air-sea CO_2 exchange or show a tendency to weak outgassing of
576 excess carbon to the atmosphere (i.e. from riverine input).

577 Neglecting tides leads to a larger part of the shallow inner-shelf being seasonally stratified (see Fig.
578 S3 in the supplementary material), which in turn affects biogeochemical cycling in the region. We

579 investigate the associated tidal impact on air-sea CO₂ exchange by evaluating the tidal impacts on
580 temperature and biological control of surface pCO₂. We use Eq. 2 and Eq. 3 to calculate the effects of
581 temperature and biology on pCO₂ from monthly mean surface pCO₂ and SST (2001-2005). We
582 subsequently use Eq. 5 and Eq. 6 to compute ΔpCO_{2T} and ΔpCO_{2bio} , the respective mean seasonal
583 amplitudes of surface pCO₂ changes related to temperature and biology, and assess the relative
584 importance of temperature and biological effects on pCO₂ over the mean annual cycle by means of
585 the T/B ratio calculated with Eq. 4.

586 The T/B ratio in the TIDE experiment (Fig. 8A) shows that the temperature effect on surface pCO₂
587 strongly dominates in inner-shelf areas, while central and outer shelf areas exhibit a stronger
588 biological effect on pCO₂. The tidal impact on the T/B ratio shown in Fig. 8B, i.e. the difference
589 between the T/B ratio in the TIDE and NOTIDE experiments, demonstrates that tidal forcing is
590 largely responsible for the relative dominance of the temperature effect on surface pCO₂ in the areas
591 that are permanently mixed in the TIDE experiment. The tidal impact on the T/B ratio in central and
592 outer shelf regions is generally low.

593 In general, tides affect both temperature and biological control on pCO₂, which in turn determines the
594 tidal impact on the T/B ratio. Tidal mixing affects temperature control of pCO₂ by modulating oceanic
595 heat uptake on the NWES (Arnold et al., 2021), which results in colder summer SST and warmer winter
596 SST in the shallow inner-shelf areas of the NWES (Fig. S4 in the supplementary material). Neglecting
597 tides thus results in a larger seasonal amplitude of the temperature effect on pCO₂ (ΔpCO_{2T} ; Eq. 5) on
598 most of the NWES (Fig. 8C), which suggests larger temperature control on air-sea CO₂ exchange in
599 the NOTIDE experiment. The tidal impact on ΔpCO_{2T} is however small compared to the tidal impact
600 on the biological effect on pCO₂ (ΔpCO_{2bio} ; Eq. 6) shown in Fig. 8D. Neglecting tides results in a
601 larger seasonal amplitude of pCO₂ changes related to biology (i.e. a stronger biological control of
602 pCO₂) on the NWES, particularly in regions that are permanently mixed regions in the TIDE
603 experiment, but are seasonally stratified in the NOTIDE experiment (Fig. S3 in the supplementary
604 material). Our results therefore indicate that it is mainly the tidal weakening of the biological effect on
605 pCO₂ that causes the tidal impact on the T/B ratio documented Fig. 8B.

606 Fig. 8E exemplifies the tidal impact on surface pCO₂ at a station in the permanently mixed Irish Sea.
607 The strong tidal mixing in the Irish Sea nearly completely offsets the biological buffering of the
608 temperature-driven pCO₂ increase during seasonal warming, and thus leads to temperature-driven net
609 outgassing in the Irish Sea over the annual cycle (Table 2). If tides are neglected, the water column at
610 the station is seasonally stratified and allows the biological buffering of the seasonal warming effect,
611 which draws down surface pCO₂ in summer and enables net oceanic CO₂ uptake in the Irish Sea over
612 the annual cycle.

613 The analysis of the tidal impact on the T/B ratio demonstrates how the partitioning of the NWES into
614 seasonally stratified and permanently mixed regions plays a key role in controlling surface pCO₂, and
615 thus air-sea CO₂ exchange. Dominance of temperature control on pCO₂ in the permanently mixed
616 shelf regions ultimately entails stronger CO₂ outgassing in summer (e.g. Thomas et al., 2004), which
617 limits annual CO₂ uptake or even leads to net outgassing like in the Irish Sea. We find that the
618 permanently mixed regions (as defined in Fig. 8B) alone account for ~40% ($-0.06 Tmol C yr^{-1}$) of
619 the difference in oceanic CO₂ uptake on the NWES between the experiments.

620

621

622 3.2.4 Tidal impacts in the seasonally stratified North Sea

623 Large parts of the deep northern and central North Sea show a moderate increase in mean annual
624 oceanic CO₂ uptake with tidal forcing (Fig. 5C), which indicates that there is a tidal impact specific
625 to these seasonally stratified central and outer-shelf regions. The evaluation of the annual cycle of
626 surface pCO₂ at a station in the northern North Sea shown in Fig. 9A demonstrates that the higher
627 annual oceanic CO₂ uptake in the TIDE experiment predominantly stems from lower surface pCO₂ in
628 winter.

629 We find that the lower winter pCO₂ at the station in the northern North Sea is the result of a weaker
630 biological mitigation of the seasonal cooling effect on pCO₂ in the TIDE experiment (Fig. 9A).
631 Heterotrophic remineralization of organic matter produced in summer increases the DIC
632 concentration in the water column in autumn and winter, which constitutes a biological buffering of
633 the effect of seasonal cooling on pCO₂ and controls winter uptake on the shelf. Fig. 9C shows that
634 mean winter surface DIC is lower in the TIDE experiment than in the NOTIDE experiment in large
635 parts of the northern and central North Sea, which indicates that the weaker biological mitigation of
636 the seasonal cooling effect on pCO₂ occurs throughout most of the seasonally stratified North Sea.

637 We find that the difference in the winter DIC concentration in the seasonally stratified North Sea is
638 caused by the tidal impact on benthic-pelagic coupling and associated differences of heterotrophic
639 remineralization between the two experiments (see Sect. 3.2.2). The comparison of the annual cycles
640 of mean DIC in the water column (2001-2005) for the station in the northern North Sea shown in Fig.
641 9E reveals significant tidal impacts on the vertical structure and seasonality of the DIC concentration.
642 In the TIDE experiment, primary production draws down surface layer DIC during the productive
643 season, while vertical POM export and subsequent heterotrophic remineralization increases DIC in
644 the bottom layer (Fig. 9D). Resuspension and mixing by strong tidal currents retains POM in the
645 water column and limits sedimentation. With seasonal cooling at the end of the summer, surface
646 cooling then convectively mixes the DIC-enriched subsurface water to the surface.

647 Neglecting tides in contrast redistributes heterotrophic remineralization from the water column into
648 the sediment, where heterotrophic remineralization is slower and only diffusively releases DIC into
649 the bottom layer. Bottom layer mixing is also low in the absence of tides, so that the respired DIC
650 accumulates in a shallow bottom boundary layer and leads to substantially higher bottom layer DIC
651 concentrations in the NOTIDE experiment (up to +30 $mmol\ C\ m^{-3}$; see Fig. 9E). The entrainment
652 of the DIC-enriched bottom layer into the water column by December results in higher winter DIC
653 throughout the water column in the NOTIDE experiment, which ultimately leads to higher surface
654 pCO₂ (Fig. 9A) and thus lower oceanic CO₂ uptake during winter compared to the TIDE experiment.

655 Local increases in NCP in the central and northern North Sea with tidal forcing (Fig. 7B) imply a
656 reduction of local heterotrophic remineralization relative to local primary production. The local
657 increases in NCP therefore suggest that subsurface advective transport of organic carbon out of the
658 respective shelf areas in the North Sea, predominantly in form of POM (not shown), is more effective
659 in the TIDE experiment than in the NOTIDE experiment. Tidally enhanced advective transport of
660 organic matter in the bottom layer ultimately reduces the magnitude of the biological buffering of the
661 effect of winter cooling on surface pCO₂, and thus contributes to the higher oceanic CO₂ uptake in
662 winter. We find that about 5% (8.3 $Gmol\ C\ yr^{-1}$; Table 2) of the high annual mean oceanic CO₂
663 uptake in the northern North Sea subarea is related to tides.

664

665 3.2.5 Tidal impacts in the seasonally stratified Celtic Sea

666 Unlike in the North Sea, the majority of the seasonally stratified Celtic Sea shows a decrease in the
667 oceanic CO₂ uptake with tidal forcing (Fig. 5C). The evaluation of surface pCO₂ at a station in the
668 central Celtic Sea (Fig. 9B) indicates that the dominant cause for the lower annual mean oceanic CO₂
669 uptake in the TIDE experiment is higher biologically-driven surface pCO₂ in late autumn/ early
670 winter. Fig. 9C shows corresponding higher winter surface DIC concentrations in the Celtic Sea in
671 the TIDE experiment. The area of higher surface winter DIC in the TIDE experiment extends from
672 the Armorican shelf in the south across the Celtic Sea to the south-west coast of Ireland.

673 We find a strong tidal impact on the large-scale residual circulation in the Celtic Sea to be the main
674 reason for the difference in winter DIC that causes the regional reduction of oceanic CO₂ uptake with
675 tidal forcing. The seasonal mean depth-averaged residual circulation (2001-2005) and respective
676 seasonal mean surface DIC fields in the TIDE and NOTIDE experiments are documented in Fig. 10.
677 Tidal forcing evokes a seasonal cyclonic circulation pattern in the Celtic Sea and Western English
678 Channel not present in the experiment without tides. In summer, Fig. 10 shows northward residual
679 transport in the Western English Channel tidal frontal zone and along the south-western UK coast,
680 westward flow at the tidal front in the St. George Channel and a tendency to southeastward flow in
681 the south-western Celtic Sea in the TIDE experiment. Winter (DJF) circulation in the TIDE
682 experiment also shows a tendency to southeastward flow in the south-western Celtic Sea, and weak
683 northwestward flow from the Armorican shelf into the Celtic Sea. The NOTIDE experiment in
684 contrast shows very weak residual circulation in summer. In winter, the NOTIDE experiment shows
685 pronounced northwestward flow from the Armorican shelf across the Celtic Sea. A vertical transect
686 of mean summer horizontal velocity across the south-western Celtic Sea reveals that the cyclonic
687 residual circulation in the TIDE experiment is caused by a near-surface baroclinic current generated
688 at the density gradient of a cold pool trapped below the seasonal thermocline (Fig. 11). Such a cold
689 pool flanked by sharp density gradients is only set up in the Celtic Sea with tidal forcing.

690 The tidal impact on the residual circulation is relevant for air-sea CO₂ exchange because it affects the
691 water mass composition in the Celtic Sea. The strong northward transport in the NOTIDE experiment
692 flushes the Celtic Sea with low-DIC waters from the Armorican shelf and Bay of Biscay in the south,
693 while in the TIDE experiment the Celtic Sea is more influenced by DIC-rich waters from the north,
694 and potentially from the Bristol Channel. Mean winter surface DIC in the Celtic Sea is consequently
695 lower in the TIDE experiment than in the NOTIDE experiment, with the largest difference (up to
696 20 *mmol C m⁻³*) occurring in December (not shown). The lower winter DIC concentration in the
697 NOTIDE experiment drives stronger oceanic CO₂ uptake in the Celtic Sea. The seasonally stratified
698 part of the Celtic Sea consequently takes up 49.2 *Gmol C yr⁻¹* more atmospheric CO₂ in the
699 NOTIDE experiment than in the TIDE experiment. This makes up more than 90% of the difference
700 in annual mean oceanic CO₂ uptake between the experiments in the Celtic Sea (~ 0.05 *Tmol C yr⁻¹*;
701 Table 2), and amounts to $\sim 34\%$ of the difference of the annual mean NWES CO₂ sink between the
702 experiments.

703

704 3.2.5.1 Impact of internal tides in the Celtic Sea

705 The Celtic Sea shelf break and adjacent outer-shelf areas also exhibit a substantial decrease of annual
706 mean oceanic CO₂ uptake with tidal forcing (Fig. 5C). The tidal impact at the Celtic Sea shelf break
707 is dominated by internal tides generated by the interaction of tidal flow with the steep local
708 topography. The internal tides produce strong pycnocline mixing at the Celtic Sea shelf break and on

709 the adjacent Celtic Sea shelf, which locally decreases SST and enhances primary production by
710 generating diapycnal nutrient fluxes into the surface layer (New and Pingree, 1990; Sharples et al.,
711 2007; Kossack et al., 2023). We calculate the net effect of pycnocline mixing on surface DIC
712 concentration by computing the difference of the diapycnal DIC flux into the euphotic zone
713 ($J_{DIC}(z_n)$; calculated with Eq. 9) and compensatory potential subsurface primary production
714 sustained by the diapycnal nutrient flux into the euphotic zone (calculated with Eq. 10). Diapycnal
715 POM and DOM fluxes into the surface layer are found to be negligible.

716 Fig. 11A demonstrates that in the Celtic Sea, the mean summer diapycnal DIC flux into the euphotic
717 zone is marginally overcompensated by primary production sustained by the diapycnal nutrient flux.
718 On the Armorican shelf and in the shallow north-eastern Celtic Sea, the diapycnal DIC flux is larger
719 than the effect of potential new production. The net reduction of surface layer DIC by potential
720 subsurface primary production is mostly $< 0.75 \text{ mmol C d}^{-1}$ in the area of tidally enhanced
721 pycnocline mixing along the shelf break of the Celtic Sea. Sites of strong pycnocline mixing at the
722 shelf break or at small-scale bathymetric features on the shelf show a net reduction of surface layer
723 DIC by up to 2 mmol C d^{-1} . Integrated for the south-western Celtic Sea subarea along the shelf
724 break (SWC in Fig. 1), the effect of the dominantly tide-driven pycnocline mixing only amounts to a
725 net reduction of surface layer DIC by -0.8 Gmol C over the entire summer (June to August). The
726 low net reduction of surface layer DIC resulting from pycnocline mixing thus only marginally affects
727 the biological control on surface pCO_2 in summer. This is further emphasized by the analysis of
728 surface pCO_2 at a station at the Celtic Sea shelf break in Fig. 12B, which only shows a small tidal
729 impact on biological pCO_2 control in summer.

730 The surface pCO_2 in Fig. 12B further illustrates that the tide-driven reduction of local mean annual
731 oceanic CO_2 uptake at the Celtic Sea shelf break rather stems from warmer winter SST and a stronger
732 biological buffering of winter cooling on surface pCO_2 in autumn and winter. The warmer winter
733 SST in the TIDE experiment (see also Fig. S4B in the supplementary material) is likely largely the
734 result of tidally enhanced heat storage in the water column. The relatively stronger biological-driven
735 increase of surface pCO_2 in the TIDE experiment is also evident in the higher winter surface DIC
736 concentrations along the Celtic Sea shelf break (Fig. 9C). Our results indicate that the higher surface
737 DIC concentration mainly result from a higher end-of-summer POM concentration in the upper water
738 column above the shelf break in the TIDE experiment (Fig. S5 in the supplementary material). The
739 higher POM concentration results from the overall tidally elevated net primary production at the shelf
740 break (see Kossack et al., 2023), but tide-induced turbulent mixing potentially also retains more
741 POM within the reach of the deep winter surface mixed layer.

742

743

744 4 Discussion and conclusion

745 We use the novel SCHISM-ECOSMO-CO2 model configuration to assess the impact of tidal forcing
746 on oceanic uptake of atmospheric CO_2 on the NWES. Tidal impacts on air-sea CO_2 exchange on the
747 NWES are multifaceted and show high spatial variability. We find tidal forcing responsible for a
748 reduction of mean annual oceanic CO_2 uptake on the NWES by $-0.15 \text{ Tmol C yr}^{-1}$, which amounts
749 to a $\sim 13\%$ stronger NWES CO_2 sink in the experiment without any tidal forcing.

750 The dominant tidal impacts on air-sea CO₂ exchange are summarized in Fig. 13. Tidal mixing in the
751 permanently mixed shelf regions accounts for the majority (~40%; $-0.06 \text{ Tmol C yr}^{-1}$) of the tidal
752 weakening of the NWES CO₂ sink. The tidal intensification of temperature control on surface pCO₂
753 in the permanently mixed shelf regions, and the corresponding decrease in oceanic CO₂ uptake,
754 agrees with prior studies that found tidal mixing to distinctly structure air-sea CO₂ exchange on the
755 NWES (Thomas et al., 2004; Thomas et al., 2005b; Prowe et al., 2009; Omar et al., 2010). Another
756 significant tidal impact on air-sea CO₂ exchange is mediated by the modulation of water mass
757 composition in the Celtic Sea by tide-induced baroclinic circulation, which accounts for ~34%
758 ($-0.05 \text{ Tmol C yr}^{-1}$) of the tidal weakening of the NWES CO₂ sink. Our results indicate that a
759 cyclonic baroclinic circulation induced by a cold and dense bottom pool that is only set up in the
760 presence of tidal forcing contributes to the seasonal near-surface southeastward transport observed in
761 the south-western Celtic Sea (Pingree and Le Cann, 1989; Charria et al., 2013). The presence of cold
762 pools in the Celtic Sea and the importance of associated cyclonic baroclinic circulation was
763 previously suggested in Brown et al. (2003) and Hill et al. (2008).

764 The evaluation of net community production in the model describes the NWES as a net heterotrophic
765 system ($\text{NCP} = -0.62 \text{ Tmol C yr}^{-1}$). Simulated net heterotrophy of $-0.32 \text{ Tmol C yr}^{-1}$ in the
766 North Sea agrees well with the observational estimate of $-0.3 \text{ Tmol C yr}^{-1}$ provided by Thomas et
767 al. (2005a). We find tidal forcing to strengthen net heterotrophy on the NWES by
768 $-0.04 \text{ Tmol C yr}^{-1}$ (~7% relative to TIDE experiment). Physical resuspension by tides affects the
769 balance of benthic and pelagic heterotrophic remineralization, which in turn modulates the lateral
770 distribution and timing of heterotrophic remineralization on the shelf. Neglecting tides however only
771 results in a minor increase in the net carbon flux to the sediment by POC deposition (by
772 $0.01 \text{ Tmol C yr}^{-1}$), which suggests that the increase in heterotrophy with tides mainly stems from
773 higher organic carbon import onto the NWES. The tidal increase in heterotrophy implies a
774 corresponding decrease in the shelf's uptake capacity for atmospheric CO₂, which contributes the
775 remaining ~26% of the difference in oceanic CO₂ uptake between the experiments. A key finding of
776 this study therefore is that the substantial increase in biological productivity with tidal forcing
777 demonstrated in Kossack et al. (2023) does not translate into a general strengthening of the oceanic
778 CO₂ sink on the shelf.

779 Our results further suggest a low net impact of the kilometrical-scale internal tide field on air-sea
780 CO₂ exchange in the Celtic Sea because of the mutual compensation of diapycnal fluxes of DIC and
781 primary production sustained by diapycnal nutrient fluxes. The identified low impact of diapycnal
782 mixing on air-sea CO₂ exchange in the Celtic Sea is in agreement with Rippeth et al. (2014), who
783 also estimated diapycnal fluxes of nitrate and DIC to largely compensate each other. The hydrostatic
784 model applied in this study however likely underestimates pycnocline mixing by the non-hydrostatic
785 internal wave field in the Celtic Sea (Vlasenko et al., 2014). The decrease of oceanic CO₂ uptake on
786 the continental slope of the Celtic Sea as a result of changes in heterotrophic remineralization and
787 heat storage in the upper water column by tide-induced pycnocline mixing merits further
788 investigation. Our results suggest that observations of air-sea CO₂ exchange in the area should
789 especially account for the full lifecycle of biologically fixed carbon and air-sea CO₂ exchange in
790 winter to determine the role of tide-induced pycnocline mixing at the Celtic Sea shelf break.

791 The presented study considers major bottom-up processes controlling the sensitivity of the shelf
792 carbon cycle to tidal forcing. The 10-m minimum water depths used in this study however limits the
793 representation of very shallow coastal regions, as a wetting and drying scheme is not implemented in
794 the model configuration. The tendency to underestimated oceanic CO₂ uptake on the NWES due to
795 underestimated primary production identified in the model validation (Sect. 2.3) is not expected to

796 significantly affect the sensitivity to tidal forcing, as the tidal response is rather determined by the
797 tidal impact on the balance between net primary production and heterotrophic remineralization. The
798 identified tidal response of the shelf carbon cycle may however be affected by the lack of sediment
799 retention by macrobenthos (e.g. Zhang et al., 2019) in the applied model configuration.

800 The results of this study generally suggest that (subsurface) primary production in seasonally
801 stratified shelf regions sustained by tide-induced pycnocline mixing does not significantly contribute
802 to air-sea CO₂ exchange. As argued in Rippeth et al. (2014), the simulated net sensitivity of the air-
803 sea CO₂ exchange to (tide-induced) pycnocline mixing in summer however relies on the Redfield
804 ratio in phytoplankton growth and is thus limited by the use of constant Redfield stoichiometry in our
805 study. The production and subsequent lateral export of long-lived organic matter with C-rich non-
806 Redfield stoichiometry, as for example shown for the seasonally stratified Celtic Sea by Humphreys
807 et al. (2019), could also marginally increase the sensitivity of oceanic CO₂ uptake to tide-induced
808 pycnocline mixing.

809 Tidal impacts, mainly the upward transport of respiratory DIC by tidal mixing and the modulation of
810 water mass composition by tide-induced baroclinic circulation in the Celtic Sea, constrain the annual
811 increase of the pelagic DIC stock on the NWES due to the rising atmospheric CO₂ concentration.
812 Neglecting tides therefore results in a higher annual increase of the NWES DIC stock of
813 $0.34 \text{ Tmol C yr}^{-1}$, while the TIDE experiment shows an increase rate of $0.23 \text{ Tmol C yr}^{-1}$.
814 Considering that neglecting tides also increases the carbon flux to the sediment by
815 $0.01 \text{ Tmol C yr}^{-1}$, the difference in the increase rate of the NWES DIC stock ($0.11 \text{ Tmol C yr}^{-1}$)
816 implies that only ~20% ($0.03 \text{ Tmol C yr}^{-1}$) of the enhanced shelf CO₂ uptake in the experiment
817 without tides ($0.15 \text{ Tmol C yr}^{-1}$) is exported off-shelf. Our results therefore suggest that tidal
818 forcing mainly affects carbon reservoirs on the shelf and only marginally modulates off-shelf carbon
819 transport into the North Atlantic. To which extent tidal forcing affects carbon export below the
820 permanent pycnocline critically depends on tidal impacts on the downwelling circulation and cross-
821 shelf fluxes at the shelf break. Tidal impacts on bed stress and friction (Tinker et al., 2022) likely
822 affect Ekman drain in the bottom boundary layer at the shelf break. Previous studies have also
823 demonstrated direct tidal impacts on the European Slope current (Stashchuk et al., 2017; Tinker et
824 al., 2022) that potentially affect the downwelling circulation. Tidal motion further directly affects
825 cross-shelf transports at the shelf break, for example through internal-tide-driven Stokes transport
826 (Spingys et al., 2020; Huthnance et al., 2022). Graham et al. (2018) for example demonstrated
827 relevant on-shelf transport at internal depths likely associated with internal tides on the NWES that is
828 only resolved at kilometrical-scale horizontal model resolution. The evaluation of tidal impacts on
829 cross-shelf fluxes and the downwelling circulation is beyond the scope of this study, but is planned
830 for future work.

831 In conclusion, our study highlights the importance of representing multifaceted tidal phenomena in
832 ocean models used to investigate marine carbon cycle dynamics on continental shelves. Our
833 simulations at kilometrical-scale horizontal resolution suggest that the effects of tidal mixing, tidal
834 impacts on shelf circulation and benthic-pelagic coupling are most relevant for air-sea CO₂ exchange
835 on the NWES. High-resolution modelling and improved realism of shelf-specific biogeochemical
836 processes has recently been shown to significantly improve coastal carbon dynamics in global ocean
837 models (Mathis et al., 2022) and these improvements in modelling skill further show potential for
838 constraining uncertainties in our understanding of the marine carbon cycle (Mathis et al., 2024).
839 However, as the computational demands likely remain challenging for the near future, further work is
840 required to improve the parameterization of tidal processes in large-scale regional and global model
841 applications.

842 **5 Tables**

843

844 **Table 1:** Statistics from validation of DIC, TA and pCO₂ against observations. DIC/ TA model data
 845 are co-located in time and space against GLODAPv2.2022 (2001-2005). pCO₂ model data is co-
 846 located in time and space against SOCATv2023 (2001-2005). The Percentage bias is defined

847 following Allen et al. (2007) as $Pbias = \frac{\sum_{n=1}^N (M_n - O_n)}{\sum_{n=1}^N O_n} * 100$. The normalized root mean square error
 848 (NRMSE) is calculated as the RMS error divided by the standard deviation of the observations in the
 849 respective subarea.

850

Subarea	DIC percentage bias	TA percentage bias	pCO ₂ percentage bias	pCO ₂ NRMSE
S. North Sea (SNS)	+1.7%	+1.1%	-13.6%	0.9
C. North Sea (CNS)	+1%	+1%	+3.7%	1
N. North Sea (NNS)	+0.6%	+0.2%	+1.3%	0.9
Skag./ Kategatt (SK)	+0.5%	+0.8%	+13.4%	1.2
Norwegian Trench (NT)	0.6%	0.8%	+10.4%	1.3
English Channel (E)	-	-	+4.1%	1.1
Celtic Sea (C)	-	-	+13.8%	1.1

851

852

853

854

855

856

857

858

859 **Table 2:** Area mean annual CO₂ flux (2001-2005) on the NWES in TIDE and NOTIDE experiments.
 860 Positive values denote oceanic uptake. Net community production calculated using Eq. 7. Differences
 861 between the experiments calculated as TIDE-NOTIDE. Proportional differences between
 862 experiments are computed relative to TIDE experiment.

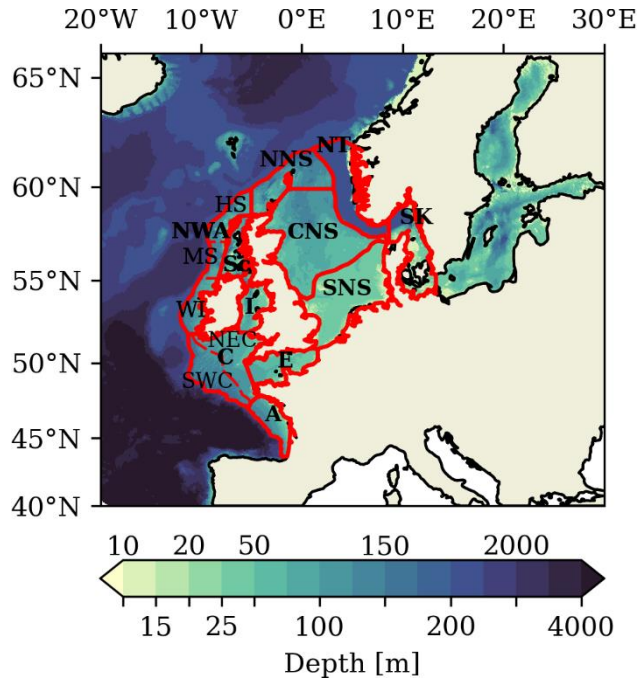
Subarea	TIDE CO ₂ Flux	NOTIDE CO ₂ Flux	Δ CO ₂ Flux	Δ NCP
	Total [<i>Gmol C yr⁻¹</i>] (Mean [<i>mol C m²yr⁻¹</i>])	Total [<i>Gmol C yr⁻¹</i>] (Mean [<i>mol C m²yr⁻¹</i>])	[<i>Gmol C yr⁻¹</i>] (TIDE-NOTIDE)/TIDE	[<i>Gmol C yr⁻¹</i>] (TIDE-NOTIDE)/TIDE
S. North Sea (SNS)	84.4 (0.4)	99.1 (0.5)	-14.6 (-17%)	-24.8 (-24%)
C. North Sea (CNS)	366 (1.5)	366.5 (1.5)	-0.5 (<-1%)	-0.9 (-2%)
N. North Sea (NNS)	165.9 (2.1)	157.6 (2)	8.3 (+5%)	4.4 (+13%)
Skag. / Kattegat (SK)	-36 (-0.5)	-30.4 (-0.4)	-5.7 (-16%)	-23 (-23%)
Norwegian Tr. (NT)	101.6 (1.3)	113.7 (1.5)	-12.1 (-12%)	-32.8 (-22%)
English Channel (EC)	37.8 (0.5)	50.8 (0.6)	-13 (-34%)	7.5 (+53%)
Celtic Sea (C)	211.4 (1.07)	265.1 (1.3)	-53.7 (-25%)	-5.6 (-10%)
Irish Sea (I)	-15.4 (-0.3)	8.7 (0.2)	-24.2 (-157%)	6.5 (+28%)
I. Sea W. of Scotl. (Sc)	27.4 (0.6)	39 (0.9)	-11.6 (-43%)	23.1 (+122%)
West Irish Shelf (WI)	73.6 (1.6)	85.4 (1.8)	-11.7 (-16%)	-1.4 (-5%)
Malin Shelf (MS)	44.5 (2.1)	46.7 (2.2)	-2.2 (-5%)	3.3 (+51%)
Hebrides Shelf (HS)	72.4 (2.1)	76.7 (2.2)	-4.3 (-6%)	-0.1 (-1%)
Sum for NWES	1.16 ± 0.08 <i>Tmol C yr⁻¹</i>	1.31 ± 0.11 <i>Tmol C yr⁻¹</i>	-0.15 <i>TmolC yr⁻¹</i> (-13%)	-0.04 <i>TmolC yr⁻¹</i> (-7%)

863

864

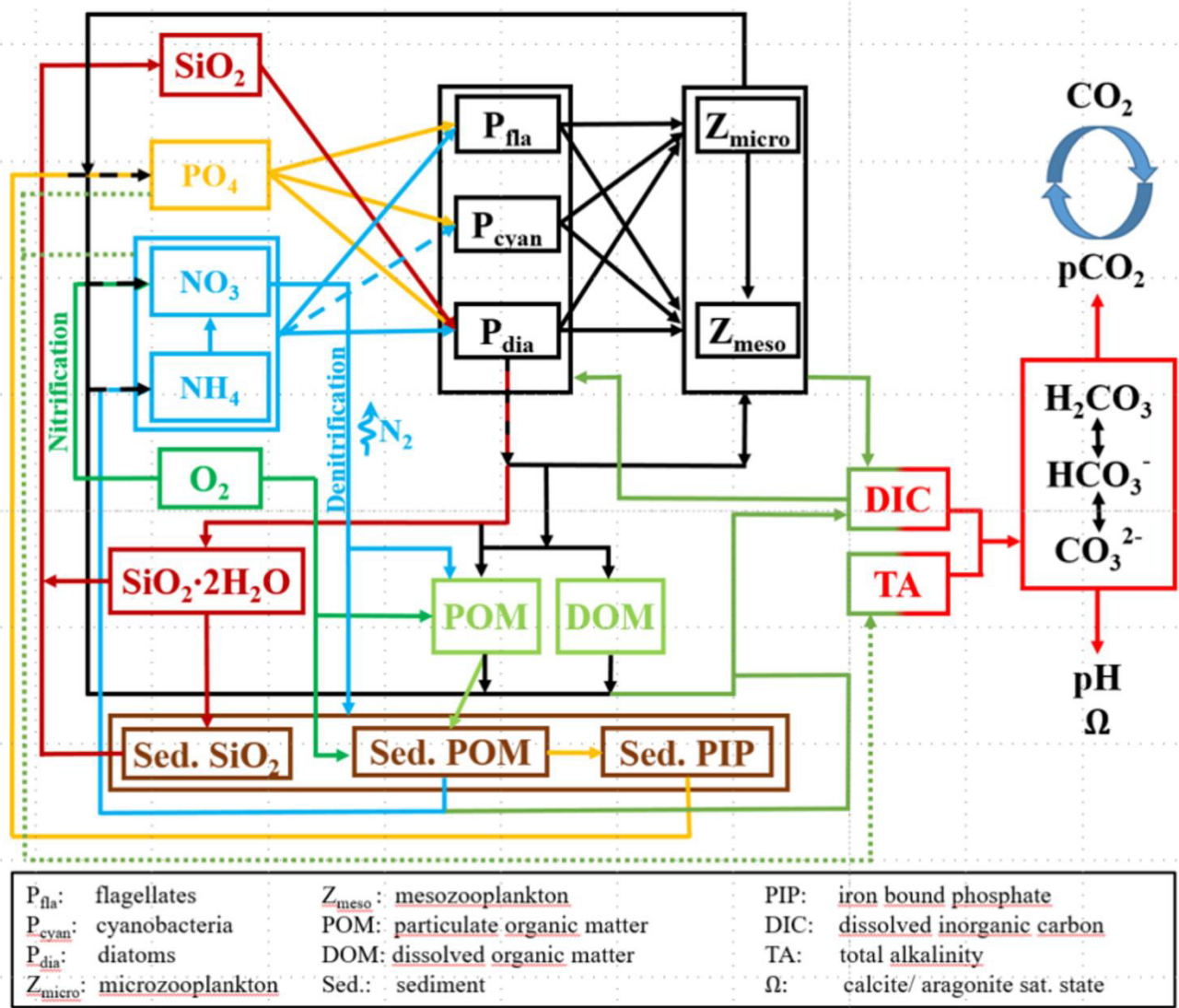
865

866 **6 Figures**



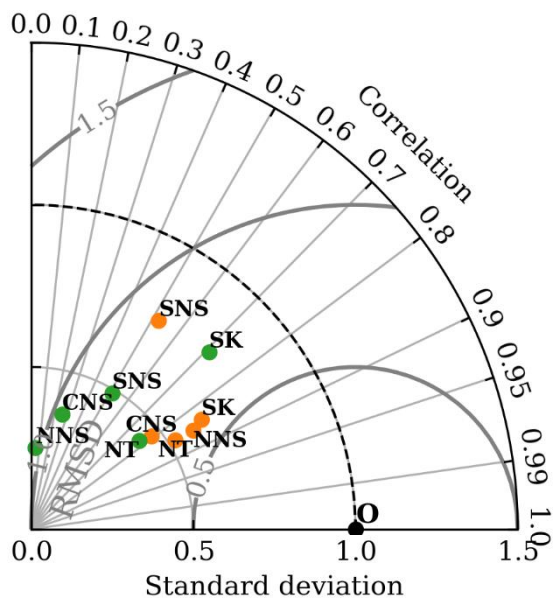
867

868 **Figure 1:** Bathymetry in the model domain. Red lines delineate subareas.



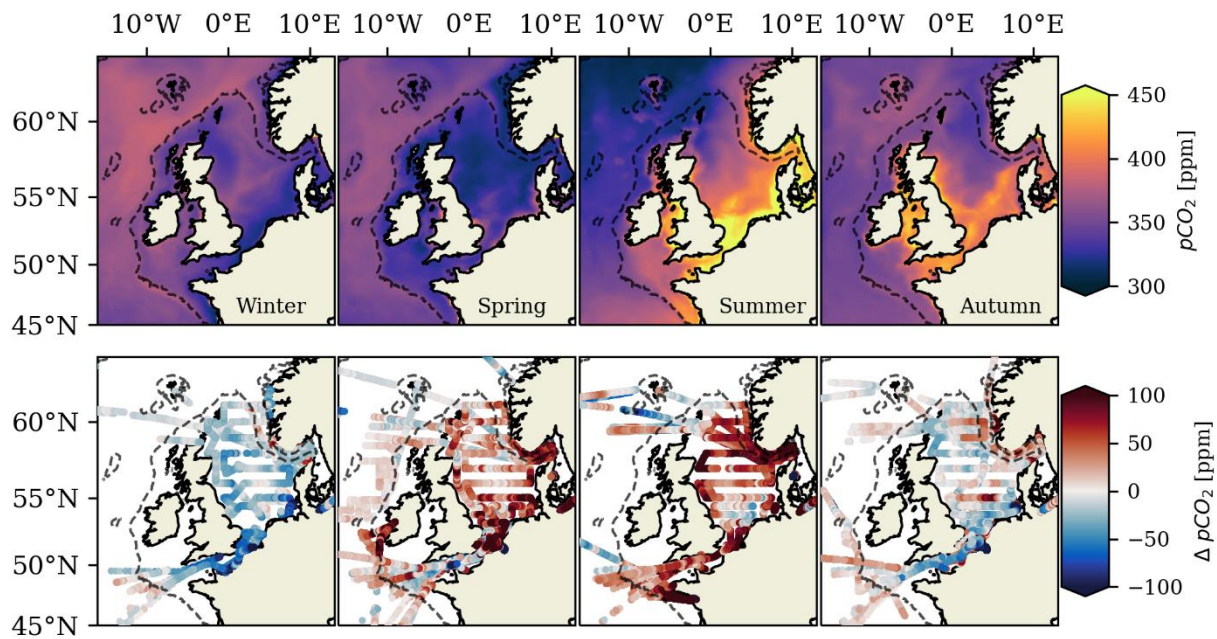
869

870 **Figure 2:** Schematic diagram of biochemical interactions in ECOSMO II and coupling to carbonate
 871 system model



872

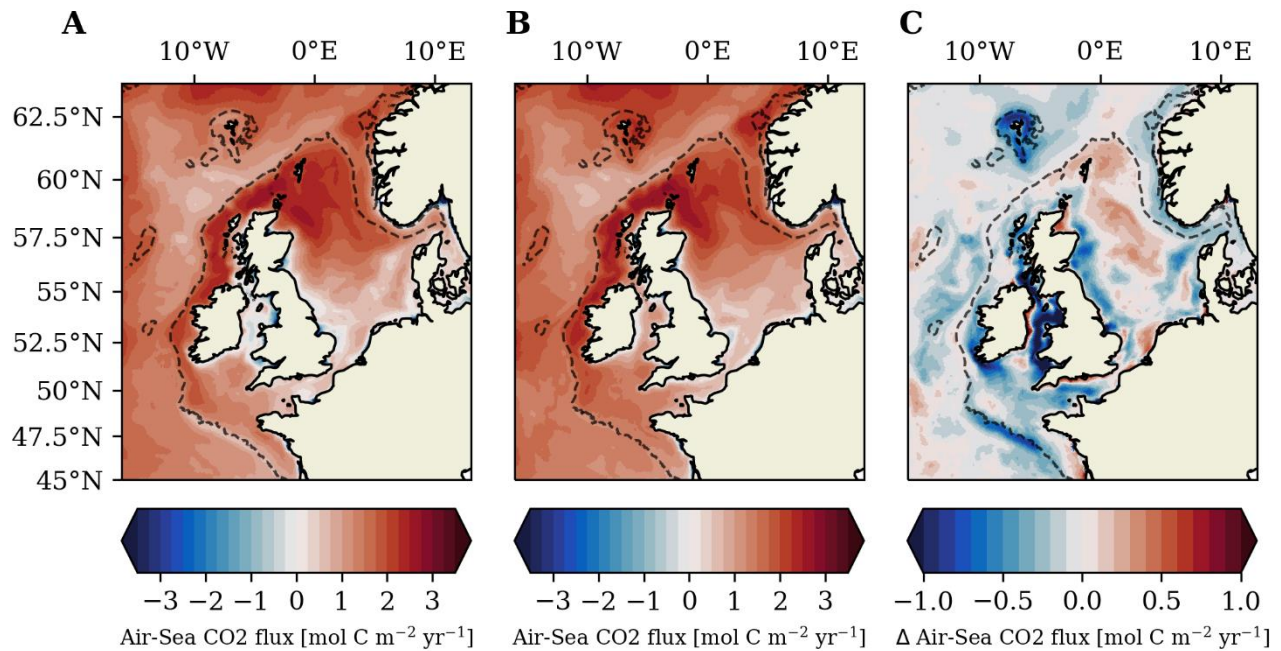
873 **Figure 3:** Taylor Plot of model DIC data (orange) and TA data (green) co-located against
 874 GLODAPv2.2022 data for 2001-2005.



875

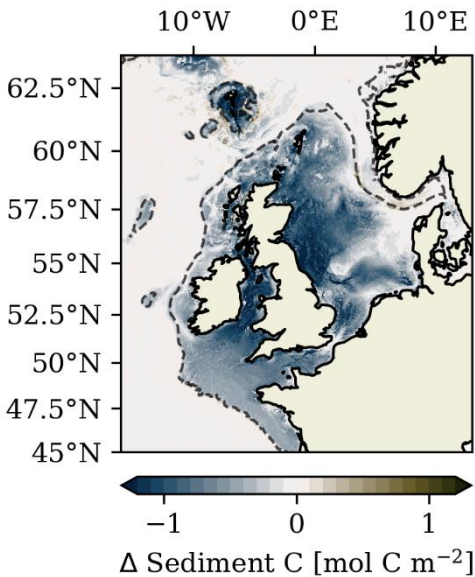
876 **Figure 4:** Simulated seasonal mean surface $p\text{CO}_2$ (2001-2005). Bottom panel shows the respective
 877 seasonally aggregated model bias (model – observations) against co-located SOCATv2023
 878 observations for 2001-2005.

879



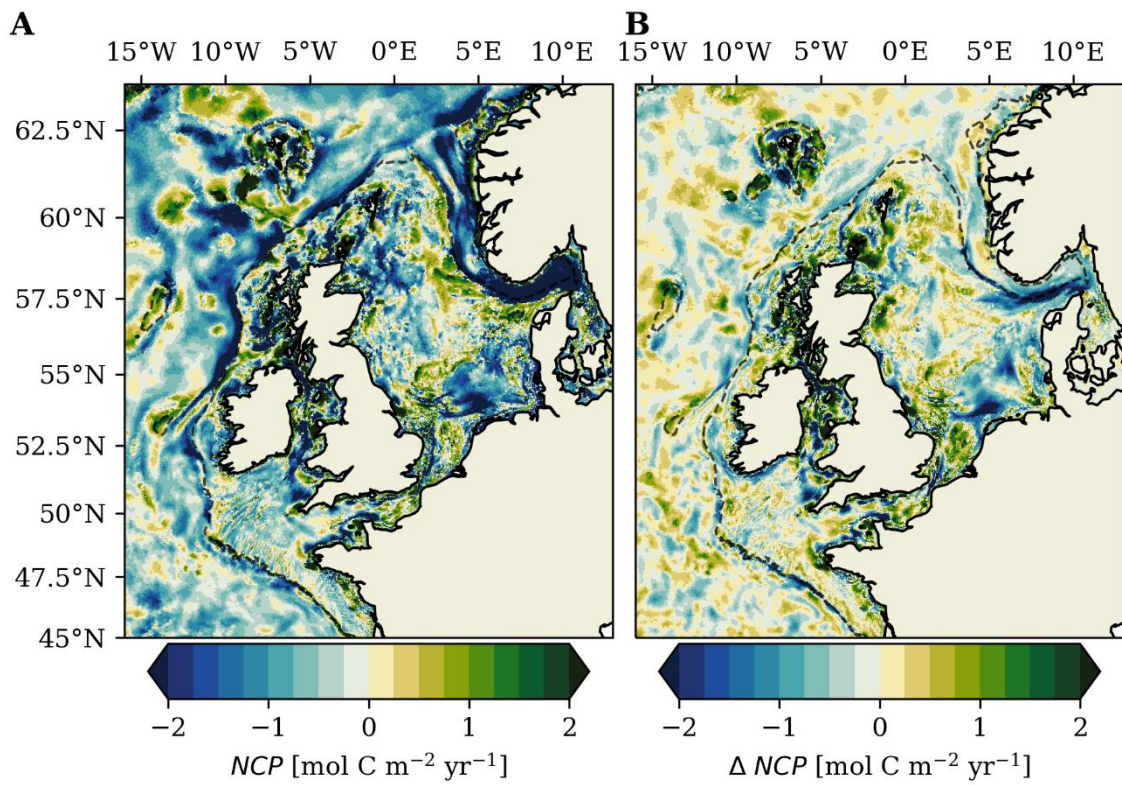
880

881 **Figure 5:** Annual mean air-sea CO₂ flux (2001-2005) for (A) TIDE experiment and (B) NOTIDE
 882 experiment. (C) shows the difference (TIDE – NOTIDE) of the air-sea CO₂ flux between the two
 883 experiments. Positive (red) values in (A) and (B) indicate oceanic CO₂ uptake, negative values (blue)
 884 indicate outgassing to the atmosphere.



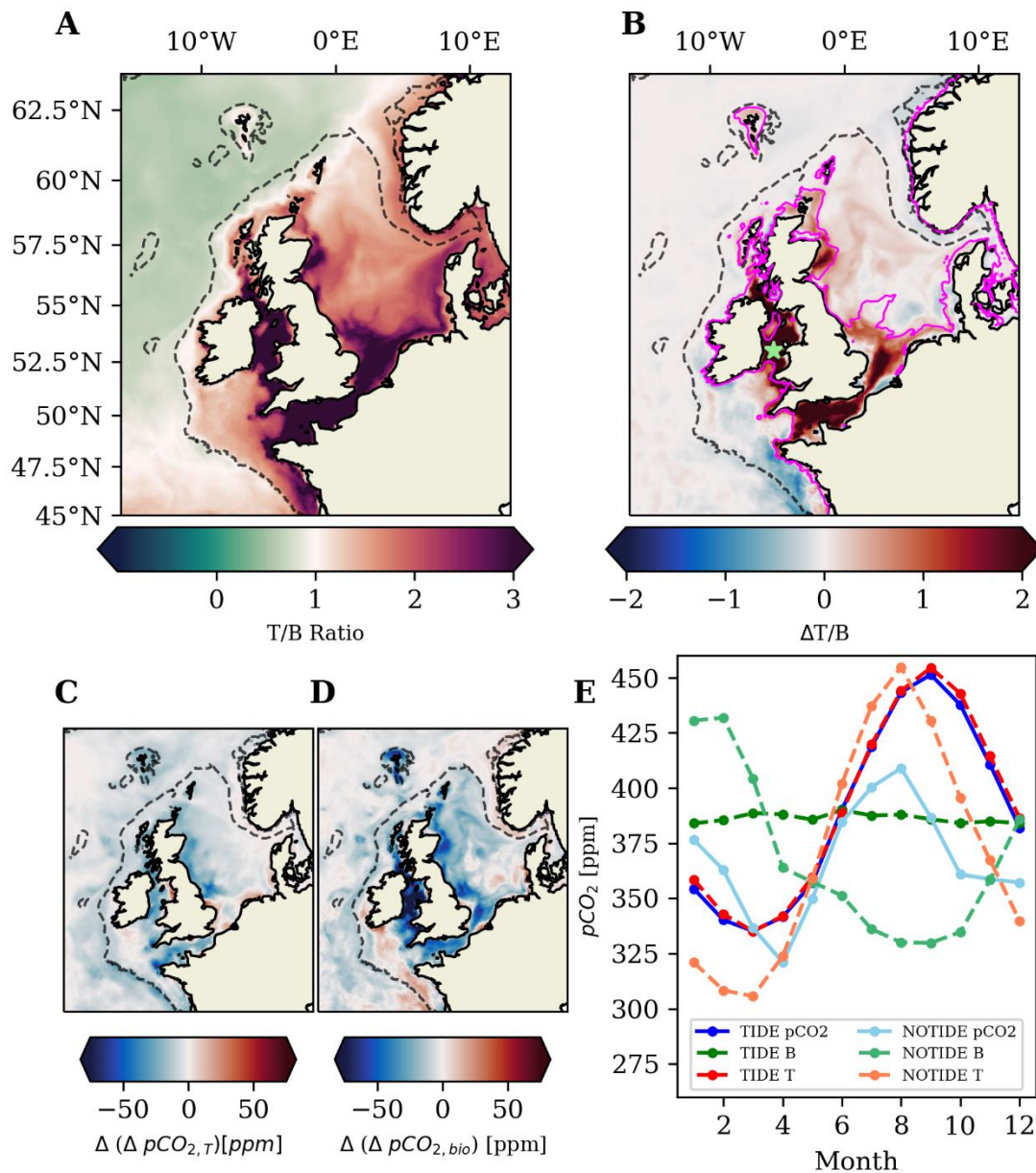
885

886 **Figure 6:** Difference of the annual mean sediment organic carbon inventories (2001-2005) between
 887 the two experiments (TIDE-NOTIDE).



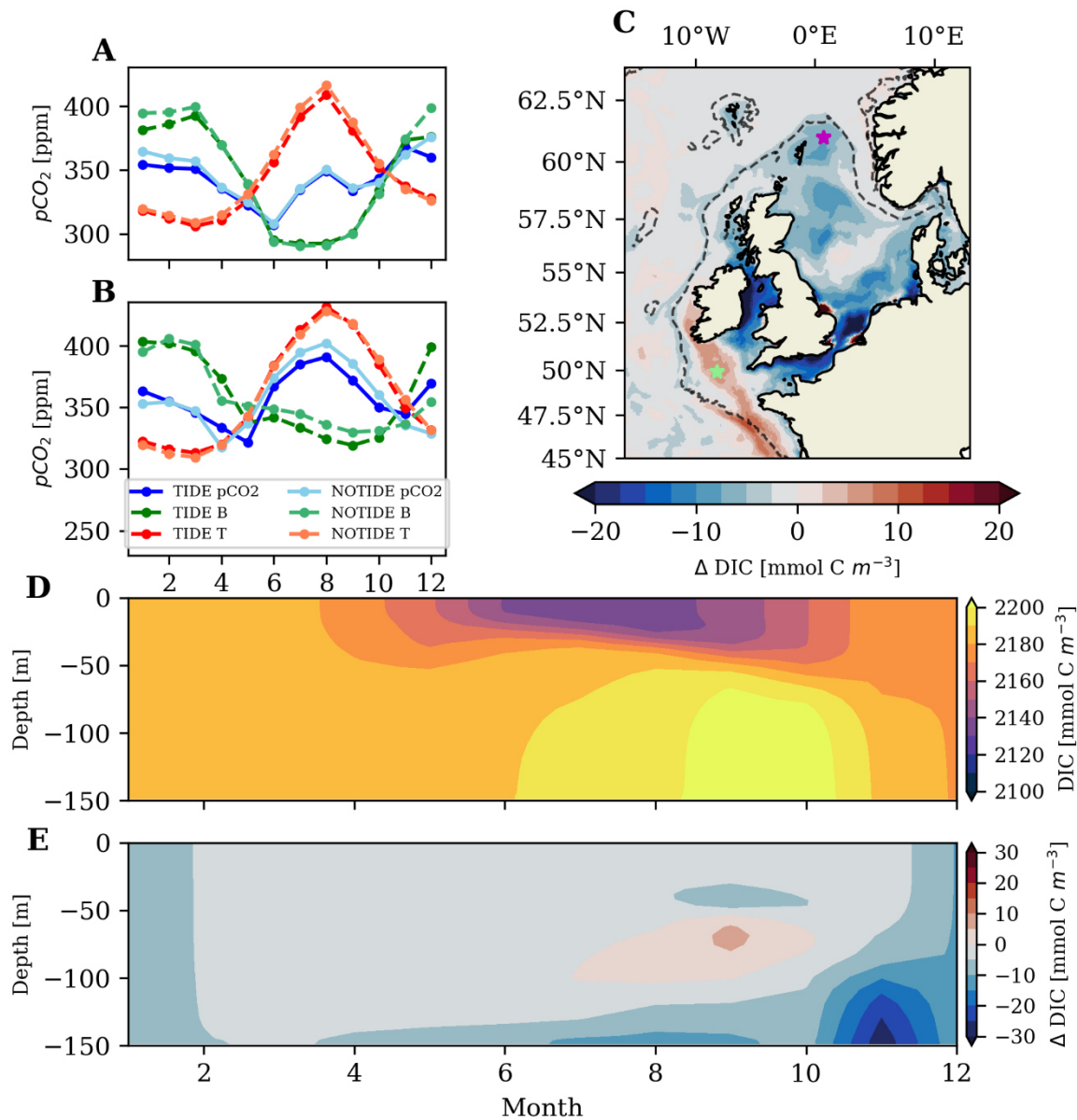
888

889 **Figure 7:** (A) Mean annual net community production (2001-2005; Eq. 7) in TIDE experiment. (B)
 890 Difference of mean annual net community production (2001-2005) in the two experiments (TIDE –
 891 NOTIDE).



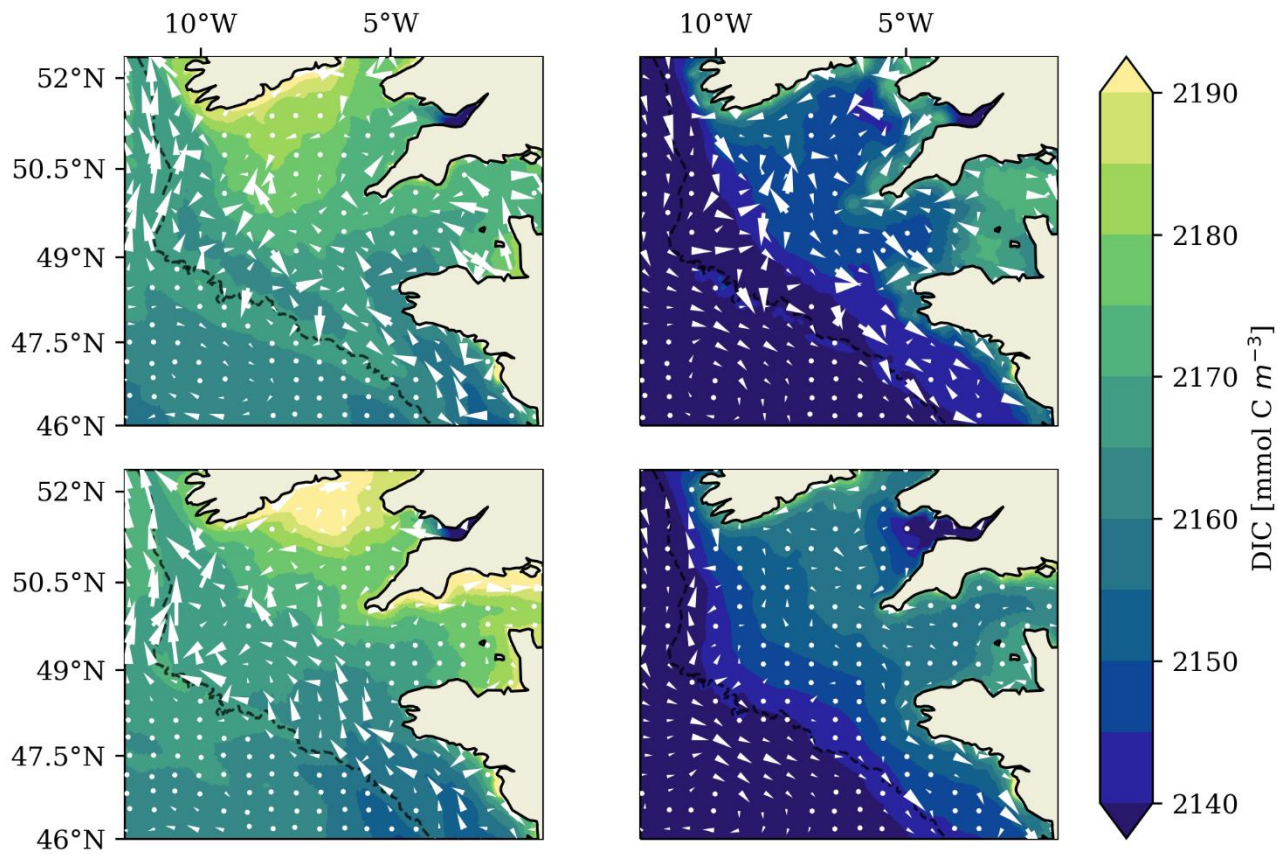
892

893 **Figure 8:** (A) T/B ratio of the temperature and biological effects on pCO₂ over the mean annual
 894 cycle (2001-2005) in the TIDE experiment calculated with Eq. 4. (B) Difference in the T/B ratio
 895 between the two experiments (TIDE-NOTIDE). Magenta contour indicates PEA=20 J m⁻³. The
 896 difference in the amplitudes of surface pCO₂ changes related to temperature (C) and biology (D)
 897 between the two experiments (TIDE-NOTIDE). (E) Surface pCO₂ evaluated at 53°N 5.25°W in the
 898 Irish Sea (marked with green star in Fig. 8B).



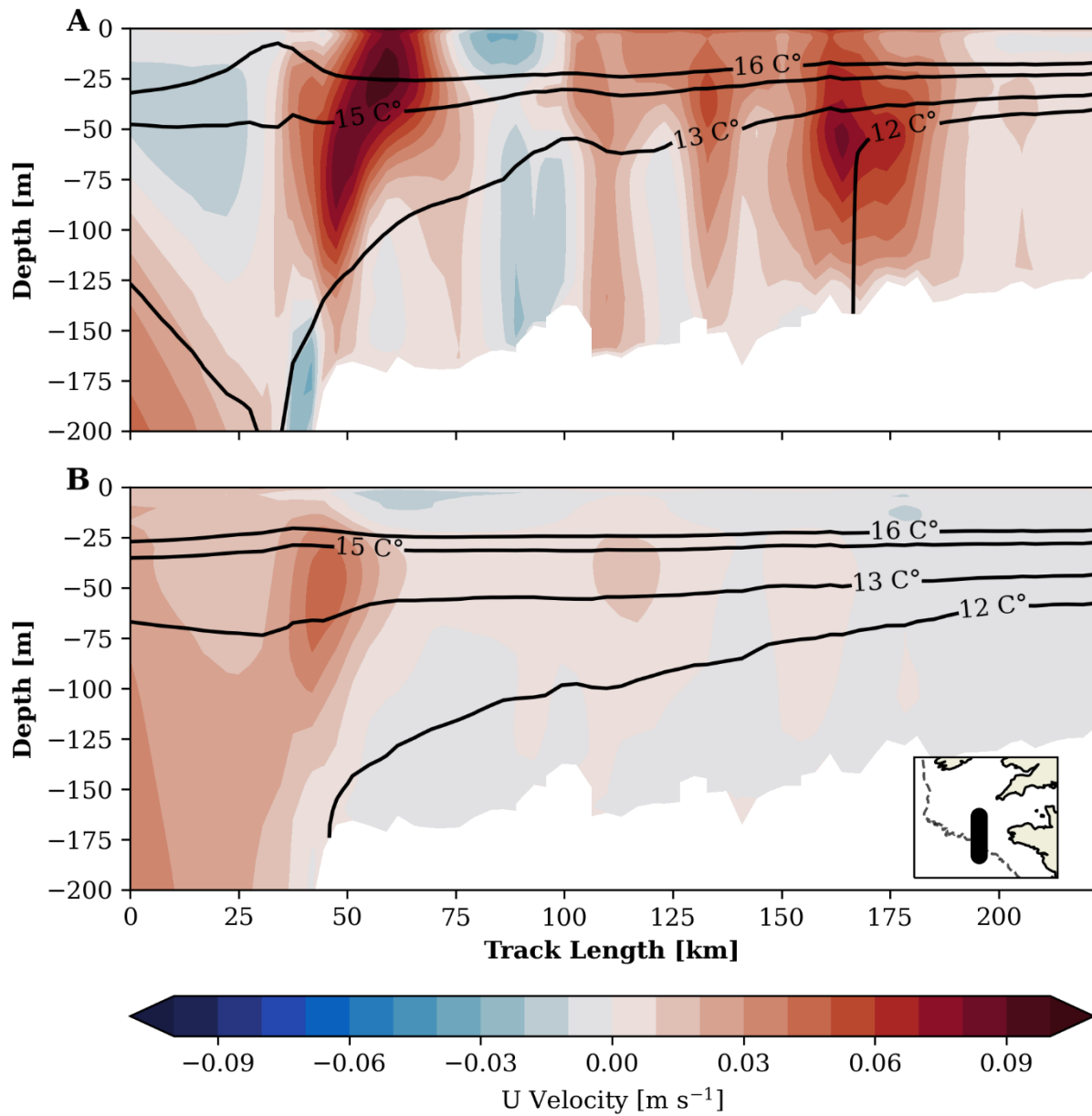
899

900 **Figure 9:** Surface pCO₂ evaluated at (A) 61°N 0.75°E in the northern North Sea (marked with
 901 magenta star in Fig. 9C) and (B) 49.9°N 8.2°W in the Celtic Sea (marked with green star in Fig. 9C).
 902 (C) Difference in mean surface winter DIC (2001-2005; TIDE-NOTIDE). (D) Mean DIC
 903 concentration in TIDE experiment and (E) difference in mean DIC concentration (TIDE-NOTIDE) at
 904 61°N 0.75°E in the northern North Sea (marked with magenta star in Fig. 9C).



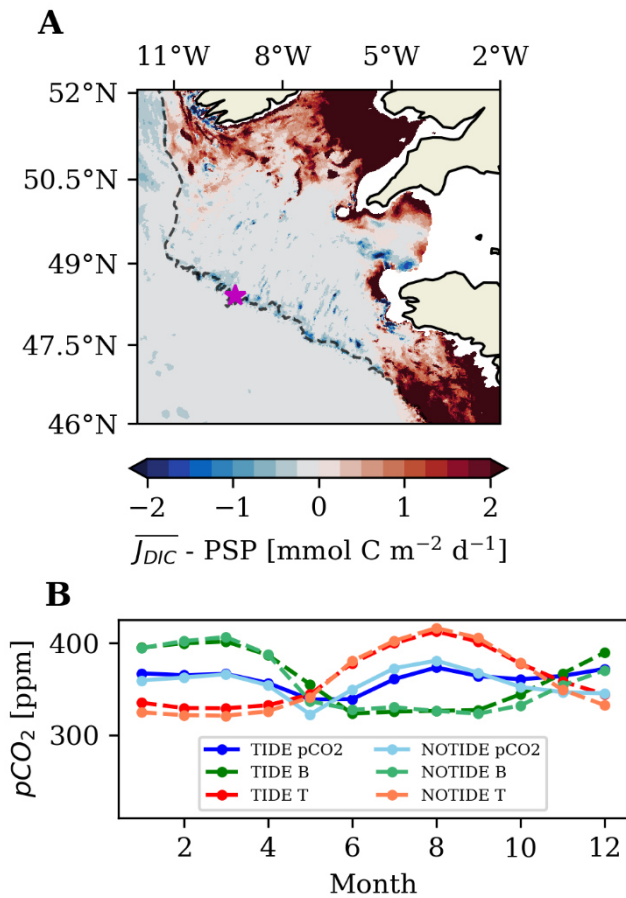
905

906 **Figure 10:** Mean winter (left) and summer (right) surface DIC and overlaid seasonal mean depth-
 907 averaged residual circulation in the Celtic Sea (2001-2005) in the TIDE experiment (top panel) and
 908 NOTIDE experiment (bottom panel).



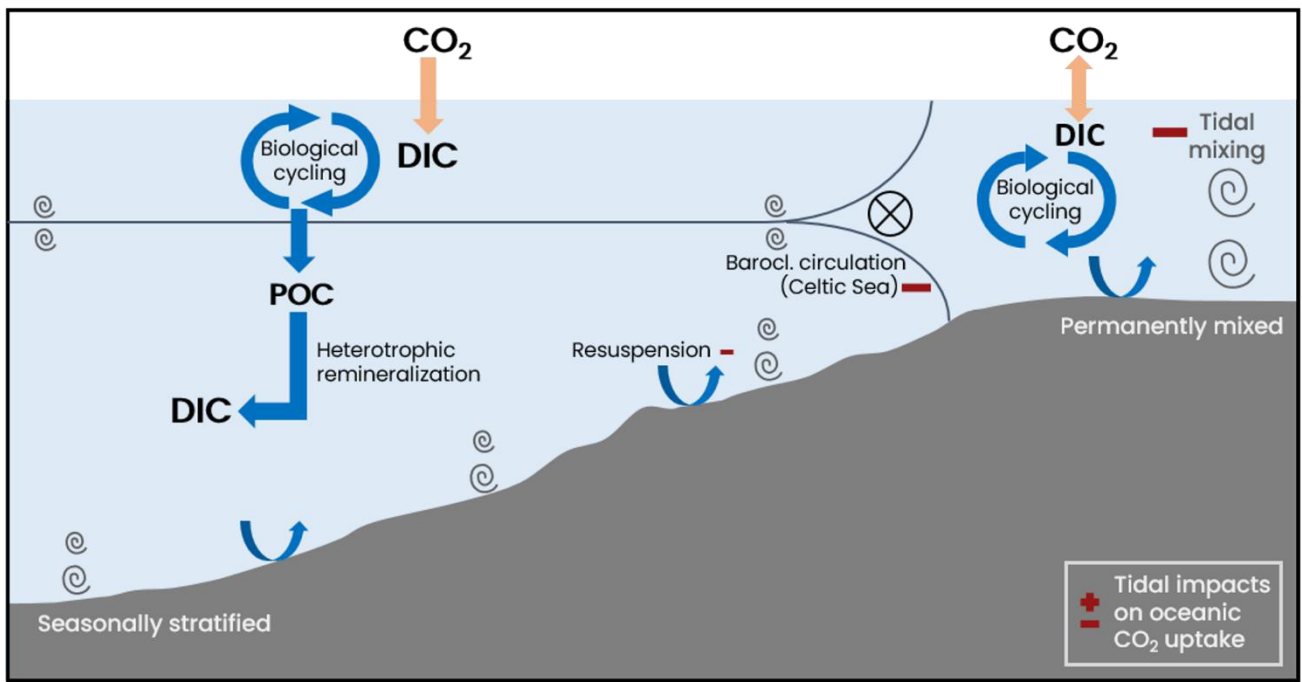
909

910 **Figure 11:** Mean summer horizontal u-velocity on transect across Celtic Sea in TIDE experiment (A)
 911 and NOTIDE experiment (B). Positive values (red) denote eastward flow. Location of transect
 912 marked in inset figure in Fig. 11B.



913

914 **Figure 12:** Difference of the summer mean turbulent DIC flux (2001-2005; Eq. 9) evaluated at the
 915 base of the euphotic zone and summer mean potential subsurface primary production (Eq. 10)
 916 sustained by the turbulent nitrate flux into the surface layer. Permanently mixed regions are masked
 917 out. (B) Surface $p\text{CO}_2$ evaluated at $14.4^\circ\text{W } 53^\circ\text{N}$ on the Celtic Sea shelf break (marked with magenta
 918 star in Fig. 12A).



919
 920 **Figure 13:** Schematic illustration of tidal impacts on air-sea CO₂ exchange on the NWES.

921
 922
 923
 924
 925
 926
 927
 928
 929
 930
 931
 932
 933
 934
 935

936 **7 Conflict of Interest**

937 The authors declare that the research was conducted in the absence of any commercial or financial
938 relationships that could be construed as a potential conflict of interest.

939 **8 Author Contributions**

940 JK performed the model experiments and generated the data set, performed the data analysis, and
941 wrote the manuscript. UD, CS, JK, FL and KD contributed to model development. MM, UD, HT and
942 CS provided essential background knowledge and advised the study. CS initiated the idea of the
943 study. All authors contributed to conception and design of the study and manuscript revision, and
944 read and approved the submitted version.

945 **9 Funding**

946 The research was funded by the Deutsche Forschungsgemeinschaft (DFG, German Research
947 Foundation) under Germany's Excellence Strategy – EXC 2037 'CLICCS - Climate, Climatic
948 Change, and Society' – Project Number: 390683824.

949 **10 Acknowledgments**

950 We would like to thank Yinglong Joseph Zhang for helpful advice regarding the SCHISM model and
951 Nils Christiansen for support with SCHISM configuration and figure design. Computational
952 resources were made available by the German Climate Computing Center (DKRZ) through support
953 from the German Federal Ministry of Education and Research (BMBF). We would like to thank
954 ICDC, CEN, University Hamburg, for data support. This study has been conducted using data from
955 the Global Ocean Data Analysis Project (GLODAP), the Surface Ocean CO2 Atlas (SOCAT) and the
956 Norwegian Meteorological Institute. The research was funded by the Deutsche
957 Forschungsgemeinschaft (DFG, German Research Foundation) under Germany's Excellence
958 Strategy – EXC 2037 'CLICCS - Climate, Climatic Change, and Society' – Project Number:
959 390683824 and contributes to the CLICCS subproject A5 – The Land-Ocean Transition Zone. The
960 article processing charges for this open-access publication were covered by the Helmholtz-Zentrum
961 Hereon.

962 **12 Data Availability Statement**

963 The raw data supporting the conclusions of this article will be made available by the authors, without
964 undue reservation.

965

966

967

968

969

970

971 REFERENCES

- 972 Allen, J. I., Holt, J. T., Blackford, J., and Proctor, R. (2007). Error quantification of a high-resolution
973 coupled hydrodynamic-ecosystem coastal-ocean model: Part 2. Chlorophyll-a, nutrients and SPM.
974 *Journal of Marine Systems* 68, 381–404. doi: 10.1016/j.jmarsys.2007.01.005
- 975 Arnold, A. K., Lewis, H. W., Hyder, P., Siddorn, J., and O’Dea, E. (2021). The Sensitivity of British
976 Weather to Ocean Tides. *Geophys Res Lett* 48, e2020GL090732. doi: 10.1029/2020GL090732
- 977 Artioli, Y., Blackford, J. C., Butenschön, M., Holt, J. T., Wakelin, S. L., Thomas, H., et al. (2012).
978 The carbonate system in the North Sea: Sensitivity and model validation. *Journal of Marine*
979 *Systems* 102-104, 1–13. doi: 10.1016/j.jmarsys.2012.04.006
- 980 Artioli, Y., Blackford, J. C., Nondal, G., Bellerby, R. G., Wakelin, S. L., Holt, J. T., et al. (2014).
981 Heterogeneity of impacts of high CO₂ on the North Western European Shelf. *Biogeosciences* 11,
982 601–612. doi: 10.5194/bg-11-601-2014
- 983 Azam, F., Fenchel, T., Field, J. G., Gray, J. S., Meyer-Reil, L. A., and Thingstad, F. (1983). “The
984 Ecological Role of Water-Column Microbes in the Sea,” in *Foundations of Ecology II : Classic*
985 *Papers with Commentaries*, eds. T. E. Miller, and J. Travis (Chicago: University of Chicago
986 Press), 384–390.
- 987 Bakker, D. C. E., Pfeil, B., Landa, C. S., Metzl, N., O’Brien, K. M., Olsen, A., et al. (2016). A multi-
988 decade record of high-quality fCO₂ data in version 3 of the Surface Ocean CO₂ Atlas (SOCAT).
989 *Earth System Science Data* 8, 383–413. doi: 10.5194/essd-8-383-2016
- 990 Bauer, J. E., Cai, W.-J., Raymond, P. A., Bianchi, T. S., Hopkinson, C. S., and Regnier, P. A. G.
991 (2013). The changing carbon cycle of the coastal ocean. *NATURE* 504, 61–70. doi:
992 10.1038/nature12857
- 993 Becherer, J., Burchard, H., Carpenter, J. R., Graewe, U., and Merckelbach, L. M. (2022). The Role of
994 Turbulence in Fueling the Subsurface Chlorophyll Maximum in Tidally Dominated Shelf Seas. *J.*
995 *Geophys. Res. Oceans* 127, e2022JC018561. doi: 10.1029/2022JC018561
- 996 Becker, M., Olsen, A., Landschützer, P., Omar, A., Rehder, G., Rödenbeck, C., et al. (2021). The
997 northern European shelf as an increasing net sink for CO₂. *Biogeosciences* 18, 1127–1147. doi:
998 10.5194/bg-18-1127-2021
- 999 Blackford, J., Artioli, Y., Clark, J., and Mora, L. de (2017). Monitoring of offshore geological carbon
1000 storage integrity: Implications of natural variability in the marine system and the assessment of
1001 anomaly detection criteria. *International Journal of Greenhouse Gas Control* 64, 99–112. doi:
1002 10.1016/j.ijggc.2017.06.020
- 1003 Blackford, J. C., and Gilbert, F. J. (2007). pH variability and CO₂ induced acidification in the North
1004 Sea. *Contributions from Advances in Marine Ecosystem Modelling Research, 27-29 June, 2005,*
1005 *Plymouth, UK* 64, 229–241. doi: 10.1016/j.jmarsys.2006.03.016
- 1006 Boyer, T. P., García, H. E., Locarnini, R. A., Zweng, M. M., Mishonov, A. V., Reagan, J. R., et al.
1007 (2018). World Ocean Atlas 2018. Dataset. Accessed July 29, 2022,
1008 <https://www.ncei.noaa.gov/archive/accession/NCEI-WOA18>
- 1009 Bozec, Y., Thomas, H., Schiettecatte, L.-S., Borges, A. V., Elkalay, K., and Baar, H. J. W. d. (2006).
1010 Assessment of the processes controlling the seasonal variations of dissolved inorganic carbon in
1011 the North Sea. *Limnol. Oceanogr.* 51, 2746–2762. doi: 10.4319/lo.2006.51.6.2746

- 1012 Brenner, H., Braeckman, U., Le Guitton, M., and Meysman, F. J. R. (2016). The impact of
1013 sedimentary alkalinity release on the water column CO₂ system in the North Sea. *Biogeosciences*
1014 13, 841–863. doi: 10.5194/bg-13-841-2016
- 1015 Broullón, D., Pérez, F. F., Velo, A., Hoppema, M., Olsen, A., Takahashi, T., et al. (2019). A global
1016 monthly climatology of total alkalinity: a neural network approach. *Earth System Science Data* 11,
1017 1109–1127. doi: 10.5194/essd-11-1109-2019
- 1018 Broullón, D., Pérez, F. F., Velo, A., Hoppema, M., Olsen, A., Takahashi, T., et al. (2020). A global
1019 monthly climatology of oceanic total dissolved inorganic carbon: a neural network approach. *Earth*
1020 *System Science Data* 12, 1725–1743. doi: 10.5194/essd-12-1725-2020
- 1021 Brown, J., Carrillo, L., Fernand, L., Horsburgh, K., Hill, A., Young, E., et al. (2003). Observations of
1022 the physical structure and seasonal jet-like circulation of the Celtic Sea and St. George's Channel
1023 of the Irish Sea. *Continental Shelf Research* 23, 533–561. doi: 10.1016/S0278-4343(03)00008-6
- 1024 Bruggeman, J., and Bolding, K. (2014). A general framework for aquatic biogeochemical models.
1025 *Environmental Modelling & Software* 61, 249–265. doi: 10.1016/j.envsoft.2014.04.002
- 1026 Charria, G., Lazure, P., Le Cann, B., Serpette, A., Reverdin, G., Louazel, S., et al. (2013). Surface
1027 layer circulation derived from Lagrangian drifters in the Bay of Biscay. *XII International*
1028 *Symposium on Oceanography of the Bay of Biscay* 109-110, S60-S76. doi:
1029 10.1016/j.jmarsys.2011.09.015
- 1030 Daewel, U., and Schrum, C. (2013). Simulating long-term dynamics of the coupled North Sea and
1031 Baltic Sea ecosystem with ECOSMO II: Model description and validation. *Journal of Marine*
1032 *Systems* 119-120, 30–49. doi: 10.1016/j.jmarsys.2013.03.008
- 1033 Dai, M., Su, J., Zhao, Y., Hofmann, E. E., Cao, Z., Cai, W.-J., et al. (2022). Carbon Fluxes in the
1034 Coastal Ocean: Synthesis, Boundary Processes, and Future Trends. *Annu. Rev. Earth Planet. Sci.*
1035 50, 593–626. doi: 10.1146/annurev-earth-032320-090746
- 1036 Frankignoulle, M., and Borges, A. V. (2001). European continental shelf as a significant sink for
1037 atmospheric carbon dioxide. *Global Biogeochem. Cycles* 15, 569–576. doi:
1038 10.1029/2000GB001307
- 1039 Graham, J. A., Rosser, J. P., O'Dea, E., and Hewitt, H. T. (2018). Resolving Shelf Break Exchange
1040 Around the European Northwest Shelf. *Geophys. Res. Lett.* 45, 12,386-12,395. doi:
1041 10.1029/2018GL079399
- 1042 Guihou, K., Polton, J., Harle, J., Wakelin, S., O'Dea, E., and Holt, J. (2018). Kilometric Scale
1043 Modeling of the North West European Shelf Seas: Exploring the Spatial and Temporal Variability
1044 of Internal Tides. *J. Geophys. Res. Oceans* 123, 688–707. doi: 10.1002/2017JC012960
- 1045 Gustafsson, E. (2013). Modelling the marine CO₂ system in BALTSEM. Stockholm University,
1046 <https://www.diva-portal.org/smash/get/diva2:1598412/FULLTEXT02>
- 1047 Hickman, A. E., Moore, C. M., Sharples, J., Lucas, M. I., Tilstone, G. H., Krivtsov, V., et al. (2012).
1048 Primary production and nitrate uptake within the seasonal thermocline of a stratified shelf sea. *Mar*
1049 *Ecol Prog Ser* 463, 39–57. doi: 10.3354/meps09836
- 1050 Hill, A. E., Brown, J., Fernand, L., Holt, J., Horsburgh, K. J., Proctor, R., et al. (2008). Thermohaline
1051 circulation of shallow tidal seas. *Geophys. Res. Lett.* 35. doi: 10.1029/2008GL033459
- 1052 Hjalmarsson, S., Wesslander, K., Anderson, L. G., Omstedt, A., Perttilä, M., and Mintrop, L. (2008).
1053 Distribution, long-term development and mass balance calculation of total alkalinity in the Baltic
1054 Sea. *Continental Shelf Research* 28, 593–601. doi: 10.1016/j.csr.2007.11.010

- 1055 Holt, J., Hyder, P., Ashworth, M., Harle, J., Hewitt, H. T., Liu, H., et al. (2017). Prospects for
1056 improving the representation of coastal and shelf seas in global ocean models. *Geoscientific Model*
1057 *Development* 10, 499–523. doi: 10.5194/gmd-10-499-2017
- 1058 Humphreys, M. P., Achterberg, E. P., Hopkins, J. E., Chowdhury, M. Z., Griffiths, A. M., Hartman,
1059 S. E., et al. (2019). Mechanisms for a nutrient-conserving carbon pump in a seasonally stratified,
1060 temperate continental shelf sea. *Shelf Sea Biogeochemistry: Pelagic Processes* 177, 101961. doi:
1061 10.1016/j.pocean.2018.05.001
- 1062 Humphreys, M. P., Schiller, A. J., Sandborn, D., Gregor, L., Pierrot, D., van Heuven, S. M. A. C., et
1063 al. (2023). PyCO2SYS: marine carbonate system calculations in Python. Zenodo,
1064 <https://doi.org/10.5281/zenodo.7550236> doi: 10.5281/zenodo.7550236
- 1065 Huthnance, J., Hopkins, J., Berx, B., Dale, A., Holt, J., Hosegood, P., et al. (2022). Ocean shelf
1066 exchange, NW European shelf seas: Measurements, estimates and comparisons. *Progress in*
1067 *Oceanography* 202, 102760. doi: 10.1016/j.pocean.2022.102760
- 1068 Key, R. M., Olsen, A., van Heuven, S., Lauvset, S. K., Velo, A., Lin, X., et al. (2015). *Global Ocean*
1069 *Data Analysis Project: Version 2 (GLODAPv2)*. ORNL/CDIAC-162. NDP-093. Carbon Dioxide
1070 Information Analysis Center, Oak Ridge National Laboratory, US Department of Energy, Oak
1071 Ridge, Tennessee.
- 1072 Kitidis, V., Shutler, J. D., Ashton, I., Warren, M., Brown, I., Findlay, H., et al. (2019). Winter
1073 weather controls net influx of atmospheric CO₂ on the north-west European shelf. *Scientific*
1074 *Reports* 9, 20153. doi: 10.1038/s41598-019-56363-5
- 1075 Kossack, J., Mathis, M., Daewel, U., Zhang, Y. J., and Schrum, C. (2023). Barotropic and baroclinic
1076 tides increase primary production on the Northwest European Shelf. *FRONTIERS IN MARINE*
1077 *SCIENCE* 10. doi: 10.3389/fmars.2023.1206062
- 1078 Krumins, V., Gehlen, M., Arndt, S., van Cappellen, P., and Regnier, P. (2013). Dissolved inorganic
1079 carbon and alkalinity fluxes from coastal marine sediments: model estimates for different shelf
1080 environments and sensitivity to global change. *Biogeosciences* 10, 371–398. doi: 10.5194/bg-10-
1081 371-2013
- 1082 Kühn, W., Pätsch, J., Thomas, H., Borges, A. V., Schiettecatte, L.-S., Bozec, Y., et al. (2010).
1083 Nitrogen and carbon cycling in the North Sea and exchange with the North Atlantic—A model
1084 study, Part II: Carbon budget and fluxes. *Continental Shelf Research* 30, 1701–1716. doi:
1085 10.1016/j.csr.2010.07.001
- 1086 Lan, X., Dlugokencky, E. J., Mund, J. W., Crotwell, A. M., Crotwell, M. J., Moglia, E., et al. (2022).
1087 Atmospheric Carbon Dioxide Dry Air Mole Fractions from the NOAA GML Carbon Cycle
1088 Cooperative Global Air Sampling Network, 1968-2021: Version: 2022-11-21. doi: 10.15138/wkgj-
1089 f215
- 1090 Legge, O., Johnson, M., Hicks, N., Jickells, T., Diesing, M., Aldridge, J., et al. (2020). Carbon on the
1091 Northwest European Shelf: Contemporary Budget and Future Influences. *FRONTIERS IN*
1092 *MARINE SCIENCE* 7. doi: 10.3389/fmars.2020.00143
- 1093 Marrec, P., Cariou, T., Macé, E., Morin, P., Salt, L. A., Vernet, M., et al. (2015). Dynamics of air–
1094 sea CO₂ fluxes in the northwestern European shelf based on voluntary observing ship and
1095 satellite observations. *Biogeosciences* 12, 5371–5391. doi: 10.5194/bg-12-5371-2015

- 1096 Mathis, M., Lacroix, F., Hagemann, S., Nielsen, D. M., Ilyina, T., and Schrum, C. (2024). Enhanced
1097 CO₂ uptake of the coastal ocean is dominated by biological carbon fixation. *Nature Climate*
1098 *Change*. doi: 10.1038/s41558-024-01956-w
- 1099 Mathis, M., Logemann, K., Maerz, J., Lacroix, F., Hagemann, S., Chegini, F., et al. (2022). Seamless
1100 Integration of the Coastal Ocean in Global Marine Carbon Cycle Modeling. *J Adv Model Earth*
1101 *Syst* 14, e2021MS002789. doi: 10.1029/2021MS002789
- 1102 Meyer, M., Pätsch, J., Geyer, B., and Thomas, H. (2018). Revisiting the Estimate of the North Sea
1103 Air-Sea Flux of CO₂ in 2001/2002: The Dominant Role of Different Wind Data Products. *J.*
1104 *Geophys. Res. Biogeosci.* 123, 1511–1525. doi: 10.1029/2017JG004281
- 1105 Millero, F. J., Graham, T. B., Huang, F., Bustos-Serrano, H., and Pierrot, D. (2006). Dissociation
1106 constants of carbonic acid in seawater as a function of salinity and temperature. *MARINE*
1107 *CHEMISTRY* 100, 80–94. doi: 10.1016/j.marchem.2005.12.001
- 1108 Neal, C., and Davies, H. (2003). Water quality fluxes for eastern UK rivers entering the North Sea: a
1109 summary of information from the Land Ocean Interaction Study (LOIS). *Land Ocean Interaction:*
1110 *processes, functioning and environmental management: a UK perspective* 314–316, 821–882. doi:
1111 10.1016/S0048-9697(03)00086-X
- 1112 New, A. L., and Pingree, R. D. (1990). Evidence for internal tidal mixing near the shelf break in the
1113 Bay of Biscay. *Deep Sea Research Part A. Oceanographic Research Papers* 37, 1783–1803. doi:
1114 10.1016/0198-0149(90)90078-A
- 1115 Olsen, A., Key, R. M., van Heuven, S., Lauvset, S. K., Velo, A., Lin, X., et al. (2016). The Global
1116 Ocean Data Analysis Project version 2 (GLODAPv2) - an internally consistent data product for the
1117 world ocean. *Earth System Science Data* 8, 297–323. doi: 10.5194/essd-8-297-2016
- 1118 Omar, A. M., Olsen, A., Johannessen, T., Hoppema, M., Thomas, H., and Borges, A. V. (2010).
1119 Spatiotemporal variations of fCO₂ in the North Sea. *Ocean Science* 6, 77–89. doi: 10.5194/os-6-
1120 77-2010
- 1121 Pätsch, J., and Lenhart, H. (2008). Daily Loads of Nutrients, Total Alkalinity, Dissolved Inorganic
1122 Carbon and Dissolved Organic Carbon of the European Continental Rivers for the Years 1977-
1123 2006. *Berichte aus dem Zentrum für Meeres- und Klimaforschung, Reihe B, Ozeanographie.*
- 1124 Pingree, R. D., and Le Cann, B. (1989). Celtic and Armorican slope and shelf residual currents.
1125 *Progress in Oceanography* 23, 303–338. doi: 10.1016/0079-6611(89)90003-7
- 1126 Polton, J. A. (2015). Tidally induced mean flow over bathymetric features: a contemporary challenge
1127 for high-resolution wide-area models. *Geophysical & Astrophysical Fluid Dynamics* 109, 207–
1128 215. doi: 10.1080/03091929.2014.952726
- 1129 Prowe, A. E. F., Thomas, H., Pätsch, J., Kühn, W., Bozec, Y., Schiettecatte, L.-S., et al. (2009).
1130 Mechanisms controlling the air–sea CO₂ flux in the North Sea. *Continental Shelf Research* 29,
1131 1801–1808. doi: 10.1016/j.csr.2009.06.003
- 1132 Redfield, A. C., Ketchum, B. H., and Richards, F. A. (1963). The influence of organisms on the
1133 composition of seawater. *The Sea* 2, 26–77.
- 1134 Resplandy, L., Hogikyan, A., Müller, J. D., Najjar, R. G., Bange, H. W., Bianchi, D., et al. (2024). A
1135 Synthesis of Global Coastal Ocean Greenhouse Gas Fluxes. *Global Biogeochem Cycles* 38,
1136 e2023GB007803. doi: 10.1029/2023GB007803
- 1137 Richardson, K., Visser, A. W., and Pedersen, F. B. (2000). Subsurface phytoplankton blooms fuel
1138 pelagic production in the North Sea. *J Plankton Res* 22, 1663–1671. doi: 10.1093/plankt/22.9.1663

- 1139 Rippeth, T. P. (2005). Mixing in seasonally stratified shelf seas: a shifting paradigm. *Philosophical*
 1140 *Transactions of the Royal Society A: Mathematical, Physical and Engineering Sciences* 363, 2837–
 1141 2854. doi: 10.1098/rsta.2005.1662
- 1142 Rippeth, T. P., and Inall, M. E. (2002). Observations of the internal tide and associated mixing across
 1143 the Malin Shelf. *J. Geophys. Res.* 107, 928. doi: 10.1029/2000JC000761
- 1144 Rippeth, T. P., Lincoln, B. J., Kennedy, H. A., Palmer, M. R., Sharples, J., and Williams, C. A. J.
 1145 (2014). Impact of vertical mixing on sea surface pCO₂ in temperate seasonally stratified shelf seas.
 1146 *J. Geophys. Res. Oceans* 119, 3868–3882. doi: 10.1002/2014JC010089
- 1147 Samuelsen, A., Schrum, C., Yumruktepe, V. Ç., Daewel, U., and Roberts, E. M. (2022).
 1148 Environmental Change at Deep-Sea Sponge Habitats Over the Last Half Century: A Model
 1149 Hindcast Study for the Age of Anthropogenic Climate Change. *FRONTIERS IN MARINE*
 1150 *SCIENCE* 9. doi: 10.3389/fmars.2022.737164
- 1151 Schiettecatte, L.-S., Thomas, H., Bozec, Y., and Borges, A. V. (2007). High temporal coverage of
 1152 carbon dioxide measurements in the Southern Bight of the North Sea. *Special issue: Dedicated to*
 1153 *the memory of Professor Roland Wollast* 106, 161–173. doi: 10.1016/j.marchem.2007.01.001
- 1154 Sharples, J. (2008). Potential impacts of the spring-neap tidal cycle on shelf sea primary production.
 1155 *J Plankton Res* 30, 183–197. doi: 10.1093/plankt/fbm088
- 1156 Sharples, J., Moore, M. C., Rippeth, T. P., Holligan, P. M., Hydes, D. J., Fisher, N. R., et al. (2001).
 1157 Phytoplankton distribution and survival in the thermocline. *Limnol. Oceanogr.* 46, 486–496. doi:
 1158 10.4319/lo.2001.46.3.0486
- 1159 Sharples, J., Tweddle, J. F., Mattias Green, J. A., Palmer, M. R., Kim, Y.-N., Hickman, A. E., et al.
 1160 (2007). Spring-neap modulation of internal tide mixing and vertical nitrate fluxes at a shelf edge in
 1161 summer. *Limnol. Oceanogr.* 52, 1735–1747. doi: 10.4319/lo.2007.52.5.1735
- 1162 Simpson, J. H., and Hunter, J. R. (1974). Fronts in the Irish Sea. *NATURE* 250, 404–406. doi:
 1163 10.1038/250404a0
- 1164 Spingys, C. P., Williams, R. G., Hopkins, J. E., Hall, R. A., Green, J. A. M., and Sharples, J. (2020).
 1165 Internal Tide-Driven Tracer Transport Across the Continental Slope. *J. Geophys. Res. Oceans* 125,
 1166 e2019JC015530. doi: 10.1029/2019JC015530
- 1167 Stashchuk, N., Vlasenko, V., Hosegood, P., and Nimmo-Smith, W. A. M. (2017). Tidally induced
 1168 residual current over the Malin Sea continental slope. *Continental Shelf Research* 139, 21–34. doi:
 1169 10.1016/j.csr.2017.03.010
- 1170 Takahashi, T., Sutherland, S. C., Sweeney, C., Poisson, A., Metz, N., Tilbrook, B., et al. (2002).
 1171 Global sea–air CO₂ flux based on climatological surface ocean pCO₂, and seasonal biological and
 1172 temperature effects. *The Southern Ocean I: Climatic Changes in the Cycle of Carbon in the*
 1173 *Southern Ocean* 49, 1601–1622. doi: 10.1016/S0967-0645(02)00003-6
- 1174 Thomas, H., Bozec, Y., Baar, H. J. W. de, Elkalay, K., Frankignoulle, M., Schiettecatte, L.-S., et al.
 1175 (2005a). The carbon budget of the North Sea. *Biogeosciences* 2, 87–96. doi: 10.5194/bg-2-87-2005
- 1176 Thomas, H., Bozec, Y., Elkalay, K., and Baar, H. J. W. d. (2004). Enhanced Open Ocean Storage of
 1177 CO₂ from Shelf Sea Pumping. *Science* 304, 1005–1008. doi: 10.1126/science.1095491
- 1178 Thomas, H., Bozec, Y., Elkalay, K., Baar, H. J. W. de, Borges, A. V., and Schiettecatte, L.-S.
 1179 (2005b). Controls of the surface water partial pressure of CO₂ in the North Sea. *Biogeosciences*
 1180 2, 323–334. doi: 10.5194/bg-2-323-2005

- 1181 Thomas, H., Friederike Prowe, A. E., Lima, I. D., Doney, S. C., Wanninkhof, R., Greatbatch, R. J., et
1182 al. (2008). Changes in the North Atlantic Oscillation influence CO₂ uptake in the North Atlantic
1183 over the past 2 decades. *Global Biogeochem. Cycles* 22. doi: 10.1029/2007GB003167
- 1184 Thomas, H., Schiettecatte, L.-S., Suykens, K., Koné, Y. J. M., Shadwick, E. H., Prowe, A. E. F., et
1185 al. (2009). Enhanced ocean carbon storage from anaerobic alkalinity generation in coastal
1186 sediments. *Biogeosciences* 6, 267–274. doi: 10.5194/bg-6-267-2009
- 1187 Tinker, J., Polton, J. A., Robins, P. E., Lewis, M. J., and O’Neill, C. K. (2022). The influence of tides
1188 on the North West European shelf winter residual circulation. *FRONTIERS IN MARINE SCIENCE*
1189 9. doi: 10.3389/fmars.2022.847138
- 1190 Tsunogai, S., Watanabe, S., and Sato, T. (1999). Is there a “continental shelf pump” for the
1191 absorption of atmospheric CO₂? *Tellus B: Chemical and Physical Meteorology* 51, 701–712. doi:
1192 10.3402/tellusb.v51i3.16468
- 1193 Vlasenko, V., Stashchuk, N., Inall, M. E., and Hopkins, J. E. (2014). Tidal energy conversion in a
1194 global hot spot: On the 3-D dynamics of baroclinic tides at the Celtic Sea shelf break. *J. Geophys.*
1195 *Res. Oceans* 119, 3249–3265. doi: 10.1002/2013JC009708
- 1196 Volk, T., and Hoffert, M. I. (1985). “Ocean Carbon Pumps: Analysis of Relative Strengths and
1197 Efficiencies in Ocean-Driven Atmospheric CO₂ Changes,” in *The Carbon Cycle and Atmospheric*
1198 *CO₂: Natural Variations Archean to Present*, 99–110.
- 1199 Wakelin, S. L., Holt, J. T., Blackford, J. C., Allen, J. I., Butenschön, M., and Artioli, Y. (2012).
1200 Modeling the carbon fluxes of the northwest European continental shelf: Validation and budgets. *J.*
1201 *Geophys. Res.* 117, n/a-n/a. doi: 10.1029/2011JC007402
- 1202 Wang, H., Gong, D., Friedrichs, M. A. M., Harris, C. K., Miles, T., Yu, H.-C., et al. (2022). A Cycle
1203 of Wind-Driven Canyon Upwelling and Downwelling at Wilmington Canyon and the Evolution of
1204 Canyon-Upwelled Dense Water on the MAB Shelf. *Front. Mar. Sci.* 9, 607. doi:
1205 10.3389/fmars.2022.866075
- 1206 Wanninkhof, R. (2014). Relationship between wind speed and gas exchange over the ocean revisited.
1207 *Limnol. Oceanogr. Methods* 12, 351–362. doi: 10.4319/lom.2014.12.351
- 1208 Ward, N. D., Megonigal, J. P., Bond-Lamberty, B., Bailey, V. L., Butman, D., Canuel, E. A., et al.
1209 (2020). Representing the function and sensitivity of coastal interfaces in Earth system models.
1210 *NATURE COMMUNICATIONS* 11, 2458. doi: 10.1038/s41467-020-16236-2
- 1211 Watson, A. J., Schuster, U., Bakker, D. C. E., Bates, N. R., Corbière, A., González-Dávila, M., et al.
1212 (2009). Tracking the Variable North Atlantic Sink for Atmospheric CO₂. *Science* 326, 1391–1393.
1213 doi: 10.1126/science.1177394
- 1214 Wolf-Gladrow, D. A., Zeebe, R. E., Klaas, C., Körtzinger, A., and Dickson, A. G. (2007). Total
1215 alkalinity: The explicit conservative expression and its application to biogeochemical processes.
1216 *Special issue: Dedicated to the memory of Professor Roland Wollast* 106, 287–300. doi:
1217 10.1016/j.marchem.2007.01.006
- 1218 Ye, F., Zhang, Y. J., Yu, H., Sun, W., Moghimi, S., Myers, E., et al. (2020). Simulating storm surge
1219 and compound flooding events with a creek-to-ocean model: Importance of baroclinic effects.
1220 *Ocean Modelling* 145, 101526. doi: 10.1016/j.ocemod.2019.101526
- 1221 Yu, H.-C., Zhang, Y. J., Yu, J. C., Terng, C., Sun, W., Ye, F., et al. (2017). Simulating multi-scale
1222 oceanic processes around Taiwan on unstructured grids. *Ocean Modelling* 119, 72–93. doi:
1223 10.1016/j.ocemod.2017.09.007

- 1224 Zhang, W., Wirtz, K., Daewel, U., Wrede, A., Kröncke, I., Kuhn, G., et al. (2019). The Budget of
1225 Macrobenthic Reworked Organic Carbon: A Modeling Case Study of the North Sea. *J. Geophys.*
1226 *Res. Biogeosci.* 124, 1446–1471. doi: 10.1029/2019JG005109
- 1227 Zhang, Y. J., Ye, F., Stanev, E. V., and Grashorn, S. (2016). Seamless cross-scale modeling with
1228 SCHISM. *Ocean Modelling* 102, 64–81. doi: 10.1016/j.ocemod.2016.05.002
- 1229 Zhao, C., Daewel, U., and Schrum, C. (2019). Tidal impacts on primary production in the North Sea.
1230 *Earth System Dynamics* 10, 287–317. doi: 10.5194/esd-10-287-2019

Supplementary Material

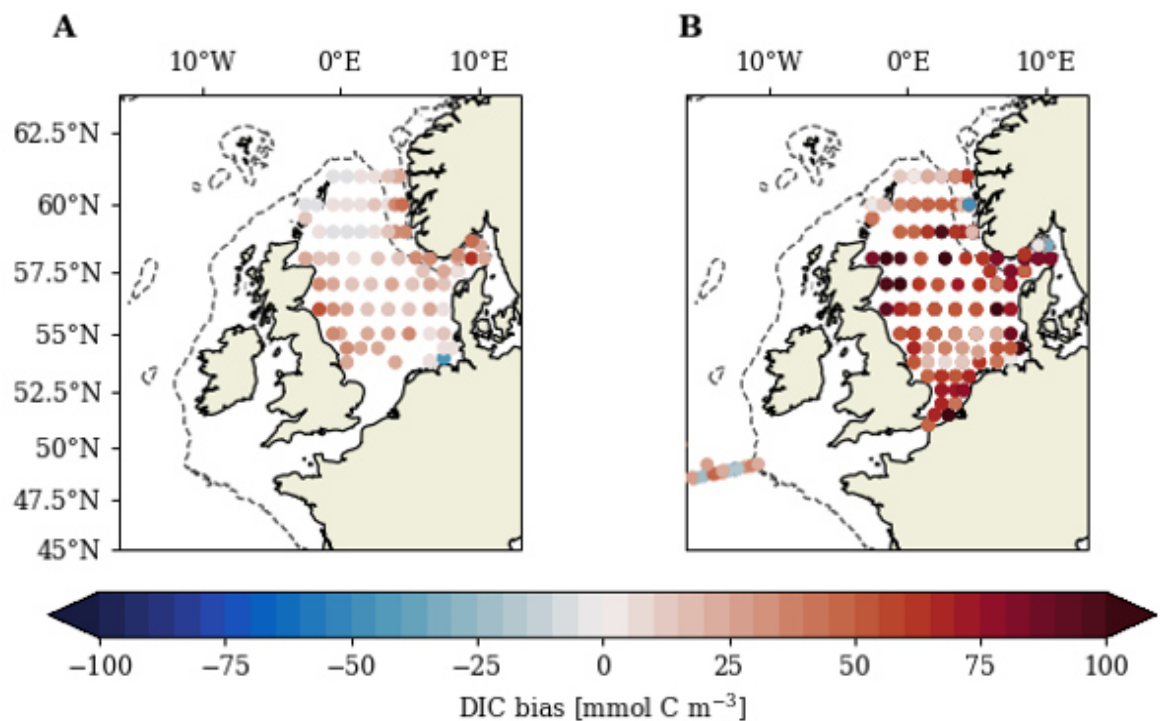
Tidal impacts on air-sea CO₂ exchange on the North-West European Shelf

Jan Kossack*, Moritz Mathis, Ute Daewel, Kubilay Timur Demir, Feifei Liu, Helmuth Thomas, Corinna Schrum

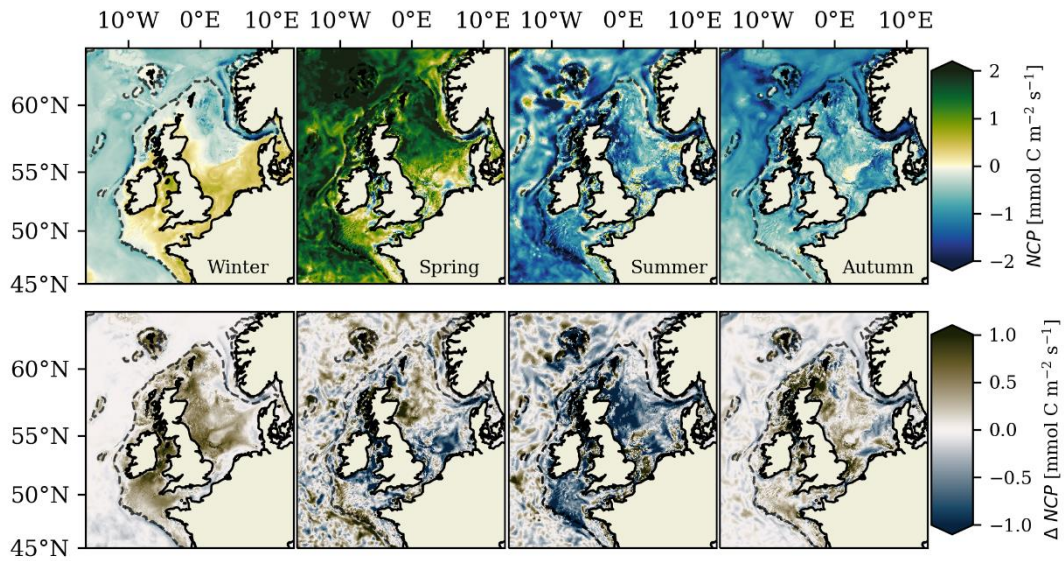
* Correspondence: Jan Kossack: jan.kossack@hereon.de

1 Supplementary Figures and Tables

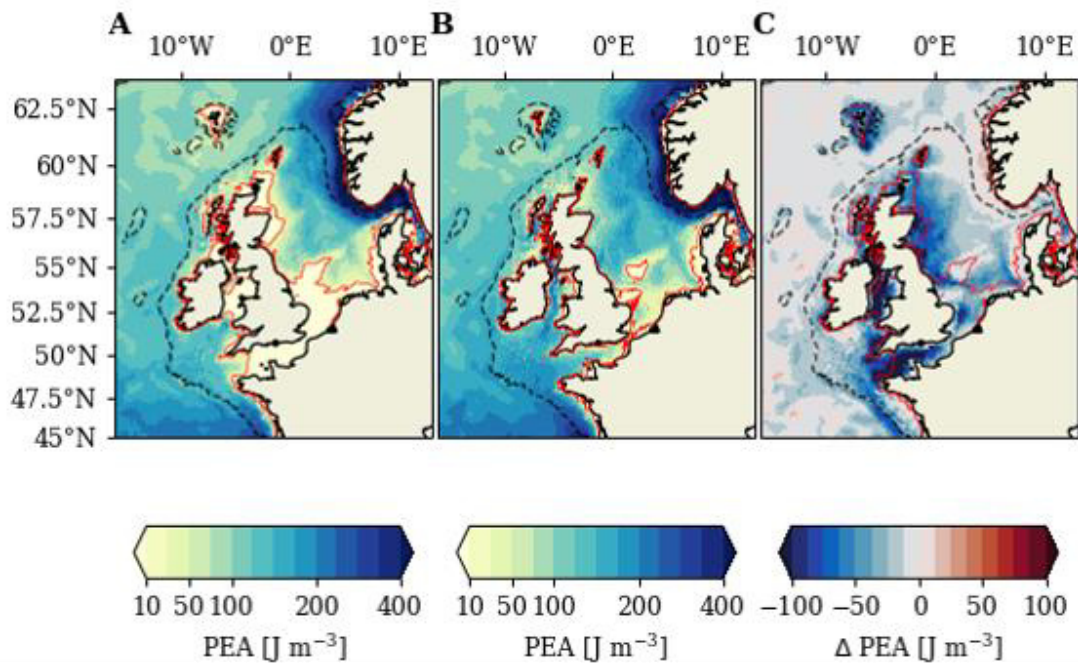
1.1 Supplementary Figures



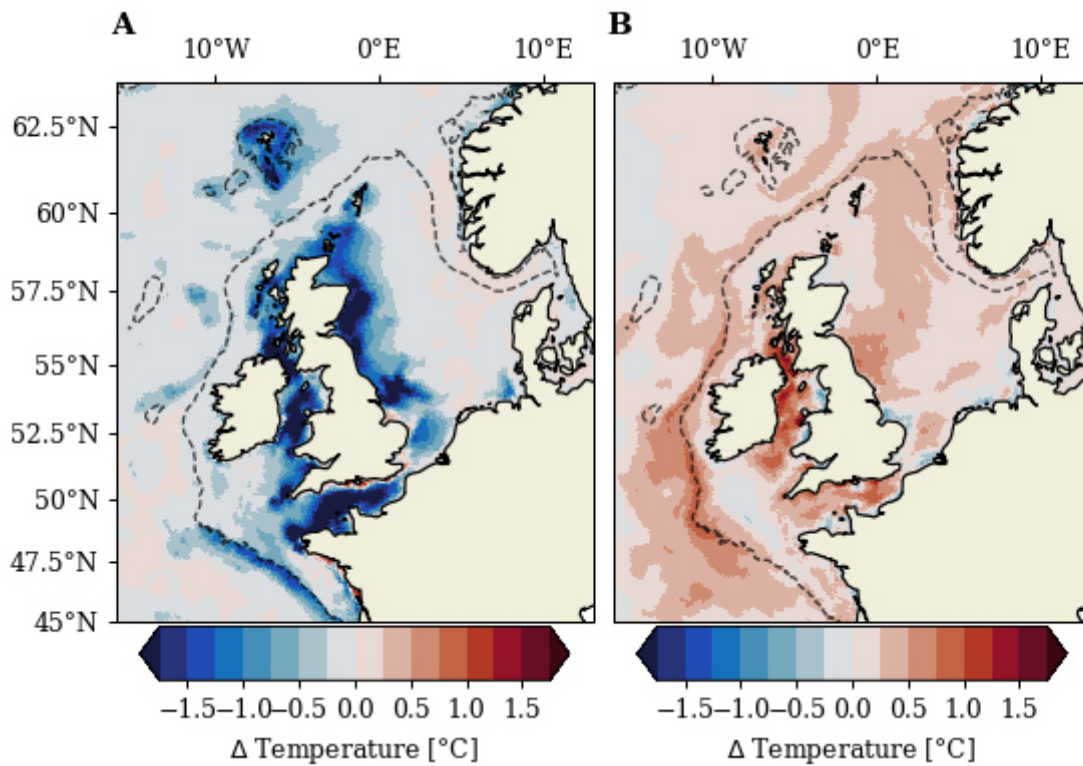
Supplementary Figure S1. Model bias in surface DIC concentrations aggregated for winter (A) and summer (B) against co-located GLODAP data for 2001-2005.



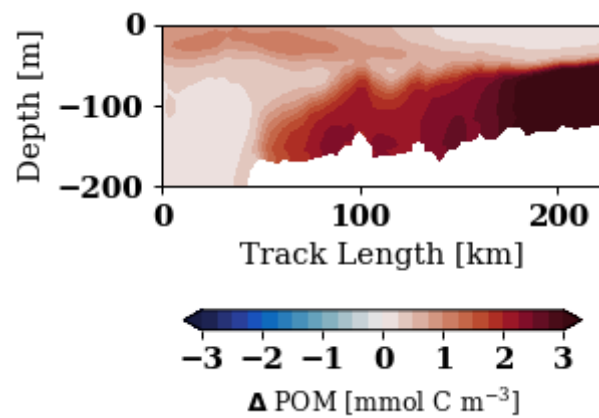
Supplementary Figure S2. Top panel shows seasonal mean net community production (2001-2005; Eq. 7) in TIDE experiment. Bottom panel shows the difference of seasonal mean net community production (2001-2005) in the two experiments (TIDE – NOTIDE).



Supplementary Figure S3. Mean Potential Energy Anomaly for period of strongest stratification (15 July – 15 August; mean for 2001–2005) computed for top 200 m in TIDE experiment (A) and NOTIDE experiment (B). Difference (TIDE-NOTIDE) in the mean Potential Energy Anomaly for period of strongest stratification between the two experiments (C). The red contour ($\text{PEA} = 20 \text{ J m}^{-3}$) marks the tidal frontal zone.



Supplementary Figure S4. Difference of mean summer (A) and winter SST (B) in the two experiments (2001-2005; TIDE – NOTIDE).



Supplementary Figure S5. Difference in mean September POM concentration on transect across Celtic Sea in TIDE experiment. Transect marked in inset in Fig. 11B.

1.2 Supplementary Tables

Supplementary Table ST1: ECOSMO II parameter set used in study.

Definition	Abbr.	Value	Unit
Max. growth rate for Pl	σ_{Pl}	1.30	1/d
Max. growth rate for Ps	σ_{Ps}	1.10	1/d
Photosynthet. effic.	α	0.01	m^2/W
Phyto. self-shading	κ_{phyto}	0.03	$m^2/mmolC$
Detr. self-shading	κ_{det}	0.20	$m^2/mmolC$
DOM self-shading	κ_{DOM}	0.29	$m^2/mmolC$
Water ext. coefficient	κ_W	0.03	1/m
External SPM ext. coeff.	κ_{SPM}	0.0	1/m/(mg/l)
PAR fraction of incident light	par_fraction	0.6	-
NH4 half saturation const.	r_{NH4}	0.20	$mmolN/m^3$
NO3 half saturation const.	r_{NO3}	0.5	$mmolN/m^3$
NH4 inhibition parameter	ψ	3.0	$m^3/mmolN$
Pl mortality rate	m_{Pl}	0.04	1/d
Ps mortality rate	m_{Ps}	0.08	1/d
Graz. r. Zl on Phytopl.	$\sigma_{Zl,P}$	0.8	1/d
Graz. r. Zs on Phytopl.	$\sigma_{Zs,P}$	1.0	1/d
Grazing rate Zl on Zs	$\sigma_{Zl,Zs}$	0.5	1/d
Zs, Zl half saturation const.	r_Z	0.5	$mmolC/m^3$
Zl mortality rate	m_{Zl}	0.1	1/d
Zs mortality rate	m_{Zs}	0.2	1/d
Zl excretion rate	μ_{Zl}	0.06	1/d
Zs excretion rate	μ_{Zs}	0.08	1/d
Zl assim. eff. on plankton	$\gamma_{Zl,P}$	0.75	-
Zs assim. eff. on plankton	$\gamma_{Zs,P}$	0.75	-
Zl & Zs assim. eff. on detr.	$\gamma_{Z,D}$	0.75	-

Supplementary Material

Detritus remineralization rate	ε_D	0.003	1/d
Detritus sinking rate	w_D	5.0	m/d
PO4 half saturation const.	r_{PO4}	0.05	$mmolP/m^3$
SiO2 half saturation const.	r_{Si}	0.5	$mmolSi/m^3$
Si remineralization rate	ε_{Si}	0.015	1/d
Max. growth rate for BG	σ_{BG}	1.0	1/d
BG Temp. control	$T_{ctrl,BG}$	1.0	1/°C
BG reference temperature	$T_{ref,BG}$	0.0	
BG max. grazing rate	β_{BG}	0.3	1/d
BG mortality rate	m_{BG}	0.08	1/d
Critic. bot. stress for resusp.	τ_{crit}	0.007	N/m^2
Resuspension rate	λ_{s2d}	25.	1/d
Sedimentation rate	λ_{d2s}	3.5	m/d
Burial rate	δ_{bur}	0.00001	1/d
Sed. remineralization rate	ε_{Sed}	0.001	1/d
Temp. control denitrification	$T_{ref,denit}$	0.15	1/°C
P sedim. rel. p1	RelSEDp1	0.15	-
P sedim. rel. p2	RelSEDp2	0.10	-
Sed. remineralization rate Si	ε_{Sed3}	0.0002	1/d
Opal sinking rate	w_{Opal}	5.0	m/d
BG sinking rate	w_{BG}	-1.0	m/d
Diatom sinking rate	w_{Pl}	0.0	m/d
Grazing preference Zs on Ps	$a_{Zs,Ps}$	0.7	-
Grazing preference Zs on Pl	$a_{Zs,Pl}$	0.25	-
Graz. preference Zs on Det.	$a_{Zs,Det}$	0.1	-
Grazing preference Zs on BG	$a_{Zs,BG}$	0.3	-
Grazing preference Zl on Ps	$a_{Zl,Ps}$	0.1	-
Grazing preference Zl on Pl	$a_{Zl,Pl}$	0.85	-

Grazing preference Zl on Zs	$a_{Zl,Zs}$	0.15	-
Grazing preference Zl on Det.	$a_{Zl,Det}$	0.1	-
Grazing preference Zl on BG	$a_{Zl,BG}$	0.3	-
Fract. of dissolved from detr.	a_{DOM}	0.4	-
Surface deposition PHO	surface_deposition_pho	0.0	$mmolP/m^2d$
Surface_deposition SIL	surface_deposition_sil	0.0	$mmolSi/m^2d$
Min. daily rad. for BG growth	I_{BG}	120.	W/m^2
Min. daily PAR N fixation	PAR_{BG}	120.	W/m^2

Bibliography

- Azam, F., Fenchel, T., Field, J. G., Gray, J. S., Meyer-Reil, L.-A., and Thingstad, F. (1983). The ecological role of water-column microbes in the sea. *Marine ecology progress series* 10, 257–263.
- Baines, P. G. (1982). On internal tide generation models. *Deep Sea Research Part A. Oceanographic Research Papers* 29, 307–338. doi: 10.1016/0198-0149(82)90098-X
- Barrón, C., and Duarte, C. M. (2015). Dissolved organic carbon pools and export from the coastal ocean. *Global Biogeochem Cycles* 29, 1725–1738. doi: 10.1002/2014GB005056
- Becherer, J., Burchard, H., Carpenter, J. R., Graewe, U., and Merckelbach, L. M. (2022). The Role of Turbulence in Fueling the Subsurface Chlorophyll Maximum in Tidally Dominated Shelf Seas. *J. Geophys. Res. Oceans* 127. doi: 10.1029/2022JC018561
- Belkin, I. M., Cornillon, P. C., and Sherman, K. (2009). Fronts in Large Marine Ecosystems. *Progress in Oceanography* 81, 223–236. doi: 10.1016/j.pocean.2009.04.015
- Bianchi, A. A., Bianucci, L., Piola, A. R., Pino, D. R., Schloss, I., Poisson, A., and Balestrini, C. F. (2005). Vertical stratification and air-sea CO₂ fluxes in the Patagonian shelf. *J. Geophys. Res. Oceans* 110. doi: 10.1029/2004JC002488
- Bianchi, A. A., Pino, D. R., Perlender, H. G. I., Osiroff, A. P., Segura, V., Lutz, V., Clara, M. L., Balestrini, C. F., and Piola, A. R. (2009). Annual balance and seasonal variability of sea-air CO₂ fluxes in the Patagonia Sea: Their relationship with fronts and chlorophyll distribution. *J. Geophys. Res. Oceans* 114. doi: 10.1029/2008JC004854
- Birchill, A. J., Hartner, N. T., Kunde, K., Siemering, B., Daniels, C., González-Santana, D., Milne, A., Ussher, S. J., Worsfold, P. J., Leopold, K., Painter, S. C., and Lohan, M. C. (2019). The eastern extent of seasonal iron limitation in the high latitude North Atlantic Ocean. *Scientific Reports* 9, 1435. doi: 10.1038/s41598-018-37436-3
- Blackford, J. C., and Gilbert, F. J. (2007). pH variability and CO₂ induced acidification in the North Sea. *Journal of Marine Systems* 64, 229–241. doi: 10.1016/j.jmarsys.2006.03.016
- Borges, A. V., Delille, B., and Frankignoulle, M. (2005). Budgeting sinks and sources of CO₂ in the coastal ocean: Diversity of ecosystems counts. *Geophys. Res. Lett.* 32. doi: 10.1029/2005GL023053
- Bowers, D. G., and Simpson, J. H. (1987). Mean position of tidal fronts in European-shelf seas. *Continental Shelf Research* 7, 35–44. doi: 10.1016/0278-4343(87)90062-8
- Broecker, W. (1991). The Great Ocean Conveyor. *Oceanography* 4, 79–89. doi: 10.5670/oceanog.1991.07
- Brown, J., Carrillo, L., Fernand, L., Horsburgh, K., Hill, A., Young, E., and Medler, K. (2003). Observations of the physical structure and seasonal jet-like circulation of the Celtic Sea and St. George's Channel of the Irish Sea. *Continental Shelf Research* 23, 533–561. doi: 10.1016/S0278-4343(03)00008-6
- Brown, J., and Gmitrowicz, E. M. (1995). Observations of the transverse structure and dynamics of the low frequency flow through the North Channel of the Irish Sea. *Continental Shelf Research* 15, 1133–1156. doi: 10.1016/0278-4343(94)00063-S
- Cadée, G. C., and Hegeman, J. (2002). Phytoplankton in the Marsdiep at the end of the 20th century; 30 years monitoring biomass, primary production, and Phaeocystis blooms. *Journal of Sea Research* 48, 97–110. doi: 10.1016/S1385-1101(02)00161-2
- Chaichana, S., Jickells, T., and Johnson, M. (2019). Interannual variability in the summer dissolved organic matter inventory of the North Sea: implications for the continental shelf pump. *Biogeosciences* 16, 1073–1096. doi: 10.5194/bg-16-1073-2019

- Cooley, S., Kite-Powell, H., and Doney, S. (2009). Ocean Acidification's Potential to Alter Global Marine Ecosystem Services. *Oceanography* 22, 172–181. doi: 10.5670/oceanog.2009.106
- Coughlan, C., and Stips, A. *Modelling the tides on the North West European Shelf*. Publications Office. <https://publications.jrc.ec.europa.eu/repository/handle/JRC93441>.
- Dabrowski, T., Hartnett, M., and Olbert, A. I. (2012). Determination of flushing characteristics of the Irish Sea: A spatial approach. *Computers & Geosciences* 45, 250–260. doi: 10.1016/j.cageo.2011.11.023
- Daewel, U., and Schrum, C. (2013). Simulating long-term dynamics of the coupled North Sea and Baltic Sea ecosystem with ECOSMO II: Model description and validation. *Journal of Marine Systems* 119-120, 30–49. doi: 10.1016/j.jmarsys.2013.03.008
- Daewel, U., Schrum, C., and Macdonald, J. I. (2019). Towards end-to-end (E2E) modelling in a consistent NPZD-F modelling framework (ECOSMO E2E_v1.0): application to the North Sea and Baltic Sea. *Geosci. Model Dev.* 12, 1765–1789. doi: 10.5194/gmd-12-1765-2019
- Dai, M., Su, J., Zhao, Y., Hofmann, E. E., Cao, Z., Cai, W.-J., Gan, J., Lacroix, F., Laruelle, G. G., Meng, F., Müller, J. D., Regnier, P. A., Wang, G., and Wang, Z. (2022). Carbon Fluxes in the Coastal Ocean: Synthesis, Boundary Processes, and Future Trends. *Annu. Rev. Earth Planet. Sci.* 50, 593–626. doi: 10.1146/annurev-earth-032320-090746
- Davis, C. E., Blackbird, S., Wolff, G., Woodward, M., and Mahaffey, C. (2019). Seasonal organic matter dynamics in a temperate shelf sea. *Progress in Oceanography* 177, 101925. doi: 10.1016/j.pocean.2018.02.021
- Ducklow, H., Steinberg, D., and Buesseler, K. (2001). Upper Ocean Carbon Export and the Biological Pump. *Oceanography* 14, 50–58. doi: 10.5670/oceanog.2001.06
- Egbert, G. D., and Ray, R. D. (2001). Estimates of M2 tidal energy dissipation from TOPEX/Poseidon altimeter data. *J. Geophys. Res. Oceans* 106, 22475–22502. doi: 10.1029/2000JC000699
- Fernand, L., Weston, K., Morris, T., Greenwood, N., Brown, J., and Jickells, T. (2013). The contribution of the deep chlorophyll maximum to primary production in a seasonally stratified shelf sea, the North Sea. *Biogeochemistry* 113, 153–166. doi: 10.1007/s10533-013-9831-7
- Friedlingstein, P., O'Sullivan, M., Jones, M. W., Andrew, R. M., Bakker, D. C. E., Hauck, J., Landschützer, P., Le Quéré, C., Luijkx, I. T., Peters, G. P., Peters, W., Pongratz, J., Schwingshackl, C., Sitch, S., Canadell, J. G., Ciais, P., Jackson, R. B., Alin, S. R., Anthoni, P., Barbero, L., Bates, N. R., Becker, M., Bellouin, N., Decharme, B., Bopp, L., Brasika, I. B. M., Cadule, P., Chamberlain, M. A., Chandra, N., Chau, T.-T.-T., et al. (2023). Global Carbon Budget 2023. *Earth Syst. Sci. Data* 15, 5301–5369. doi: 10.5194/essd-15-5301-2023
- Gattuso, J.-P., Frankignoulle, M., and Wollast, R. (1998). CARBON AND CARBONATE METABOLISM IN COASTAL AQUATIC ECOSYSTEMS. *Annual Review of Ecology, Evolution, and Systematics* 29, 405–434. doi: 10.1146/annurev.ecolsys.29.1.405
- Graham, J. A., O'Dea, E., Holt, J., Polton, J., Hewitt, H. T., Furner, R., Guihou, K., Brereton, A., Arnold, A., Wakelin, S., Castillo Sanchez, J. M., and Mayorga Adame, C. G. (2018a). AMM15: a new high-resolution NEMO configuration for operational simulation of the European north-west shelf. *Geoscientific Model Development* 11, 681–696. doi: 10.5194/gmd-11-681-2018

- Graham, J. A., Rosser, J. P., O'Dea, E., and Hewitt, H. T. (2018b). Resolving Shelf Break Exchange Around the European Northwest Shelf. *Geophys. Res. Lett.* 45. doi: 10.1029/2018GL079399
- Green, J. A. M., Simpson, J. H., Legg, S., and Palmer, M. R. (2008). Internal waves, baroclinic energy fluxes and mixing at the European shelf edge. *Continental Shelf Research* 28, 937–950. doi: 10.1016/j.csr.2008.01.014
- Gröger, M., Maier-Reimer, E., Mikolajewicz, U., Moll, A., and Sein, D. (2013). NW European shelf under climate warming: implications for open ocean – shelf exchange, primary production, and carbon absorption. *Biogeosciences* 10, 3767–3792. doi: 10.5194/bg-10-3767-2013
- Guihou, K., Polton, J., Harle, J., Wakelin, S., O'Dea, E., and Holt, J. (2018). Kilometric Scale Modeling of the North West European Shelf Seas: Exploring the Spatial and Temporal Variability of Internal Tides. *J. Geophys. Res. Oceans* 123, 688–707. doi: 10.1002/2017JC012960
- Gypens, N., Lacroix, G., Lancelot, C., and Borges, A. V. (2011). Seasonal and inter-annual variability of air–sea CO₂ fluxes and seawater carbonate chemistry in the Southern North Sea. *Progress in Oceanography* 88, 59–77. doi: 10.1016/j.pocean.2010.11.004
- Häkkinen, S., Rhines, P. B., and Worthen, D. L. (2011). Warm and saline events embedded in the meridional circulation of the northern North Atlantic. *J. Geophys. Res. Oceans* 116. doi: 10.1029/2010JC006275
- Hallberg, R. (2013). Using a resolution function to regulate parameterizations of oceanic mesoscale eddy effects. *Ocean Modelling* 72, 92–103. doi: 10.1016/j.ocemod.2013.08.007
- Hammer, K., Schneider, B., Kuliński, K., and Schulz-Bull, D. E. (2017). Acid-base properties of Baltic Sea dissolved organic matter. *Journal of Marine Systems* 173, 114–121. doi: 10.1016/j.jmarsys.2017.04.007
- Hansell, D. A. (2013). Recalcitrant dissolved organic carbon fractions. *Ann Rev Mar Sci* 5, 421–445. doi: 10.1146/annurev-marine-120710-100757
- Hartman, S. E., Humphreys, M. P., Kivimäe, C., Woodward, E., Kitidis, V., McGrath, T., Hydes, D. J., Greenwood, N., Hull, T., Ostle, C., Pearce, D. J., Sivyer, D., Stewart, B. M., Walsham, P., Painter, S. C., McGovern, E., Harris, C., Griffiths, A., Smilenova, A., Clarke, J., Davis, C., Sanders, R., and Nightingale, P. (2019). Seasonality and spatial heterogeneity of the surface ocean carbonate system in the northwest European continental shelf. *Progress in Oceanography* 177, 101909. doi: 10.1016/j.pocean.2018.02.005
- Hauck, J., Zeising, M., Le Quéré, C., Gruber, N., Bakker, D. C. E., Bopp, L., Chau, T. T. T., Gürses, Ö., Ilyina, T., Landschützer, P., Lenton, A., Resplandy, L., Rödenbeck, C., Schwinger, J., and Séférian, R. (2020). Consistency and Challenges in the Ocean Carbon Sink Estimate for the Global Carbon Budget. *Frontiers in Marine Science* 7.
- Hickman, A. E., Moore, C. M., Sharples, J., Lucas, M. I., Tilstone, G. H., Krivtsov, V., and Holligan, P. M. (2012). Primary production and nitrate uptake within the seasonal thermocline of a stratified shelf sea. *Mar. Ecol. Prog. Ser.* 463, 39–57. doi: 10.3354/meps09836
- Hill, A. E., Brown, J., Fernand, L., Holt, J., Horsburgh, K. J., Proctor, R., Raine, R., and Turrell, W. R. (2008). Thermohaline circulation of shallow tidal seas. *Geophys. Res. Lett.* 35. doi: 10.1029/2008GL033459
- Holt, J., Butenschön, M., Wakelin, S. L., Artioli, Y., and Allen, J. I. (2012). Oceanic controls on the primary production of the northwest European continental shelf: model experiments

- under recent past conditions and a potential future scenario. *Biogeosciences* 9, 97–117. doi: 10.5194/bg-9-97-2012
- Holt, J., Hyder, P., Ashworth, M., Harle, J., Hewitt, H. T., Liu, H., New, A. L., Pickles, S., Porter, A., Popova, E., Allen, J. I., Siddorn, J., and Wood, R. (2017). Prospects for improving the representation of coastal and shelf seas in global ocean models. *Geoscientific Model Development* 10, 499–523. doi: 10.5194/gmd-10-499-2017
- Holt, J., and Proctor, R. (2008). The seasonal circulation and volume transport on the northwest European continental shelf: A fine-resolution model study. *J. Geophys. Res. Oceans* 113. doi: 10.1029/2006JC004034
- Holt, J., Wakelin, S., and Huthnance, J. (2009). Down-welling circulation of the northwest European continental shelf: A driving mechanism for the continental shelf carbon pump. *Geophysical Research Letters* 36. doi: 10.1029/2009GL038997
- Hopkins, J. E., Stephenson, G. R., Green, J. A. M., Inall, M. E., and Palmer, M. R. (2014). Storms modify baroclinic energy fluxes in a seasonally stratified shelf sea: Inertial-tidal interaction. *J. Geophys. Res. Oceans* 119, 6863–6883. doi: 10.1002/2014JC010011
- Hopkinson, C. S., and Vallino, J. J. (2005). Efficient export of carbon to the deep ocean through dissolved organic matter. *Nature* 433, 142–145. doi: 10.1038/nature03191
- Humphreys, M. P., Achterberg, E. P., Hopkins, J. E., Chowdhury, M. Z., Griffiths, A. M., Hartman, S. E., Hull, T., Smilenova, A., Wihsgott, J. U., Woodward, E. M. S., and Moore, C. M. (2019). Mechanisms for a nutrient-conserving carbon pump in a seasonally stratified, temperate continental shelf sea. *Progress in Oceanography* 177, 101961. doi: 10.1016/j.pocean.2018.05.001
- Huthnance, J., Hopkins, J., Berx, B., Dale, A., Holt, J., Hosegood, P., Inall, M., Jones, S., Loveday, B. R., Miller, P. I., Polton, J., Porter, M., and Spingys, C. (2022). Ocean shelf exchange, NW European shelf seas: Measurements, estimates and comparisons. *Progress in Oceanography* 202, 102760. doi: 10.1016/j.pocean.2022.102760
- Huthnance, J. M. (1984). Slope Currents and “JEBAR”. *Journal of Physical Oceanography* 14, 795–810. doi: 10.1175/1520-0485(1984)014<0795:SCA>2.0.CO;2
- Hydes, D., Gowen, R., Holliday, N., Shammon, T., and Mills, D. (2004). External and internal control of winter concentrations of nutrients (N, P and Si) in north-west European shelf seas. *Estuarine, Coastal and Shelf Science* 59, 151–161. doi: 10.1016/j.ecss.2003.08.004
- Ikeda, M., Johannessen, J. A., Lygre, K., and Sandven, S. (1989). A Process Study of Mesoscale Meanders and Eddies in the Norwegian Coastal Current. *J. Phys. Oceanogr.* 19, 20–35. doi: 10.1175/1520-0485(1989)019<0020:APSOMM>2.0.CO;2
- Inall, M., Aleynik, D., Boyd, T., Palmer, M., and Sharples, J. (2011). Internal tide coherence and decay over a wide shelf sea. *Geophys. Res. Lett.* 38, n/a-n/a. doi: 10.1029/2011GL049943
- Jiao, N., Herndl, G. J., Hansell, D. A., Benner, R., Kattner, G., Wilhelm, S. W., Kirchman, D. L., Weinbauer, M. G., Luo, T., Chen, F., and Azam, F. (2010). Microbial production of recalcitrant dissolved organic matter: long-term carbon storage in the global ocean. *Nat Rev Microbiol* 8, 593–599. doi: 10.1038/nrmicro2386
- Kitidis, V., Shutler, J. D., Ashton, I., Warren, M., Brown, I., Findlay, H., Hartman, S. E., Sanders, R., Humphreys, M., Kivimäe, C., Greenwood, N., Hull, T., Pearce, D., McGrath, T., Stewart, B. M., Walsham, P., McGovern, E., Bozec, Y., Gac, J.-P., van Heuven, S. M. A. C., Hoppema, M., Schuster, U., Johannessen, T., Omar, A., Lauvset, S. K., Skjelvan, I., Olsen, A., Steinhoff, T., Körtzinger, A., Becker, M., et al. (2019). Winter weather controls

- net influx of atmospheric CO₂ on the north-west European shelf. *Scientific Reports* 9, 20153. doi: 10.1038/s41598-019-56363-5
- Kuliński, K., Szymczycha, B., Koziorowska, K., Hammer, K., and Schneider, B. (2018). Anomaly of total boron concentration in the brackish waters of the Baltic Sea and its consequence for the CO₂ system calculations. *Marine Chemistry* 204, 11–19. doi: 10.1016/j.marchem.2018.05.007
- Kwiatkowski, L., Aumont, O., Bopp, L., and Ciais, P. (2018). The Impact of Variable Phytoplankton Stoichiometry on Projections of Primary Production, Food Quality, and Carbon Uptake in the Global Ocean. *Global Biogeochem Cycles* 32, 516–528. doi: 10.1002/2017GB005799
- Laruelle, G. G., Lauerwald, R., Pfeil, B., and Regnier, P. (2014). Regionalized global budget of the CO₂ exchange at the air-water interface in continental shelf seas. *Global Biogeochem Cycles* 28, 1199–1214. doi: 10.1002/2014GB004832
- Legge, O., Johnson, M., Hicks, N., Jickells, T., Diesing, M., Aldridge, J., Andrews, J., Artioli, Y., Bakker, D. C. E., Burrows, M. T., Carr, N., Cripps, G., Felgate, S. L., Fernand, L., Greenwood, N., Hartman, S., Kröger, S., Lessin, G., Mahaffey, C., Mayor, D. J., Parker, R., Queirós, A. M., Shutler, J. D., Silva, T., Stahl, H., Tinker, J., Underwood, G. J. C., van der Molen, J., Wakelin, S., Weston, K., et al. (2020). Carbon on the Northwest European Shelf: Contemporary Budget and Future Influences. *Frontiers in Marine Science* 7. doi: 10.3389/fmars.2020.00143
- Lessin, G., Artioli, Y., Almroth-Rosell, E., Blackford, J. C., Dale, A. W., Glud, R. N., Middelburg, J. J., Pastres, R., Queirós, A. M., Rabouille, C., Regnier, P., Soetaert, K., Solidoro, C., Stephens, N., and Yakushev, E. (2018). Modelling Marine Sediment Biogeochemistry: Current Knowledge Gaps, Challenges, and Some Methodological Advice for Advancement. *Frontiers in Marine Science* 5. doi: 10.3389/fmars.2018.00019
- Liang, Z., Letscher, R. T., and Knapp, A. N. (2023). Global Patterns of Surface Ocean Dissolved Organic Matter Stoichiometry. *Global Biogeochem Cycles* 37. doi: 10.1029/2023GB007788
- Luneva, M. V., Wakelin, S., Holt, J. T., Inall, M. E., Kozlov, I. E., Palmer, M. R., Toberman, M., Zubkova, E. V., and Polton, J. A. (2019). Challenging Vertical Turbulence Mixing Schemes in a Tidally Energetic Environment: 1. 3-D Shelf-Sea Model Assessment. *J. Geophys. Res. Oceans* 124, 6360–6387. doi: 10.1029/2018JC014307
- Mann, C. R. (1967). The termination of the Gulf Stream and the beginning of the North Atlantic Current. *Deep Sea Research and Oceanographic Abstracts* 14, 337–359. doi: 10.1016/0011-7471(67)90077-0
- Marsh, R., Haigh, I. D., Cunningham, S. A., Inall, M. E., Porter, M., and Moat, B. I. (2017). Large-scale forcing of the European Slope Current and associated inflows to the North Sea. *Ocean Science* 13, 315–335. doi: 10.5194/os-13-315-2017
- Martiny, A. C., Pham, C. T. A., Primeau, F. W., Vrugt, J. A., Moore, J. K., Levin, S. A., and Lomas, M. W. (2013). Strong latitudinal patterns in the elemental ratios of marine plankton and organic matter. *Nature Geosci* 6, 279–283. doi: 10.1038/ngeo1757
- Mathis, M., Logemann, K., Maerz, J., Lacroix, F., Hagemann, S., Chegini, F., Ramme, L., Ilyina, T., Korn, P., and Schrum, C. (2022). Seamless Integration of the Coastal Ocean in Global Marine Carbon Cycle Modeling. *Journal of Advances in Modeling Earth Systems* 14, e2021MS002789. doi: 10.1029/2021MS002789

- Mathis, M., Mayer, B., and Pohlmann, T. (2013). An uncoupled dynamical downscaling for the North Sea: Method and evaluation. *Ocean Modelling* 72, 153–166. doi: 10.1016/j.ocemod.2013.09.004
- Middelburg, J. J., and Herman, P. M. (2007). Organic matter processing in tidal estuaries. *Marine Chemistry* 106, 127–147. doi: 10.1016/j.marchem.2006.02.007
- Middelburg, J. J., Soetaert, K., and Hagens, M. (2020). Ocean Alkalinity, Buffering and Biogeochemical Processes. *Rev Geophys* 58, e2019RG000681. doi: 10.1029/2019RG000681
- Minx, J. C., Lamb, W. F., Callaghan, M. W., Fuss, S., Hilaire, J., Creutzig, F., Amann, T., Beringer, T., Oliveira Garcia, W. de, Hartmann, J., Khanna, T., Lenzi, D., Luderer, G., Nemet, G. F., Rogelj, J., Smith, P., Vicente Vicente, J. L., Wilcox, J., and Del Mar Zamora Dominguez, M. (2018). Negative emissions—Part 1: Research landscape and synthesis. *Environ. Res. Lett.* 13, 63001. doi: 10.1088/1748-9326/aabf9b
- Moreno, A. R., and Martiny, A. C. (2018). Ecological Stoichiometry of Ocean Plankton. *Ann Rev Mar Sci* 10, 43–69. doi: 10.1146/annurev-marine-121916-063126
- Omar, A. M., Olsen, A., Johannessen, T., Hoppema, M., Thomas, H., and Borges, A. V. (2010). Spatiotemporal variations of fCO₂ in the North Sea. *Ocean Sci.* 6, 77–89. doi: 10.5194/os-6-77-2010
- Otto, L., Zimmerman, J., Furnes, G. K., Mork, M., Saetre, R., and Becker, G. (1990). Review of the physical oceanography of the North Sea. *Netherlands Journal of Sea Research* 26, 161–238. doi: 10.1016/0077-7579(90)90091-T
- Painter, S. C., Hartman, S. E., Kivimäe, C., Salt, L. A., Clargo, N. M., Daniels, C. J., Bozec, Y., Daniels, L., Allen, S., Hemsley, V. S., Moschonas, G., and Davidson, K. (2017). The elemental stoichiometry (C, Si, N, P) of the Hebrides Shelf and its role in carbon export. *Progress in Oceanography* 159, 154–177. doi: 10.1016/j.pocean.2017.10.001
- Paris, P. J., Walsh, J. P., and Corbett, D. R. (2016). Where the continent ends. *Geophys. Res. Lett.* 43, 12,208–12,216. doi: 10.1002/2016GL071130
- Pingree, R. D., and Le Cann, B. (1989). Celtic and Armorican slope and shelf residual currents. *Progress in Oceanography* 23, 303–338. doi: 10.1016/0079-6611(89)90003-7
- Pingree, R. D., and Mardell, G. T. (1985). Solitary internal waves in the Celtic Sea. *Progress in Oceanography* 14, 431–441. doi: 10.1016/0079-6611(85)90021-7
- Pingree, R. D., Sinha, B., and Griffiths, C. R. (1999). Seasonality of the European slope current (Goban Spur) and ocean margin exchange. *Continental Shelf Research* 19, 929–975. doi: 10.1016/S0278-4343(98)00116-2
- Polton, J. A. (2015). Tidally induced mean flow over bathymetric features: a contemporary challenge for high-resolution wide-area models. *Geophysical & Astrophysical Fluid Dynamics* 109, 207–215. doi: 10.1080/03091929.2014.952726
- Porter, E. T., Mason, R. P., and Sanford, L. P. (2010). Effect of tidal resuspension on benthic–pelagic coupling in an experimental ecosystem study. *Mar. Ecol. Prog. Ser.* 413, 33–53. doi: 10.3354/meps08709
- Porz, L., Zhang, W., Christiansen, N., Kossack, J., Daewel, U., and Schrum, C. (2024). Quantification and mitigation of bottom-trawling impacts on sedimentary organic carbon stocks in the North Sea. *Biogeosciences* 21, 2547–2570. doi: 10.5194/bg-21-2547-2024
- Powley, H. R., Polimene, L., Torres, R., Al Azhar, M., Bell, V., Cooper, D., Holt, J., Wakelin, S., and Artioli, Y. (2024). Modelling terrigenous DOC across the north west European Shelf: Fate of riverine input and impact on air-sea CO₂ fluxes. *Sci Total Environ* 912, 168938. doi: 10.1016/j.scitotenv.2023.168938

- Prowe, A., Thomas, H., Pätsch, J., Kühn, W., Bozec, Y., Schiettecatte, L.-S., Borges, A. V., and Baar, H. J. de (2009). Mechanisms controlling the air–sea flux in the North Sea. *Continental Shelf Research* 29, 1801–1808. doi: 10.1016/j.csr.2009.06.003
- Pugh, D. T. (1996). *Tides, surges and mean sea-level*. John Wiley & Sons Ltd. ISBN 047191505X.
- Queirós, A. M., Stephens, N., Widdicombe, S., Tait, K., McCoy, S. J., Ingels, J., Rühl, S., Airs, R., Beesley, A., Carnovale, G., Cazenave, P., Dashfield, S., Hua, E., Jones, M., Lindeque, P., McNeill, C. L., Nunes, J., Parry, H., Pascoe, C., Widdicombe, C., Smyth, T., Atkinson, A., Krause-Jensen, D., and Somerfield, P. J. (2019). Connected macroalgal-sediment systems: blue carbon and food webs in the deep coastal ocean. *Ecological Monographs* 89. doi: 10.1002/ecm.1366
- Reissmann, J. H., Burchard, H., Feistel, R., Hagen, E., Lass, H. U., Mohrholz, V., Nausch, G., Umlauf, L., and Wiczorek, G. (2009). Vertical mixing in the Baltic Sea and consequences for eutrophication – A review. *Progress in Oceanography* 82, 47–80. doi: 10.1016/j.pocean.2007.10.004
- Resplandy, L., Hogikyan, A., Müller, J. D., Najjar, R. G., Bange, H. W., Bianchi, D., Weber, T., Cai, W.-J., Doney, S. C., Fennel, K., Gehlen, M., Hauck, J., Lacroix, F., Landschützer, P., Le Quéré, C., Roobaert, A., Schwinger, J., Berthet, S., Bopp, L., Chau, T. T. T., Dai, M., Gruber, N., Ilyina, T., Kock, A., Manizza, M., Lachkar, Z., Laruelle, G. G., Liao, E., Lima, I. D., Nissen, C., et al. (2024). A Synthesis of Global Coastal Ocean Greenhouse Gas Fluxes. *Global Biogeochem Cycles* 38, e2023GB007803. doi: 10.1029/2023GB007803
- Richardson, K. (2000). Subsurface phytoplankton blooms fuel pelagic production in the North Sea. *Journal of Plankton Research* 22, 1663–1671. doi: 10.1093/plankt/22.9.1663
- Rippeth, T. P. (2005). Mixing in seasonally stratified shelf seas: a shifting paradigm. *Philos Trans A Math Phys Eng Sci* 363, 2837–2854. doi: 10.1098/rsta.2005.1662
- Rippeth, T. P., Lincoln, B. J., Kennedy, H. A., Palmer, M. R., Sharples, J., and Williams, C. A. J. (2014). Impact of vertical mixing on sea surface p CO₂ in temperate seasonally stratified shelf seas. *J. Geophys. Res. Oceans* 119, 3868–3882. doi: 10.1002/2014JC010089
- Roobaert, A., Laruelle, G. G., Landschützer, P., Gruber, N., Chou, L., and Regnier, P. (2019). The Spatiotemporal Dynamics of the Sources and Sinks of CO₂ in the Global Coastal Ocean. *Global Biogeochem Cycles* 33, 1693–1714. doi: 10.1029/2019GB006239
- Sarmiento, J., Gruber, N., and McElroy, M. (2007). Ocean Biogeochemical Dynamics. *Physics Today* 60, 65. doi: 10.1063/1.2754608
- Schrum, C., Lowe, J., Meier, H. E. M., Grabemann, I., Holt, J., Mathis, M., Pohlmann, T., Skogen, M. D., Sterl, A., and Wakelin, S. (2016). “Projected Change—North Sea,” in *North Sea Region Climate Change Assessment*, eds. M. Quante, and F. Colijn (Springer International Publishing), 175–217. doi: 10.1007/978-3-319-39745-0_6.
- Schwichtenberg, F., Pätsch, J., Böttcher, M. E., Thomas, H., Winde, V., and Emeis, K.-C. (2020). The impact of intertidal areas on the carbonate system of the southern North Sea. *Biogeosciences* 17, 4223–4245. doi: 10.5194/bg-17-4223-2020
- Seidel, M., Manecki, M., Herlemann, D. P. R., Deutsch, B., Schulz-Bull, D., Jürgens, K., and Dittmar, T. (2017). Composition and Transformation of Dissolved Organic Matter in the Baltic Sea. *Front. Earth Sci.* 5. doi: 10.3389/feart.2017.00031
- Sharples, J. (2007). Potential impacts of the spring-neap tidal cycle on shelf sea primary production. *Journal of Plankton Research* 30, 183–197. doi: 10.1093/plankt/fbm088

- Sharples, J., Moore, M. C., Rippeth, T. P., Holligan, P. M., Hydes, D. J., Fisher, N. R., and Simpson, J. H. (2001). Phytoplankton distribution and survival in the thermocline. *Limnol. Oceanogr.* 46, 486–496. doi: 10.4319/lo.2001.46.3.0486
- Sharples, J., Tweddle, J. F., Mattias Green, J. A., Palmer, M. R., Kim, Y.-N., Hickman, A. E., Holligan, P. M., Moore, C. M., Rippeth, T. P., Simpson, J. H., and Krivtsov, V. (2007). Spring-neap modulation of internal tide mixing and vertical nitrate fluxes at a shelf edge in summer. *Limnol. Oceanogr.* 52, 1735–1747. doi: 10.4319/lo.2007.52.5.1735
- Simpson, J. H. (1998). “The Celtic Seas coastal segment,” in *The Sea, Volume 11: The Global Coastal Ocean – Regional Studies and Syntheses* (New York: John Wiley & Sons Ltd), 659–695.
- Simpson, J. H., and Hunter, J. R. (1974). Fronts in the Irish Sea. *Nature* 250, 404–406. doi: 10.1038/250404a0
- Simpson, J. H., and Sharples, J. (2012). *Introduction to the Physical and Biological Oceanography of Shelf Seas*. Cambridge University Press.
- Song, S., Bellerby, R. G. J., Wang, Z. A., Wurgaft, E., and Li, D. (2023). Organic Alkalinity as an Important Constituent of Total Alkalinity and the Buffering System in River-To-Coast Transition Zones. *J. Geophys. Res. Oceans* 128. doi: 10.1029/2022JC019270
- Song, S., Wang, Z. A., Gonneea, M. E., Kroeger, K. D., Chu, S. N., Li, D., and Liang, H. (2020). An important biogeochemical link between organic and inorganic carbon cycling: Effects of organic alkalinity on carbonate chemistry in coastal waters influenced by intertidal salt marshes. *Geochimica et Cosmochimica Acta* 275, 123–139. doi: 10.1016/j.gca.2020.02.013
- Sündermann, J., and Pohlmann, T. (2011). A brief analysis of North Sea physics. *Oceanologia* 53, 663–689. doi: 10.5697/oc.53-3.663
- Svendsen, E., Stre, R., and Mork, M. (1991). Features of the northern North Sea circulation. *Continental Shelf Research* 11, 493–508. doi: 10.1016/0278-4343(91)90055-B
- Thomas, H., Bozec, Y., Baar, H. J. W. de, Elkalay, K., Frankignoulle, M., Schiettecatte, L.-S., Kattner, G., and Borges, A. V. (2005). The carbon budget of the North Sea. *Biogeosciences* 2, 87–96. doi: 10.5194/bg-2-87-2005
- Thomas, H., Bozec, Y., Elkalay, K., and Baar, H. J. W. d. (2004). Enhanced Open Ocean Storage of CO₂ from Shelf Sea Pumping. *Science* 304, 1005–1008. doi: 10.1126/science.1095491
- Thomas, H., Schiettecatte, L.-S., Suykens, K., Koné, Y. J. M., Shadwick, E. H., Prowe, A. E. F., Bozec, Y., Baar, H. J. W. de, and Borges, A. V. (2009). Enhanced ocean carbon storage from anaerobic alkalinity generation in coastal sediments. *Biogeosciences* 6, 267–274. doi: 10.5194/bg-6-267-2009
- Tinker, J., Polton, J. A., Robins, P. E., Lewis, M. J., and O’Neill, C. K. (2022). The influence of tides on the North West European shelf winter residual circulation. *Frontiers in Marine Science* 9. doi: 10.3389/fmars.2022.847138
- Toggweiler, J. R. (1993). Carbon overconsumption. *Nature* 363, 210–211. doi: 10.1038/363210a0
- Tonani, M., Sykes, P., King, R. R., McConnell, N., Péquignot, A.-C., O’Dea, E., Graham, J. A., Polton, J., and Siddorn, J. (2019). The impact of a new high-resolution ocean model on the Met Office North-West European Shelf forecasting system. *Ocean Science* 15, 1133–1158. doi: 10.5194/os-15-1133-2019

- Tsunogai, S., Watanabe, S., and Tetsuro, S. (1999). Is there a “continental shelf pump” for the absorption of atmospheric CO₂? *Tellus B: Chemical and Physical Meteorology* 51, 701–712. doi: 10.3402/tellusb.v51i3.16468
- Tweddle, J. F., Sharples, J., Palmer, M. R., Davidson, K., and McNeill, S. (2013). Enhanced nutrient fluxes at the shelf sea seasonal thermocline caused by stratified flow over a bank. *Progress in Oceanography* 117, 37–47. doi: 10.1016/j.pocean.2013.06.018
- Umlauf, L., and Burchard, H. (2003). A generic length-scale equation for geophysical turbulence models. *Journal of Marine Research* 61, 235–265. doi: 10.1357/002224003322005087
- Umweltbundesamt (2024). *Climate emissions fall by 10.1 per cent in 2023 – biggest decline since 1990: UBA projection: National climate target for 2030 achievable*. Dessau-Roßlau.
- van Haren, H., Maas, L., Zimmerman, J. T. F., Ridderinkhof, H., and Malschaert, H. (1999). Strong inertial currents and marginal internal wave stability in the central North Sea. *Geophys. Res. Lett.* 26, 2993–2996. doi: 10.1029/1999GL002352
- van Leeuwen, S., Tett, P., Mills, D., and van der Molen, J. (2015). Stratified and nonstratified areas in the North Sea: Long-term variability and biological and policy implications. *J. Geophys. Res. Oceans* 120, 4670–4686. doi: 10.1002/2014JC010485
- van Leeuwen, S. M., van der Molen, J., Ruardij, P., Fernand, L., and Jickells, T. (2013). Modelling the contribution of deep chlorophyll maxima to annual primary production in the North Sea. *Biogeochemistry* 113, 137–152. doi: 10.1007/s10533-012-9704-5
- Vlasenko, V., Stashchuk, N., Inall, M. E., and Hopkins, J. E. (2014). Tidal energy conversion in a global hot spot: On the 3-D dynamics of baroclinic tides at the Celtic Sea shelf break. *J. Geophys. Res. Oceans* 119, 3249–3265. doi: 10.1002/2013JC009708
- Voynova, Y. G., Petersen, W., Gehrung, M., Aßmann, S., and King, A. L. (2019). Intertidal regions changing coastal alkalinity: The Wadden Sea-North Sea tidally coupled bioreactor. *Limnol. Oceanogr.* 64, 1135–1149. doi: 10.1002/lno.11103
- Wakelin, S. L., Holt, J. T., Blackford, J. C., Allen, J. I., Butenschön, M., and Artioli, Y. (2012). Modeling the carbon fluxes of the northwest European continental shelf: Validation and budgets. *Journal of Geophysical Research: Oceans* 117. doi: 10.1029/2011JC007402
- Wihsgott, J. U., Sharples, J., Hopkins, J. E., Woodward, E. M. S., Hull, T., Greenwood, N., and Sivyer, D. B. (2019). Observations of vertical mixing in autumn and its effect on the autumn phytoplankton bloom. *Progress in Oceanography* 177, 102059. doi: 10.1016/j.pocean.2019.01.001
- Williams, C., Sharples, J., Green, M., Mahaffey, C., and Rippeth, T. (2013). The maintenance of the subsurface chlorophyll maximum in the stratified western Irish Sea. *Limn Fluids and Environments* 3, 61–73. doi: 10.1215/21573689-2285100
- Xie, X. H., Cuypers, Y., Bouruet-Aubertot, P., Pichon, A., Lourenço, A., and Ferron, B. (2015). Generation and propagation of internal tides and solitary waves at the shelf edge of the Bay of Biscay. *J. Geophys. Res. Oceans* 120, 6603–6621. doi: 10.1002/2015JC010827
- Zhang, W., Wirtz, K., Daewel, U., Wrede, A., Kröncke, I., Kuhn, G., Neumann, A., Meyer, J., Ma, M., and Schrum, C. (2019). The Budget of Macrobenthic Reworked Organic Carbon: A Modeling Case Study of the North Sea. *JGR Biogeosciences* 124, 1446–1471. doi: 10.1029/2019JG005109
- Zhang, Y. J., Ye, F., Stanev, E. V., and Grashorn, S. (2016). Seamless cross-scale modeling with SCHISM. *Ocean Modelling* 102, 64–81. doi: 10.1016/j.ocemod.2016.05.002
- Zhao, C., Daewel, U., and Schrum, C. (2019). Tidal impacts on primary production in the North Sea. *Earth System Dynamics* 10, 287–317. doi: 10.5194/esd-10-287-2019

Acknowledgements

Science is a collaborative effort that I am very happy to be a part of. The completion of this thesis has only been possible with the support of many people. I firstly want to thank my supervisor, Corinna Schrum. Thank you for the support and guidance, and all the motivating and enlightening discussions. I am very grateful for the unique opportunity to grow in face of a challenge. I would like to thank my co-supervisor Moritz Mathis for his mentorship and pervasive support throughout the last years. Thank you for sharing your extensive and invariably useful knowledge in the field, for all the helpful feedback, and for always setting things into perspective. I would like to thank my second co-supervisor Helmuth Thomas for sharing his immense experience and the constructive discussions fundamental to decisive parts of this thesis. Special thanks to Ute Daewel, who's experience and enthusiasm in ecosystem modelling are truly inspirational, and to Joseph Zhang, who always found time to share his experience and help with the challenges of modelling.

I also would like to thank all the colleagues at Hereon and beyond. The shared enthusiasm in our KST group was a great inspiration, and not facing the struggles of scientific work in these challenging times was very important for me. Many thanks to Fabian Werner for sharing the first steps into science and all the informative discussions. Special thanks to Johannes Pein and Benjamin Jacob for their assistance with the modelling and to Nils Christiansen for all the joint technical troubleshooting.

I would not be here without all the support, care and understanding of friends and family. Thank you Lena, for all the support, for having my back and keeping me grounded. And thank you, Elin, for motivating me on the final stretch.

Eidesstattliche Versicherung | Declaration on Oath

Hiermit erkläre ich an Eides statt, dass ich die vorliegende Dissertationsschrift selbst verfasst und keine anderen als die angegebenen Quellen und Hilfsmittel benutzt habe.

I hereby declare upon oath that I have written the present dissertation independently and have not used further resources and aids than those stated.

Hamburg, 2.6.2024

A handwritten signature in blue ink, appearing to read 'J. Kossack', written in a cursive style.

Jan Felix Gottlieb Kossack